Implicit LES of Turbulent Compressible High-Speed Flows with Transverse Jet Injection

by

Zeeshan Ahmed Rana

Submitted for the Degree of Doctor of Philosophy

Department of Fluid Mechanics & Computational Sciences
School of Engineering
Cranfield University
Cranfield, UK

2011

Cranfield University

School of Engineering

Ph.D. Thesis

Academic Year: 2008-2011

Zeeshan Ahmed Rana

Implicit LES of Turbulent Compressible High-Speed Flows with Transverse Jet Injection

Supervisors:
Dr. Ben Thornber & Prof. Dimitris Drikakis

A Thesis Submitted to the Cranfield University in Partial Fulfillment of the Requirements for the Degree of Doctor of Philosophy (Ph.D.)

Abstract

Implicit Large Eddy Simulation (ILES) has rapidly emerged as a powerful technique which is utilised to explore the unsteady compressible turbulent flows. Apart from offering accuracy in numerical simulations, ILES is also computationally efficient compared to Direct Numerical Simulations or conventional Large Eddy Simulations. This report focuses on the validation of the existing high-resolution methods within the framework of ILES and explores its applications to the high-speed compressible turbulent flows such as a typical flow field inside a scramjet engine. The methodology applied in the current work employs a fifth-order MUSCL scheme with a modified variable extrapolation and a three-stage second-order Runge-Kutta scheme for temporal advancement.

In order to simulate a realistic and accurate supersonic turbulent boundary layer (STBL) a synthetic turbulent inflow data generation method based upon digital filters has been implemented. This technique has been validated and compared against various other turbulent inflow data generation methods in order to find the most accurate, reliable and computationally efficient technique. The high-speed complex multi-species flow of a transverse sonic jet injection into a supersonic crossflow (JISC), which is typical fuel injection strategy inside a scramjet engine, has been investigated for time-averaged and instantaneous flow. It has been demonstrated that the incoming STBL plays a vital role in establishing the correct flow dynamics in JISC study as it enhances the KH instabilities in the flow field.

Thermally perfect gas formulation has been implemented according to the NACA-1135 report to study the effects of high temperatures on the ratio of specific heats (γ). Using this, the full geometry of the HyShot-II scramjet engine is investigated to obtain the inflow conditions for the HyShot-II combustion chamber. Although the design of HyShot-II allowed to disgorge the shock and boundary layer which could otherwise enter the combustion chamber, but, it has been demonstrated that the flow field inside the combustion chamber still consists of a weak shock-train. Finally, the hydrogen injection is analysed inside the HyShot-II combustion chamber, with the shock-train travelling inside and the incoming STBL using digital filters based technique, to explore various time-averaged and instantaneous flow structures and parameters with a view to enhance the understanding of the complex flow field inside the combustion chamber. It is demonstrated from the detailed investigations of a complex high-speed flow that ILES methodology has the potential to develop the understandings of the high-speed compressible turbulent flows using comparatively less computational resources.

Acknowledgements

First and foremost I would like to sincerely thank ALLAH the almighty for granting me strength and ability to complete this challenging task.

I very humbly thank my supervisors Dr. Ben Thornber and Prof. Dimitris Drikakis for giving me the opportunity and then their continued support and guidance throughout the research work at the Cranfield University.

My gratitude also goes to all the academics and staff at the SoE and the HPC Centre at Cranfield University; without any doubt their efforts are huge contributions to any Ph.D. researcher in the FMaCS group.

It is just impossible to name every one of my friends I made at Cranfield (and I know I can be in trouble for this), but I am highly obliged for all of your support and encouragement during tough times and sharing joys of life at good times; I hope that this friendship will last. Sharing the office with several people turned out to be a good experience as during those little chit-chats, we almost solved the entire world's problems. Without the encouragements I received from all of my friends this task would have become very difficult if not impossible.

On the similar note, I would like to thank Cafe Comet and its entire staff for continually supplying doses of caffeine in the form of tea, as the tea-time discussions in the forum of building-83 proved to be very constructive for personal development at SoE.

I would also like to acknowledge my Ex-Boss (at Jeld-Wen UK Ltd) and now friend, Mr. C. Ian Purkis, for his continuous guidance that shaped me as a person and a professional.

I left a good job to start my PhD and it was my wife who had to bear the fall out of it (financially and time wise) but never once complained. Without her support I would be a very different person today, and it would have been certainly much harder to finish a PhD, therefore, the most special thanks belongs to my wife (Saiqa) and I dedicate this thesis to her. Here, how can I forget those little angelic faces, my boys (Bilal and Zaid) and my little princess (Umaiza), who can take the troubles-of-the-day out of dad's mind with their lovely stories and gestures.

Looking back, my time here at Cranfield University has certainly shaped me as a person and the impression Cranfield University left on me is ever lasting.

Zeeshan Ahmed Rana

Contents

List of Figures

List of Tables

Nomenclature

Acronyms

AFRL Air Force Research Laboratory

CFD Computational Fluid Dynamics

CRVs Counter Rotating Vortices

DARPA Defence Advanced Research Projects Agency

DNS Direct Numerical Simulations

HEG High Enthalpy Shock Tunnel Gottingen

ILES Implicit Large Eddy Simulations

JISC Jet Injection into a Supersonic Crossflow

KHI Kelvin-Helmholtz instability

LAPCAT Long-Term Advanced Propulsion Concepts and Technologies

LES Large Eddy Simulations

MILES Monotonically Integrated Large-Eddy Simulation

MUSCL Monotonic Upwind Scheme for Scalar Conservation Laws

RANS Reynolds Averaged Numerical Simulations

RS Reynolds Stresses

SGS Subgrid Scale

SSTO Single-Stage-To-Orbit

STBL Supersonic Turbulent Boundary Layer

TBL Turbulent Boundary Layer

TCRVs Trailing Counter Rotating Vortices

TKE Turbulent Kinetic Energy

$TSTO$ Two-Stage-To-Orbit

TVD Total Variation Diminishing

Latin & Greek Symbols

$\dot{Q}$ Rate of heat transfer

ϵ Rate of dissipation of energy

γ Ratio of specific heats

κ Thermal diffusivity

μ Dynamic viscosity

ν Kinematic viscosity

ρ Density

τ Shear stress

$\vec{U}$ Velocity vector

a Speed of sound

C_p Specific heat at constant pressure

C_v Specific heat at constant volume

E Total energy

e Internal energy

h Enthalpy

M Mach number

p, P Pressure

Pr Prandtl number

R Gas constant

Re Reynolds number

T Temperature

t time

u Component of velocity along x-axis

V Volume

v	Component of velocity along y-axis
w	Component of velocity along z-axis

CHAPTER 1

Introduction

1.1 Background

The dream of flying has lead humans to several challenges. The time line to search for the answer to *Can we fly?* is far longer than the time line for answering the question of *How fast can we fly?* although the challenges involved in the latter quest are perhaps the greatest of all. From Leonardo de Vinci's flying machine to Hezarfen Celebi's glider, then the jet era and now the NASA's X-43A unmanned research vehicle were all another steps towards answering the later quest. First flown in 1969, the Aérospatiale-BAC Concorde was a turbojet based supersonic passenger aircraft that flew at a Mach[1] number of 2.04 (~2,170 kph / 1,350 mph) was perhaps the master-piece of aircraft engineering. In November 16, 2004, NASA launched a research vehicle X-43A into air using a booster rocket to achieve the hypersonic velocity before the X-43A was separated from the booster rocket successfully. It achieved a breath-taking speed of Mach 9.8 (~ 12,144 kph or 7,546 mph) for almost 10 second and is recognized as the fastest controlled flight ever by the Guinness Book of World Records. Figure 1.1 gives a brief review of aircraft technology developments.

The research into hypersonic flight (above Mach ~ 5) dates back to 1950's. Initial attempts utilized the turbo-machinery based jet engines and then it involved research into the ramjet technology. In 1964, Dr. Frederick S. Billig and Dr. Gordon L. Dugger received patent for a modification proposed to a ramjet engine. The idea was a modified ramjet engine where the compressed air is passed on to the combustion chamber at supersonic speeds and the combustion takes place at supersonic velocities, hence the ramjet was named supersonic combustion ramjet (or scramjet) engine. This paved the way towards realizing the dream of hypersonic flight, and the scramjet concept is now considered as the back-bone of the research into hypersonic manned flight. Before going into further details an introduction to scramjet engine concept is presented below.

[1] Mach Number is the ratio of speed of an object moving through the air to the speed of sound. At sea level speed of sound is 340 m/s. Mach=1 means object is travelling at speed of sound. Mach>1 mean object is moving at a speed higher than speed of sound.

Scramjet Engines

Jet engines (Air Breathing Propulsion devices) can be of three types; turbo-machinery based jet engines, ramjets and scramjets. In all the jet engines, the fuel and oxidizer are mixed and then combusted to generate thrust. A jet engine carries fuel on board the flight and oxygen for combustion is ingested through the atmosphere. A turbo-machinery based jet engine is highly efficient at subsonic flight velocities but at transonic velocities it becomes very inefficient mainly because of its moving parts like compressors and turbines. At the same time a turbo-machinery based jet engine can operates from standstill as it has compressors to compress the air when the engine is stationary.

A ramjet uses the ramming action of the air on its inlet ramp to compress the air which is passed to the combustion chamber where it is diffused to low subsonic velocities for combustion. Ramjets do not have any mechanism to compress the air when it is

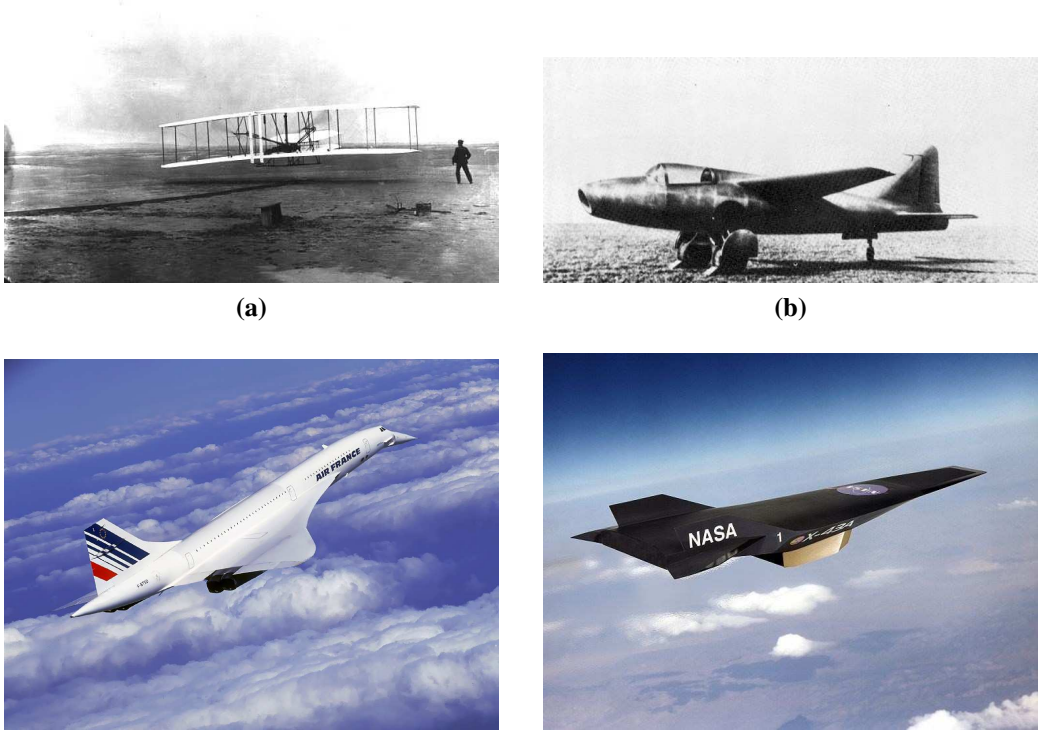

(a) **(b)** **(c)** **(d)**

Figure 1.1: *(a) Orville Wright piloted the first ever flight of a heavier-than-air machine [22]; (b) Heinkel He 178, the world's first aircraft to fly purely on turbojet power on August 27, 1939 [33]; (c) The Aérospatiale-BAC Concorde was a turbojet based supersonic passenger aircraft flew at Mach ~ 2.04 [34]; (d) NASA's X-43A research vehicle achieve the milestone of Mach 9.8 at an altitude of 33,500 m on November 16, 2004 [35].*

standing still and thus can be used only along with a turbo-machinery based jet engine or rocket which can take the flight to reasonable high speeds where the ramjets can produce enough thrust and take over. The efficiency of a ramjet engine is lower than a turbo-machinery based jet engine but it can allows for higher supersonic speeds. For hypersonic speeds (above Mach $\sim$ 5) it is not efficient to decelerate the flow for combustion and the combustion process must take place at locally supersonic velocities.

In order to achieve hypersonic speeds, a scramjet is utilized which uses the same ramming action of air on its inlet ramp to compress it but as the compressed supersonic air is passed on to the combustion chamber it is not diffused and the combustion takes place at supersonic velocities (typically at Mach $\sim$ 2). The scramjet inlet is designed to allow compression of the air such that the temperature rise at the inlet and inside the combustion chamber is at desired levels. The high speeds of the air inside the combustion chamber do not allow for conventional ignition mechanisms and thus the high temperature of the air is utilized to auto-ignite the fuel as it is injected into the combustion chamber. For this reason hydrogen has been found to be the best candidate for a scramjet engine but research into alternative conventional fuels is also on going. A simple ramjet/scramjet engine has three major sections; the inlet, the combustion chamber and the exhaust. Minimum functional Mach number is an important parameter for ram/scramjets which is dependent upon their design and fuel. Typically a ramjet can be used for high supersonic flight speeds (up to Mach $\sim$ 4) whereas a scramjet operates at hypersonic speeds (above Mach $\sim$ 5). Figure 1.2 shows a schematic diagrams for the three types of jet engines discussed above.

Although the NASA's X-43A is the fastest successful scramjet based hypersonic research vehicle, but the Anglo-French Concorde, the Russian Tupolev Tu-144 and

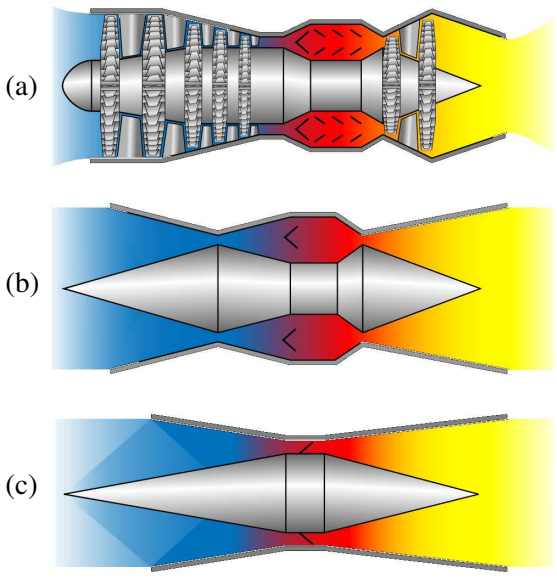

Figure 1.2: *Schematic diagram of, (a) a turbo-machinery based jet engine, (b) a ramjet engine and (c) a scramjet engine [36].*

American SR-71 (turbojet based) are considered as first steps towards manned super/hypersonic flight. The first ever scramjet was flown by Russia in 1991 by the Central Institute of Aviation Motors (CIAM), Moscow, which achieved a speed of Mach 6.4 and provided insight into hypersonic flight controls. In July 2002, in Australia, a team of researchers from the University of Queensland carried out a test flight to study the supersonic combustion using hydrogen as the fuel. The test flight was successful and the research vehicle called "HyShot-II" achieved a massive speed of Mach 7.6 utilising successful supersonic combustion.

Rockets vs. Scramjet

To fly faster and higher is the aim and rockets are already doing this, so, why not use rocket engines and why scramjets? The answer to this question is very simple. Scramjet is a Hypersonic Air-breathing Propulsion (HAP) device which means there is no need to carry around oxygen on board the flight as it would scoop oxygen from the atmosphere as it goes along and that is a huge savings in terms of weight and possibly size. But this is not as simple as it sounds. Scramjets have no thrust at all while standing still. The need, therefore, is to develop a Single-Stage-To-Orbit (SSTO) propulsion system that can operate from zero runway speed to hypersonic cruise. This means at hypersonic velocities the scramjet needs to start and take control of the flight possibly at a range of hypersonic speeds.

Hiraiwa *et al.* [77] presented their study of a scramjet and Rocket-ramjet combined cycle engine which included both wind tunnel experiments and CFD evaluation of the combined cycle engine. The experiments were carried out at HIEST (High Enthalpy Shock Tunnel) and RJTF (Ramjet engine Test Facility) at the Kakuda space centre, Japan. Mach 6 conditions were tested using a subscale model of the engine. The engine was designed to operate at Ejector-jet mode at low speed (start from zero velocity), Then Ramjet mode activated at supersonic speeds and to achieve hypersonic speeds the Scramjet and Rocket modes activated. The work presented achieved a net thrust in lower Mach numbers and tests are underway for higher Mach numbers. Earlier in 2001, Escher [49] proposed seven operating modes of a supercharged ejector scramjet engine (SESJ) combined cycle engine. In this study Escher examined both SSTO and TSTO applications for this engine.

Major Scramjet Projects

Hypersonic air-breathing propulsion is considered as the future of aerospace. Major research is ongoing in this sector involving both commercial and defence related projects [84]. The most up-to-date and advanced of these is the Boeing X-51 (Figure 1.3(a)) project which is a defence project in collaboration of Air Force Research Laboratory (AFRL), Defence Advanced Research Projects Agency (DARPA), NASA, Boeing and Pratt and Whitney Rocketdyne. Initial tests on the X-51 scramjet have been successfully completed at NASA Langley Research Centre for Mach numbers of 4.6, 5 and

6.5 [1]. The X-51 scramjet engine demonstrator took its first flight on 26^{th} of May 2010 and successfully achieved Mach 5 and flew for over 200 seconds with the longest ever scramjet burning of 140 seconds. Further test are also planned which will use the same flight trajectory.

LAPCAT (Long-Term Advanced Propulsion Concepts and Technologies) is a program funded by European Union to study the possibility of developing an Air-Breathing propulsion engine for passenger aircraft travelling at hypersonic speeds of Mach 4-8 [1] (Figure 1.3(b)). FALCON (Force Application and Launch from Continental United States) is another project between DARPA and US Air Force. The first part of the project involves development of a Hypersonic Cruise Vehicle (HCV) for rapid strike and is re-usable and the second part is the development of launch system for Hypersonic Cruise Vehicles to hypersonic speeds. "Blackswift" is the name given to a fighter

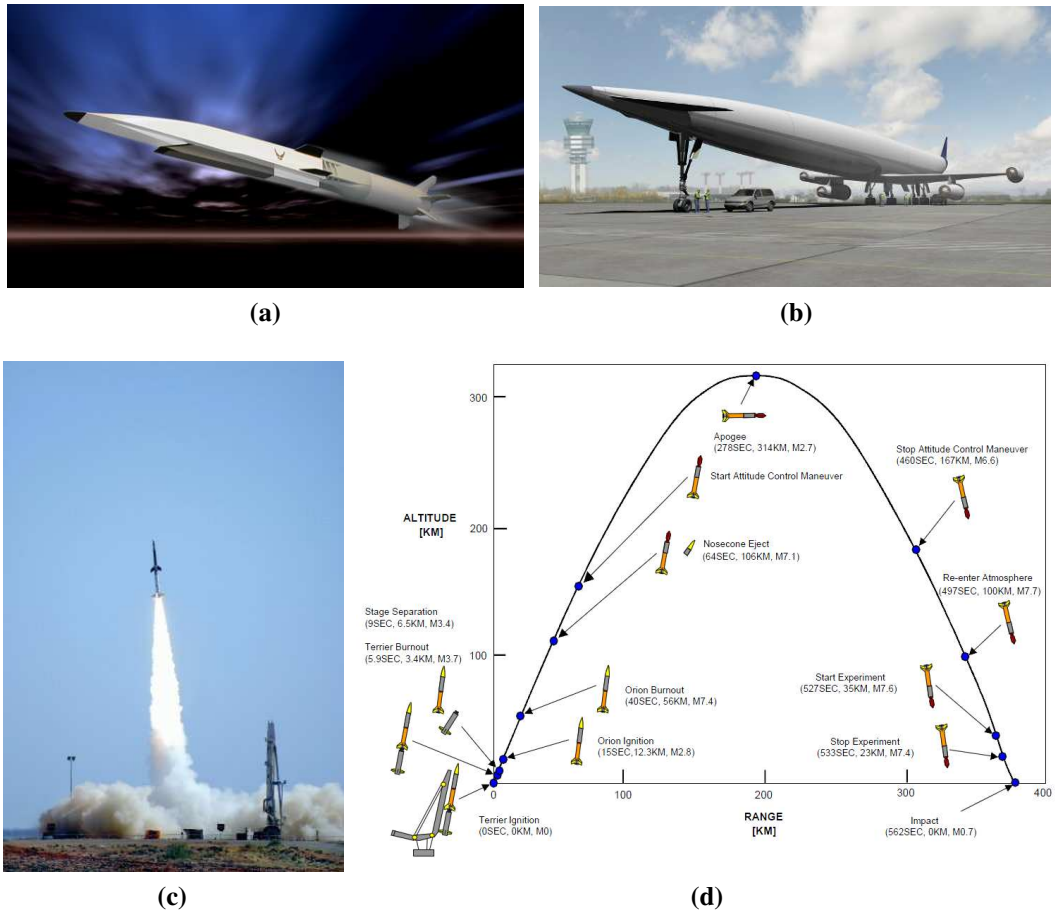

Figure 1.3: *(a) Concept of Boeing X-51A [37]; (b) Concept of Civil Transport aircraft to fly at Mach 5 by Reaction Engines Limited under LAPCAT project [38]; (c) HyShot-II Flight test: Research vehicle launched on July 30, 2002 was a success and achieved Mach 7.6 and sustained supersonic combustion for 6 seconds [39]; (d) Flight trajectory of HyShot-II launch (source: Gardner and Hannemann [57]).*

sized aircraft to be developed under the FALCON project [1].

HyShot and HyCAUSE Project is a major experimental project that was started by the University of Queensland in Australia to obtain pressure measurements in a scramjet engine during supersonic combustion. Currently it has developed into a multi-national project with sponsorships from various organizations from Australia, UK, USA, Japan, South Korea and Germany. The main objective is to develop the understanding of supersonic combustion and its application for passenger aircraft and support the projects like LAPCAT. Five experimental scramjets flight tests have been carried out under this program and supersonic combustion has been observed. The latest flight test experiment is called the "HyCAUSE". HyShot being the core of it, the project has now evolved into developing the concept technology demonstrators that can achieve scramjet-powered atmospheric flight at Mach 8 and is called the "SCRAMSPACE" project lead by the University of Queensland, Australia. The project related to this thesis is the "HyShot-II" (Figure 1.3(c) and (d)) which was successful and achieved Mach $\sim$ 7. Valuable data have been obtained through these experiments which are now going through analysis at various institutions. Figures 1.4 and 1.5 below presents the assembly diagram of the HyShot-II scramjet model and a schematic diagram of the scramjet engine used in the HyShot-II test model showing various sections of the scramjet engine.

1.2 Problem Identification

Wind tunnel testing has been at the forefront of aerospace research; from the first "The Wright Flyer" to modern day supersonic cruise crafts like Concorde. But as the air-

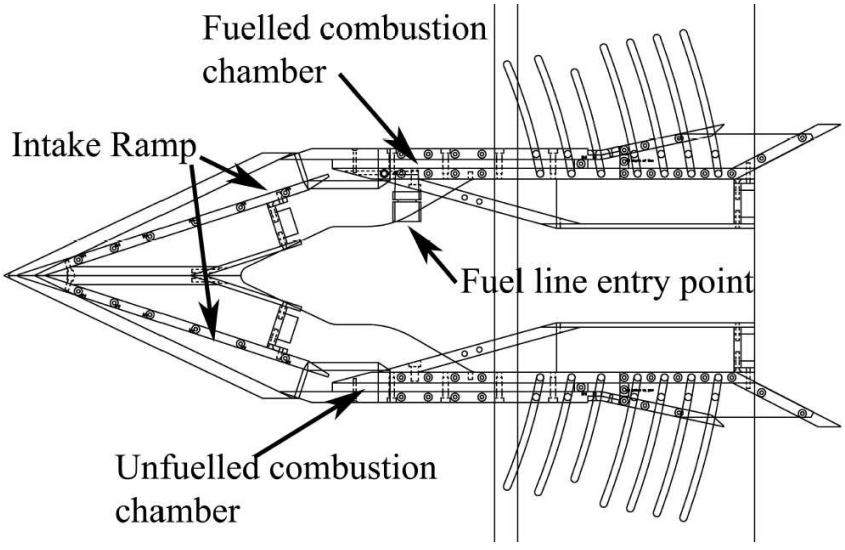

Figure 1.4: *Assembly Diagram of HyShot-II Model for Testing in HEG at DLR (source: Gardner and Hannemann [57]).*

crafts become more and more sophisticated and expensive to build and flight speeds increase, wind tunnels are not the best options, especially for hypersonic flights, mainly because of the costs involved in hypersonic wind tunnels. There are only few wind tunnels available that can operate at hypersonic velocities; the NASA Langley Research Centre in Virginia (USA), the High Enthalpy Tunnel Goettingen (HEG) of the German Aerospace Centre (DLR) in Germany and the T4 Shock Tunnel at the University of Queensland in Australia [122, 148] are the leading hypersonic wind tunnel experimental facilities. In civil sector, by far, the largest amount of wind tunnel testing of a scramjet engine has been carried out within the HyShot and HyCause project. Apart from actual test flights of the scramjet engine further studies were carried out at the T4 Shock Tunnel [122, 148] and the HEG [57].

The High Enthalpy Shock Tunnel Gottingen (HEG) is capable of testing a complete scramjet with internal combustion and external aerodynamics. It can generate a pulse of gas to a nozzle at stagnation pressure of up to 200 MPa and stagnation Enthalpy of up to 24 MJ/kg. Figure 1.6 shows a schematic view of the HEG. The HyShot-II flight tests carried out to date were all designed for a single velocity and the data obtained represent conditions for one particular velocity. After successful test flight of the HyShot-II scramjet, ground based testing was carried out to further analyze the data from flight test. For this purpose two test conditions were developed for nominal flight altitudes of 32.5 km and 27.1 km which is the altitude range where the HyShot-II achieved supersonic combustion and data was collected. The idea behind is to develop a methodology for ground based testing of scramjet engines for further developments [57, 74, 48, 58]. A most recent study of scramjet wind tunnel test was presented by Schramm *et al.* [143]. In this ground based test of the HyShot-II model at the DLR, the HEG tunnel was used and the actual flight test conditions were duplicated for the ground test for measurement of surface pressure, heat transfer and high speed flow visualization inside the HyShot-II combustion chamber.

The process of developing a hypersonic propulsion device involves lots of unknown areas where research is required extensively, including high temperature gas effects and chemical reactions that are very difficult to reproduce in the wind tunnels. Furthermore, scramjet engine integration to the aircraft, materials, fuels, heating and cooling, controls, and mixing of the fuels are some of the major issues related to the scramjet based air-breathing hypersonic propulsion system which needs to be examined care-

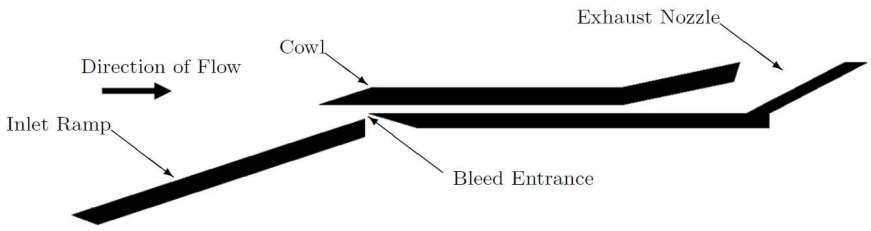

Figure 1.5: *A Schematic Diagram of HyShot-II Model for CFD Study (source: Gardner and Hannemann [57]).*

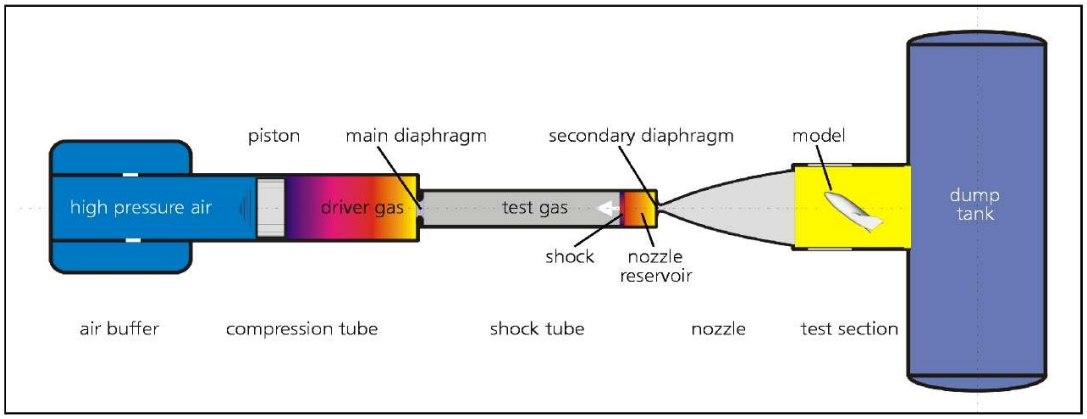

Figure 1.6: *A schematic diagram of the High Enthalpy Shock Tunnel Gottingen, HEG, of the German Aerospace Centre, DLR (source: Gardner and Hannemann [57]).*

fully [6, 76, 84]. Computational Fluid Dynamics (CFD) can help resolve many issues related to the development of flow outside and inside the scramjet technology. As computing power increases and sophisticated CFD tools become available, it is playing a major role in the development of scramjets for the external and internal flows especially the supersonic combustion. Figure 1.7 shows an integrated approach between theory, experiments and computational fluid dynamics. Heiser and Pratt [76] acknowledged the efforts of CFD for the scramjet technological developments as:

> *"Of all the components of a hypersonic propulsion system, the burner is the least understood in terms of achieving desired design requirements. Just from the point of view of performance, burner design differ at low, moderate and high hypersonic, flight Mach numbers, ... , valid fluid dynamics models and uncertainties in them are needed for properly analyzing a burner's flow-field and for determining the burner's performance. In both these activities, computational fluid dynamics (CFD) is an extremely useful tool."*

He further emphasizes (on page 377):

> *" ... estimates of performance quantities, such as the mixing efficiency, as well as the visualization of the highly complex fluid dynamics occurring in realistic burners throughout the Mach number range of air-breathing, hypersonic propulsion systems are only feasible with CFD tools..."*

Numerous CFD studies have been presented to understand the supersonic flow and combustion taking place inside the combustion chamber of a scramjet. Some of them with hydrocarbon fuels and some use hydrogen as fuel. In 2003, Davidenko[23] presented supersonic combustion of hydrogen using RANS (Reynolds Average Navier-Stokes Simulations) approach. He used an implicit first order scheme for time marching and the second order MUSCL scheme for numerical fluxes. Moreover, Roe type

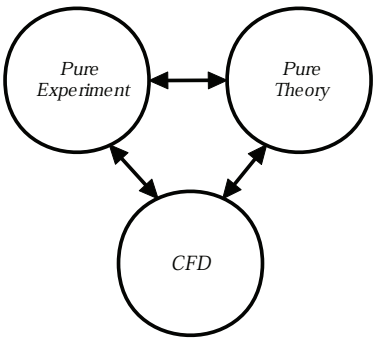

Figure 1.7: *The "Three Dimensions" of Fluid Dynamics (source: Anderson[5]).*

averaging was used to provide parameters on the cell interfaces in order to calculate fluxes from the interpolated primitive variables. He used k-ϵ turbulence model to determine the turbulent properties of the flow. Various combustion models were employed using number of reactions (from 7 to 19 reactions) and the flow mixing and combustion was studied. Also, wall pressure distribution were calculated and compared with the experimental data in order to understand its effects on the mixing. Several other studies[56, 114, 85] have been presented on the supersonic combustion to compare the results with the experiments to enhance/improve the development work and flow visualization but most of them used RANS approach. One of the most important aspects of supersonic flow inside the combustion chamber is the shocks. Shocks can be dangerous as well as useful in the combustion chamber of a scramjet. Because of extremely short resident time for the fuel-air mixture in the combustion chamber of a scramjet engine, shocks can help increase the fuel-air mixing and the combustion efficiency as presented by Hakim [73] and Mack [110].

The HyShot-II flight test and wind tunnel test campaign also include the use of CFD approach in order to understand the supersonic combustion further. For this several studies has been presented which actually follow the wind tunnel testing at the HEG and compare the CFD results with those obtained through the actual flight tests [17, 16, 111, 86, 94]. Karl *et al.* [86] presented, in 2008, CFD study of the latest experimental tests carried out at HEG, DLR. In this paper numerical simulations for a complete HyShot-II model are presented with fuel off and fuel on conditions at Mach 7.4 using DLR-TAU code using RANS approach. They utilized the two equations Wilcox k-ω and one equation Spalart-Allmaras turbulence models and reached to a fair agreement between the experimental and numerical results for static pressure distribution and surface heat flux distribution. Although significant amount of work has already been done in the area of scramjets, it is evident from Karl *et al.* that the supersonic flow inside the combustion chamber is the area where more research needs to be done in all three dimensions of fluid dynamics. The flow instabilities inside the combustion chamber especially present major challenges as it require instantaneous flow studies of fuel injection, penetration and mixing mechanisms through the instabilities in the flow which are not possible through RANS approach.

Karl *et al.* [86] emphasizes:

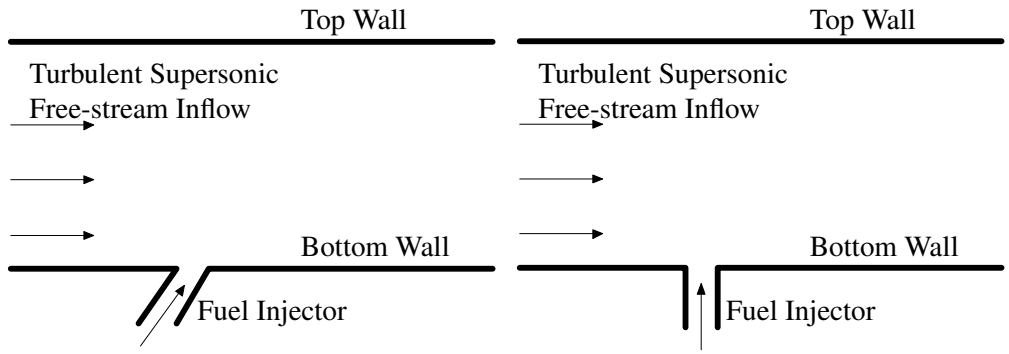

(a) *Inclined Fuel Injection* **(b)** *Transverse Fuel Injection*

Figure 1.8: *Schematic diagram of (a) inclined, (b) transverse fuel injection inside the combustion chamber of a typical scramjet engine.*

> *"The numerical analysis of chemically reacting supersonic flows inside scramjet engines is still subjected to uncertainties which are mainly caused by variations in the predictions of the behavior of boundary and mixing layers obtained by the application of different turbulence models. These uncertainties underline the necessity and urgency of precise validation experiments and of a close link between ground testing, CFD analysis and flight experiments."*

One important aspect of hypersonic flight is the Knudsen number (Kn) which is a dimensionless number and is defined as the ratio of the molecular mean free path length (λ) to the representative physical length. It is useful for determining whether statistical mechanics or the continuum mechanics formulation of fluid dynamics should be used: If the Knudsen number is near or greater than one, the mean free path of a molecule is comparable to a length scale of the problem, and the continuum assumption of fluid mechanics is no longer a good approximation. In this case statistical methods must be used. For the HyShot-II scramjet case, to be discussed in this thesis, it is important at this stage to estimate the Knudsen number in order to establish that the continuum approach (to be explained later) is applicable. McNabb, in 2004, plotted the Knudsen number as a function of altitude. For the HyShot-II scramjet case the plot presented in [115] is used to estimate the Knudsen number for HyShot-II at an altitude of nearly 30 km to be nearly 10^{-5}. This indicates that the flow can be considered as a continuum at this altitude. Therefore, all the CFD analysis referenced above for the HyShot-II case also utilized the continuum approach to analysis the external and internal flow for the HyShot-II scramjet.

The fuel injection system inside the combustion chamber is very critical issue as the supersonic free-stream flows can strongly affect the fuel penetration, air-fuel mixing and flame stability. The instabilities and the shock waves can significantly change the flow properties inside the combustion chamber. Several arrangement can be used for fuel injection in a typical scramjet combustion chamber for example backward step injection, inclined or transverse injection (Figure 1.8). This thesis will concentrate on

the transverse fuel injection because of the obvious reason that the HyShot-II scramjet employs this method for hydrogen injection into the combustion chamber.

The combustion chamber is a wall-bounded structure and the high Reynolds number supersonic flow inside it would be dominated by turbulence near the solid walls to create a thick supersonic turbulent boundary layer. In order to understand the turbulence and instabilities in such flows, this thesis employs the Implicit Large-Eddy Simulations (ILES) technique to study the flow outside and inside the HyShot-II scramjet engine, turbulence inside the combustion chamber, the instabilities in the supersonic flow that can affect the fuel penetration and mixing inside the combustion chamber. For this purpose the instantaneous flow field is analyzed along with the time-averaged flow properties. The results will be used to further enhance the understandings in the field of instabilities and turbulence in high speed propulsion devices. Moreover, a digital filter based turbulent inflow data generation method is employed which bases its validity on an exponential correlation. The importance of the exponential correlation is also investigated by comparing the data with other turbulent data generations methods. The aims and objectives can be itemized as below:

- The application of 5^{th} order accurate MUSCL scheme with modified variable extrapolation to a complex multi-species turbulent flow mixing.
- To explore the turbulent inflow boundary conditions for the generation of turbulent data for unsteady simulations using ILES.
- Implementation of digital filters based turbulent inflow data generation.
- The explore the complex turbulent flow of sonic jet injection into a supersonic cross flow using the digital filter based turbulent inflow data generation technique.
- To demonstrate the better accuracy and efficiency of the digital filter based technique for the generation of turbulent inflow data.
- The explore the full HyShot-II geometry to obtain the combustion chamber inflow condition and then implementation of these combustion chamber inflow conditions to analyze the three-dimensional combustion chamber of HyShot-II scramjet engine.

1.2.1 Thesis Structure

This chapter has explained the background and introduction to the project. The next chapter (Chapter 2) deals with the fundamental knowledge related to turbulence. Chapter 3 discusses the numerical methods employed in the thesis in details along with the thermally perfect gas formulation employed to study the high-temperature gas effects inside the scramjet engine. A synthetic turbulence inflow data generation method based upon digital filter technique has been employed in this thesis with some modifications

which is also presented in the Chapter 3. Chapter 4 discusses the *Jet Injection into a Supersonic Cross-flow* (JISC) flow where the synthetic turbulence data generated from the digital filter based technique is employed as the turbulent inflow boundary condition to generate a supersonic turbulent boundary layer (STBL) to study JISC. This chapter also acts as verification and validation chapter for the turbulence boundary condition employed.

The Chapter 5 investigates the reliability and accuracy of various turbulent inflow data generation methods by comparing the digital filter based synthetic turbulent boundary condition with laminar flow and the random white-noise based turbulent boundary condition. After the validation and verification of the numerical methods, the HyShot-II scramjet engine will be the focus point of Chapter 6 where the external flow will be investigated in two-dimensions to obtain the combustion chamber inlet conditions. These will then be used to study the transverse hydrogen fuel injection inside the HyShot-II scramjet combustion chamber in three-dimensions. Finally Chapter 7 will present the conclusions and some ideas for the future work.

1.2.2 Publications

Below is a list of international journal and conference papers resulted from the work presented in this thesis.

- **Z.A. Rana**, B. Thornber, D. Drikakis, "Transverse jet injection into a supersonic turbulent cross-flow", Physics of Fluids, Vol:23, Iss:4, April 2011, (DOI: 10.1063/1.3570692)
- **Z.A. Rana**, B. Thornber, D. Drikakis, "On the Importance of Generating Accurate Turbulent Boundary Condition for Unsteady Simulations", Journal of Turbulence, Vol. 12, No. 35, 2011. (DOI: 10.1080/14685248.2011.613836)
- **Z.A. Rana**, B. Thornber, D. Drikakis, "Dynamics of Under-Expanded Hydrogen Jet Injection and Mixing inside a Scramjet Combustor", (Under Review: Physics of Fluids)
- **Z.A. Rana**, B. Thornber, D. Drikakis, "Large Eddy Simulation of the fuel injection in scramjet combustion chambers", The Proceedings of the 7th Aero-Thermodynamics Symposium (7th-ATD Symp), Brugge (Belgium), 9th May 2011. ESA Special Publication SP-692, paper: 2218933.
- **Z.A. Rana**, B. Thornber,D. Drikakis, "Analysis of hydrogen injection into the combustor of HyShot-II scramjet engine using ILES", (AIAA-2011-506), 49th AIAA Aerospace Sciences Meeting, 4-7 January 2011, Florida, USA.
- **Z.A. Rana**, B. Thornber, D. Drikakis, "An ILES analysis of transverse jet injection into supersonic cross-flow with synthetic turbulent boundary layer", (AIAA-2011-231), 49th AIAA Aerospace Sciences Meeting, 4-7 January 2011, Florida, USA.

- **Z.A. Rana**, D. Drikakis, "Investigation of sonic jet mixing in a stream of supersonic cross-flow using Large Eddy Simulations", 27th Congress of the International Council of the Aeronautical Sciences, 19-24 September 2010, Nice, France.

- **Z.A. Rana**, B. Thornber, D. Drikakis, "CFD analysis of a scramjet model using high resolution methods", European Air and Space Conference, October 2009, Manchester, UK.

- **Z.A. Rana**, B. Thornber, D. Drikakis, "Simulations of the HyShot-II (scramjet) model using high-resolution methods", (AIAA-2009-4844), 45th AIAA Joint Propulsion Conference and Exhibit, 2-5 August 2009, Denver, USA.

- **Z.A. Rana**, Consortium on Computational Combustion for Engineering Applications (COCCFEA), 2-3 April 2009, Fitzwilliam College, Cambridge, UK.

- **Z.A. Rana**, "Analysis of HyShot-II scramjet combustor using ILES". Research Students Poster Conference, Cranfield University, Cranfield, U.K. 19th January, 2011.

CHAPTER 2

Turbulence: Fundamental Concepts

This chapter introduces the basic concepts related to the turbulence and various characteristics associated with the turbulent flows. Its explains the scales of turbulence, transition from laminar to turbulent flow, the turbulent boundary layer, shear-layer flows and instabilities present in turbulent flows.

2.1 Turbulence

Turbulence is one of the most challenging and mathematically unsolved physical phenomenons in the field of fluid dynamics. It is characterized by random property changes in the flow field that give rise to stochastic fluctuations in the velocity and pressure distributions. To understand the "randomness" in the context of turbulence, Pope [126] presented an example where a fluid flow experiment is undertaken repeatedly under a given fixed set of conditions. In these experiments an event $\boldsymbol{E}$ occurs such that $\boldsymbol{E}$ is the velocity of the fluid flow equal to, say, 5 ms^{-1}. Although there are fluctuations present in the velocity field, if this event occurs in the experiment at a specific location and time then it is a *certain* event but if the event does not occur then it is an *impossible* event. Third possibility is that the event occurs intermittently then it is referred to as a *random* event and such randomness present in the flow field is characterized as turbulence. It is argued that intermittent and random events can occur in a laminar flow as well there in order to differentiate a turbulent flow from laminar several other factors has been identified which must be considered.

Viscosity is a very important parameter in fluids. As the fluid viscosity decreases the viscous forces, that keep the flow laminar, decrease and the inertial forces tend to dominate making the flow turbulent. Turbulence can be observed in many natural flows as illustrated in the Figure 2.1. In most of the engineering flows the presence of turbulence can be considered beneficial as it can enhance the fluid mixing process but in several cases the presence of turbulence can be a problem especially in aerodynamic flows. In aerodynamic turbulent flows unsteady vortices consisting of several scales are created near the solid surface and interact with each other in the boundary layer thus

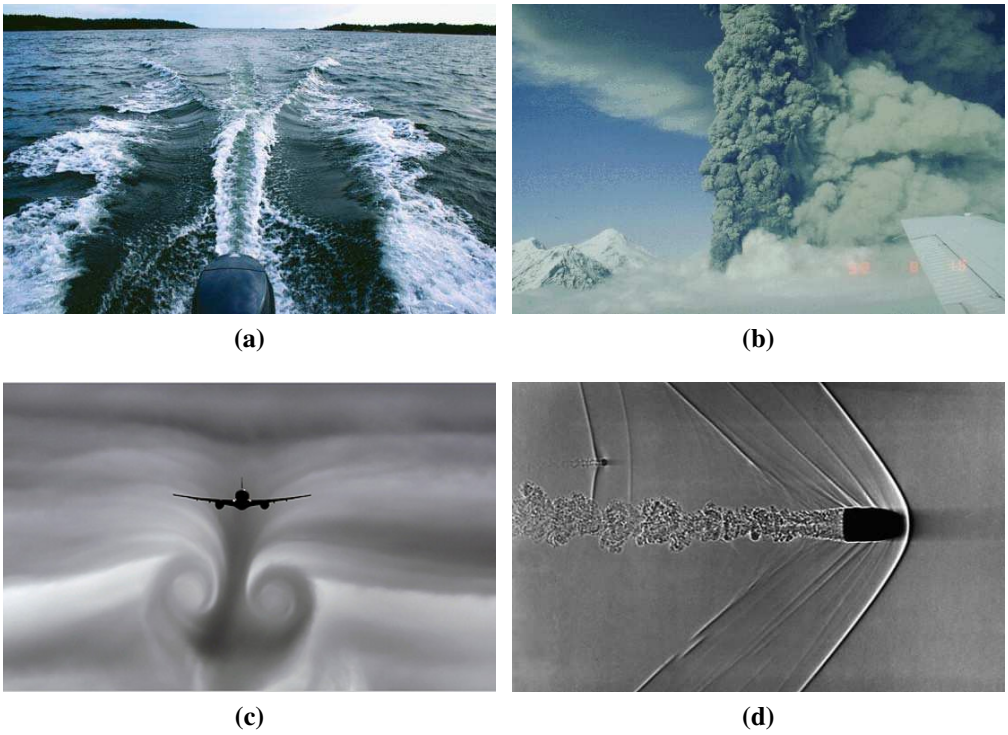

Figure 2.1: *Turbulence in nature, (a) wake of behind a boat [24]; (b) Eruption of the Mt. Spurr near Anchorage in 1992 [25];(c) wake behind an aircraft [32]; (d) wake behind a bullet at hypersonic velocity [26].*

increasing the drag. The concept of controlled turbulence in aerodynamic flows can define the location and structure of the boundary layer to create flow separation such that the drag would actually reduce at critical design points such as using aero-spike and vortex generators.

Figure 2.2 shows a schematic diagram for the time history of streamwise velocity component measured at a point in a turbulent flow where the mean velocity ($\bar{u}$) and fluctuations (u') at any time instant are shown for a time-dependent simulation. It can be observed that for a time-dependent flow simulations there are significant fluctuations in the velocity component which are not periodic but show variations on a wide range of length and time scales. The actual velocity component at any time instant would be the sum of the mean and the fluctuation as below:

$$u = \bar{u} + u' \tag{2.1}$$

Turbulence is a three-dimensional phenomenon, therefore, the above formulation is valid for other components of the velocity in each direction. Several factors define the characteristics of a turbulent flow where Reynolds number (Re) can be considered the most important one. Turbulent flows can be categorized into three types; wall-bounded flows (boundary layer), shear layer flows and grid-generated turbulent flows; the work

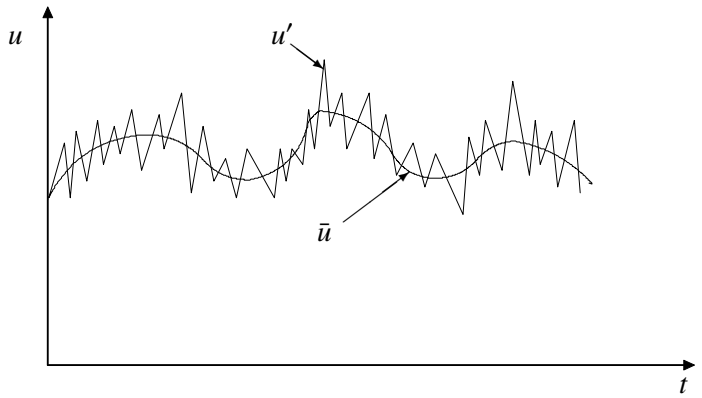

Figure 2.2: *Schematic of time history of streamwise velocity component showing the mean ($\bar{u}$) and instantaneous (u') velocities for a time dependant turbulent flow simulation.*

presented here deals with the first two types of turbulent flows. In the first type[82], the wall-bounded flows, maximum turbulence is produced in the near wall regions. The small scale eddies present in the near wall regions exhibit organized and self-similar structures. Such flows can be further sub-categorized as the boundary layer flows and fully developed flows. The boundary layer flows are where there is free-stream flow bounded by a wall such as a flat-plate flow, whereas, the fully developed flows are bounded by surfaces such as channel or pipe flows. The second category[82] important from the view point of current work is the turbulent shear layer flow. This is the flow where there is a shear layer present in the flow and the turbulence grows in the streamwise direction. Such flows can be sub-categorized into three types; a free shear layer flow, jet flow and wakes.

In order to understand turbulence one must be familiar with the physical processes involved in a turbulent flow such as *production*, *diffusion* and *dissipation* [82, 126, 163]. "Production", in the context of turbulence, relates to the physical processes that are involved in producing turbulence in the flow such as the formation of hairpin vortices and eddies (coherent structures) in a flow. "Diffusion" is termed as the process where the eddies generated during the production move around the turbulent flow in a random fashion and transport the fluid properties in the turbulent flow from one region to the other thus contributing to an increase in the mixing of the fluid. During the production process, various sizes of eddies are formed and the larger scale eddies define the thickness of the boundary layer. The smaller eddies close to the wall are under the influence of viscosity and as they get smaller their velocity gradient becomes larger. Due to the large velocity gradients on smallest eddies the viscous forces overcome and the energy dissipates from the flow which is also termed as "Dissipation".

2.2 Scales of Turbulence

An eddy is considered as a turbulent motion with a local region of finite size and is at least reasonably coherent within this region. A region consisting of a large eddy can also have small eddies. The turbulent flows are characterized by wide range of these coherent structures and vortex dynamics of these eddies. Each of the large scale eddies is characterized by its length scale which can be compared to the flow characteristic length. L.F. Richardson, in 1922, brought forward the idea of *energy cascade* which implies that in turbulent flows the kinetic energy produced during the production process in the large scale eddies is transferred to the eddies of smaller scales through diffusion process until it reaches the smallest scales of the eddies from where the kinetic energy just dissipates away by viscous action. This means that the large scale eddies are fundamentally unstable and break up to transfer their energy to the smaller scales until the Reynolds number is small enough to make the eddy motion stable and thus creating an energy cascade. He presented this idea very nicely as below [126]:

Big whorls have little whorls,
Which feed on their velocity;
And little whorls have lesser whorls,
And so on to viscosity.

In this way the kinetic energy transfer through turbulence can be seen as where energy is entering on one side (at the largest scale level) and leaving the turbulence at the other end (smallest scale level). Therefore, the rate of energy dissipation (ϵ) is estimated from the rate of energy production. At the largest scale, the eddies have energy of the order of u_c^2 and timescale $\tau = l/u_c$, where u_c is the characteristic velocity and l is the size of the eddy. Timescale (τ) is the turnover time for one eddy which can be regarded as its lifespan in the turbulent flow. Thus the rate of transfer of energy can be estimated as below and is independent of molecular viscosity:

$$\epsilon = \frac{u_c^2}{\tau} = \frac{u_c^3}{l} \tag{2.2}$$

Kolmogorov's Scaling

Several unanswered questions about the size, the characteristic velocity and timescales of the smallest eddy were addressed by Kolmogorov [100]. In 1941, Kolmogorov proposed a universal equilibrium theorem according to which the rate of energy transfer from large eddies to the smaller ones is approximately same as the dissipation of energy from smaller eddies and proposed that the smallest eddies have the primary parameters of mean dissipation rate (ϵ) and kinematic viscosity (ν). Based upon these parameters and using the dimensional analysis, the Kolmogorov's length (η_k), velocity (u_η) and time (τ_η) scales are obtained as below:

$$\eta_k = \left(\frac{\nu^3}{\epsilon}\right)^{1/4} \tag{2.3a}$$

$$u_\eta = \left(\nu^3\epsilon\right)^{1/4} \tag{2.3b}$$

$$\tau_\eta = \left(\frac{\nu}{\epsilon}\right)^{1/2} \tag{2.3c}$$

These Kolmogorov scales are related to the largest scales in turbulent flow using the Reynolds number as below:

$$\frac{\eta_k}{l} \sim Re^{-3/4} \tag{2.4a}$$

$$\frac{u_\eta}{u_c} \sim Re^{-1/4} \tag{2.4b}$$

$$\frac{\tau_\eta}{\tau} \sim Re^{-1/2} \tag{2.4c}$$

For convenience the intermediate range of the scales are often referred to as *Taylor micro-scales* (λ_T) which mainly define the mean spatial level of the velocity gradients but are not related to the smallest scales. These are found as below:

$$\frac{\lambda_T}{l} \sim Re^{-1/2} \tag{2.5a}$$

$$\frac{\lambda_T}{\eta} \sim Re^{1/4} \tag{2.5b}$$

Energy Spectrum

Several length scales in a turbulent flow have been introduced and the turbulent kinetic energy is distributed over these scales and can be observed using a spectral analysis. In the spectrum analysis different length scales are represented using their *wavenumber* (k) and the velocity field is represented in Fourier space. The kinetic energy can be calculated by multiplying the velocity at a particular wavenumber with its complex conjugate and thus a spectrum analysis presents the distribution of kinetic energy across the complete range of wavenumbers or length scales.

This energy spectra can be divided into two major sections; firstly small wavenumber range representing the largest scales which comprise of the most of the energy and represent the energy production process and is termed as *energy containing range*, and secondly the higher wavenumbers range representing the small scales which contain the universal equilibrium range of energy and is termed as *inertial subrange*. Sometimes another section can be visible in a spectrum analysis which consists of highest wavenumbers or smallest scales which represent the Kolmogorov scales and represent the energy dissipation under viscous forces and is called the *dissipation range*. Figure

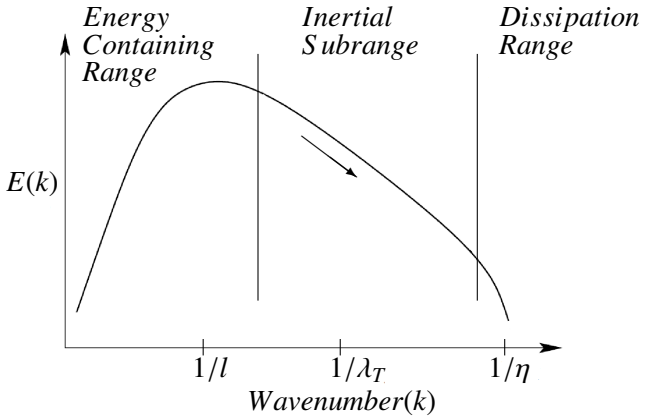

Figure 2.3: *Schematic diagram showing a typical turbulent energy density.*

2.3 shows a schematic diagram of typical energy spectrum function (energy density with units of L^3T^{-2}) for a turbulent flow on a logarithmic scale showing various sections as described above. Kolmogorov derived an expression based upon dimensional analysis for the energy density in the inertial subrange as:

$$E(k) = C\epsilon^{2/3}k^{-5/3} \tag{2.6}$$

where C represents a universal constant. Although this relation has not been analytically proven but several experimental and numerical studies have confirmed its validity and is considered as a milestone in the analysis of turbulent flows as shown in the Figure 2.4.

2.3 Transition To Turbulence

Reynolds number is one of the most important characteristic of a turbulent flow. As the Reynolds number increases in a laminar flow, the instabilities are generated near the wall surface which results in transition of the laminar flow into a turbulent flow in boundary layer flows. The transition process is enhanced by several factors such as surface shape and roughness, heat transfer, turbulence in free-stream and pressure gradients which lead to vortex stretching/breakdown until the flow becomes fully turbulent. The stability of a laminar flow has been extensively discussed by [167, 121, 102] where they presented the mathematical details associated with stability in a laminar flow and the generation of instabilities in the transition process. It has been established that at a critical Reynolds number a range of wavenumbers are present in the flow which are inherently unstable and are referred to as *Tollmein-Schlichting* waves which can be considered as the first instability towards the transition process [82].

These waves are initially two-dimensional but gradually grow into three-dimensional vortex structures. As these three-dimensional instabilities have established in the flow, their non-linearity and interactions with the free-stream mean flow result in alteration

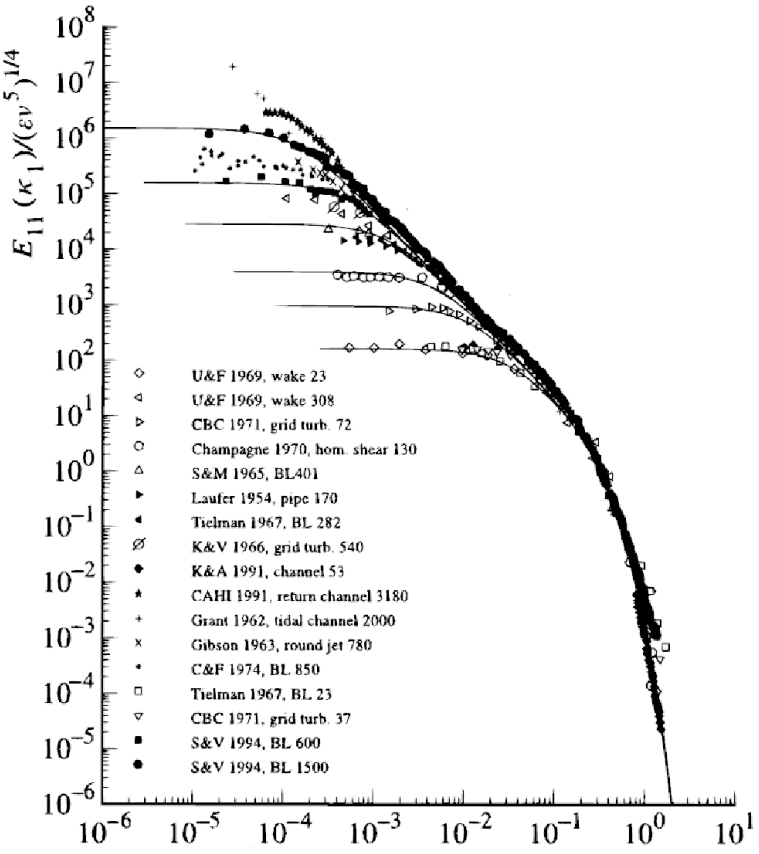

Figure 2.4: *Turbulent kinetic energy spectrum obtain from various experiment show same trends as proposed by Kolmogorov (Image source: S. Pope [126]).*

of mean flow velocities and vortex stretching occurs. This also result in the formation of internal shear layers in the flow which are highly unstable. Due to these the stretched vortices start to break. This process of vortex breaking results in smaller vortices exhibiting random frequencies and produce local regions of high shear and fluctuations in the shear layer and are referred to as turbulent spots. As an overall effect of these processes a random field is created called turbulence in the flow field which grows in size as it travels downstream. As the turbulent spots increase in number the flow becomes fully turbulent and transition process completes at this stage resulting in fully turbulent flow which is full of turbulent spots. If the free-stream is supersonic or hypersonic the process of transition would be affected but it mainly depends upon several factors mentioned previously. The resulting region closer to the wall in the fully turbulent flow is called the *turbulent boundary layer* which is a very interesting and challenging active research area and is shown schematically in Figure 2.5.

2.4 Types of Turbulent Flows

Two major types of turbulent flows that are important within the context of this work are explored as presented below.

2.4.1 Turbulent Boundary Layer (TBL)

It is well understood that the forces dominant in the region near the wall are the viscous forces in a high Reynolds number flow. The boundary layer region starts with well-behaved streamlines but then due to various effects transition takes place into turbulence. Figure 2.5 shows the development of a laminar flow into a fully turbulent boundary layer. In the TBL heavy mixing of fluid occurs at macroscopic levels and due to this and associated momentum fluxes the velocity profile in a TBL is different from a laminar flow. Figure 2.6(a) shows the velocity profile for a laminar boundary layer and TBL where the normal wall distance (y) is normalized by the thickness of the boundary layer for comparison purpose. It is shown that for a TBL the velocity profile is much fuller than the laminar boundary layer and a steep gradient in velocity is found closer to the wall. Figure 2.6(b) shows the instantaneous view of a supersonic turbulent boundary layer (STBL) over a flat-plate where the free-stream streamlines are shown clearly as mostly undisturbed away from the wall. Closer to the wall, disturbances can

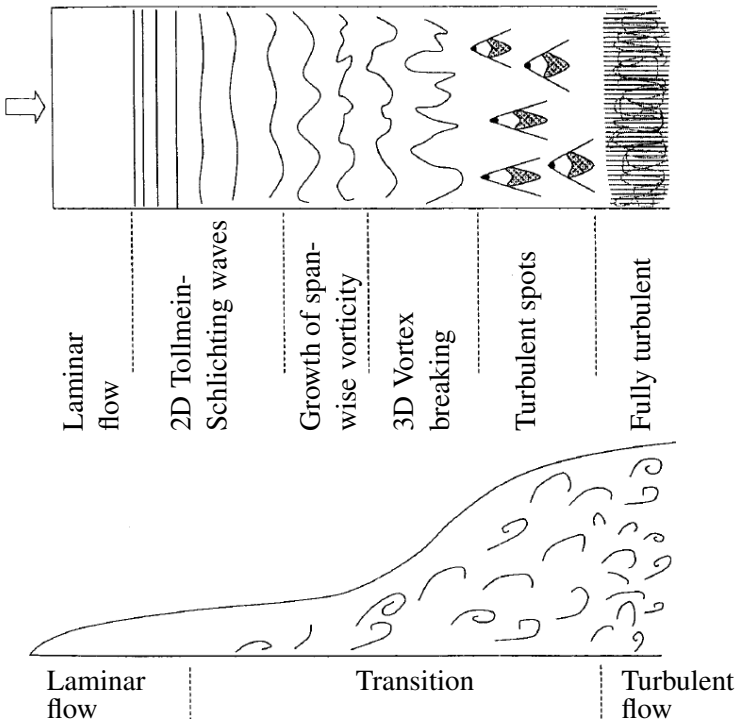

Figure 2.5: *Schematic of an idealized transition process. (Image source A.K. Hoffmann [82])*

be observed in the STBL which are due to the vortex stretching/breaking and the generation of turbulent spots. The instantaneous view of a fully turbulent boundary layer shows that is full of turbulent spots.

A TBL is generally divided into three regions where each region exhibits distinct turbulent characteristics. Figure 2.7 shows a schematic of the laminar boundary layer being transitioning into a fully turbulent boundary layer. The overall thickness over the TBL is a very important parameter in the study of viscous flows. The *boundary layer thickness* (δ_{99}) is generally defined as the value of wall-normal distance (y) at which the velocity becomes equal to 99% of the free-stream velocity. The velocity profile for the TBL is shown in the Figure 2.6 and in Figure 2.8 this velocity profile has been plotted for non-dimensional velocity (u^+) versus the non-dimensional wall-normal distance (y^+) where (y^+) is shown on logarithmic scale, where,

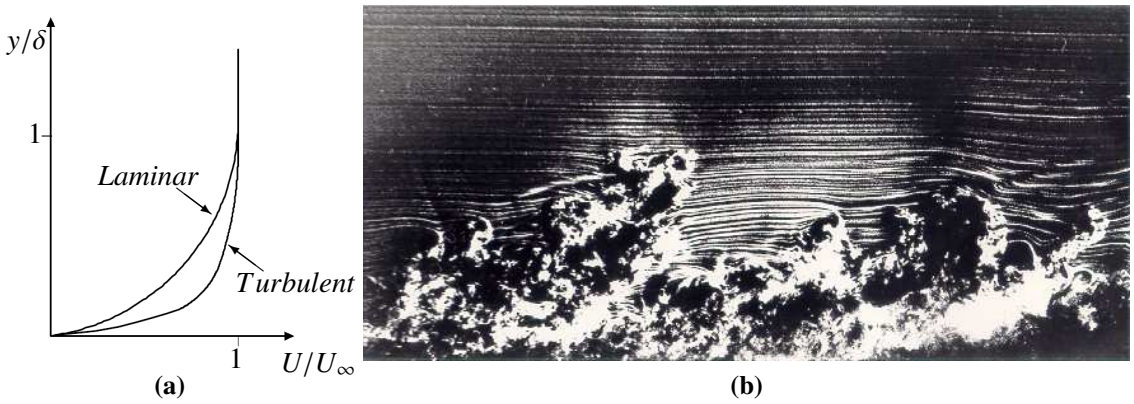

Figure 2.6: *(a) Schematic diagram showing velocity profiles for a laminar flow and a turbulent flow (After A.K. Hoffmann [82]).; (b) Instantaneous view of a supersonic turbulent boundary layer [27].*

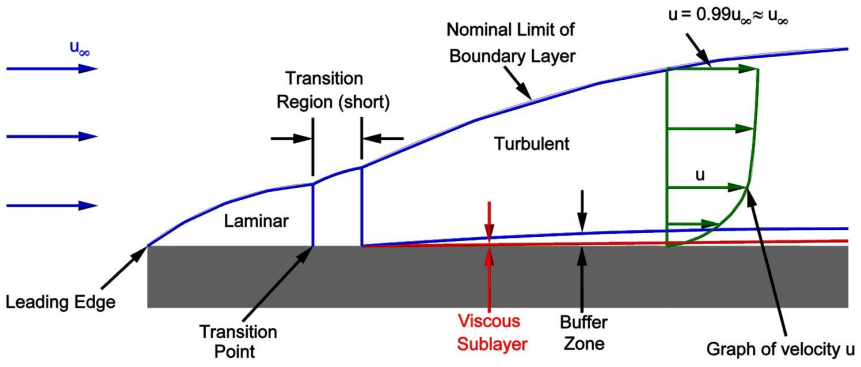

Figure 2.7: *Schematic diagram of transition from laminar to turbulence on a flat-plate showing various flow regimes near the wall [28].*

$$u^+ = \frac{u}{u_\tau} \tag{2.7}$$

and,

$$y^+ = y\frac{u_\tau}{\nu} \tag{2.8}$$

where, u_τ is called the friction velocity and,

$$u_\tau = \sqrt{\frac{\tau_w}{\rho}} \tag{2.9}$$

here, τ_w is the wall shear stress and ρ is the density.

In order to understand the TBL, Figures 2.7 and 2.8 should be considered at the same time. The boundary layer thickness (δ_{99}) is not a clear division between the two regions but in fact it is a "poorly-conditioned" [126] quantity which depends upon a very small velocity differentials, nevertheless the region on the free-stream side of the boundary is called the *outer region* while the region close to the wall is referred to as the *inner region*. In the inner region of the TBL, as shown in Figure 2.7, a very thin layer near the wall is referred to as a *viscous sublayer*. There is another zone just above the viscous sublayer commonly termed as the *buffer zone*. The TBL region above the buffer zone is called the *fully turbulent zone* or a *log layer*. Collectively all these three zones within the inner region are called *law of the wall* regions.

Theodore von Kármán, in 1930 [166], introduced the law of the wall which implicates that the average velocity profile at any point in a TBL is proportional to the non-

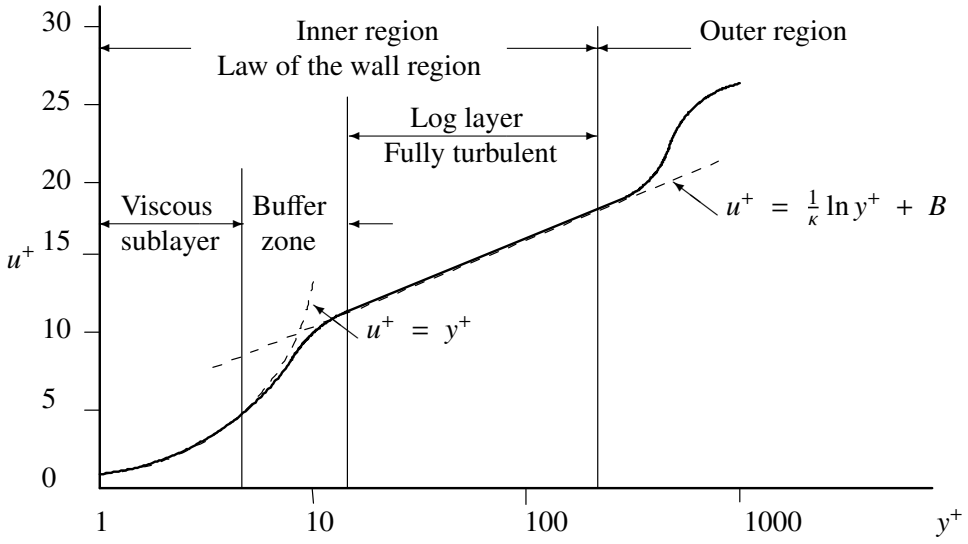

Figure 2.8: *Schematic diagram of non-dimensional velocity profile for a turbulent flow over a flat-plate identifying various regions of turbulent boundary layer. (After A.K. Hoffmann [82])*

dimensional wall-normal distance (y^+) of that point on a logarithmic scale. Pope [126] demonstrated the universality of the law of the wall in the log layer, buffer zone and the viscous layer by plotting the velocity profiles for the TBL from various experimental data but it must be noted that the law of the wall does not take into account the surface roughness which is one of the important factors affecting the velocity profiles near the wall. Therefore for a smooth wall,

$$u^+ = f(y^+) \tag{2.10}$$

which is known as the law of the wall. The non-dimensional velocity (u^+) in the log layer is calculated using the following relation,

$$u^+ = \frac{1}{\kappa} \ln y^+ + B \tag{2.11}$$

where, κ is called the von Kármán constant and B is another constant which is a function of y/δ and both of these constants are determined from experiments. Typical values used for $\kappa = 0.4$ and $B = 5.0 \sim 5.5$. Very close to the wall, in the viscous sublayer region, the viscous shear dominates therefore in this region the velocity profile is approximated to be linear,

$$u^+ = y^+ \tag{2.12}$$

The merger of the two velocity profiles (the viscous sublayer profile and the log layer profiles) must be smooth. Based upon this analysis, the various regions in the turbulent boundary layer are defined as below [82]:

$$\begin{array}{rcccll} & & y^+ & < & 2 \sim 8 & \Rightarrow \textit{viscous sublayer}, \\ 2 \sim 8 & < & y^+ & < & 50 & \Rightarrow \textit{buffer zone}, \\ & & y^+ & > & \sim 50 & \Rightarrow \textit{fully turbulent zone}, \end{array} \tag{2.13}$$

2.4.2 Turbulent Shear Layer Flows

Another type of turbulent flows is the free shear layer flows where “free” means that the area of concern in such flows is away from the wall and the turbulence in the flow is due to the mean velocity differences in the flow. This can be understood from the example of to fluids flowing at different velocities on either side of a splitter plate as explained by Hoffmann [82]. As the flows pass the edge of the plate, due to difference in the velocities, instability occurs in the flow at the interface which is known as the Kelvin-Helmholtz (KH) instability as shown in the Figure 2.9. Kelvin[90] showed that the instability in the free shear layer flows is due to inviscid characteristics of the flow which means that molecular viscosity has very little or no influence in the generation

of KH instabilities. This is the major difference between the turbulent free shear layer flows and the turbulent wall-bounded flows where instabilities are generated due to the viscous effects of the flow.

For the growth analysis of the KH instability, two parallel flows can be considered with an infinitesimal perturbation that can be decomposed into separate modes. The stability of each mode is analysed to determine its growth in amplitude. The instabilities are centred around the points at the vortex sheet where the fluid is in compression. Drazin and Reid[40], in 2004, presented a thorough analysis of the instability by two modes:

$$s = -Ik_x \frac{\rho_1 U_1 + \rho_2 U_2}{\rho_1 + \rho_2} \pm \left[\frac{k_x^2 \rho_1 \rho_2 \left(U_1 - U_2\right)^2}{\left(\rho_1 + \rho_2\right)^2} - \frac{kg\left(\rho_1^2 - \rho_2^2\right)}{\rho_1 + \rho_2} \right]^{1/2} \tag{2.14}$$

where s is the interface and is stable if $kg(\rho_1^2 - \rho_2^2) \geq k_x^2 \rho_1 \rho_2 (U_1 - U_2)^2$. On the other hand if $kg(\rho_1^2 - \rho_2^2)$ ł $k_x^2 \rho_1 \rho_2 (U_1 - U_2)^2$ then one mode is stable and other is unstable. For a simple shear case where $g = 0$,

$$s = -Ik_x \frac{\rho_1 U_1 + \rho_2 U_2}{\rho_1 + \rho_2} \pm \frac{k_x \sqrt{\rho_1 \rho_2}\left(U_1 - U_2\right)}{\left(\rho_1 + \rho_2\right)} \tag{2.15}$$

which demonstrate that in KH instability the interface s is unstable at all wavelengths and the modes grow proportional to the wavenumbers. This means that small wavelengths grow much faster than the large wavelengths. Further details of this analysis can be found in [40, 154].

Figure 2.10 shows multiple KH instabilities being generated in a free shear layer flow. With time, these instabilities grow in size start to occupy more area of the flow. Instability in the fluid in each side of the shear layer entrains the fluid on the other side and gradual development in the KH instabilities results in a very active region of mixing in the turbulent free shear layer flows. An example is the jet injected in a sub/supersonic flow where the jet fluid is the fuel and the free-stream could be air. Effective mixing of the two would start immediately as the fuel jet is injected into the free stream on the upper free shear layer of the jet [133, 89].

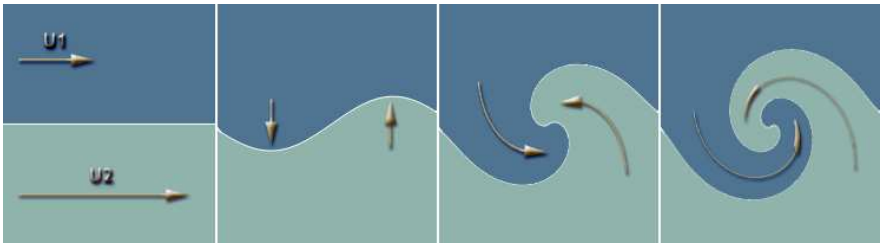

Figure 2.9: *Schematic diagram showing the mechanism of Kelvin-Helmholtz (KH) instability in a free shear layer flow [29].*

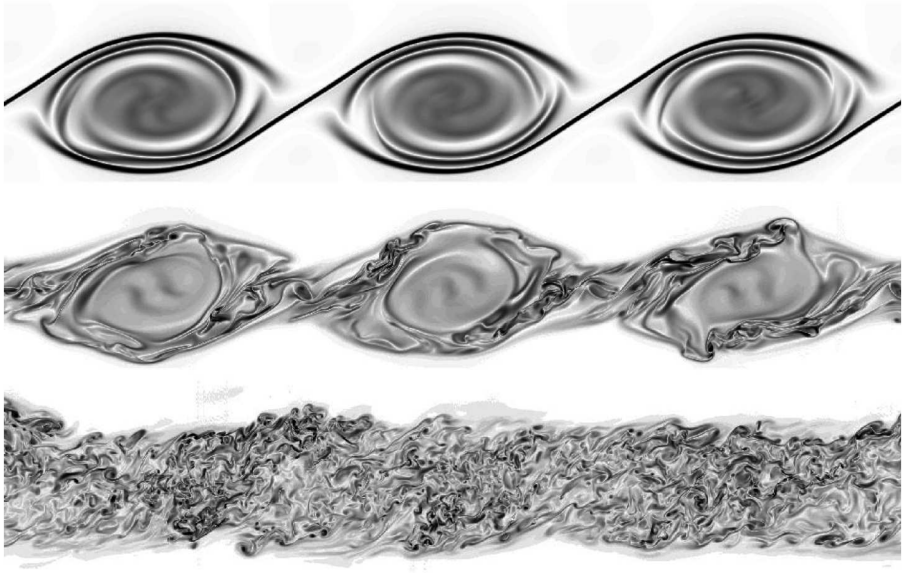

Figure 2.10: *Generation of Kelvin-Helmholtz (KH) instabilities and mixing of the two fluids in the turbulent free shear layer [30].*

CHAPTER 3

Governing Equations and Numerical Methods

*This chapter presents the three-dimensional unsteady compressible Navier-Stokes equations along with the numerical methods within the framework of Implicit Large-Eddy Simulations technique as implemented in the code **CNS3D**. For high speed flows, where temperature changes can affect the flow properties behind the discontinuities, a formulation for thermally perfect gas is presented and validated. Furthermore, a digital filter based turbulent boundary condition is presented with some modifications in implementation to generate turbulent inflow data for unsteady flows simulations.*

3.1 Conservation Laws and Governing Equations

In CFD, The *fluid* is approximated as a *continuum*, which is a branch of mechanics that deals with materials modelled as a continuous mass, as opposed to discrete. Modelling a fluid as a continuum assumes that even an infinitesimally small volume of fluid contains sufficient amount of discrete particles (atoms or molecules) such that they fill the complete volume and ignores the constituents of the volume. In this manner the fluid volume can be attributed with mean properties such as velocity, pressure, temperature and density etc.

The governing equations for the dynamics of a Newtonian[1] fluid are called the Navier-Stokes equations (NS-equations), named after Claude-Louis Navier and George Gabriel Stokes, and their derivation is based upon the fact that the fluid dynamics obey certain *conservation laws* as below:

1. Conservation of Mass,
2. Conservation of Momentum, and
3. Conservation of Energy.

[1] After Isaac Newton; the fluid in which the shear stress is proportional to the time rate of strain.

The conservation of any of the above fluid property means that it's total change inside an arbitrary control volume of fluid is the net effect of *flux* being transported across its boundaries plus the internal and external forces acting on the control volume. Flux is a term that represents the amount of a fluid property cross the boundaries of control volume and can be categorized as *convective (or advective)* and *diffusive* fluxes. The major difference between the two is that the diffusive flux is dependent upon the gradients, whereas, the convective flux is present even in the absence of the gradients.

Following the conservation laws, the *flux variables* conserved through the NS-equations are the density (ρ), momentum ($\rho\vec{U}$) and total energy (E) in all three directions *x, y, z* respectively. The fluid flow equations obtained by directly applying the conservation laws to a stationary finite control volume are in *integral* form which can be manipulated to obtain a *partial differential* form, and are called *conservation* form of the governing equations[2]. Both of these, the *integral* and the *differential*, forms are presented (in conservation form) in the following sub-sections.

3.1.1 Integral Form

The integral form of the NS-equations are obtained[5, 7, 44] by considering an arbitrarily shaped fixed control volume $\mathcal{V}$ of fluid with surface area $\vec{S}$. By applying the three conservation laws the integral form of the NS-equations for the Continuity (mass), Momentum and Energy conservation are obtained as below in Equations (3.1a), (3.1b) and (3.1c), respectively.

$$\frac{\partial}{\partial t}\iiint_{\mathcal{V}} \rho d\mathcal{V} + \oiint_{S} \rho\vec{U}\cdot d\vec{S} = 0 \tag{3.1a}$$

$$\frac{\partial}{\partial t}\iiint_{\mathcal{V}} \rho\vec{U} d\mathcal{V} + \oiint_{S} \left(\rho\vec{U}\cdot d\vec{S}\right)\vec{U} = -\oiint_{S} p d\vec{S} + \oiint_{S} \mathbf{T} d\vec{S} + \iiint_{\mathcal{V}} \rho\vec{f} d\mathcal{V} \tag{3.1b}$$

$$\frac{\partial}{\partial t}\iiint_{\mathcal{V}} \rho E d\mathcal{V} + \oiint_{S} \rho E\vec{U}\cdot d\vec{S} = -\oiint_{S} p\vec{U}\cdot d\vec{S} + \oiint_{S} \mathbf{T}\vec{U} d\vec{S} + \dot{Q} + \iiint_{\mathcal{V}} \rho\left(\vec{f}\cdot\vec{U}\right) d\mathcal{V} \tag{3.1c}$$

where, ρ , $\vec{U}$, $\mathbf{T}$, $\vec{f}$, p, $\dot{Q}$ and E represents the density, velocity vector, stress tensor, body forces, pressure, rate of heat transfer and total energy respectively. The velocity vector has three components u, v and w along the Cartesian coordinates x, y and z respectively.

[2] *non-conservation* form of the governing equations can be obtained by applying the conservation laws to a moving finite control volume of fluid.

3.1.2 Differential Form

Similarly, by applying the conservation laws to an infinitesimally small element of control volume fixed in space, the NS-equations can be directly obtained in the partial differential form for the Continuity (mass), Momentum and Energy conservation as shown in Equation (3.2) below[5, 44, 163].

$$\frac{\partial \rho}{\partial t} + \nabla \cdot \left(\rho \vec{U}\right) = 0 \tag{3.2a}$$

$$\frac{\partial \left(\rho \vec{U}\right)}{\partial t} + div\left(\rho \vec{U} \otimes \vec{U}\right) = -\nabla p + div\left(\mathbf{T}\right) + \rho \vec{f} \tag{3.2b}$$

$$\frac{\partial \rho E}{\partial t} + \nabla \cdot \left(\rho E \vec{U}\right) = -\nabla \cdot p\vec{U} + \nabla \cdot \mathbf{T}\vec{U} + \nabla \cdot \dot{Q} + \rho \vec{U} \vec{f} \tag{3.2c}$$

Various quantities in the above partial differential form of the NS-equations are defined below for a particular case of Cartesian co-ordinates, where, in Equation (3.2a):

$$\nabla \cdot \left(\rho \vec{U}\right) = \frac{\partial \left(\rho u\right)}{\partial x} + \frac{\partial \left(\rho v\right)}{\partial y} + \frac{\partial \left(\rho w\right)}{\partial z} \tag{3.3}$$

and, in Equation (3.2b):

$$\frac{\partial \left(\rho \vec{U}\right)}{\partial t} = \left[\frac{\partial \left(\rho u\right)}{\partial t}, \frac{\partial \left(\rho v\right)}{\partial t}, \frac{\partial \left(\rho w\right)}{\partial t}\right]^T \tag{3.4}$$

$$\vec{U} \otimes \vec{U} = \begin{bmatrix} u^2 & uv & uw \\ vu & v^2 & vw \\ wu & wv & w^2 \end{bmatrix} \tag{3.5}$$

$$div\left(\rho \vec{U} \otimes \vec{U}\right) = \begin{bmatrix} \nabla \cdot \left(\rho u \vec{U}\right) \\ \nabla \cdot \left(\rho v \vec{U}\right) \\ \nabla \cdot \left(\rho w \vec{U}\right) \end{bmatrix} = \begin{bmatrix} \frac{\partial \left(\rho u^2\right)}{\partial x} + \frac{\partial \left(\rho uv\right)}{\partial y} + \frac{\partial \left(\rho uw\right)}{\partial z} \\ \frac{\partial \left(\rho uv\right)}{\partial x} + \frac{\partial \left(\rho v^2\right)}{\partial y} + \frac{\partial \left(\rho vw\right)}{\partial z} \\ \frac{\partial \left(\rho uw\right)}{\partial x} + \frac{\partial \left(\rho vw\right)}{\partial y} + \frac{\partial \left(\rho w^2\right)}{\partial z} \end{bmatrix} \tag{3.6}$$

$$\nabla p = \frac{\partial p}{\partial x} + \frac{\partial p}{\partial y} + \frac{\partial p}{\partial z} \tag{3.7}$$

$$\mathbf{T} = \begin{bmatrix} \tau_{xx} & \tau_{xy} & \tau_{xz} \\ \tau_{yx} & \tau_{yy} & \tau_{yz} \\ \tau_{zx} & \tau_{zy} & \tau_{zz} \end{bmatrix} \tag{3.8}$$

$$div\,(\mathbf{T}) = \begin{bmatrix} \frac{\partial \tau_{xx}}{\partial x} + \frac{\partial \tau_{xy}}{\partial y} + \frac{\partial \tau_{xz}}{\partial z} \\ \frac{\partial \tau_{yx}}{\partial x} + \frac{\partial \tau_{yy}}{\partial y} + \frac{\partial \tau_{yz}}{\partial z} \\ \frac{\partial \tau_{zx}}{\partial x} + \frac{\partial \tau_{zy}}{\partial y} + \frac{\partial \tau_{zz}}{\partial z} \end{bmatrix} \tag{3.9}$$

and, finally in Equation (3.2c):

$$\nabla \cdot p\vec{U} = \frac{\partial (pu)}{\partial x} + \frac{\partial (pv)}{\partial y} + \frac{\partial (pw)}{\partial z} \tag{3.10}$$

$$\nabla \cdot \mathbf{T}\vec{U} = \begin{bmatrix} \frac{\partial (u\tau_{xx})}{\partial x} + \frac{\left(v\tau_{xy}\right)}{\partial x} + \frac{(w\tau_{xz})}{\partial x} \\ \frac{\partial (u\tau_{xx})}{\partial y} + \frac{\left(v\tau_{xy}\right)}{\partial y} + \frac{(w\tau_{xz})}{\partial y} \\ \frac{\partial (u\tau_{xx})}{\partial z} + \frac{\left(v\tau_{xy}\right)}{\partial z} + \frac{(w\tau_{xz})}{\partial z} \end{bmatrix} \tag{3.11}$$

$$\nabla \cdot \dot{Q} = \kappa\frac{\partial T}{\partial x} + \kappa\frac{\partial T}{\partial y} + \kappa\frac{\partial T}{\partial z} \tag{3.12}$$

$$\rho\vec{U}\vec{f} = \rho u f_x + \rho v f_y + \rho w f_z \tag{3.13}$$

$$E = \rho\left(e + \frac{\vec{U}^2}{2}\right) = \rho\left(e + \frac{u^2 + v^2 + w^2}{2}\right) \tag{3.14}$$

The integral (Equation (3.1)) and the partial differential form (Equation (3.2)) of the NS-equations are fundamentally the same and one form can be obtained from the other through manipulation. The NS-equations present a coupled system of non-linear equations and are difficult to solve analytically. Any of the above two sets of three conservation equations along with an equation of state (to be discussed later) can be used to analyze a compressible Newtonian fluid.

3.1.3 Viscous Stresses

In the above NS-equations, one of the unknowns is the stress tensor which constitutes shear and normal stresses acting on the surface of the body. The elements of the stress tensor **T** as shown in Equation (3.12) are defined as below[5, 44]:

$$\tau_{xx} = -\frac{2}{3}\mu\left(\nabla \cdot \vec{U}\right) + 2\mu\frac{\partial u}{\partial x} \quad , \tag{3.15a}$$

$$\tau_{yy} = -\frac{2}{3}\mu\left(\nabla \cdot \vec{U}\right) + 2\mu\frac{\partial v}{\partial y} \quad , \tag{3.15b}$$

$$\tau_{zz} = -\frac{2}{3}\mu\left(\nabla \cdot \vec{U}\right) + 2\mu\frac{\partial w}{\partial z} \quad , \tag{3.15c}$$

$$\tau_{xy} = \tau_{yx} = \mu\left[\frac{\partial v}{\partial x} + \frac{\partial u}{\partial y}\right] \quad , \tag{3.15d}$$

$$\tau_{xz} = \tau_{zx} = \mu\left[\frac{\partial w}{\partial x} + \frac{\partial u}{\partial z}\right] \quad , \tag{3.15e}$$

$$\tau_{yz} = \tau_{zy} = \mu\left[\frac{\partial w}{\partial y} + \frac{\partial v}{\partial z}\right] \quad . \tag{3.15f}$$

where, μ is the dynamic viscosity.

3.1.4 Equation of State: Calorically Perfect Gas Formulation

Close analysis of the sets of equations in Equations (3.1) and (3.2) reveals that there are more unknown variables than the number of equations. Such a system of equations is termed as open system of equations. In order to close this system of equations the number of unknown must at least of equal to the number of equations. In the field of aerodynamics, it is generally reasonable to assume that the air behaves as a calorically perfect gas. The equation of state used in this case to close the set of NS-equations is:

$$p = \rho RT \tag{3.16}$$

where, T and R represent the temperature and the specific gas constant. For a temperature range between STP and below $\approx$ 1000 K [6], the gas can be referred to as a Calorically Perfect Gas where the coefficients of specific heats (C_v *and* C_p) remain constant and:

$$R = C_p - C_v \tag{3.17}$$

The ratio of specific heats (γ) is defined as:

$$\gamma = \frac{C_p}{C_v} \tag{3.18}$$

which also remain a constant (for air, $\gamma = 1.4$) which can be used with the Equation (3.17), resulting in:

$$C_p = \frac{\gamma R}{\gamma - 1} \quad , \tag{3.19a}$$

$$C_v = \frac{R}{\gamma - 1} \quad . \tag{3.19b}$$

The calorically perfect gas model is the most restrictive with the assumption that:

$$h = C_p T \quad , \tag{3.20a}$$

$$e = C_v T \quad . \tag{3.20b}$$

where, h and e represent the enthalpy and internal energy of the gas respectively, but, it is adequately accurate to make predictions within the limits specified[6].

Using Equations (3.17) - (3.20), the Equation (3.16) take the form:

$$p = (\gamma - 1)\rho e \tag{3.21}$$

Thus the total energy (in Equation (3.14) can be calculated as below:

$$E = \frac{p}{(\gamma - 1)} + \rho\left(\frac{u^2 + v^2 + w^2}{2}\right) \tag{3.22}$$

For a calorically perfect gas ($\gamma = 1.4$), Equation (3.22) along with Equation (3.1) or (3.2) forms a closed system of equations where the number of unknowns is at least equal to the number of equations. In order to calculate the temperature in the flow field, Sutherland's formula is used which defines relationship between the temperature variations and dynamic viscosity (μ), such that:

$$\frac{\mu}{\mu_0} = \left(\frac{T}{T_0}\right)^{3/2} \times \frac{T_0 + S_c}{T + S_c} \tag{3.23}$$

where, μ_0 is the reference viscosity at the reference temperature T_0, and S_c is the Sutherland's constant for the gas.

3.1.5 Non-Dimensional Form

The governing equations contain the variables in dimensional form which can cause problems such as numerically ill-conditioned flow. In order to reduce such risks and to obtain a well-behaved solution it is common in CFD to non-dimensionalise the governing equations. The non-dimensional form of the physical and geometrical quantities is obtained by relating them to some characteristic values.

$$
\begin{aligned}
x^* &= \frac{x}{l_c} \ , & y^* &= \frac{y}{l_c} \ , & z^* &= \frac{z}{l_c} \ , & t^* &= \frac{t}{l_c/U_c} \ , \\
u^* &= \frac{u}{U_c} \ , & v^* &= \frac{v}{U_c} \ , & w^* &= \frac{w}{U_c} \ , & \rho^* &= \frac{\rho}{\rho_\infty} \ , \\
p^* &= \frac{p}{\rho_c U_c^2} \ , & E^* &= \frac{E}{\rho_c U_c^2} \ , & \mu^* &= \frac{\mu}{\mu_c} \ , & T^* &= \frac{T}{T_c} \ ,
\end{aligned}
\tag{3.24}
$$

where,

$$U_c \ = \ M_\infty \times \sqrt{\frac{\gamma p_\infty}{\rho_\infty}} \tag{3.25a}$$

$$T_c \ = \ \frac{U_c}{C_v} \tag{3.25b}$$

In the study of fluid dynamics, Reynolds number (Re) plays very important role for Newtonian fluids. Reynolds Number is a non-dimensional parameter that defines the ratio of inertial forces to the viscous forces in the flow field and quantifies the importance of these forces in a flow field. It is also used to characterize the flow field in terms of *laminar* or *turbulent* flow. The turbulent flow, which is dominated by inertial forces (as explained in Chapter 2), is associated with the high Reynolds numbers. Reynolds number is a non-dimensional parameter such that:

$$Re \ = \ \frac{\text{Inertial Forces}}{\text{Viscous Forces}} \ = \ \frac{\rho_\infty U_c l_c}{\mu_c} \tag{3.26}$$

Prandtl number (Pr) is also a non-dimensional parameter which gives the ratio of kinematic viscosity (μ) to the thermal conductivity (κ) and is named after Ludwig Prandtl who first used this concept as below:

$$Pr \ = \ \frac{\text{Viscous Diffusion}}{\text{Thermal Conduction}} \ = \ \frac{\mu C_p}{\kappa} \tag{3.27}$$

A low Prandtl number indicates strong conductive forces and high Prandtl number is indicative of strong convective transfer. Related to Prandtl number is another non-dimensional number Turbulent Prandtl Number (Pr_t) which gives the ratio between the momentum eddy diffusivity and the heat transfer eddy diffusivity. The Pr_t can range from 0.7 to 0.9 and in the CNS3D code a value of 0.9 in used.

Substituting the non-dimensional quantities in the Equations (3.1) and (3.2) would result in a non-dimensional (*integral or differential*) form of the governing NS-equations. The CNS3D employs the non-dimensional form of the governing NS-equations and for simplicity the superscript $(.)^*$ will not be used in the text from here on.

3.1.6 Vector Form

In CFD, the non-dimensionalised governing equations (*integral or differential*) can be written in *vector* form for ease of presentation. The vector form for three-dimensional NS-equations is given below[44]:

$$\frac{\partial \mathbf{U}}{\partial t} + \frac{\partial \mathbf{F}}{\partial x} + \frac{\partial \mathbf{G}}{\partial y} + \frac{\partial \mathbf{H}}{\partial z} = \frac{\partial \mathbf{L}}{\partial x} + \frac{\partial \mathbf{M}}{\partial y} + \frac{\partial \mathbf{N}}{\partial z} \tag{3.28}$$

where,

$$\mathbf{U} = \begin{pmatrix} \rho \\ \rho u \\ \rho v \\ \rho w \\ E \end{pmatrix} \tag{3.29}$$

$$\mathbf{F} = \begin{pmatrix} \rho u \\ \rho u^2 + p \\ \rho uv \\ \rho uw \\ u\,(E + p) \end{pmatrix} \quad , \quad \mathbf{G} = \begin{pmatrix} \rho v \\ \rho uv \\ \rho v^2 + p \\ \rho wv \\ v\,(E + p) \end{pmatrix} \quad , \quad \mathbf{H} = \begin{pmatrix} \rho w \\ \rho uw \\ \rho vw \\ \rho w^2 + p \\ w\,(E + p) \end{pmatrix} \tag{3.30}$$

$$\mathbf{L} = \begin{pmatrix} 0 \\ \tau_{xx} \\ \tau_{xy} \\ \tau_{xz} \\ u\left(\tau_{xx} + \tau_{xy} + \tau_{xz}\right) - \kappa \dfrac{\partial \mathrm{T}}{\partial x} \end{pmatrix} \quad , \quad \mathbf{M} = \begin{pmatrix} 0 \\ \tau_{yx} \\ \tau_{yy} \\ \tau_{yz} \\ v\left(\tau_{yx} + \tau_{yy} + \tau_{yz}\right) - \kappa \dfrac{\partial \mathrm{T}}{\partial y} \end{pmatrix},$$

$$\mathbf{N} = \begin{pmatrix} 0 \\ \tau_{zx} \\ \tau_{zy} \\ \tau_{zz} \\ w\left(\tau_{zx} + \tau_{zy} + \tau_{zz}\right) - \kappa \dfrac{\partial \mathrm{T}}{\partial z} \end{pmatrix} \tag{3.31}$$

where, κ is the thermal diffusivity. The Equation (3.29) is called *Solution Vector*, Equations (3.30) are called *Flux vectors* in $x-$, $y-$ and $z-$ axes respectively. Neglecting dissipative and transport phenomenon of viscosity, mass diffusion, thermal conductivity and the source terms, the NS-equation can be called the Euler equation after Leonhard Euler.

3.1.7 Grid Transformation

The NS-equations discussed earlier are presented in Cartesian co-ordinate system, but most of the engineering problems that are solved using CFD do not lie in such co-ordinate. In fact the type of grid generated is the *body-fitted* grid i.e., the grid co-ordinates follow the curvilinear co-ordinates that can better represent the actual body under investigation. It is therefore necessary to transform the vector form of the governing equations from Cartesian co-ordinate system (x, y, z, t) into Curvilinear co-ordinate system[44] (ξ, η, ζ, t) such that:

$$\xi = \xi(x, y, z, t) \quad , \qquad \eta = \eta(x, y, z, t) \quad , \qquad \zeta = \zeta(x, y, z, t) \tag{3.32}$$

In Curvilinear co-ordinate system the vector form of the NS-equations (Equation (3.27)) can be written as follows.

$$\frac{\partial \overline{\mathbf{U}}}{\partial t} + \frac{\partial \overline{\mathbf{F}}}{\partial \xi} + \frac{\partial \overline{\mathbf{G}}}{\partial \eta} + \frac{\partial \overline{\mathbf{H}}}{\partial \zeta} = \frac{\partial \overline{\mathbf{L}}}{\partial \xi} + \frac{\partial \overline{\mathbf{M}}}{\partial \eta} + \frac{\partial \overline{\mathbf{N}}}{\partial \zeta} \tag{3.33}$$

where,

$$\begin{aligned}
\overline{\mathbf{U}} &= J\mathbf{U} \\
\overline{\mathbf{F}} &= J\left(\mathbf{F}\xi_x + \mathbf{G}\xi_y + \mathbf{H}\xi_z\right) \\
\overline{\mathbf{G}} &= J\left(\mathbf{F}\eta_x + \mathbf{G}\eta_y + \mathbf{H}\eta_z\right) \\
\overline{\mathbf{H}} &= J\left(\mathbf{F}\zeta_x + \mathbf{G}\zeta_y + \mathbf{H}\zeta_z\right) \\
\overline{\mathbf{L}} &= J\left(\mathbf{L}\xi_x + \mathbf{M}\xi_y + \mathbf{N}\xi_z\right) \\
\overline{\mathbf{M}} &= J\left(\mathbf{L}\eta_x + \mathbf{M}\eta_y + \mathbf{N}\eta_z\right) \\
\overline{\mathbf{N}} &= J\left(\mathbf{L}\zeta_x + \mathbf{M}\zeta_y + \mathbf{N}\zeta_z\right)
\end{aligned} \tag{3.34}$$

where, J is the Jacobian of the co-ordinates transformation and is equal to:

$$J = x_\xi\left(y_\eta z_\zeta - y_\zeta z_\eta\right) + x_\eta\left(y_\zeta z_\xi - y_\xi z_\zeta\right) x_\zeta\left(y_\xi z_\eta - y_\eta z_\xi\right) \tag{3.35}$$

and,

$$\begin{aligned}
\xi_x &= \frac{y_\eta z_\zeta - y_\zeta z_\eta}{J}, \quad \xi_y = \frac{-x_\eta z_\zeta + x_\zeta z_\eta}{J}, \quad \xi_z = \frac{x_\eta y_\zeta - x_\zeta y_\eta}{J} \\
\eta_x &= \frac{-y_\xi z_\zeta + y_\zeta z_\xi}{J}, \quad \eta_y = \frac{x_\xi z_\zeta - x_\zeta z_\xi}{J}, \quad \eta_z = \frac{-x_\xi y_\zeta + x_\zeta y_\eta}{J} \\
\zeta_x &= \frac{y_\xi z_\eta - y_\eta z_\xi}{J}, \quad \zeta_y = \frac{-x_\xi z_\eta + x_\eta z_\xi}{J}, \quad \zeta_z = \frac{x_\xi y_\eta - x_\eta y_\xi}{J}
\end{aligned} \tag{3.36}$$

This system of equations represents body-fitted NS-equation in three-dimensions and can be applied to uniform and rectangular computational grids. Details of this transformation can be found in [44] and for simplicity the $\overline{(.)}$ is omitted from the Equation (3.33). The NS-equations for Newtonian fluid flow can be solved using three major approaches which are discussed in the next section.

3.2 Turbulence Modelling Approaches

CFD has played a major role in understanding various experimental and industrial flows at various speeds and Reynolds numbers. Unlike laminar flow simulations, the simulations of the turbulent flows present major challenges from the numerical and computational point-of-views. There are three main techniques used in the field of CFD for turbulent flow simulations; Direct Numerical Simulations (DNS), Reynolds Averaged Navier-Stokes Simulations (RANS) and Large-Eddy Simulations (LES). All three techniques solve the fundamental governing equations of fluid motion (discussed in Section 3.1) but in a different manner to predict the dynamics of fluids. Based upon the way the NS-equations are solved, each method has its benefits and drawbacks which will be briefly discussed in this section. An introduction for Implicit LES or ILES technique which will also be presented with respect to the turbulence modelling as this is the technique utilized in this thesis.

3.2.1 Direct Numerical Simulations (DNS)

In DNS, the governing equations of fluid flow are numerically solved for comprehensive time-accurate simulations of turbulent flows. The size of the flow field and the grid resolution are the major factors to be considered in a numerical simulation. The turbulent flows comprise of several scales, from large enough that are visible with naked eye to the smallest Kolmogorov scales. In DNS every scale is resolved therefore the spatial resolution has to be fine enough to resolve Kolmogorov scale eddies and at the same time has to be several times large enough to accommodate the eddies of largest scale present in the flow. Based upon this, an estimate has been established for the grid resolution required for DNS simulation based upon the ratio of the largest to the smallest (Kolmogorov's scale) as in Equation (2.4) where this ratio is proportional to $Re^{3/4}$.

For a three-dimensional DNS simulation, resolving all the scales of turbulence present in the flow, the number of grid points in the computational domain required are at least $Re^{9/4}$. This presents a major problem in using the DNS for a wide variety of engineering flows; as for a three-dimensional turbulent flow simulation of a comparatively small Reynolds number of 6000 the minimum grid points required would be of the order of 10^9 million cells. As most of the turbulent flow simulations would be of Reynolds number of the order of 10^6 the grid points estimate would be even larger. At

the same time one has to consider the timestep involved in DNS which needs to accommodate the life-span of the smallest eddy so that it must be resolved; which again, brings attention to the Equation (2.4) for the ratio of largest timescale to the smallest Kolmogorov timescale. Considering both requirements at the same time the total computational time for DNS of a fully turbulent flow with a conservative Reynolds number of around 10^6 could be in months or years based upon the current available computational powers even with the use of parallel computing.

Other challenges for DNS could be the development of solution algorithms which are completely free from numerical errors and precise initial and boundary conditions. Nevertheless, the accuracy of currently available DNS data can be compared well with the experiments and, therefore, widely used for validation and verification purposes of research CFD codes. Currently, the applications for DNS are in relatively low Reynolds number flows consisting of very simple geometries rather than complex geometries and higher Reynolds number flows. With technological growth in the computational power available the dream of usage of DNS in engineering applications can be realized but it could take another $50 \sim 100$ years unless there is a major breakthrough in computational technology.

3.2.2 Reynolds Averaged Navier-Stokes Simulations (RANS)

Probably the most common approach in solving the engineering/industrial flows is RANS where the governing equation of fluid dynamics are solved numerically using the variable decomposition into the mean and the fluctuating components. Two decomposition approaches are in wide use, Reynolds averaging and Favre averaging, and the solution is found for the averaged flow variables and hence the name "Averaged" comes in the title. The resolved flow field is free of any fluctuations and the turbulence in the flow field is modelled instead of resolved as in the case of DNS. This is important as the averaging process introduces additional unknowns in the governing equations which present problem in resolving them for flow variables (For details see [80, 81, 82].

Several turbulence models are in use today which are used to mimic the unsteady effects of a turbulent flow in numerical simulations. The main advantage of this approach is that when compared to DNS a very coarse grid can be used in RANS to obtain an averaged solution and thus it is very light on computational resources and time. Therefore, this approach is widely used in the industry for quick solutions to engineering problems. But at the same time, the solution from RANS does not predict instantaneous turbulent features for specialized problems such as flow mixing and combustion where an instantaneous flow field analysis would be required in order to understand the flow field development and the effects of turbulence.

3.2.3 Large Eddy Simulations (LES)

DNS and RANS can be viewed as two extremes where for DNS all the scales are resolved and in RANS where all the scales of turbulence must be modelled[82]. LES can be regarded as "best of both world" where the large scales are resolved but the small scales of turbulence are filtered out of the governing equations and are modelled. The principal operation in large eddy simulation is low-pass filtering. This operation is applied to the Navier-Stokes equations to eliminate small scales of the solution. This reduces the computational cost of the simulation. There are differences between the incompressible and compressible LES governing equations, which lead to the definition of a new filtering operation (for details on filters and filtering process, see Pope[126]). The filtered governing equations of fluid flow are used to solve for the macro scale dynamics of the fluid flow which is mainly responsible for the energy transport and momentum. The small scales are modelled using the turbulence models called the *subgrid scale* (SGS) models which commute with the large scale eddies.

In the classical LES, these sub-grid scale terms are modelled explicitly by adding extra terms to close the system of equations. Various SGS models are available and most common of them could the *Smagorinsky* and *Dynamic* models. The Smagorinsky model, oldest model, is still in use because of its simplicity although several modifications have been introduced to improve the capabilities, and the Dynamic model is one of the improvements. The Dynamic model overcomes some of the physical difficulties (such as backscatter) observed in some flows and the asymptotic behaviour of SGS stresses near the walls. These SGS models are considered to be applicable to a wide variety of flows based upon the assumption that the small scale eddies are universal and homogeneous. This gives an edge to LES compared to RANS where the turbulence models exhibit limited applicability based upon the fact that they model a wide variety of scales. LES provides a higher level of accuracy in the solution but this comes at a price imposed upon the computational costs involved.

Finite-volume method (explained later) imply cell-averaging and reconstruction steps which, with respect to classical LES, can be interpreted as filtering process like tophat filter which allows for a primitive-function reconstruction. The resulting reconstructions on the left and right hand side of a cell are denoted by $\phi^L_{1-1/2}$ and $\phi^R_{1+1/2}$ respectively. LES can provide a time-accurate three-dimensional solution which makes this approach closer to the DNS. In DNS the grid resolution is set to resolve the smallest eddy but as understood from turbulent flows most of the energy is contained in the larger scales. As LES resolves the large scales and models the smaller scales it allows LES grid spacing to be kept much higher than the Kolmogorov scales and thus allowing LES to simulate much higher Reynolds number flows. This benefit, in turn, offers significant savings on the computational resources and time. LES has been applied to many complex flows with high levels of accuracy which is another benefit over the DNS approach.

Several errors associated with the approximation, numerical discretisation, truncation and commutation present major challenges in LES as well. Apart from several major

advantages, LES poses some difficulties of excessive dissipation in transitioning flows [126] thus presenting difficulties for simulating compressible flows with discontinuities. For this reason most of the SGS models employ additional numerical dissipation in the regions of high gradients. This, although, resulted in better solution in the discontinuous regions but highlighted that the results are independent of the models employed [55]. Geurts [60] demonstrated that the coefficients used in the SGS models are problem dependent as well as grid dependent. Because of these uncertainties in the numerical schemes LES have also been performed without explicit SGS models and the approach is termed as Implicit LES (or ILES) technique.

3.2.4 Implicit Large Eddy Simulations (ILES)

The classical LES, with explicit SGS model, has been successfully employed to study various flows but it is known to provide excessive dissipation of kinetic energy where the fully turbulent flow needs to be resolved. In ILES the scales of turbulence are determined exactly as in the classical LES approach but the assumption that the numerical discretisation filters the large and small scales based upon the computational grid makes the use of explicit SGS models obsolete in case of ILES. The small scale turbulent features which are not resolved still need to be accounted for. The basic idea behind the ILES is that the truncation error in numerical discretisation is similar in form to the SGS model in LES. It is argued that the SGS model can be implicitly added to the numerical scheme using the limiters in an upwind scheme or it can be assumed that the numerical method contains some self-adjusting mechanism to obtain the correct kinetic energy dissipation [63]. Considering above assumptions, Finite Volume method is highly attractive scheme for ILES formulation which contains very well known methods such as the piecewise parabolic method (PPM), the flux-corrected Transport (FCT) and the total variation diminishing (TVD) methods [63]. The Finite Volume method offers non-oscillatory solution and higher order of the accuracy (up to the level of numerical scheme) can be achieved using the reconstruction techniques.

Implicit LES (ILES) being relatively a simpler methodology offers several advantages for simulating turbulent flows that include ease of implementation and computational efficiency. In 1969, Hirt [79] proposed that SGS models are of the same order of magnitude as the truncation error of second order accurate methods. Similar findings were quoted by Lesieur and Metais [107] and Youngs [170] who used unfiltered governing equation of fluid flow to study the decaying homogeneous turbulence and mixing flows. The order of truncation error was correlated to the SGS model based upon the observation that an upwind numerical scheme can be rewritten as a central scheme plus a dissipative term [42, 44, 63]. Boris *et al.*[15] in 1992 explored the concept that monotone schemes feature an implicit sub-grid scale (Implicit SGS) model and presented examples of free shear layer flows. These types of implicit SGS models are classified as structural models as these are not adopted to any particular type of subgrid flow[104]. Grinstein and DeVorce[64, 65], in 1996, presented an ILES study of jet transition from laminar initial conditions into fully turbulent flow. This was the begin-

ning of the recognition of ILES methodology to study turbulence and since then several works has been presented that involve investigations into turbulence phenomenon using ILES, especially in the high Reynolds number regimes involving compressible flows[53, 54, 112, 113, 72, 65, 66, 41, 96, 97].

3.3 Finite Volume Method

The code employed in this thesis, employs the method of lines which allows for separate discretisation of spatial and temporal advancements. This method allows for flexibility in terms of attaining different levels of spatial and temporal accuracies. A structured body-fitted grid represents the physical space in the Curvilinear co-ordinates and consists of quadrilateral grid cells in two-dimensions and hexahedral grid cells in three-dimensions. Each grid cell can be considered as a control volume, where the conservative form of the NS-equations is integrated over the control volume to evaluate the fluxes at cell interface thus rendering it a cell-cantered scheme. This method, generally, is termed as the Finite Volume method of discretisation.

Several discretisation methods are available within the Finite Volume approach such as the Total Variation Diminishing (TVD) scheme. Harten[75], in 1983, first presented the idea of preventing the generation of new extrema in the solution and applied the condition that the total variation of the solution decrease in time. Therefore, TVD based Finite Volume discretisation methods allow strong shock waves to be resolved accurately and without any spurious oscillations and are considered ideal for compressible flows with discontinuous solutions as they satisfy the Rankine-Hugoniot jump condition.

In TVD schemes, the conservative fluxes are implemented along with an additional flux-limited dissipation term that complies with the TVD condition mentioned above. One way to achieve this is by *upwinding* the discretisation where the solution is biased towards the direction of the characteristic speed; such a scheme is termed as *upwind* TVD scheme. As naturally, the information travels in waves along the lines called characteristics in several directions where along the characteristics the solution remains constant. Thus in order to obtain more physically correct solution the knowledge of the structure of the solution is used in such schemes. Upwind schemes are generally used for spatial discretisation of the convective fluxes in Euler equations. For a detailed information on the Finite Volume method see Blazek [14].

3.3.1 Shock Tube and The Riemann Problem

In order to preserve the basic physical and mathematical characteristics of the governing equations, high-resolution methods incorporate the exact or approximate solution to a local Riemann problem. Analytical solutions for a Riemann problem are available for several systems of equations and are often used as a reference for assessing

the performance of numerical methods, e.g. the Euler Equations, scalar conservation laws or any linear system of equations. If the governing equations are more complex or if the computational cost of the Riemann solver is a concern, however, physical or mathematical approximations are inevitable. In practice, almost all Riemann solvers are of the approximate type and produce nearly identical results compared to the exact solution at a fraction of the cost[103, 155].

In order to understand the physics of a Riemann problem, a special case of Riemann problem is discuss called the one dimensional shock-tube. The shock-tube is a one-dimensional closed tube which is divided into two regions with a pressure difference between and separated by a diaphragm. Initially, the fluid is at rest when the diaphragm is instantly removed and the pressure gradient causes a shock wave that travels towards the right, a rarefaction wave (expansion fan) that travels towards left and a contact surface that separates the two fluid regions. Theoretically, one or even two of these waves can be non-existent but the structure remains the same as shown in the Figure 3.1.

Generally, the shock-tube is also called a Riemann problem and the solution can consist of four states (shown as numbers from 1 to 4 in Figure 3.1), which are separated by the three waves. The states 1 and 4 are the initial conditions before the removal of the diaphragm, whereas, the states 2 and 3 are the states for which the solution is required. On the left, the rarefaction wave is composed of diverging characteristics and travelling at a speed given by the difference of local speed $u(x,t)$ and the local speed of sound $a(x,t)$ reduces the density within its boundaries ($Head$) and ($Tail$). Inside the fan the data follows a smooth transition which can be found using isentropic conditions.

On the right, the shock wave is a non-linear wave that increases the pressure, density, temperature and entropy as it passes the fluid from state 3 to 4. It is a jump discontinuity and exhibit converging characteristics travelling at a speed defined as $u(x,t) + a(x,t)$, where state 3 can be determined using the Rankine-Hugoniot relations from state 4. The region in-between the state 1 and state 4 is called the *star (*)* region where the states 2 and 3 are connected through the contact wave travelling at speed u^*. The characteristics in this region run parallel to each other and therefore both the velocity and pressure in these regions are constant, described as u^* and p^*. The other properties can be determined at the contact discontinuity which acts as a jump discontinuity like in shock wave and Riemann invariants are also constant as in the case of rarefaction wave.

In modern high-resolution methods an exact or approximate solution to the local Riemann problem is incorporated on the left and right side of a cell interface. Laney, in 1998, presented an analytical solution to the Riemann problem and ideal gases, details of which can be found in [103]. For complex equations where the exact solution to the Riemann problem can be computationally expensive, approximate Riemann solvers are employed. It should be noted that the approximate Riemann solvers gain near exact results at a fraction of the computational cost [103, 155]. In numerical solutions, majority of the computational time is spent on solving the Riemann problem therefore this part of the CFD code presents huge potential for improving the cost of simulation.

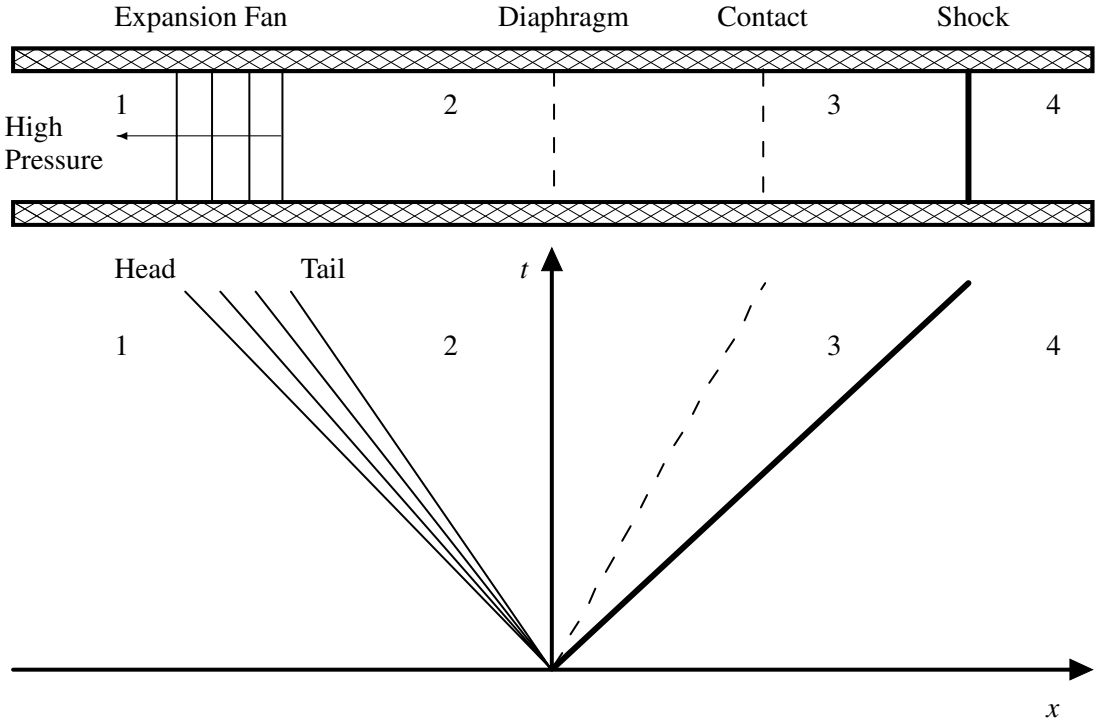

Figure 3.1: *One dimensional (1D) shock-tube problem and the wave diagram showing characteristics in the x-t plane [103].*

Moreover, the mathematical or physical approximations leading to explicit solutions rarely present any significant change to the results as compared to the exact solution. Therefore, the approximate Riemann solvers have almost completely replaced the exact Riemann solvers in practice.

A schematic diagram of wave patterns generally considered in the numerical solution of the Riemann problem are shown in the Figure 3.2. The left and the right waves can either be a rarefaction wave or a shock wave, whereas, the middle wave is always a contact discontinuity. Therefore, the unknown state in the star (*) region can always be determined according to the type of the left and right non-linear wave. In order to encompass all possible scenarios, however, special cases such as supersonic flow or sonic rarefaction waves are often treated separately. For supersonic flow, all waves are propagating downstream with the flow and no information can travel upstream and the solution simply assumes the initial left or right state depending on the flow direction. Otherwise, the state at x = 0 is given by the continuous solution through the expansion fan in case of a sonic rarefaction wave.

The approximate Riemann solver employed in this thesis is the Harten-van Leer-Lax-Contact (HLLC) Riemann solver [155] (an extension of HLL Riemann solver) which takes into account the existence of the contact surface. The pressure (p) and speed of wave (a) depend upon the ratio of the specific heats (γ). For a constant value of γ, the

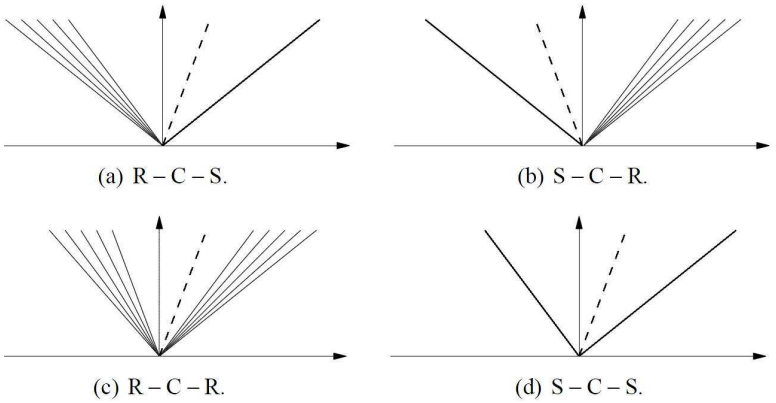

Figure 3.2: *Possibilities of wave patterns in a numerical solution of the Riemann problem where R, C and S represent a rarefaction, contact and shock discontinuity respectively[155].*

left and right states of the pressure (p_L and p_R) and the speed of sound (a_L and a_R) can be calculated, on either side of the cell interface, using Equation (3.21), and Equation (3.37) below:

$$a = \gamma(\gamma - 1)\left(\frac{E - \frac{u^2+v^2+w^2}{2}}{\rho}\right) \tag{3.37}$$

Using these relations, the *left* and *right* wave speeds a_L and a_R can be obtained and the speed of the contact wave a_* can be obtained. Then the HLLC numerical flux is obtained as explained by Toro [155].

3.3.2 Godunov's Method

Monotonicity is a property of a function which means that the solution exhibits a systematic increase when it is increasing and vice versa when it is decreasing. As a result of this property in a numerical method it does not allow spurious oscillations in the solution if the initial conditions are also monotone (which is almost always the case). In Modern high-resolution methods, apparently contradictory concepts are targeted i.e., achieving high accuracy and preservation of monotonicity, which are actually properties of an exact solution.

Godunov [61], in 1959, stated that *"there are no monotone, linear schemes of second or higher order of accuracy"*. The answer to the problem can be found in the statement itself i.e., a *non-linear* scheme can provide higher accuracy by using higher order methods along with non-spurious monotone solutions in the vicinity of higher gradients. Modern high-resolution methods [44, 75, 155] employ non-linear techniques where the differencing stencil is based upon the solution of the local Riemann problem

and thus avoid unphysical oscillations. The methods adaptively select operator which ensures a *well-behaved* solution resulting in physically substantive results even in the areas of high gradients. Harten [75] defined high-resolution methods the ones that satisfy the following:

1. Provide at least second order of accuracy in smooth areas of the flow.
2. Produce numerical solutions (relatively) free from spurious oscillations.
3. In the case of discontinuities, the number of grid points in the transition zone containing the shock wave is smaller in comparison with that of first-order monotone methods.

The high-resolution method employed in the code **CNS3D** are based upon Godunov's method [61] who first employed local Riemann problem in the discretised NS-equations. The first order classical Godunov's method in one-dimension can be written in the vector form of the governing NS-equations:

$$\mathbf{U}_i^{n+1} \;=\; \mathbf{U}_i^n \;+\; \frac{\Delta t}{\Delta x}\left(\mathbf{F}_{i-\frac{1}{2}} - \mathbf{F}_{i+\frac{1}{2}}\right) \tag{3.38}$$

where, $\mathbf{F}_{i-\frac{1}{2}}$ and $\mathbf{F}_{i+\frac{1}{2}}$ are the inter-cell numerical fluxes which are computed using the (approximate) Riemann solver using ($\mathbf{U}_{i-1}^n$,$\mathbf{U}_i^n$) and ($\mathbf{U}_i^n$,$\mathbf{U}_{i+1}^n$) respectively, and n is the timestep. The approach was further developed and van Leer [159] developed Godunov type higher order methods. The solution proceeds as below:

1. In the first step, piece-wise constant discretisation is applied to the cell volumes using the finite volume method that represents the volumetric averages of a continuous problem.
2. A *reconstruction* step is introduced which interpolates the discretely sampled data thus introduces higher order of accuracy to the overall method. A non-linear stability constraint is employed to avoid spurious oscillations in this step.
3. The values thus obtained at the left and right hand sides of the cell faces act as *left* and *right* states of a discontinuity as in the fundamental Riemann problem. This can now be solved using an exact or approximate Riemann solver.
4. In the final step the solution is obtained over the entire computational cell as per the concept of finite volume method.

3.3.3 Godunov Type 5^{th} Order Accurate MUSCL Scheme

The code, **CNS3D** [42, 46, 45, 172], includes different Riemann solvers [42, 10], including flux vector splitting methods, a characteristics-based scheme and the HLLC

Riemann solver[155] within the framework of high-resolution methods [44]. In the present study, the HLLC Riemann solver is used, which assumes a three-wave structure to the Riemann problem, allowing for two intermediate states enclosed by the two fastest waves. The HLLC Riemann solver does not use linearization of the equations and works well for low-density problems and sonic points without any fixes. It has successfully been used to simulate a variety of flows in conjunction with the CNS3D code[129, 149, 151, 150, 152, 128, 127]. Higher order accuracy is obtained by employing a fifth-order accurate MUSCL Scheme[159].

For the family of MUSCL schemes, the *left* (U^L) and *right* (U^R) states of the conservative (or primitive) variables at the cell interface ($i + 1/2$) are computed as[155]:

$$\begin{aligned}
\mathbf{U}^L_{i+\frac{1}{2}} &= \mathbf{U}_i + \frac{1}{4}\left[(1-k)\,\phi\left(r^L\right)(\mathbf{U}_i - \mathbf{U}_{i-1}) \;+\; (1+k)\,\phi\left(\frac{1}{r^L}\right)(\mathbf{U}_{i+1} - \mathbf{U}_i)\right] \\
\mathbf{U}^R_{i+\frac{1}{2}} &= \mathbf{U}_{i+1} + \frac{1}{4}\left[(1-k)\,\phi\left(r^R\right)(\mathbf{U}_{i+2} - \mathbf{U}_{i+1}) \;+\; (1+k)\,\phi\left(\frac{1}{r^R}\right)(\mathbf{U}_{i+1} - \mathbf{U}_i)\right]
\end{aligned} \tag{3.39}$$

where, integer i represent the cell numbers, r is the ratio of the slopes, k is a free parameter within the interval [-1,1], ϕ is the limiter function which is based upon the slopes of the conserved variables and superscripts L and R represent the *left* and *right* states on a face of a computational cell. Kim and Kim [93], in 2005, presented a 5^{th} order MUSCL scheme using a six point stencil and defined the ratio of the slopes as:

$$\begin{aligned}
r^L_i &= \frac{\mathbf{U}_{i+1} - \mathbf{U}_i}{\mathbf{U}_i - \mathbf{U}_{i-1}} \\
r^R_i &= \frac{\mathbf{U}_{i+1} - \mathbf{U}_i}{\mathbf{U}_{i+2} - \mathbf{U}_{i+1}}
\end{aligned} \tag{3.40}$$

and, the fifth order limiter employing one-dimensional implementation of Kim and Kim[93] is as follows:

$$\begin{aligned}
\phi*^{lim}_{M5,L} &= \frac{-2/r^L_{i-1} + 11 + 24r^L_i - 3r^L_i r^L_{i+1}}{30} \\
\phi*^{lim}_{M5,R} &= \frac{-2/r^R_{i-1} + 11 + 24r^R_i - 3r^R_i r^R_{i+1}}{30}
\end{aligned} \tag{3.41}$$

The Monotonicity in the above is maintained as below:

$$\phi^{lim}_{M5,L} = max\left(0, min\left(2, 2r^L_i, \phi*^{lim}_{M5,L}\right)\right)$$
$$\phi^{lim}_{M5,R} = max\left(0, min\left(2, 2r^R_i, \phi*^{lim}_{M5,R}\right)\right) \tag{3.42}$$

This method gives the solution for the inviscid fluxes **F, G** and **H**. The viscous fluxes **L, M** and **N** as shown in Equation (3.31) the solution is simply calculated using a *central differencing* scheme. It should be noted that although this scheme is 5^{th} order accurate but this is effectively in one dimension (1D) only. In two or three dimensions (2D or 3D) due to the cross terms the order of accuracy becomes 2^{nd} order. Furthermore, as the viscous terms are calculated using the 2^{nd} order central difference scheme, it can be argued that even by using the 5^{th} order MUSCL scheme the overall order of accuracy of the scheme is still 2^{nd} order. On the other hand, this method has been extensively used[71, 154, 99] to compare results with 2^{nd} order MUSCL scheme to show much better results and highly comparable results with even higher order scheme, which make this method particularly important to investigate further.

3.3.4 Low Mach Number Treatment

In the FV high-resolution methods, the Euler equations can demonstrate steep discontinuities in the solution of compressible flows in order to provide a stable and non-oscillatory solution by adding a certain level of artificial dissipation in the solution. In Godunov type methods this is added by the upwind behaviour of the numerical method which results in anomalous increase in entropy and thus a corresponding decrease in the kinetic energy. Several studies have been carried out to investigate the influence of the artificial viscosity on the solution of inviscid flows within the low Mach number regiems [117, 12, 165]. In fact, Volpe [165] used many examples to show that the FV methods generate inaccurate results for low Mach number flows mainly due to the excessive numerical dissipation.

Guillard *et al* [70, 69, 68] established the incorrect pressure difference scaling for low Mach numbers for standard Godunov schemes and proposed a form of preconditioning of the governing equations to correct this error. In 2008, Thornber *et al* [150] presented a theoretical analysis demonstrating that the incorrect pressure scaling at low Mach numbers is caused by the large velocity jumps at the cell interfaces. They adopted a low Mach treatment for this excessive numerical dissipation and proposed that the velocity jumps at the cell interfaces can be modified by a function z which gives the reconstructed velocities $\mathbf{u}$ as follows [151]:

$$\mathbf{u}_{L,M5+LM} = \frac{\mathbf{u}_L + \mathbf{u}_R}{2} + z\frac{\mathbf{u}_L - \mathbf{u}_R}{2}$$
$$\mathbf{u}_{R,M5+LM} = \frac{\mathbf{u}_L + \mathbf{u}_R}{2} + z\frac{\mathbf{u}_R - \mathbf{u}_L}{2} \tag{3.43}$$

where z is defined as the local Mach number and,

$$\begin{aligned} z &= min\left(M_{total}, 1\right) \\ M_{total} &= max\left(M_L, M_R\right) \end{aligned} \tag{3.44}$$

It was also demonstrated that with this modification the leading-order kinetic energy dissipation is proportional to $u^3/\Delta x$, which is similar to that proposed by Kolmogorov [100] for the decaying turbulence and validated this approach for a deep cavity [152] and ship analysis [153]. This dissipation rate plays the role of an implicit sub-grid scale (SGS) model in the numerical scheme. As no explicit SGS model is employed in the code this class of high resolution scheme can be termed as Implicit Large Eddy Simulations (ILES) [63]. This has been successfully adopted in several studies to investigate the near wall flows and presented much accurate result using this method as compared to without using this method[154, 71, 99].

3.3.5 Time Integration

To obtain a time-dependent solution of the NS-equations time-marching is employed which progressively evaluates the solution at each timestep. For this purpose, explicit Runge-Kutta (RK) methods are widely preferred because of their simplicity in implementation and computation of unsteady flows. The vector form of the equations (Equation (3.32)) can be written as below:

$$\frac{\partial \mathbf{U}}{\partial t} = -\frac{\partial \mathbf{F}}{\partial \xi} - \frac{\partial \mathbf{G}}{\partial \eta} - \frac{\partial \mathbf{H}}{\partial \zeta} + \frac{\partial \mathbf{L}}{\partial \xi} + \frac{\partial \mathbf{M}}{\partial \eta} + \frac{\partial \mathbf{N}}{\partial \zeta} = f\left(\mathbf{U}, t\right) \tag{3.45}$$

for which, first-order approximation can be written as:

$$\frac{\mathbf{U}^{n+1} - \mathbf{U}^n}{\Delta t} = f\left(\mathbf{U}, t\right) \tag{3.46}$$

which is also called forward Euler method or first order RK method. For higher order algorithms, multiple stages can be introduced in the RK methods. In the current work, an explicit three-stage 2^{nd}-order accurate strong-stability-preserving Runge-Kutta (SSPRK) [146, 43] scheme has been employed which extends the stability of the method up to a Courant-Friedrichs-Lewy [21] (CFL) number of 2 which is given as below:

$$\begin{aligned} \mathbf{U}_i^1 &= \mathbf{U}_i^n + \frac{1}{2}\frac{\Delta t}{\Delta x} f\left(\mathbf{U}_i^n\right) \\ \mathbf{U}_i^2 &= \mathbf{U}_i^n + \frac{1}{2}\frac{\Delta t}{\Delta x}\left[f\left(\mathbf{U}_i^1\right)\right] \\ \mathbf{U}_i^{n+1} &= \frac{1}{3}\left(2\mathbf{U}_i^2 + \mathbf{U}_i^n + \frac{\Delta t}{\Delta x}\left[f\left(\mathbf{U}_i^2\right) + f\left(\mathbf{U}_i^1\right)\right]\right) \end{aligned} \tag{3.47}$$

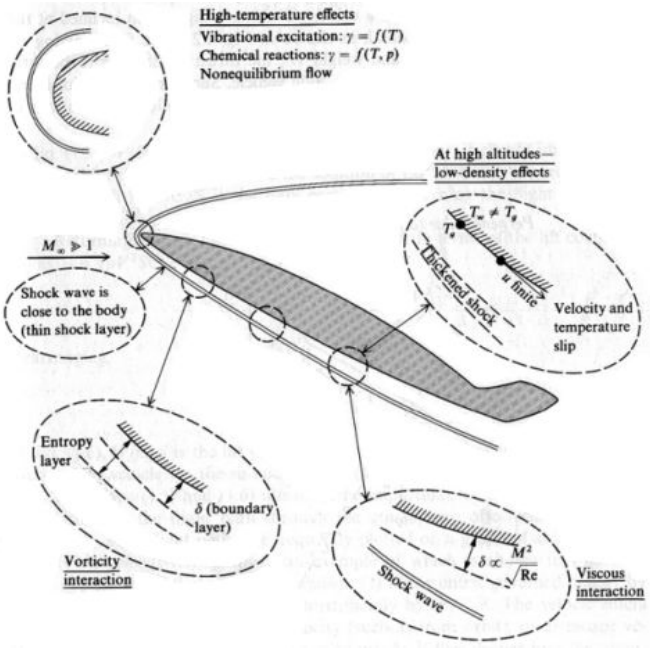

Figure 3.3: *Physical characteristics of hypersonic flow[6].*

3.4 High-Temperature Real-Gas Effects

3.4.1 Hypersonic Flow

There is no specific definition for the hypersonic flow. Roe, in 1970 in a lecture at the Von Karman Institute, made a comment that everyone would have a different Mach number to define a flow as hypersonic flow [6]. If one defines Mach 5 as a hypersonic flow, then this does not mean that Mach 4.95 is not hypersonic. Hypersonic flow can be best understood by defining some properties/phenomenon of the fluid. One or more of these phenomenon might become important at one Mach number say Mach 3 and others might become prominent at relatively higher Mach number say Mach 12, but any of these flow properties when observable can help identify a flow as Hypersonic [7, 6, 76]. Figure 3.3 presents a physical characterization of hypersonic flow and these phenomenon are described below (Anderson[6]):

Thin Shock Layers

The shock layer is the flow field between the shock and the body. At high Mach numbers, the shock layers can be very thin due to the fact that at higher Mach numbers the shock angle decreases. For example applying the oblique shock relations to calculate the shock angle on a 15° wedge would give a shock angle of 18° for Mach number of 35. This would reduce if we apply the effects of higher temperatures and real gas affects.

Entropy Layer

Entropy increases across a shock. At very high Mach numbers the entropy increase would be very high as well. If instead of a wedge we consider a blunt body in a very high Mach flow then the entropy increase in the nose area would "wet"[6] the whole surface of the body. The boundary layer then actually develops inside the entropy layer. This very high entropy rise can create problems in analytically solving the boundary layer problems for a very high Mach number flows.

Viscous Interaction

For a high Mach number flow the boundary layer that grows on the outer surface of the body can grow to extreme thickness. This growth in the boundary layer then starts affecting the outer inviscid flow and it greatly changes it. These interactions between the boundary layers and the outer inviscid flow are called Viscous Interactions. Viscous interaction can create a lot of problems such as very high drag, lift, pressure distribution and stability issues for the body in a hypersonic flow.

High Temperature Flows

Kinetic energy in a hypersonic flow is dissipated through the viscous sublayer. This dissipation of energy can create very high temperatures inside the thin viscous sublayer which in turn can excite the vibrational or even the electronic energies in the flow field. The air does not behave as a calorifically perfect gas but in fact as a thermally perfect gas or even a real gas if the electronic excitation occurs at extremely high Mach numbers. These additionally excited energy levels change the ratio of the specific heats (γ) such that it cannot be considered as constant anymore and it becomes a function of the temperature itself. NACA technical report (NACA-1135), provides in more details the affects vibrational energy can have on the value of γ and it also provide formulae for calculation of γ at high temperatures[147].

Low Density Flow

This is a phenomenon that mostly becomes prominent at an altitude of more than 100 km from the sea level. At very high altitudes, the air molecules becomes so far apart from each other that the mean free path(λ) becomes very large, almost equal to 30 cm, whereas at standard conditions at sea level it is approximately $7\text{x}10^{-6}$ cm. The region of atmosphere at this altitude is called "Low Density Flow"[6] and the air cannot be considered as a *continuum*.

3.4.2 High Temperature and Flow Behind Shock Waves

If the super/hypersonic flow contains discontinuities, changes in temperature and hence in the ratio of specific heats would have considerable impact on the flow properties behind the discontinuities. Figure 3.4 show a flow with oblique shock and the impact on the flow properties behind the shock. For a given inflow Mach number (M_1) with constant γ across the shock, the Mach number (M_2) of the flow behind the oblique shock always decreases whereas, the temperature, pressure and density increase. If the inflow temperature is high enough that it can change the γ behind the shock which be reduced. This reduction in the γ can change the flow properties even more such that the M_2 is higher with variable γ than with a constant γ. Similarly the increase in the temperature, pressure and density will also correspond to the change in the γ and these will be higher than that obtained with a constant γ, as shown below. Therefore, it is important in the study of high speed flow to take into account any changes in the γ with the temperature in order to obtain realistic results. To summarize, as the γ reduces:

$$\begin{aligned} M_{2\ (variable\ \gamma)} &> M_{2\ (constant\ \gamma)} \\ T_{2\ (variable\ \gamma)} &< T_{2\ (constant\ \gamma)} \\ P_{2\ (variable\ \gamma)} &< P_{2\ (constant\ \gamma)} \\ \rho_{2\ (variable\ \gamma)} &> \rho_{2\ (constant\ \gamma)} \\ Shock\ Angle_{variable\ \gamma} &< Shock\ Angle_{constant\ \gamma} \end{aligned} \tag{3.48}$$

It is clear from the results shown above that the hypersonic flow is much more complicated than a low Mach flow. There are no definite shock tables available to account for these high temperature effects in a hypersonic flow as these properties would change with every change in the deflection angle of the body.

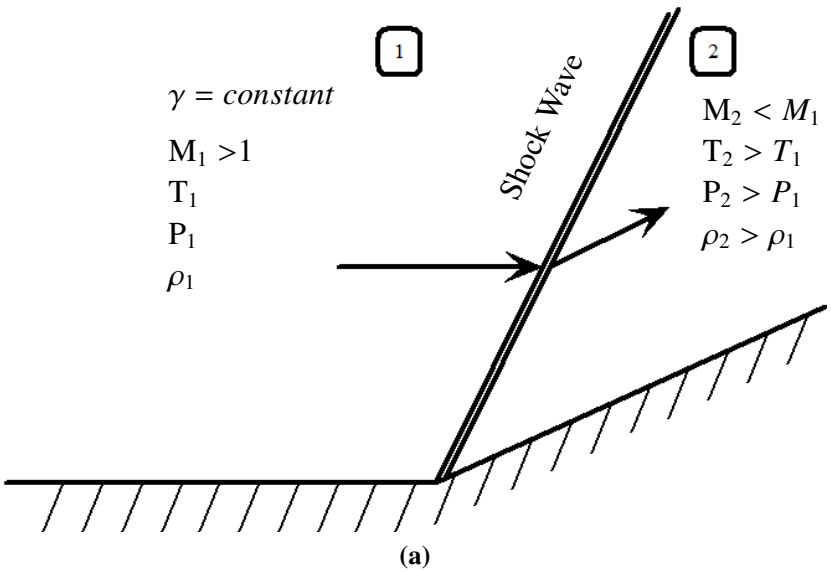

Figure 3.4: *Oblique shock over a ramp* [7].

3.4.3 Equation of State: Variable Gamma (γ) Formulation

Gamma (γ) is defined as the ratio of specific heats. A gas is a collection of particles such as atoms, molecules, and ions etc. that are in a constant random motion in space. These particles exhibit a force field when they move around in a random fashion because of their electronic structure. The force field of one particle reaches out and interacts with force fields of neighbouring particles in the gas and hence they are termed as *intermolecular forces*. These intermolecular forces contains energy and this energy can take many forms as below[6]:

- Translational Energy (e_{tran})
- Rotational Energy (e_{rot})
- Vibrational Energy (e_{vib})
- Electronic Energy (e_{elec})

Collectively all these modes of energy are called the *internal energy* (e) of the particles of gases where,

$$e = e_{trans} + e_{rot} + e_{vib} + e_{elec} \tag{3.49}$$

Each of these modes activate/excite at a different temperatures. Figure 3.5 shows a schematic relation between the stagnation temperature of a gas and Mach number with different modes of energy being excited. In the previous section, the properties of the hypersonic flow were explained. Carefully looking at those properties, one of the most important property or characteristic of hypersonic flows is the involvement of high temperatures. A calorically perfect gas (as explained in the section 3.1.4) only exhibits two modes of energy; translational and rotational. As the temperature of the gas increases, the molecules in the gas acquire more degrees of freedom and vibrational energy is excited. At extremely high temperatures (above $\approx$ 9000 K), the bonds between the electrons revolving around the nucleus of the atoms of gas start to break and electronic energy is excited. The gas at extremely high temperatures is a mixture of charged particles or ions which is called *plasma*.

In Section 3.1.4, the Equation of State has been presented for a calorically perfect gas formulation where at the given temperature range the specific heat capacities of the gas are considered constants as shown by the Equation (3.20). Section 3.1.4 also explains the calculation of the total energy for the calorically perfect gas.

In equilibrium, as the temperature increases to higher levels (above 1000 K), the gas does not behave as a calorifically perfect gas anymore. Considering the molecular dynamics at these temperatures the vibrational energy of molecules excites the dissociation of molecules. In air, the oxygen molecules start to dissociate at about 2500

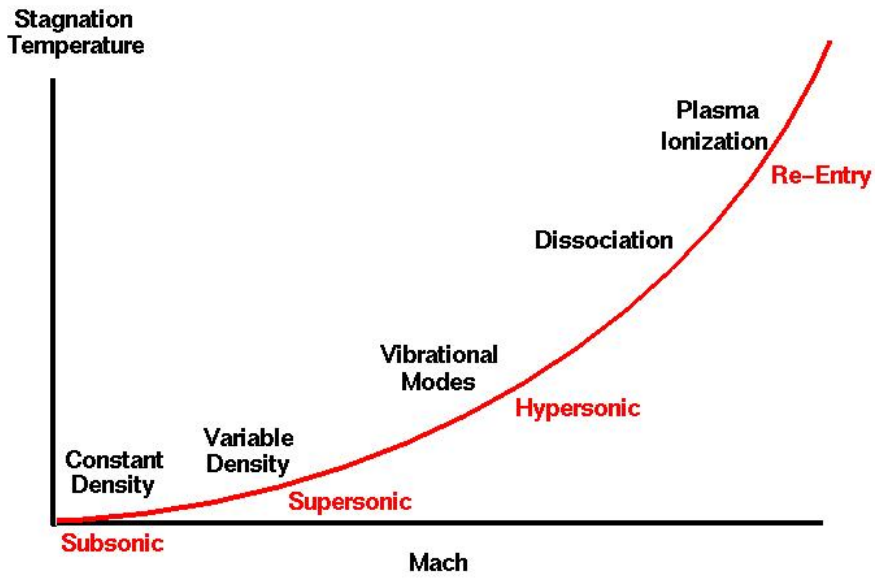

Figure 3.5: *A schematic plot showing relation between the stagnation temperature of a gas and the Mach number showing stages for excitation of various energy modes in relation to Mach number rise [31].*

K and at about 4000 K all the oxygen molecules dissociate. At this temperature the nitrogen molecules start dissociation and it completes at about 9000 K. At temperatres above 1000 K, the calorically perfect gas formulation would produce considerably wrong predictions and must not be used. Instead the, so-called, Thermally perfect gas formulation[147, 6] should be used. A thermally perfect gas assumes a thermodynamic and chemical equillibrium (i.e., non-reacting) where the Equations (3.17), (3.18) and (3.19) still hold true but the internal energy (e) and the enthalpy (h) of the gas become a function of temperature such that:

$$\begin{aligned} e &= e(T) \\ h &= h(T) \end{aligned} \tag{3.50}$$

Thus the co-efficients of specific heats and their ratio cannot be considered constant and must be calculated for a thermally perfect gas (which is presented in the Section 3.4.3). The total energy for a thermally perfect gas must be adjusted/corrected now which is discussed in the Reference [147] and briefly presented below as a correction related to the vibrational mode of internal energy:

$$e_{vib} = \frac{R\Theta}{(\exp^{\Theta/T} - 1)^2} \tag{3.51}$$

Thus the total internal energy for a thermally perfect gas is calculated as:

$$e = \frac{p}{\rho\,(\gamma' - 1)} + \frac{R\Theta}{\left(\exp^{\Theta/T} - 1\right)^2} \tag{3.52}$$

where, Θ is called a characteristic temperature and γ' is discussed in the Section 3.4.3 below. Hirschel [78] has defined the values of Θ for different molecules. NACA-1135 [147] defines the value of Θ for air as 3055 K and is useful if air is considered as one species. It is interesting to understand the asymptotes of the second term on the right hand side of the Equation (3.52). If the gas temperature T is closer to zero (0) then the term $\exp^{\Theta/T}$ tends to be large resulting in the overall second term on the right hand side of the Equation (3.52) being neglected as it becomes very small. On the other hand, if the temperature T is very high (higher than the characteristic temperature Θ) then the term $\exp^{\Theta/T}$ tend to be closer to unity (1) which would result in the right hand term in the Equation (3.52) being neglected. This defines the limits of aplicability of the Equation (3.52) and it has been found to be valid for temperatures between 270 K and 3055 K for a characteristic temperature Θ of 3055 K. Higher temperatures in the case of chemically reacting gases and combustion are beyond the scope of this work.

Variable Ratio of Specific Heats (γ')

As explained above, for a thermally perfect gas the specific heats (C_p and C_v) can no longer be considered constant, instead, these become function of temperature. As we are dealing with the thermally perfect gases only in this work, in order to calculate the specific heats special treatment is implemented in the code CNS3D which is according to the NACA report (NACA-1135) [147] as below:

$$C'_p = C_p \left(1 + \left(\frac{\gamma - 1}{\gamma}\right)\left[\left(\frac{\Theta}{T}\right)^2 \frac{e^{\Theta/T}}{\left(e^{\Theta/T} - 1\right)^2}\right]\right) \tag{3.53}$$

$$C'_v = C_v \left(1 + (\gamma - 1)\left[\left(\frac{\Theta}{T}\right)^2 \frac{e^{\Theta/T}}{\left(e^{\Theta/T} - 1\right)^2}\right]\right) \tag{3.54}$$

The $(.)'$ (prime) over any quantity represent that it is a variable quantity in the context of a thermally perfect gas formulation. From Equation (3.18), for a thermally perfect gas:

$$\gamma' = \frac{C'_p}{C'_v} \tag{3.55}$$

where, γ' represents the variable ration of specific heats. Using the values of C'_p and C'_v in Equation (3.55):

$$\gamma' = \frac{C_p \left(1 + \left(\frac{\gamma-1}{\gamma}\right)\left[\left(\frac{\Theta}{T}\right)^2 \frac{e^{\Theta/T}}{\left(e^{\Theta/T}-1\right)^2}\right]\right)}{C_v \left(1 + (\gamma-1)\left[\left(\frac{\Theta}{T}\right)^2 \frac{e^{\Theta/T}}{\left(e^{\Theta/T}-1\right)^2}\right]\right)} \tag{3.56}$$

now, assuming:

$$A = \left[\left(\frac{\Theta}{T}\right)^2 \frac{e^{\Theta/T}}{\left(e^{\Theta/T}-1\right)^2}\right] \tag{3.57}$$

and using this in Equation (3.56) gives:

$$\gamma' = \frac{C_p \left(1 + \left(\frac{\gamma-1}{\gamma}\right)A\right)}{C_v \left(1 + (\gamma-1)A\right)} \tag{3.58}$$

and after some manipulation Equation (3.58) take the form:

$$\gamma' = 1 + \frac{\gamma-1}{1 + (\gamma-1)A} \tag{3.59}$$

and now using the value of A from Equation (3.57) give the variable ratio of specific heats (γ') for a thermally perfect gas.

$$\gamma' = 1 + \frac{\gamma-1}{1 + (\gamma-1)\left[\left(\frac{\Theta}{T}\right)^2 \frac{e^{\Theta/T}}{\left(e^{\Theta/T}-1\right)^2}\right]} \tag{3.60}$$

Calculation of Temperature (T)

To determine the temperature fluctuations, following equation is solved iteratively for temperature (T):

$$T = \left(e - \frac{R\Theta}{\left(\exp^{\Theta/T}-1\right)^2}\right)\left(\frac{(\gamma'-1)}{R}\right) \tag{3.61}$$

The iterative process to solve Equation (3.61) would require an initial guess to start off the iterations but it has been noticed to converge after five (5) iterations although that would require a sensible guess for the temperature which can be obtained by using a constant γ and equation of state as in Equation (3.16). This calculation of temperature does not explicitly account for the degrees of freedom under the formulation presented in this work. However, as it can be noticed that the Equation (3.51) has been added as a correction factor for vibrational energy in the Equation (3.52) to calculate the internal energy (e) of a thermally perfect gas (where the translational, rotational and vibrational

modes of energy are excited), thus, the temperature calculated here implicitly represent all these modes of energy.

Changes to HLLC Riemann Solver

In order to implement the above formulation, some modifications have been implemented in the HLLC Riemann solver. The change is in two aspects namely the calculations of pressure and the speed of sound. For the calculation of the pressure, in the HLLC Riemann solver the temperature *left* and *right* states are calculated using a Newton iteration for Equation (3.61). These left and right states of temperature are used to calculate the respective pressure states using the Equation (3.16). The speed of waves is calculated using the same left and right states of the temperature and the local gamma using the relation below:

$$a = \sqrt{\gamma' RT} \tag{3.62}$$

The left and right states of temperature are known at this stage, therefore, this method for the calculation of the speed of waves is adopted for simplicity in the calculations only. Further details of HLLC Riemann solver remain exactly as explained by Toro[155].

3.4.4 Validations of Variable Gamma (γ) Formulation

Validation Against NACA Report 1135

In order to understand the effects a change in the temperature can have on the γ' in a high speed flow, a series of simulations are carried out using a planar shock tube to obtain the γ' at a specified temperature using the code CNS3D where the γ' changes with the temperature using the above formulation. The results are obtained at a series of temperatures and are compared with those given in NACA-1135 report. Table 3.1 gives the values of γ' for a thermally perfect gas at various temperatures from the NACA-1135 report and corresponding results obtained from CNS3D simulations. It can be observed that at high temperatures the value of the ratio of specific heat reduces considerable which will have its effects on the flow downstream especially if the flow contains discontinuities.

Validation against NASA TPG code

In order to validate the variable ratio of specific heat formulation with the changes in the temperature in high speed flow two cases are assumed; a) a normal shock case and, b) an oblique shock case. For a normal shock, a planar shock tube is analyzed with high speed inflow at Mach 4.0 and the results are compared with NASA TPG (Thermally Perfect Gas) code. The NASA TPG code utilizes a set of compressible

Table 3.1: *Variation of ratio of specific heats with temperature [147]*

Temperature°R (Kelvin)	NACA-1135	CNS3D Results	% Abs. Error
500 (277.778)	1.4	1.3993988	0.04294
600 (333.333)	1.399	1.3983236	0.04834
700 (388.889)	1.396	1.3959376	0.00447
800 (444.444)	1.392	1.3920519	0.00372
900 (500.000)	1.387	1.3868552	0.01044
1000 (555.556)	1.381	1.3807517	0.01798
1100 (611.111)	1.375	1.3741837	0.05937
1200 (666.667)	1.368	1.3675246	0.03547
1500 (833.333)	1.349	1.3492024	0.01500
2000 (1111.111)	1.328	1.3274946	0.03806
2400 (1333.333)	1.317	1.3165735	0.03238
3000 (1666.667)	1.306	1.3064563	0.03493
3500 (1944.445)	1.301	1.3012886	0.02218
4000 (2222.222)	1.298	1.2977931	0.01594
4500 (2500.000)	1.296	1.2953310	0.05162
5000 (2777.778)	1.294	1.2935368	0.03579

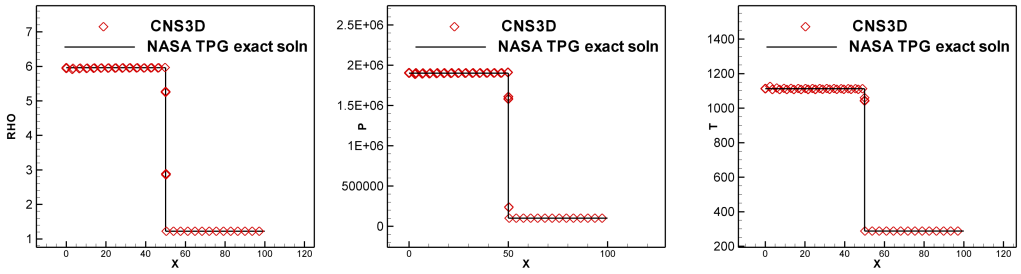

(a) *Density* **(b)** *Pressure* **(c)** *Temperature*

Figure 3.6: *Density, Pressure and Temperature profiles of Mach 4.0 flow across a normal shock wave in thermally perfect gas; comparison between the CNS3D and NASA TPG results.*

flow equations for a thermally perfect, calorifically imperfect gas where the relations are expressed as a polynomial function of temperature. The code produces tables of compressible flow properties similar to those found in NACA Report 1135. TPG code has been validated by comparison with the methods of NACA Report 1135 and the major advantage of this code over the NACA Report 1135 is that it is applicable to any type of gas (whether mono-atomic or poly-atomic).

The one-dimensional normal shock simulation is performed on a shock tube which is 100 mm long and has 500 cells in x-direction. CFL number is taken as 1.0 and the

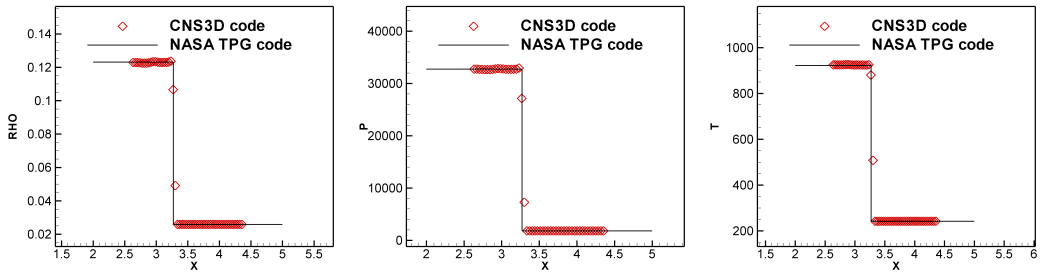

(a) *Density* **(b)** *Pressure* **(c)** *Temperature*

Figure 3.7: *Density, Pressure and Temperature profiles of Mach 10.0 flow over an* 18° *angle ramp in thermally perfect gas; comparison between the CNS3D and NASA TPG results.*

shock position is fixed at x = 50 mm. The results are shown in the Figure 3.6 where solid line represents the exact solution and the diamond shapes represent the CFD solution. Using the methodology described in earlier sections for thermally perfect gas and modified fifth order MUSCL scheme with low Mach correction the results for density, pressure and temperature agree with the NASA TPG code. Similarly, the oblique shock test case is performed for a hypersonic flow of Mach 10.0 over a ramp of 18° angle. The grid size used is 10 mm x 7 mm with ramp starting at x = 2 mm with 101 x 71 grid points. The CFL used is 1.0 and the results obtained from the simulation of a thermally perfect gas are compared with those from NASA TPG code for oblique shock waves and presented in Figure 3.7.

3.5 Turbulent Boundary Conditions

Fluid dynamics problems involving turbulent flows demonstrate the importance of incorporating turbulent boundary conditions to capture the correct flow dynamics and the benefits have been identified in several CFD studies of turbulent engineering flows[101, 116, 105, 52, 63, 66]. Initial and boundary conditions play a major role in the solution of governing equations and it becomes vital when solving using the time-dependent DNS, LES or ILES techniques. Initial conditions specify the state of the flow at time = 0 and therefore the initial guess has to be realistic numerically and thermodynamically in order to obtain a well-behaved solution and to avoid numerical breakdown of the solution process. Apart from initial conditions, the boundary conditions also play a major role in the flow field development in any simulation.

In the Reynolds Averaged Navier-Stokes (RANS) approach, where turbulence is modelled, using various turbulence models which are now well developed and tuned for specific cases[80, 81], turbulent inflow conditions can also play important role. In the case of time-evolving simulations [Direct Numerical Simulation (DNS) or Large Eddy Simulations (LES)] where turbulence in the flow field is mainly resolved, turbulent

inflow boundary conditions are required[95, 82] and the velocity profiles prescribed at the boundary substantially influence the results. Research into effective methods of generating a turbulent boundary condition has led to several techniques that are in use today where the most widely used are random white-noise and rescaling/reintroduction methods. The former method offers a very simple solution where a random signal is added to the averaged velocity profiles to mimic the fluctuations in the flow field. Apart from simplicity in implementation, this method offers a cost effective solution from computational point of view. However this is not an effective method as explained by Klein *et al.*[95] as,

> "*the energy of the signal is equally distributed over the whole wavenumber range which means that the spectrum is approximately a horizontal line ... and because of this lack of energy in the low wavenumber range the pseudo turbulence is immediately damped to zero and the result is identical to laminar flow*".

A modification to this was proposed by Lee *et al.*[106] where they utilized a prescribed energy spectra at the inflow plane with randomized phases and introduced an inverse Fourier Transform to convert the spectral to physical space. The phases are functionally dependent upon the time, frequency and wavenumbers to eliminate periodicity in time. Although improved, this method still involved serious programming challenges as described in [95].

The latter method which is rescaling/re-introduction[145, 109, 89, 59, 91] is a technique where a recycling plane is selected inside the computational domain, the resolved fluctuation from this plane are extracted and then rescaled based upon the law-of-the-wall and finally reintroduced as fluctuations to the mean velocity profiles at the inflow. This method can produce very accurate turbulent inflow data, although, it is limited to simple geometries and can be difficult to implement. Furthermore, the computational costs involved with this method can be very high. Another technique could be using a precursor domain simulations[99] where boundary condition is a modified periodic boundary condition such that it mirrors all the variables but it is different in that the mirrored values of the streamwise velocity are 'corrected' such that the mass flow rate across the inlet and outlet achieves a target value. This method is used to inverstigate a low Mach number flow and generates reasonable results in comparison to DNS data but no information has been provided to the efficiency of the method.

Incorporating a spatially developing turbulent boundary layer is another technique in turbulence generation especially in the area of DNS[105, 125, 144, 145, 124] but again this could become very expensive from the point of view of transition to turbulence as it could require a long domain and time for transition. However a good compromise has been achieved by Druault *et al.*[47] where they used Proper Orthogonal Decomposition (POD) and linear stochastic estimation to generate turbulent velocity profiles for the DNS of the mixing layer at an intermediate cost compared to pure spatially developing turbulent boundary layer. Overall, spatially evolving/transitioning turbulent boundary layer is an expensive solution to the problem which can produce result in case of DNS

but in the case of classical LES or Implicit LES of high speed and high Reynolds number flows it would require much higher resolution and simulations would need to be run for a very long period of time owing to prohibitive computational costs.

Generally termed as synthetic turbulence, Klein *et al.*[95], in 2003, proposed a new method for the generation of inflow data for unsteady simulations (DNS or LES) based upon digital filters. They developed the technique of generating the artificial velocities as the inflow data based upon the assumption that the second order correlation for the homogeneous turbulence take a Gaussian form. They devised a three-dimensional digital filter using spatial correlations to obtain a two-dimensional data slice that would become the turbulent inflow boundary condition. The temporal correlation was also utilized to shift the data slice to the next plane at the new time step and again creating a new data for the first plane and so on. In 2005, Kempf *et al.*[92] used a similar technique to generate synthetic turbulent inflow boundary condition but instead of a correlation function they used a diffusion equation to obtain the random data. Later in 2007, Veloudis *et al.*[162] proposed an improvement in the efficiency of the three-dimensional digital filter by using Fast Fourier Transform for the filtering operation. Xie and Castro[169] argued that the correlation for the turbulent shear-layer flows takes the Exponential form rather than Gaussian and used this approach to study the high Reynolds number urban flows using LES.

Another similar synthetic turbulence generation approach was developed by Sandham *et al.*[138] where the inflow conditions were prescribed at the inflow for several modes of turbulence for the inner-layer near-wall disturbances. This technique requires short domains from the inflow plane to develop fully turbulent flow, however, this technique "*does not attempt to match the proper statistical moments*"[156]. Touber and Sandham[156] utilized a method for the generation of synthetic turbulent data for the LES to study the low-frequency unsteadiness in a turbulent shock-induced separation bubble to find excellent agreement with the experimental data. In this thesis a method based upon references [95, 169, 156] has been implemented with some modifications in order to generate turbulent inflow data for the time-evolving ILES investigations carried-out in this thesis. Below the technique is presented in details.

3.5.1 Digital Filter Based Turbulent Boundary Condition

The generation of turbulent inflow data based upon the digital filter technique [95, 169, 156] starts with set of random numbers r_k where $1 \leq k \leq p$, and p is the total of the random numbers. The mean and variance of the random numbers set is zero and unity, respectively, i.e.,

$$\overline{r_k} \equiv \sum_{k=1}^{p} r_k/p = 0 \quad , \tag{3.63a}$$

$$\overline{r_k r_k} \equiv \sum_{k=1}^{p} r_k^2/p = 1 \quad , \tag{3.63b}$$

A filter operator (F_N) is defined as, where N is a positive integer, then:

$$v_k \equiv F_N(r_k) = \sum_{j=-N}^{N} b_j r_{k+j} \quad , \tag{3.64}$$

here, v_k is the velocity field in one-dimension and b_j is a set of real numbers and is called the *filter coefficient*. This can be obtained as below:

$$b_j \approx \frac{\tilde{b_k}}{\left(\sum_{j=-N}^{N} \tilde{b_k^2}\right)^{1/2}} \quad , \tag{3.65}$$

where,

$$\tilde{b_k} = \exp\left(-\frac{\pi k}{n}\right) \quad , \tag{3.66}$$

This gives the filter coefficient in one-dimension. Klein *et al.*[95] describe this as a good approximation when $N \geq 2n$. In order to get the two-dimensional filter coefficient, the following is applied as described by Xie and Castro [169] and Touber and Sandham[156]:

$$b_{jk} = b_j \cdot b_k \quad , \tag{3.67}$$

The two point correlation function is defined as:

$$R(x_k + x) = \exp\left(-\frac{\pi x}{2I_x}\right) \quad , \tag{3.68}$$

where, x_k is a point of reference and x is the point some distance away from the reference point. I_x is defined as the integral length scale. The correlation function is after Xie and Castro [169] who identified the correlation to be of Exponential form instead of Gaussian as originally proposed by Klein [95]. Here, n can be defined in a way such that $I_x = n\Delta x$ and $x = m\Delta x$ then the two point correlation function takes the form as below:

$$R(x_k + m\Delta x) \approx \frac{\overline{v_k v_{k+m}}}{\overline{v_k v_k}} = \exp\left(-\frac{\pi m}{2n}\right) \quad , \tag{3.69}$$

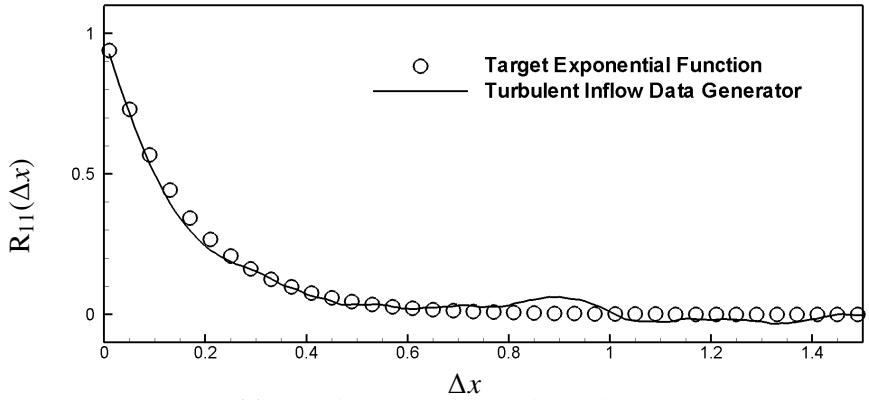

(a) *One-dimensional spatial correlation*

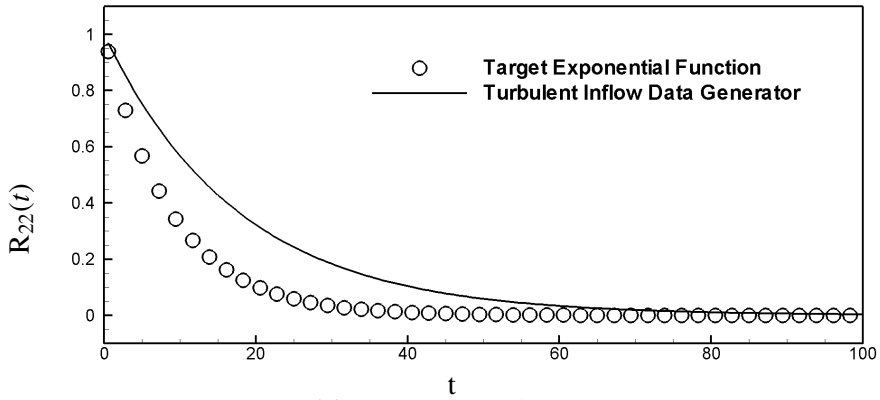

(b) *Temporal correlation*

Figure 3.8: *One-dimensional spatial(a) and temporal(b) correlations obtained by the digital filter based turbulent inflow data generator showing reasonable match with the corresponding target exponential functions.*

Using normally distributed random numbers, then filtering them through the filter coefficients, Equation 3.64 is used to calculate the velocity field which would have the prescribed length scales. This is calculated for the very first time step only. For the second timestep and so on the velocity field is calculated in the same manner, and then correlated in time to the previously calculated velocity field as below:

$$\psi_k = \nu_k^{old} \exp\left(-\frac{\pi\Delta t}{2\tau}\right) + \nu_k \sqrt{1 - \exp\left(-\frac{\pi\Delta t}{\tau}\right)} \quad , \tag{3.70}$$

where, ψ is the velocity field for new timestep, Δt is the timestep and τ is the Lagrangian time scale. In this way, two-dimensional velocity fields can be obtained which contains all the prescribed integral length and time scales and two point correlation. In order to determine the fluctuations in the prescribed velocity profiles, the relation given by Lund *et al* [109], is used:

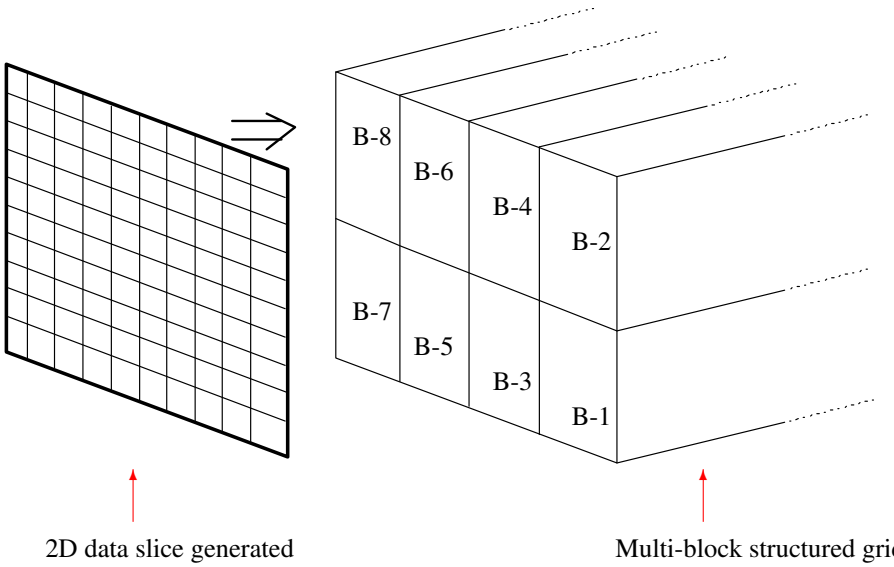

Figure 3.9: *A schematic showing the two-dimensional data slice generated using the digital filter based turbulent inflow data generated using the modified technique[133]. The data slice is then imposed upon the inflow plane of the structured grid with multi-blocks, as shown in the figure.*

$$\begin{bmatrix} u(0,y,z,t) \\ v(0,y,z,t) \\ w(0,y,z,t) \end{bmatrix} = \underbrace{\begin{bmatrix} \langle u(0,y,z,t)\rangle \\ \langle v(0,y,z,t)\rangle \\ \langle w(0,y,z,t)\rangle \end{bmatrix}}_{U_i(0,y,z)} + \underbrace{\begin{bmatrix} \sqrt{R_{11}} & 0 & 0 \\ R_{21}/\sqrt{R_{11}} & \sqrt{R_{22}-\left(R_{21}/\sqrt{R_{11}}\right)^2} & 0 \\ 0 & 0 & \sqrt{R_{33}} \end{bmatrix} \begin{bmatrix} \psi^u(y,z) \\ \psi^v(y,z) \\ \psi^w(y,z) \end{bmatrix}}_{u_i'(0,y,z,t)} \quad (3.71)$$

where, R_{xx} are the Reynolds stresses.

In the case of compressible turbulent flows, the density variations also play an important role therefore, it is important at this stage to include density fluctuations in the inflow data as well. Although Touber and Sandham [156] used Strong Reynolds Analogy (SRA) for the generation of density fluctuations, the validity of the SRA is widely questionable[156]. Also because the SRA utilizes the temperature fluctuations in the field to calculate the density fluctuations and at the first timestep we do not have any temperature fluctuation, therefore, in this case the SRA is not applied. Instead, fluctuations calculated in the above equations for the velocity field, which are based upon the Reynolds stresses are also utilized as the fluctuations in the density. Hence,

$$\rho(0, y, z, t) = \rho(0, y, z)\left(1 - \frac{\sqrt{R_{11}}}{U_\infty} \cdot \psi^u(y, z)\right) \quad , \tag{3.72}$$

where, $\rho(0, y, z, t)$ is the instantaneous density at any point, $\rho(0, y, z)$ is the averaged density profile for STBL and fluctuations are added to the density profiles as shown in the Equation (3.72). This completes the generation of the turbulent inflow data for the complete flow field which contains all the integral length scales and the time scales built in to it. For further details of this method please refer to Xie and Castro[169] and Touber and Sandham[156].

Figure 3.8 presents the actual/target exponential plots in space and time. Also plotted are the exponential trends in the spatial and temporal correlations obtained from the turbulent inflow data generator. Although the spatial correlation data fits the targeted exponential function but there is a discrepancy in the temporal data fit, nevertheless, it exhibits the same exponential trend as expected from the two point correlation function. Based upon this modification, a two dimensional (imaginary) data slice can be generated using digital filters at every time step. This two-dimensional data slice is then imposed upon the inflow plane of the computational grid as shown in the Figure 3.9.

The fluctuations/turbulent inflow data obtained through the digital filter based turbulent boundary condition can be used as inflow condition for any time-evolving simulations technique. For the work presented in this thesis, the inflow conditions are implemented on a rectangular grid for the simulations of supersonic TBL in the next Chapters.

3.6 General Boundary Conditions

A numerical solution of any physical problem can only consider a part of the actual physical system. Truncation of the physical domain to create computational domain requires introduction of the artificial boundaries prescribed to the system. Solid walls in the system also require special consideration to represent the flow physics correctly. Various boundary conditions are available in the CFD but the boundary conditions utilized in the computational domains in this research work make use of the following five boundary conditions:

Supersonic Inflow

At the inlet the CNS3D provides only one inflow condition that can be called a supersonic inflow. In supersonic inflow condition the eigenvalues have the same sign. As the flow is entering the physical domain, the conservative variables on the boundary are determined by freestream values only. Thus,

$$\vec{\Phi}_b = \vec{\Phi}_{b+1} \tag{3.73}$$

where Φ is any conserved variable and the subscript b represents a point on the boundary, for details see Blazek[14]). The values U_{b+1} are specified based on the given Mach number (M), and on two flow angles (angle of attack, side-slip angle) when initializing the flow field at the initial time step.

Supersonic Outflow

In the case of supersonic outflow boundary conditions, all eigenvalues have also the same sign. However, in this case the flow leaves the physical domain and all conservative variables at the boundary take values from the next cell update the cell at the boundary. The remainder of the boundary cells use a standard extrapolation method for the update, as below:

$$\vec{\Phi_b} = 2 \times \vec{\Phi}_{b-1} - \vec{\Phi}_{b-2} \tag{3.74}$$

where the subscript b represents a point on the boundary.

Subsonic Outflow

CNS3D also provides option of a subsonic outflow boundary condition. For subsonic boundary conditions, the eigen values do not have the same sign. In this case, the pressure at this boundary face is specified (as PEXIT in CNS3D). The density and the momentums at the boundary are assigned the values from the next cell and the total energy is calculated using the total density of all the species and the specified exit pressure at the boundary. For higher order reconstruction, the standard extrapolation method is used as presented above for the supersonic outflow condition. But this boundary condition is rarely utilised and in this particular work only the supersonic inflow and outflow boundary conditions are employed.

No-Slip

The no-slip condition is attributed to a viscous flow on a solid wall. The flow over a solid wall can be of two type; inviscid flow where the flow over the wall slips over the surface as there is no friction, or a viscous flow the relative velocity between the surface and the fluid directly at the surface is assumed to be zero and is generally refered to as "no-slip" boundary condition. As in this work a viscous flow is analysed, therefore, on no-slip boundary condition is discussed here. As per the definition of the viscous flow, the no-slip boundary condition is implemented as below:

$$u = v = w = 0 \tag{3.75}$$

Symmetry

For a symmetry boundary conidtion the condition that needs to be met is that there is no flux across the boundary. This is equivalent to the requirement that the velocity normal to the symmetry boundary is zero. Furthermore, the following gradients have to vanish:

- Gradient normal to boundary of a scalar quantity,
- Gradient normal to boundary of a tangential velocity,
- Gradient along the boundary of the normal velocity

which can be written as:

$$\vec{n} \cdot \vec{\nabla} U = 0 \tag{3.76}$$
$$\vec{n} \cdot \vec{\nabla} \left(\vec{v} \cdot \vec{t} \right) = 0 \tag{3.77}$$
$$\vec{t} \cdot \vec{\nabla} \left(\vec{v} \cdot \vec{n} \right) = 0 \tag{3.78}$$
$$\tag{3.79}$$

where U represents a scalar variable and $\vec{t}$ is a vector tangential to the symmetry boundary[14].

Farfield

The CFD simulations of external flows (e.g., around airfoils, wings, cars etc.) has to be conducted within a bounded domain and for this reason an artificial farfield boundary condition is utilized. The numerical implementation of the farfield boundary conditions has to fulfil two basic requirements; firstly the truncation of the domain should have no notable effects on the flow solution as compared to the infinite domain, and secondly, any outgoing disturbances must not reflect back into the flow field. For further details of the boundary condition see Balzek[14].

The digital filter based turbulent inflow boundary condition as described in the Section 3.5.1 is implemented in the CNS3D code contains a velocity profile which means that in the TBL region the flow is subsonic. The implementation of the Digital Filter based boundary layer can be termed as a mixed inflow boundary condition. The mixed inflow boundary condition allows both subsonic and supersonic inflow within a single boundary condition. The blending between the two flow regimes is based on

the user-specified inflow velocity components, total pressure and total temperature or static pressure and static temperature. In either case, the flow solver evaluates the local Mach number from the user-specified values. The temperature fluctuations are dealt with using the density fluctuations and the Equation of state, however in our case studies (as explained in the next Chapters), the pressure fluctuation data is not avaiable and thus constant pressure is assumed in the current study which can, perhaps, introduce some error but it was not possible to quantify this error.

CHAPTER 4

Jet Injection into Supersonic Crossflow

This chapter presents the ILES study of an experiment on transverse sonic circular jet injection into a supersonic flow using the digital filter based turbulent boundary condition to generate supersonic turbulent boundary layer on the flat-plate and analyses has been presented for the time averaged and instantaneous flow fields. This chapter acts as a validation case for the digital filter based turbulent boundary condition which will be utilized to study the transverse hydrogen injection into HyShot-II scramjet combustion chamber.

4.1 Introduction

In recent years, LES technique has contributed significantly towards understanding the dynamics of certain flows for which it is very difficult to carry out experiments. This is mainly due to the efficiency of LES based CFD codes and the computational resources available today. One such flow is a jet injected into a freestream crossflow, where the freestream flow could be subsonic or supersonic. For the subsonic flow cases an important example is a jet emerging through a hole from a gas tank (e.g., hydrogen) at high pressure. Important examples for a jet emerging into a supersonic freestream flow could be part of a missile thrust vector control system[83, 98], noise control in cavities during flight[140, 157, 158, 137, 18] and the combustion chamber of a typical scramjet engine[143, 23, 58, 56]. Both of these flow types require understanding of the flow mechanics/physics for proper design of the equipment. For both (subsonic and supersonic) examples, the under-pinning knowledge of the jet entering into a transverse flow is similar, therefore most of the experimental/theoretical studies of this phenomenon started with subsonic main flow and expanded to include supersonic freestream flows[108, 13].

In 1959, Adamson and Nicholls[3] presented the internal structure of an under-expanded jet into a quiescent air in order to study the structure of the jet and discussed a method to calculate the position of the Mach disc as the jet expanded into the air. Schetz and Billig[141] explored the transverse jet penetration into a supersonic freestream using

a *solid body* drag model and presented an analytical method for the prediction of jet penetration. They introduced the jet-to-crossflow momentum flux ratio (J) as the most important parameter in order to determine the jet penetration in the crossflow as shown in the Equation (4.1):

$$J \equiv \frac{\rho_j U_j^2}{\rho_c U_c^2} = \frac{\gamma_j P_j M_j^2}{\gamma_c P_c M_c^2} \tag{4.1}$$

where ρ, U, γ, P and M represent density, velocity, ratio of specific heats, pressure and Mach number respectively; the subscripts j and c represent *jet* and *crossflow* respectively. Further experimental studies[20, 120, 13] were carried out in a supersonic flow at various Mach numbers using the correlations provided by Schetz and Billig[141] to estimate the jet penetration. Cohen *et al.*[20], in 1971, devise an empirical correlation to determine the height of the jet penetration into the transverse flow as in Equation (4.2):

$$\frac{H_{mid}}{D} = \left[\frac{2\left(1+\frac{\gamma_j-1}{2}M_j^2\right)}{\gamma_j^2 M_j\left(\gamma_j+1\right)}\right]^{0.25} \times \left[\frac{1.25\left(1+\gamma_c\right)\gamma_c M_c^2}{\left(1-\gamma_c\right)+2\gamma_c M_c^2}\right]^{0.5} \times J \tag{4.2}$$

where H_{mid}/D represents the height (non-dimensionalised by the diameter of the jet hole) of the midpoint of the Mach disc. These two correlations have been utilized in this work to determine the corresponding values of jet-to-crossflow momentum flux ratio (J) and jet penetration.

Over the years, several more experimental studies[174, 171, 87, 67, 11, 160] have had been conducted which has resulted in a good understanding of jet injection into a supersonic crossflow (JISC) today. There have been several computational studies[19, 173, 9] carried out as well to determine various averaged flow features at various Mach

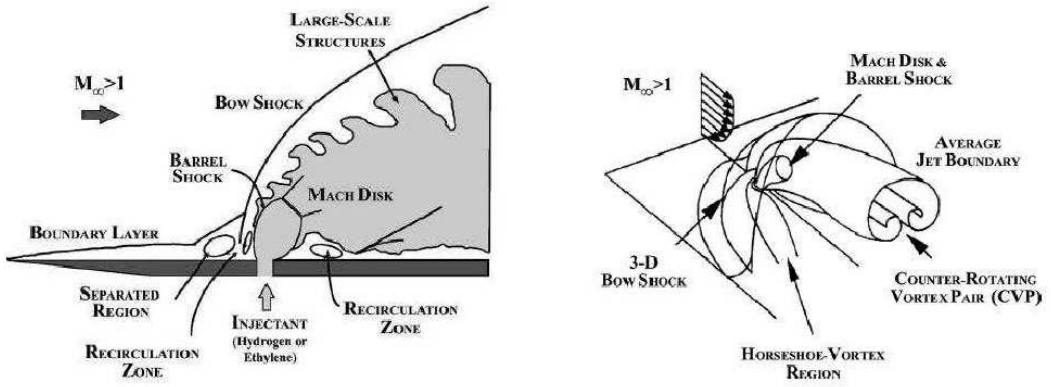

(a) *Two-dimensional instantaneous view* **(b)** *Three-dimensional averaged view*

Figure 4.1: *Schematic diagram of a sonic jet injection into a transverse stream of supersonic flow; (a) instantaneous view of middle plane to show various two-dimensional flow features, (b) three-dimensional schematic diagram to show major averaged flow features (image source: [11, 67]).*

numbers. As most of the computational studies were based upon RANS methodology which provides averaged flow properties, hence there is still opportunity to understand the instantaneous flow features and instabilities in JISC which cause the flow mixing. This is important as it can help improve the mixing efficiency of air and fuel inside the combustion chamber of a scramjet engine. Recently, Santiago and Dutton[139] carried out experiments on a sonic jet of air injected into a crossflow of air at Mach 1.6 and measured all three velocity components (*u, v, w*) and five Reynolds stresses using Laser Doppler Velocimeter (LDV). Further experiments using the same conditions were carried out to determine the pressure distributions on the flat-plate using Pressure-Sensitive-Paint (PSP)[50] and mixing of the jet with the supersonic freestream[161].

Figure 4.1 presents a well understood schematic diagram for a typical under-expanded sonic circular jet injected transversely into a supersonic freestream along with a three-dimensional schematic showing the structure of the shock waves generated when the jet interacts with the crossflow in Figure 4.1(b). As the under-expanded jet enters the crossflow, it expands through a Prandtl-Meyer expansion fan and at the same time deflects and turns along the main flow. Due to the difference in velocities, the jet acts as an obstruction to the main supersonic crossflow and generates a bow shock ahead of the injection hole. The incoming supersonic turbulent boundary layer (STBL) starts to separate just ahead of the bow shock and a small separation zone is created which results in a smaller weak shock, called a lambda shock, that interacts with the stronger bow shock. The lambda shock and the size of the separation zone are mainly dependent upon the momentum of the freestream flow[141]. The jet emerges from the orifice and expands to the atmospheric pressure at the jet boundary. This constant pressure on the jet boundary causes it to bend towards the axis of flow and the barrel shock emerges. Due to the high pressure ratio of the flow, the barrel shock does not meet at the axis of jet flow but instead a normal shock (Mach disc) is generated which has its centre at the axis of flow. Another small recirculation/separation zone is also created immediately downstream of the jet. There is a horseshoe vortex which wraps around the jet column and forms wake vortices in the flow. Further downstream the jet boundary takes the form of a pair of counter rotating vortices (CRVs) and some trailing counter-rotating vortices (TCRVs). All these separation zones, shocks and vortex structures give rise to a very complex flow downstream of the jet which is helpful for the mixing of the two fluids.

The experiments[139, 50, 161] were carried out the the Gad Dynamics Laboratory of the University of Illinois. The facility has two compressors arranged in parallel that provided a 115 m^3 tank farm with about 1 kg/s of air at 862 kPa. The supersonic wind tunnel used a Mach 1.6 nozzle and is 76 mm wide over the entire length. Flow conditioning is accomplished just upstream of the wind-tunnel nozzel by means of a short length of honeycomb and two screens. The streamwisw velocity component of the approaching freestream boundary layer was measured down to nearly y = 0.25 mm and the authors presented[139] a plot of the boundary layer velocity profile obtained five jet diameters upstream of the jet orifice. Further, the measurements were taken in several planes, and the accuracy of the measurement technique is considered very

good, the experiments provide an excellent opportunity for validation/verification of state-of-the-art CFD research codes employing time-evolving LES or direct numerical simulations (DNS) methodology. One important aspect of these experiments is the supersonic turbulent boundary layer (STBL) in the incoming freestream flow. Recently, Genin and Menon[59] presented an LES study to understand the dynamics of JISC using similar initial conditions as in experiment[139] and also further expanded the study to include various jet-to-crossflow momentum flux ratios and Mach numbers, but did not provide comparison of the upstream STBL. Kawai and Lele [88, 89] performed a comprehensive LES of the same JISC experiment[139] including the STBL in the freestream flow upstream of the jet plume and their results were found to be in a reasonable agreement with the experiment. They also elaborated that the freestream STBL is vital to capture the correct flow physics and mixing, as opposed to freestream laminar flow.

In order to numerically introduce the turbulent boundary layer in the flow field there have been several options used for various CFD applications which have been reviewed in the Section 3.5. First option would be to simulate laminar flow and allow it to develop turbulence over a long computational domain for a long period of time. But of course this method is not a reasonable one considering the computational costs involved. An alternative would be to utilize a rescaling-reintroduction method as presented in [89] as well. This could require a comparatively smaller computational domain but still require a long period of time for the STBL to grow to a required size and hence could be computationally expensive. Another alternative to this is synthetic turbulence data generation[95] based upon a digital filter and correlation functions that generate turbulent data for the inflow plane at every time step and can be a very efficient method as explained in the Section 3.5 which is utilized here to develop the STBL for the analysis of JISC.

4.2 Computational Domain and Initialization

The JISC experiments[139, 161, 50] were carried out on a flat-plate with a circular injection port that allowed the sonic jet of air to emerge into the supersonic freestream air flow (at Mach number 1.6). For CFD analysis the computational domain for this geometry comprises of a solid surface that represents the flat-plate with a circular hole as the injection port. Figure 4.2 is a schematic diagram of the computational domain selected for the ILES showing all the boundary conditions associated with the domain and Figure 4.3 shows the actual three-dimensional structured computational grid used for the simulations (for clarity, every third grid line is shown for the finest grid resolution). Although slight skewness can be seen in the grid very close to the jet injection port, but it was necessary to solve for the shear layer and the results achieved demonstrate that the flow is not compromised to any significant level. Note the turbulent inflow boundary condition which is based upon the digital filters based turbulent inflow data generator in order to generate the incoming turbulent boundary layer in the freestream

flow. This method should not be confused with supersonic inlet boundary condition as it can be used for supersonic or subsonic turbulence data generation without any modifications (as employed by another researcher at the Cranfield University for low mach studies on backward step/channel flow). The turbulence in the circular jet is ingorned (as also in the classical LES[89]) because not data is available. Furthermore, the fuel pipe is not modelled; instead only the exit from the fuel pipe into the main domain is modelled which introduce very little error into the results (of the order of 2-3% based upon personal communications with Dr Karl Sabastian from DLR, Germany).

Four grid levels (coarse, medium, fine and finest grids) are used in these simulations, details of which are presented in the Table 4.1. The grids are refined by an incremental factor of approximately $\sqrt{2}$ but also considering the parallel processing node distribution requirements and the clustering generally follow the parameters used for the classical LES simulations[89]. The Table also provides the details of the prescribed length scales used for the digital filter based technique. A plot for the composition of length scales of synthetic eddies in LES where average length scale is around 0.2 was presented by Graf and Kleiser[62] where they presented LES of a jet injection for a particular film-cooling configuration. Although in this work the length scales are not calculated but they are based upon intelligent estimate based upon a series of simulations conducted on a flat-plate (without transverse injection) with various length scales and at the same grid level prior to the final simulations. The prescribed length scales are critical for the evaluation of digital filter co-efficient[95, 169, 156] and are non-dimensionalised by the diameter (D) of the injection hole.

The Reynolds number used for the computations is based upon the freestream Mach number and the diameter (D) of the injection port such that:

Table 4.1: *Computational mesh used for the simulation of the STBL and JISC; using ILES and digital filters based turbulent inflow data generator. Also in the bottom part of the table the grid sizes for the computational domain used in LES[89] has been provided for comparison only.*

Grid	N_x [(a)]	N_y	N_z	Total (x10^6)	L_y	L_z	y^+
Coarse	274 (127+147)	85	85	2.0 (0.9 + 1.1)	0.5	0.2	14.0
Medium	404 (187+217)	101	115	4.7 (2.2 + 2.5)	0.5	0.2	14.0
Fine	522 (242+280)	116	151	9.2 (4.3 + 4.9)	0.5	0.2	14.0
Finest	522 (242+280)	200	151	15.8(7.3 + 8.5)	0.5	0.2	4.0
Coarse	552 (251 + 301)	131	87+115	7.4 (2.9 + 4.5)	–	–	14.5
Medium	772 (361 + 411)	187	101+154	18.6 (6.8 + 11.8)	–	–	20.5
Fine	912 (361 + 551)	243	120+204	37.8 (10.5 + 27.3)	–	–	29.0

(a) Numbers in the parentheses refer to STBL domains and JISC domains, respectively.

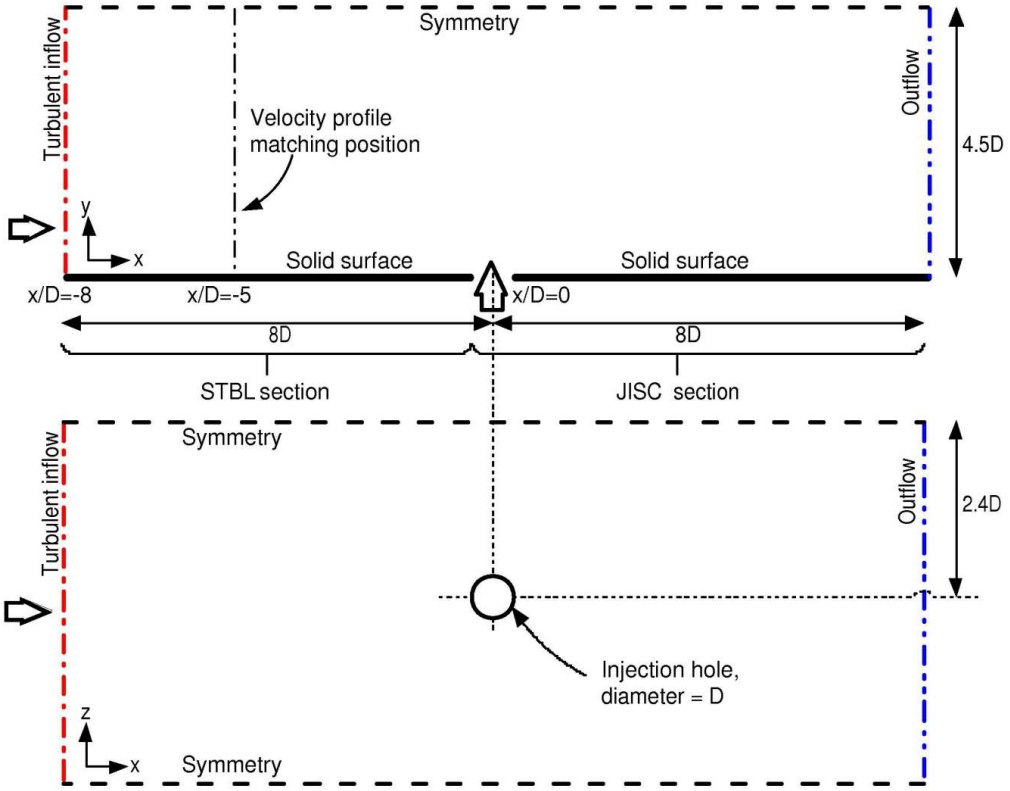

Figure 4.2: *Schematic diagram of the computation domain selected for the JISC simulations; Red line is turbulent inflow; Thick solid black line is solid surface; Blue line is out-flow; Dashed black line is symmetry; Dash-dot-dash black line is X/D=-5 position where velocity profile is matched between experiment and CFD; Green circle is inlet for jet injection.*

$$Re_D = \frac{\rho_\infty U_\infty D}{\mu_\infty} = 2.4 \times 10^4 \tag{4.3}$$

which is six times smaller compared to the experiment. This is to allow for a reasonable resolution of the computational domain for ILES and also to match the initial conditions used for the classical LES by Kawai and Lele [88, 89]. The initial conditions prescribed for the simulations are the same as the stagnation conditions used for the experiment which are tabulated in Table 4.2. Although the Reynolds number Re_D used is smaller, the thickness of the turbulent boundary layer ($\delta_{99}/D = 0.775(3.1mm)$) has been matched to the experimental data at the X/D = -5 position. The momentum flux ratio (J) is calculated to be 1.7, which also matches the experimental data. It can be noted that the inlet pressure is assumed to be constant at the inlet of the computational domain as there is no fluctuation data available for the pressure. In reality it would not be the case as they would be coupled to the acoustic waves and the convection velocity.

In order to obtain the fluctuations for the density and velocity the digital filter based method is used as presented in the Section 3.5.1. For the first timestep the sets of

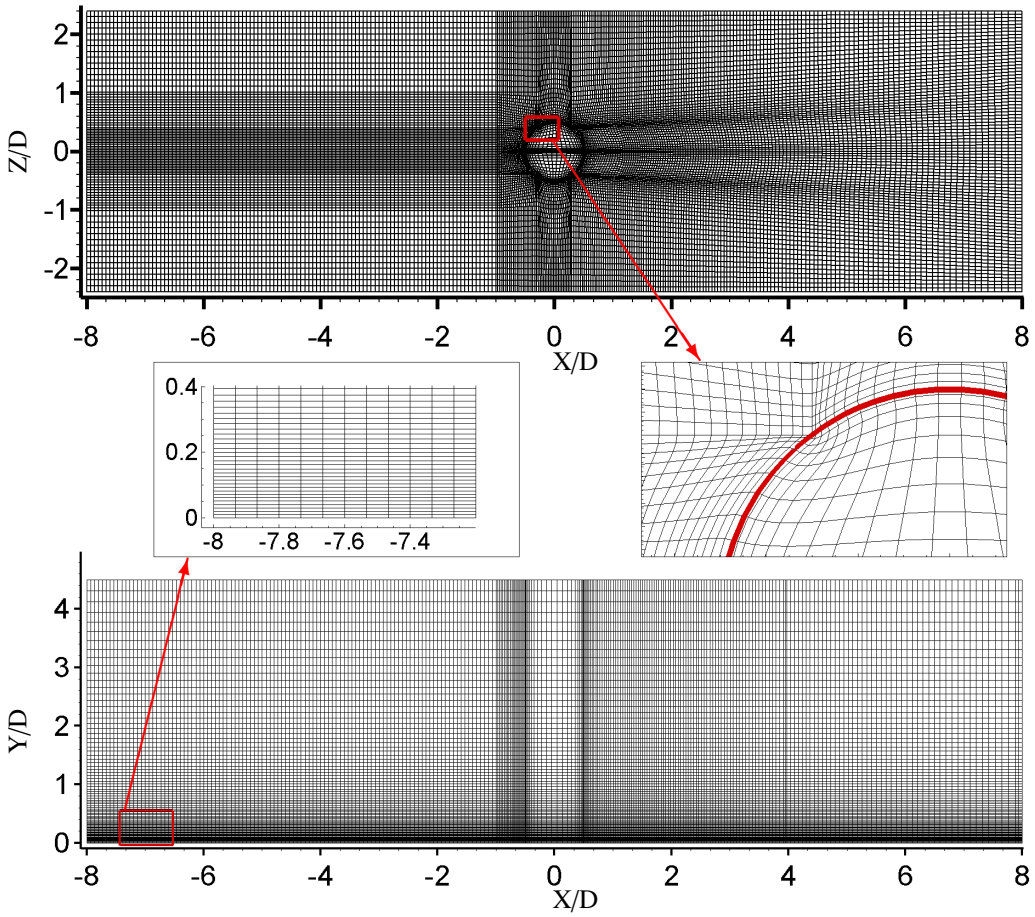

Figure 4.3: *Computational grid along with the dimensions used for the analysis with every third grid line shown for clarity.*

Table 4.2: *Averaged stagnation inflow conditions from experiment. The subscripts c and j refer to crossflow and jet properties respectively.*

Property	Value	Units	Property	Value	Units
Mach Number(c)	1.6		Mach Number(j)	1.0	
Stag. Pressure(c)	241	kPa	Stag. Pressure(j)	476	kPa
Stag. Temperature(c)	295	K	Stag. Temperature(j)	295	K
Average Velocity(c)	446.1	m/s	Reynolds Number	2.4E+04	

random numbers are filtered and Exponentially correlated to incorporate the length scales of the problem and the velocity field is obtained from Equation (3.64). For the all the next timesteps, the velocity field is temporally correlated to the previously obtained velocity field using the Equation (3.70). At each timestep the fluctuations are obtained by using the velocity field and the Reynolds stress tensor according to Lund

et al.[109]:

$$\begin{bmatrix} u' \\ v' \\ w' \end{bmatrix} = \begin{bmatrix} \sqrt{R_{11}} & 0 & 0 \\ R_{21}/\sqrt{R_{11}} & \sqrt{R_{22} - \left(R_{21}/\sqrt{R_{11}}\right)^2} & 0 \\ 0 & 0 & 0 \end{bmatrix} \begin{bmatrix} \psi^u(y,z) \\ \psi^v(y,z) \\ \psi^w(y,z) \end{bmatrix} \tag{4.4}$$

where $()'$ are the fluctuations from digital filter process, ψ is the velocity field at each timestep and the Reynolds stresses are obtained from the experimental data[139]. According to experiment, the inflow is highly two-dimensional, therefore above equation gives $w' = 0$, and the density fluctuations are as follows:

$$\rho' = \rho(0,y,z) \cdot \frac{\sqrt{R_{11}}}{U_\infty} \cdot \psi^u(y,z) \tag{4.5}$$

The flow field is initialized using the Equation (4.6) as below:

$$\begin{aligned} \rho_{(x=0)} &= \rho_0 + \rho' \quad , \\ u_{(x=0)} &= u_0 + u' \quad , \\ v_{(x=0)} &= v_0 + v' \quad , \\ w_{(x=0)} &= 0 \quad , \\ E_{(x=0)} &= \frac{p}{\gamma - 1} + \frac{\rho}{2}\left[u^2 + v^2 + w^2\right] \quad , \end{aligned} \tag{4.6}$$

where ρ is the density, *u, v, w and E* are the three velocity components and total internal energy respectively, The subscript $x = 0$ represents the start of the grid and $()_0$ represents the averaged profiles for the density, stream-wise and wall-normal velocity at X/D = -5 position from the experiment[139] where $v_0 \ll u_0$ and $v_0 \approx 0$. The $(\_)'$ represents the fluctuations from digital filter based inflow data generator at any time-step. For the next time-step, a new two-dimensional data slice is generated and is correlated to the previous data slice as explained in the Section 3.5. The velocity profiles from the experiment, obtained at X/D = -5 for a fully developed STBL along with fluctuations, are applied at the X/D = -8 position in the computational domain as shown in Figure 4.2. The long upstream domain is to allow for the numerical expansion fan developed at the start of the computational domain which was unavoidable and thus the STBL is generated in the computational domain that replicates the STBL in the experiments[139] for all four grid levels.

Figure 4.4 presents the non-dimensionalised pressure measurements at a selected point (X/D, Y/D = -0.75, 0.5) within the computational domain at the wall-normal mid plane (Z/D = 0) for all four grid levels. Results are shown for a non-dimensional time ($\tau = tU_\infty/D$, where t is the computational time), of nearly 150. As the unsteady

ILES simulations never achieve full convergence, but a reasonable convergence level is achieved for all four grid levels as shown in the Figure 4.4. The flow is allowed nearly 9 cycles over the full flow field and the time-averaged results are obtained by averaging nearly 2000 equi-timesteped solutions obtained after the first complete flow cycle. The flow is assumed to be statistically stationery within these time windows. It has been noticed that the number of solution files used to obtain the time-averaged solution can impact the accuracy of the results. Ideally the time-averaging should be computed using solutions at all the timesteps in the computations. In this particular case, however, major restriction was imposed by the size of the solution files at each timestep and the accumulative size of all the solution files obtained over the course of computations which prohibited the time-averaging using all the solution files. However the quality of the results obtained using the 2000 equi-timesteped solutions obtained is excellent as demonstrated by the quantitative analysis provided in this chapter. It can be concluded that increasing the number of files for time-averaging can even improve the quality of the results. Table 4.3 presents the non-dimensional time and computational time the simulations were conducted for each grid resolution.

4.3 Supersonic Turbulent Boundary Layer (STBL)

Methods for examining the spatial and temporal convergence of CFD simulations are presented bt Roache [136, 135, 134]. Roache suggested a grid convergence index (GCI) to provide a consistent manner in reporting the results of grid convergence stud-

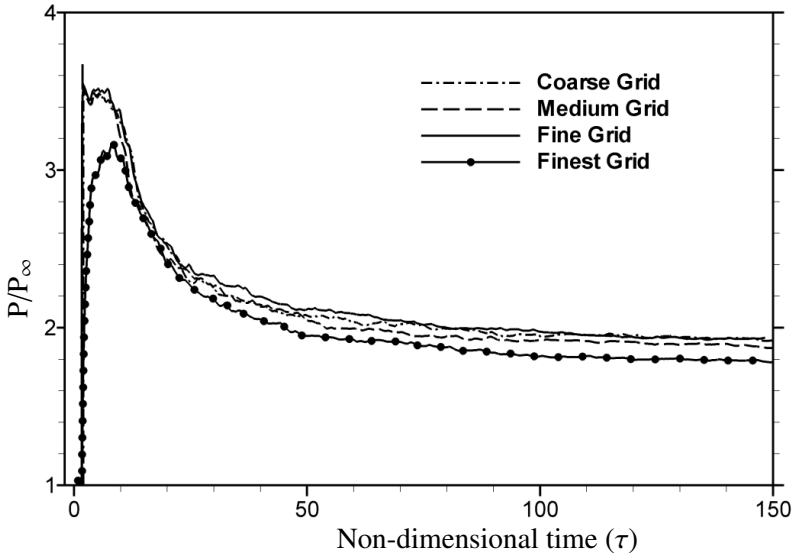

Figure 4.4: *Convergence plots for the five cases analyzed in this chapter showing same levels of convergence achieved for all four grids over a period of approximately 150 non-dimensional time (τ).*

Table 4.3: *Simulation times for all four grid levels.*

Grid	Total Sim Time(τ)[(a)]	Computational time[(b)]
Coarse grid	157.28	448.88
Medium grid	156.96	1027.78
Fine grid	148.31	1861.17
Finest grid	186.05	10486.67

(a) Non-dimensional time for simulations.
(b) CPU Time in hours; Simulation performed on Astral Supercomputer at Cranfield University, U.K.

ies and perhaps provide an error band on the grid convergence of the solution. The GCI can be computed using two levels of grid; however, three levels are recommended in order to accurately estimate the order of convergence and to check that the solutions are within the asymptotic range of convergence. Although this method has not been utilised in the current work and thus it can be argued that the results presented in the Figures 4.4 and 4.5 do not neccessarily demonstrate grid convergence but they provide a comparison of physical properties of the flow and a reasonable estimate of grid convergence. Figure 4.5(a) presents the non-dimensional velocity versus the wall-distance on log-scale for all four grid levels. Comparing it with the Figure 2.8 in Chapter 2, it can be observed that for coarse and medium grids the fully turbulent log-layer region is not captured which could be due to low grid resolution in this area whereas for fine and finest grids the log-layer region is well captured. This is also demonstrated by plotting the u^+ according to the Equation (2.11) which indicates a smooth transition between

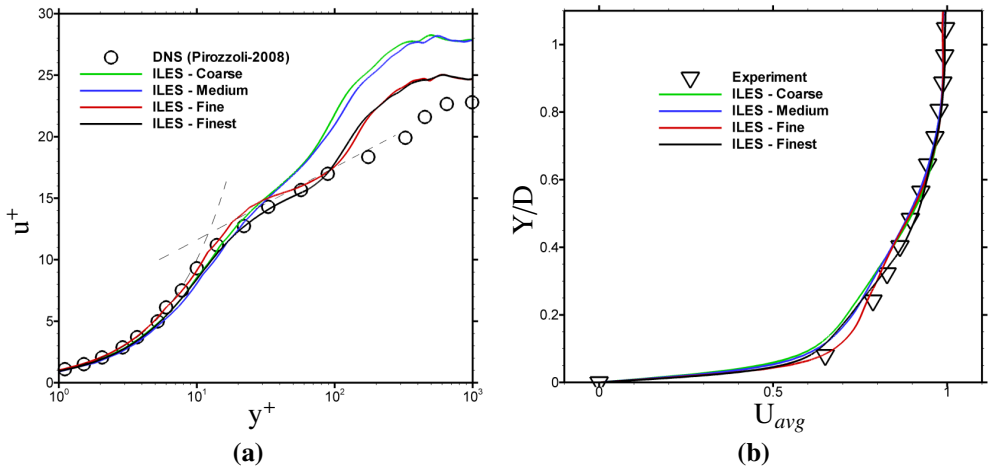

Figure 4.5: *Grid sensitivity and STBL analysis; (a) mean stream-wise velocity in semi-logarithmic scale [125], (b) averaged velocity profile compared with the experimental results[139] at three grid resolutions.*

the inner region and the outer region and the ILES data for the fine and finest grids shows a reasonable match with the DNS data[125, 123]. As the y^+ is set to around 14 which lies above the viscous sublayer region, the data is extrapolated for this region for all the grid level and is still a good match with the DNS data. The ($u^+ = y^+$) curve intersects the ($u^+ = \frac{1}{\kappa} \ln y^+ + B$) line at a point indicating the location of the buffer-zone in the STBL.

In order to validate the velocity profile of the STBL generated through the digital filters technique and bring confidence to the initial conditions applied, the velocity profile from the simulations is compared with that from the experiment at X/D = -5 location as shown in Figure 4.5(b). Although slight discrepancy is found nearer the wall but generally a good match has been obtained between the simulations and the experimental data. Figure 4.6 presents u_{rms}, v_{rms} *and* w_{rms} in comparison with the DNS data[144] where, although, coarse and medium grids are slightly under resolved but the fine and finest grids are showing a reasonable match with DNS data. It can be established from the Figure 4.6 that the plots shown are tending towards self-similarity as the Reynolds stresses exhibit approximate self-similarity in the log-law region (i.e.

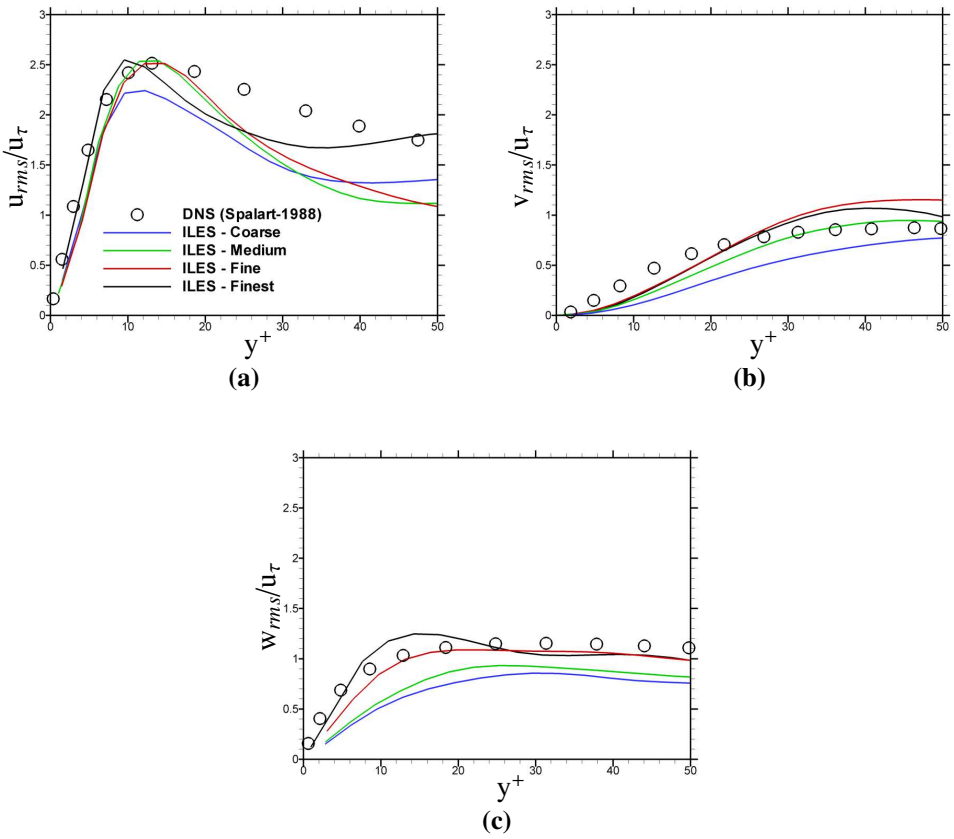

Figure 4.6: *Grid sensitivity and STBL analysis; (a) RMS of stream-wise velocity component, (b) RMS of wall-normal velocity component, (c) RMS of wall-parallel velocity component [144].*

above $y^+ \sim 50$), whereas, the viscous wall region (i.e., below $y^+ \sim 50$) demonstrate very robust turbulent region. Instantaneous overview of the STBL and JISC simulation is shown in Figure 4.7, where the velocity is on the horizontal plane and density gradient on the vertical middle plane.

4.4 Time Averaged Flow

4.4.1 Jet Penetration

Figure 4.8 represents the JISC flow structure generated when a transverse sonic jet of fluid emerges into a stream of Mach 1.6 turbulent flow. Figure 4.8(a) shows all the major flow features (bow, barrel and lambda shocks Mach disc and recirculation zones) captured using ILES as they are generally understood (finest grid results shown) on the mid plane (Z/D = 0). For the given initial conditions from the experiment[139], it is understood that there should be three recirculation zones in the flow which are successfully captured as "R1", "R2" and "R3". As the jet emerges into the freestream flow, it expands and turns along the main flow at the same time as shown by the Prandtl-Meyer expansion fan (PMEF) in Figure 4.8(a). It is clear that maximum Mach number is inside and towards the top end of the jet plume just before the Mach disc.

The boundary of the jet that forms the barrel shock and the Mach disc meets at a point referred to as the triple point, where reflected shocks are also visible. There are also present in the flow structure a horseshoe vortex, a pair of CRVs and a pair of TCRVs

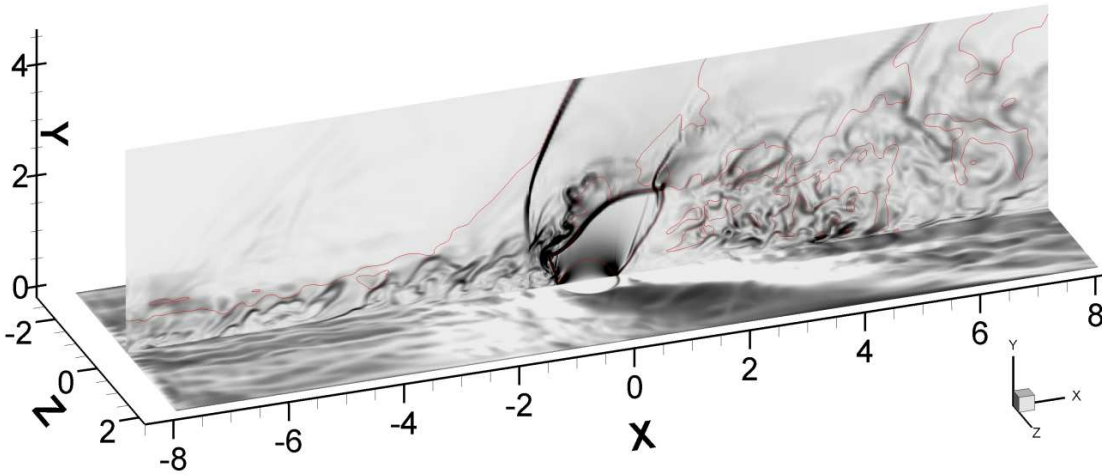

Figure 4.7: *Instantaneous snapshot of incoming STBL using digital filters based turbulent inflow data generator and the injection of a sonic jet creating a complex flow structures upstream and downstream the jet plume; density gradient contours (vertical plane) and velocity contours (horizontal plane).; Red line indicates the Mach 1.5 position to demonstrate the location of lambda shock just upstream of the jet plume.*

(Trailing CRVs) which will be discussed later (Figure 4.8(b)). Using Equations (4.1) and (4.2) the height of the midpoint of Mach disc non-dimensionalised by the diameter of the jet hole (i.e. jet penetration) has been measured to be ≈ 1.4D (as shown in Figure 4.8(a) by H/D). Abramovich[2] presented a correlation as shown in Equation (4.7) based upon the trajectory of maximum injectant concentration.

$$Y/D = \left(P_j/P_c\right)^{0.434} (X/D)^{0.333} \tag{4.7}$$

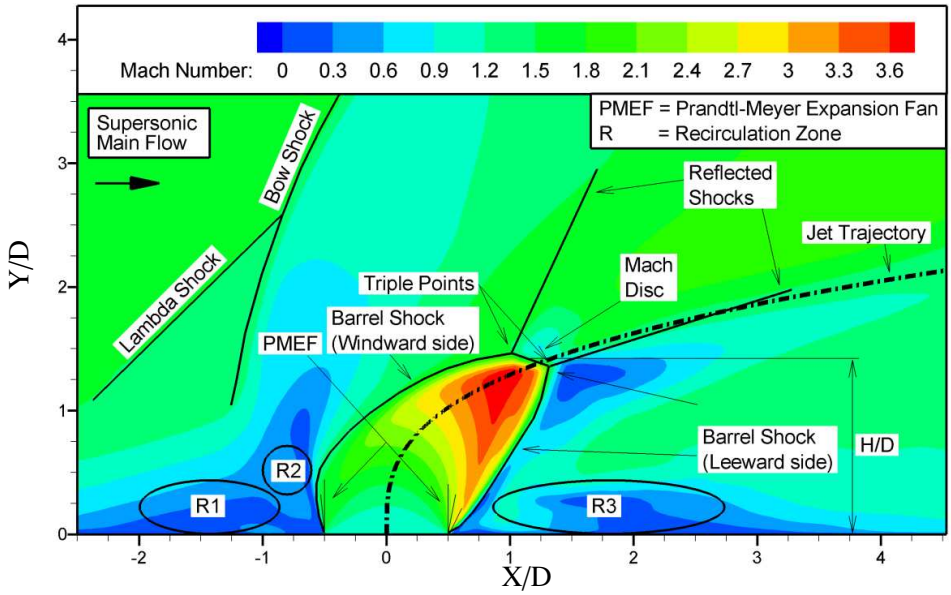

(a)

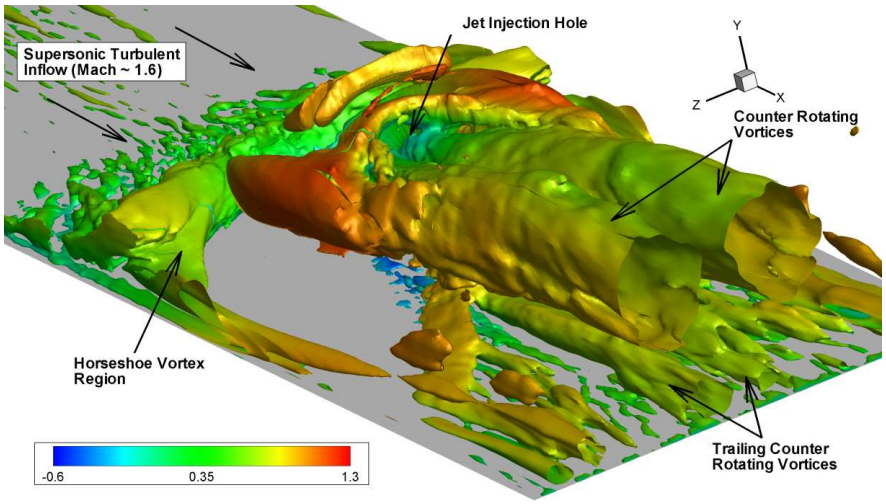

(b)

Figure 4.8: *Typical shocks and flow features are identified as the sonic jet mixes with transverse supersonic flow at Mach 1.6; (a) two-dimensional flow structure at the wall-normal mid plane (Z/D=0), (b) three-dimensional flow features using iso-surfaces for the Q-criterion.*

where, P represents the dynamic pressure. This has been used by Orth and Funk[120] in their experiments to study the jet penetration in supersonic flow where they demonstrated that the Equation (4.7) agrees *"reasonably well with the experimental values"* for X/D $\leq$ 8. This correlation has been plotted in Figure 4.8(a) for the jet trajectory of maximum jet concentration. It can be noticed that the trajectory path follows the jet plume deflection reasonably well and passes through the Mach disc; however, there is a slight discrepancy in determining the midpoint of the Mach disc using the correlation in Equation (4.7). This small discrepancy was also observed in the experiment[120].

4.4.2 Contour Plots

Time averaged analysis has been presented for flow visualization of various properties for the finest grid level in Figures 4.9-4.12 showing the contours of Mach number, passive scalar (jet fluid), turbulent kinetic energy (TKE) and Reynolds shear-stress (RS) at various locations in the domain along with stream lines. These stream lines clearly show three recirculation zones in Figure 4.9(a). It can be noted from Figure 4.9(a) that most of the jet fluid is passing through the windward side of the jet plume and the Mach disc and then diverts towards the direction of freestream flow where mixing occurs. This contour plot also reveals that the lambda shock is a weak shock as

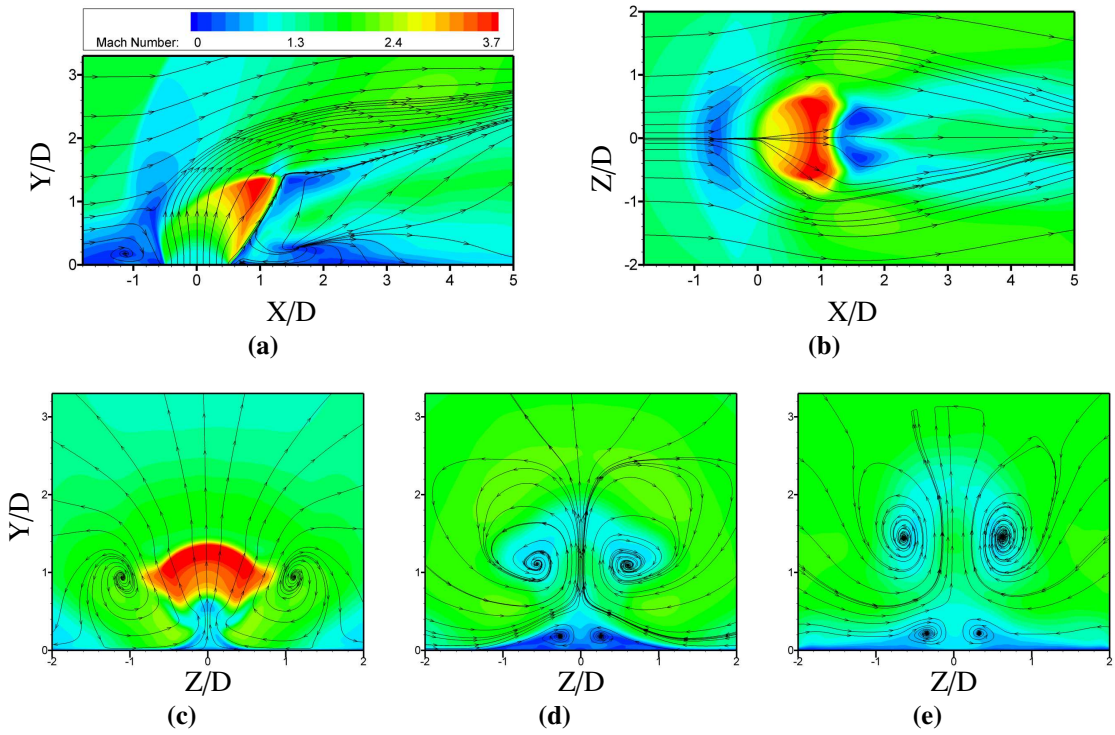

Figure 4.9: *Time averaged contours of Mach number at various locations in the flow field; (a) wall-normal mid plane (Z/D = 0), (b) wall-parallel plane (Y/D = 1), (c)-(e) wall-normal cross-view planes (X/D = 1, 3 and 5 respectively).*

represented by small change in contour colours. Figure 4.9(b) shows the streamlines for the flow when it is obstructed by the jet plume on the wall-parallel plane (Y/D = 1). At this point, due to low pressure, a recirculation zone is created which runs around the jet plume and just above the flat-plate to create a horseshoe vortex as shown in Figure 4.8(b).

Figures 4.9(c-e) presents the streamlines of the flow downstream the jet plume. At location X/D = 1 a pair of CRVs appear due to the interaction of the freestream flow with the jet fluid. This pair of CRVs then grow in size further downstream (X/D = 3 and 5) and provide a major area where mixing of the two fluids occurs. As this pair of CRVs start to grow in size (as in Figure 4.9(d)) another pair of small TCRVs is created. This small pair is due to the low pressure recirculation zone ("R3" as in Figure 4.8(a)) and the suction action of the major pair of CRVs. Close analysis of the Figure 4.9(e) reveals that the TCRVs rotates in the opposite direction to the major CRVs which further enhances the mixing in the region below the major CRVs. Viti *et al.*[164] mentioned another small pair of TCRVs just on top of the major CRVs for a Mach 4 JISC but for Mach 1.6 JISC this has not been observed in the experiment[139], the classical LES[89] or current investigations. Therefore, it can be deduced from this that the major CRVs are common feature of JISC but the TCRVs are dependent upon the freestream Mach number.

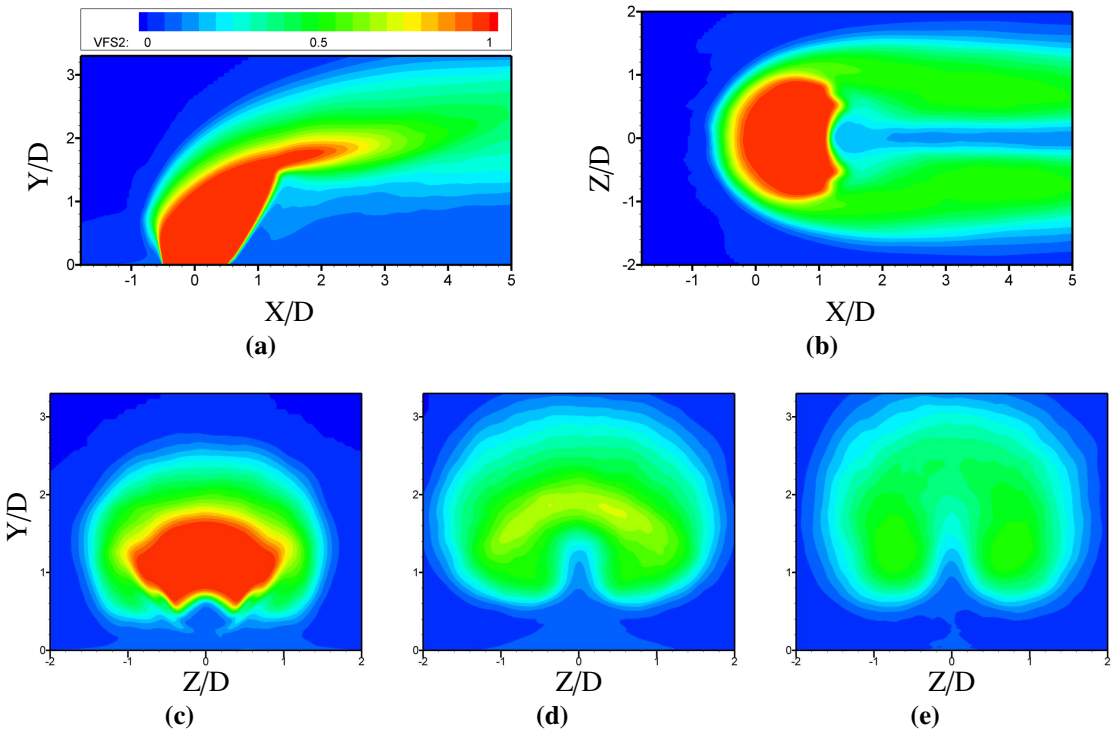

Figure 4.10: *Time averaged contours of jet passive scalar at various locations in the flow field; (a) wall-normal mid plane (Z/D = 0), (b) wall-parallel plane (Y/D = 1), (c)-(e) wall-normal cross-view planes (X/D = 1, 3 and 5 respectively).*

Figure 4.10 shows the contour map for the passive scalar (jet fluid). It is observed from the contours in the Figure 4.10(a) and (c) that after injection the jet fluid quickly mixes with the freestream fluid (X/D = 1) and then gradually dilutes further downstream (X/D = 3 and 5) in the Figures 4.10(d) and (e). The important factor to note here is that the mixing starts immediately after the jet injection and most of it occurs in the thicker shear layer on the windward side of jet plume as shown in Figure 4.10(c) which is also shown by the stream-lines in Figure 4.9(a). Downstream from the jet injection the mixing region increases its size as the CRVs increase in size spanwise and wall-normal directions (Figures 4.10(d) and 4.10(e)).

Turbulent kinetic energy (TKE) non-dimensionalised by the freestream velocity is calculated as:

$$TKE = \left(\langle u'u' \rangle + \langle v'v' \rangle + \langle w'w' \rangle\right) / 2U_{\infty}^{2} \tag{4.8}$$

and is presented in Figure 4.11 at various planes in the computational domain. There are three regions of high TKE just upstream and downstream of the jet plume, also identified in previous LES[89] results and shown in Figure 4.11(a). The high TKE region just upstream of the jet plume is the region of shock/boundary layer interaction.

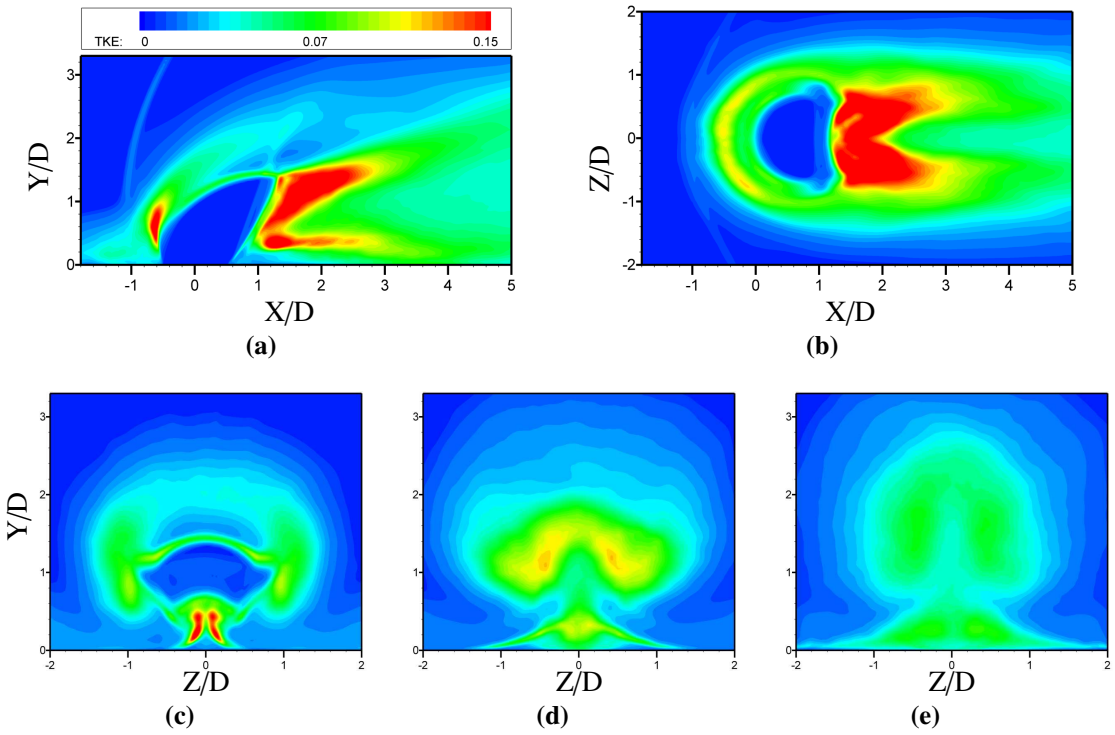

Figure 4.11: *Time averaged contours of turbulent kinetic energy (TKE) at various locations in the flow field; (a) wall-normal mid plane (Z/D = 0), (b) wall-parallel plane (Y/D = 1), (c)-(e) wall-normal cross-view planes (X/D = 1, 3 and 5 respectively).*

Also the barrel shock region displays high TKE due to the presence of shear layer between the inner region of jet plume and the cross flow. The third high TKE region just downstream of the jet plume is around the third recirculation zone ("R3" as shown in Figure 4.8(a)). This is the region where the CRVs are originating, the low-pressure recirculation zone just below the CRVs is generated and the CRVs create a very active mixing zone. Further downstream of the jet plume the TKE dissipates gradually as shown in the Figures 4.11(c)-4.11(e).

Figure 4.12 represents the dimensionless Reynolds shear-stress non-dimensionalised by the freestream velocity (RS = $(\langle u'v' \rangle)/(U_\infty^2)$) in various planes. There are two high RS zones identified just upstream of the jet plume shown as points "A" and "B" in Figure 4.12(a). These two locations show high RS in opposite directions (i.e., +ve and -ve) which is also identified in the experiment[139]. As shown earlier, this is the region of shock/boundary-layer interaction and high TKE is also observed in this section produced by Reynolds shear-stresses; both of these high values are due to the fact that this region presents high mean velocity gradients. Figures 4.12(c)-4.12(e) show the RS in the cross-view planes (X/D = 1, 3 and 5) which represent the diffusion of TKE and RS further downstream. In fact it is clear from the RS contours that further downstream majority of the flow consists of only -ve RS.

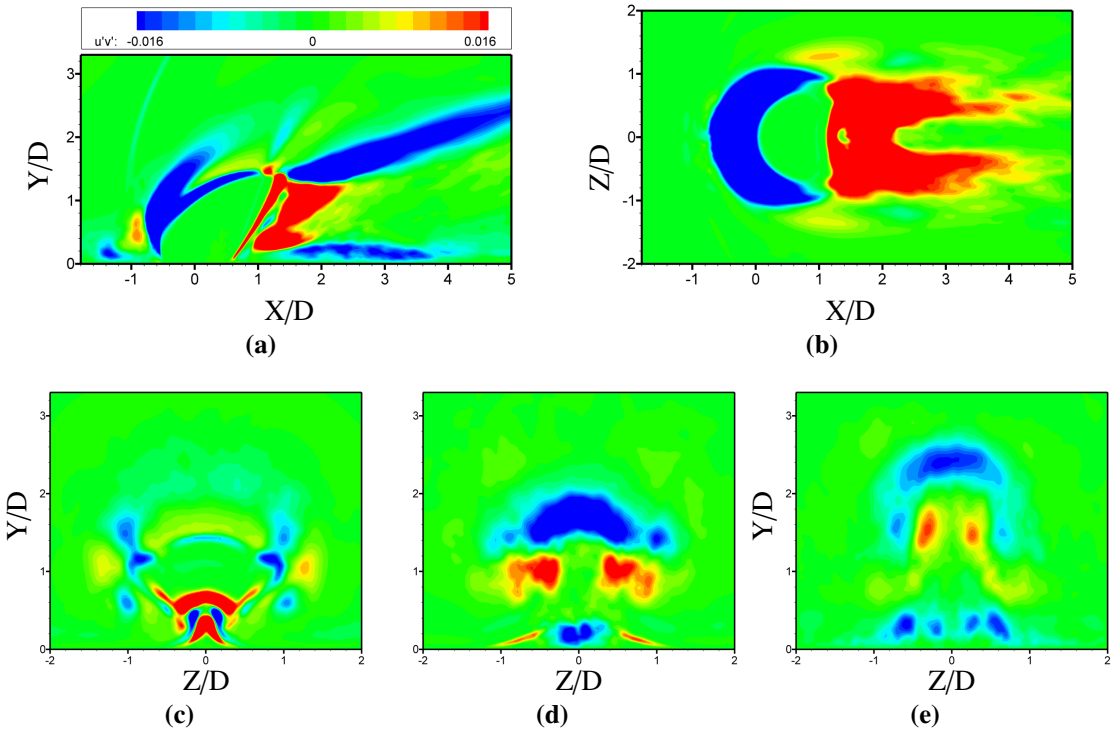

Figure 4.12: *Time averaged contours of Reynolds shear-stress (RS) at various locations in the flow field; (a) wall-normal mid plane (Z/D = 0), (b) wall-parallel plane (Y/D = 1), (c)-(e) wall-normal cross-view planes (X/D = 1, 3 and 5 respectively).*

4.4.3 Velocity Profiles

Further analysis is carried out to compare the plots of the mean stream-wise and wall-normal velocities in the flow field with the experiment and the classical LES results using the three grid resolutions explained earlier. Figures 4.13 and 4.14 show comparison of the mean stream-wise and wall-normal velocities (non-dimensionalised by the mean freestream velocity) at one upstream location (X/D = -1.5) and further four downstream locations (X/D = 2, 3, 4 and 5) at the wall-normal mid plane (Z/D = 0). It must be mentioned here that the "fine grid" results presented in the current work are obtained with one-third of the "fine grid" points in the classical LES[89] using $1/45^{th}$ of computational resources.

It has been shown[89] that the upstream velocity profiles (at location X/D = -1.5) are

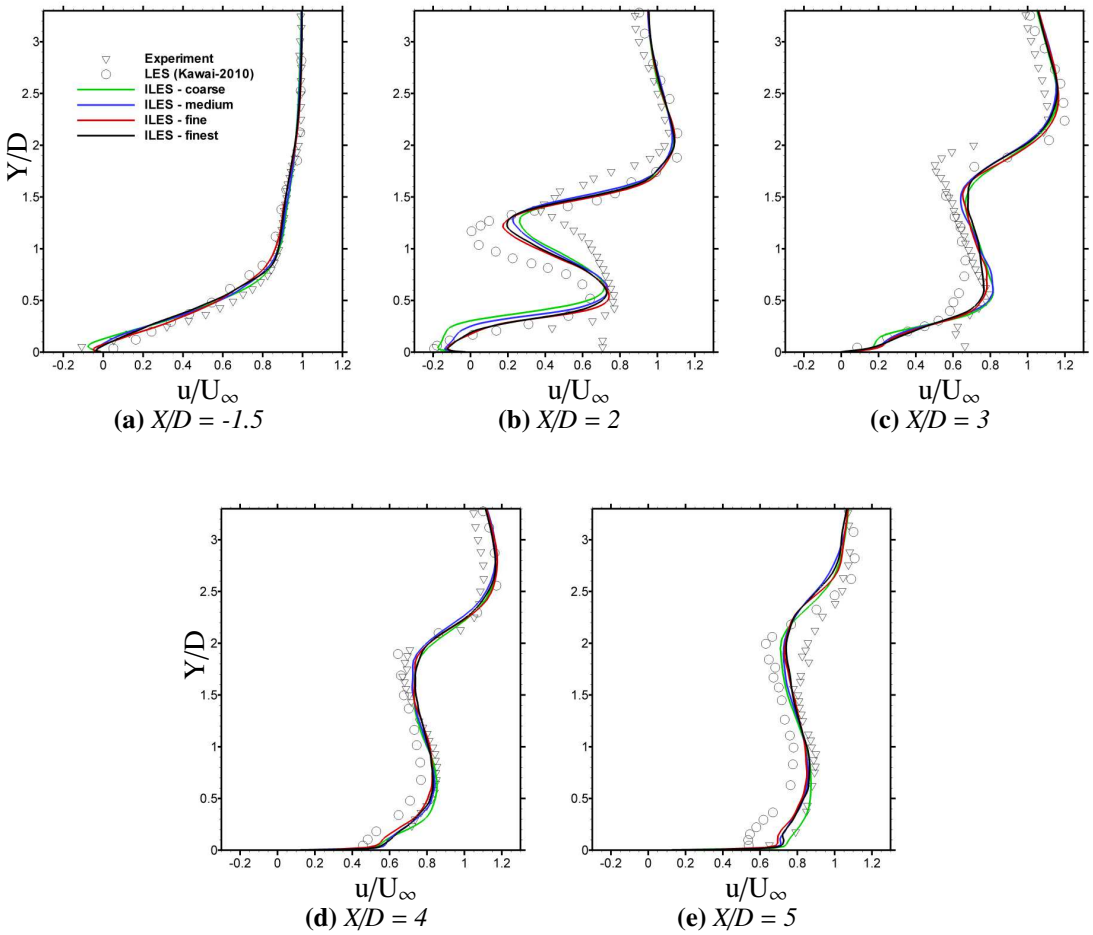

(a) *X/D = -1.5* **(b)** *X/D = 2* **(c)** *X/D = 3*

(d) *X/D = 4* **(e)** *X/D = 5*

Figure 4.13: *Mean stream-wise velocity profiles are compared with the experimental and previous LES results on all grid levels. X/D = -1.5 position is just upstream of the jet plume which is important for comparing the effect of upstream STBL. The downstream position compared are at X/D = 2, 3, 4 and 5 on the mid plane (Z/D=0).*

influenced by the incoming STBL. The STBL affects the growth of the separation zone ("R1" in Figure 4.8(a)) i.e., restricts its growth and the lambda shock is developed. On the other hand, with laminar incoming flow this separation zone grows too large and thus no lambda shock is visible which is an unphysical behaviour[89]. This highlights the importance of simulating this flow with the STBL. Using digital filter based turbulent inflow data the required thickness (as in experiment[139]) of STBL is generated; a good match has been found for the velocity profiles at X/D = -1.5 position for both the stream-wise and wall-normal velocities. It is noted that with increased resolution (fine grid) the results are getting even better and are tending towards the LES results (Figure 4.14(a)).

Downstream velocity profiles are shown in the Figures 4.13-4.14(*b, c, d and e*) and compared with the experiment and the LES results. The stream-wise velocity profiles

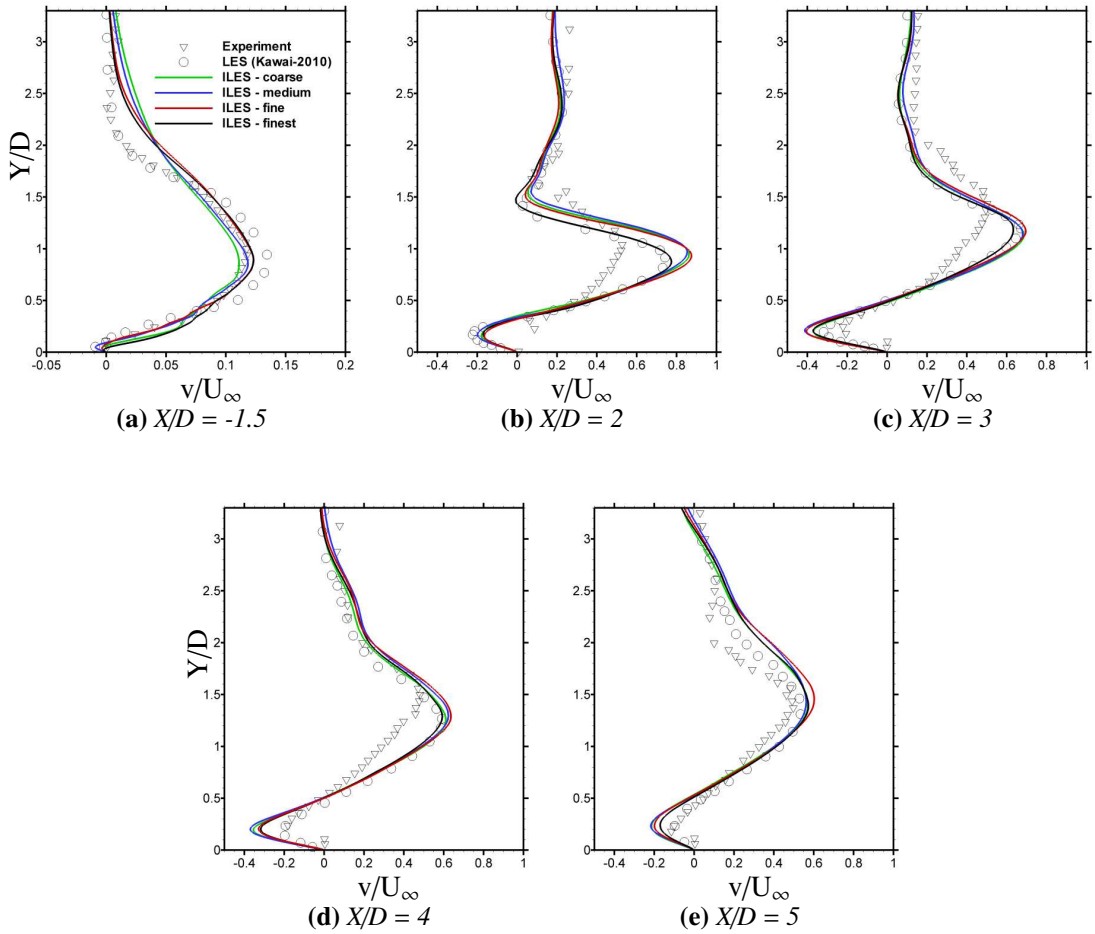

(a) *X/D = -1.5* **(b)** *X/D = 2* **(c)** *X/D = 3*

(d) *X/D = 4* **(e)** *X/D = 5*

Figure 4.14: *Mean wall-normal velocity profiles are compared with the experimental and previous LES results on all grid levels. X/D = -1.5 position is just upstream of the jet plume which is important for comparing the effect of upstream STBL. The downstream position compared are at X/D = 2, 3, 4 and 5 on the mid plane (Z/D=0).*

are slightly under-predicted compared to the experiment at the X/D = 2 position but better agreement with experiment has been found compared to classical LES. Moving further downstream the jet plume, the ILES results tend towards the experimental data, whereas, the classical LES is slightly offset from the experiment. In Figure 4.13(e), however, the profile above the Y/D = 1.5 position is close to the classical LES but below this position they are matching with the experiment again. The wall-normal velocity profiles in the downstream direction are all following the trends presented in classical LES which are slightly over-predicted from the experiment (Figure 4.14(b)-4.14(d)), however, at location X/D = 5 (in Figure 4.14(e)) all the three methods show same profiles. Although like experimental uncertainties, the CFD results can also be influenced by the computational errors but high resolution scheme can reduce the computational errors considerably. The best way ahead would be to analyze the experiment

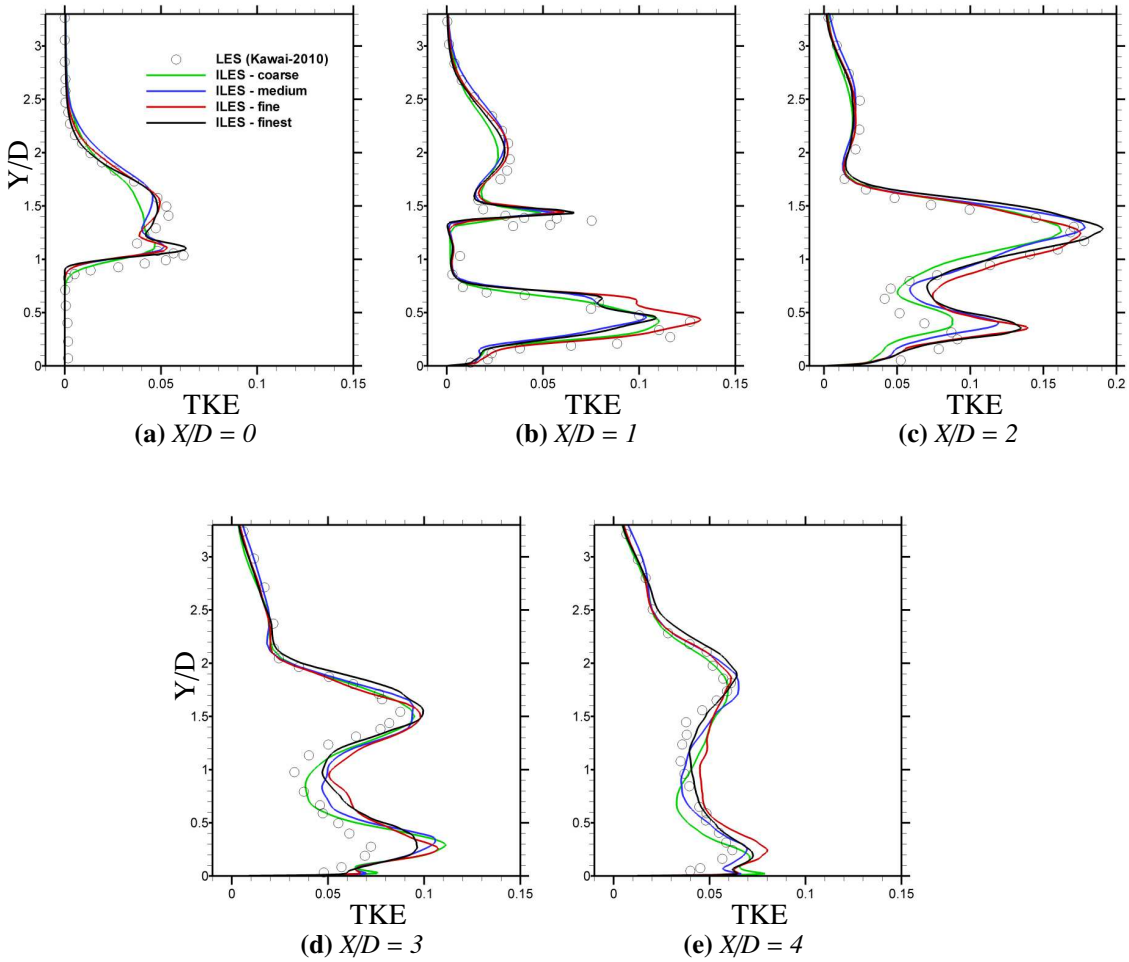

(a) *X/D = 0* **(b)** *X/D = 1* **(c)** *X/D = 2*

(d) *X/D = 3* **(e)** *X/D = 4*

Figure 4.15: *Turbulent kinetic energy (TKE) profiles are compared with the previous LES results on all grid levels at locations X/D = 0, 1, 2, 3 and 4 on the mid plane (Z/D=0).*

and CFD together in order to get better understanding of the problem under investigation for which the results shown in Figure 4.13 and 4.14 are excellent examples.

4.4.4 Turbulent Kinetic Energy and Reynolds Stresses

A qualitative analysis has been presented above for the turbulent kinetic energy and Reynolds shear-stress. Figures 4.15 and 4.16 present a quantitative perspective into the analysis of turbulent kinetic energy and Reynolds shear-stress in the JISC flow field. A comparison of these two has been presented with the previous classical LES[89] results showing concord between the two methods. Figures 4.11 and 4.12 show very high TKE and RS zones on the leeward side of the jet plume. The TKE and RS plots in Figure 4.15 4.16 show that the maximum TKE and RS are present in the region between X/D = 1 and X/D = 3. Also it can be noticed that the majority of the TKE and RS are present

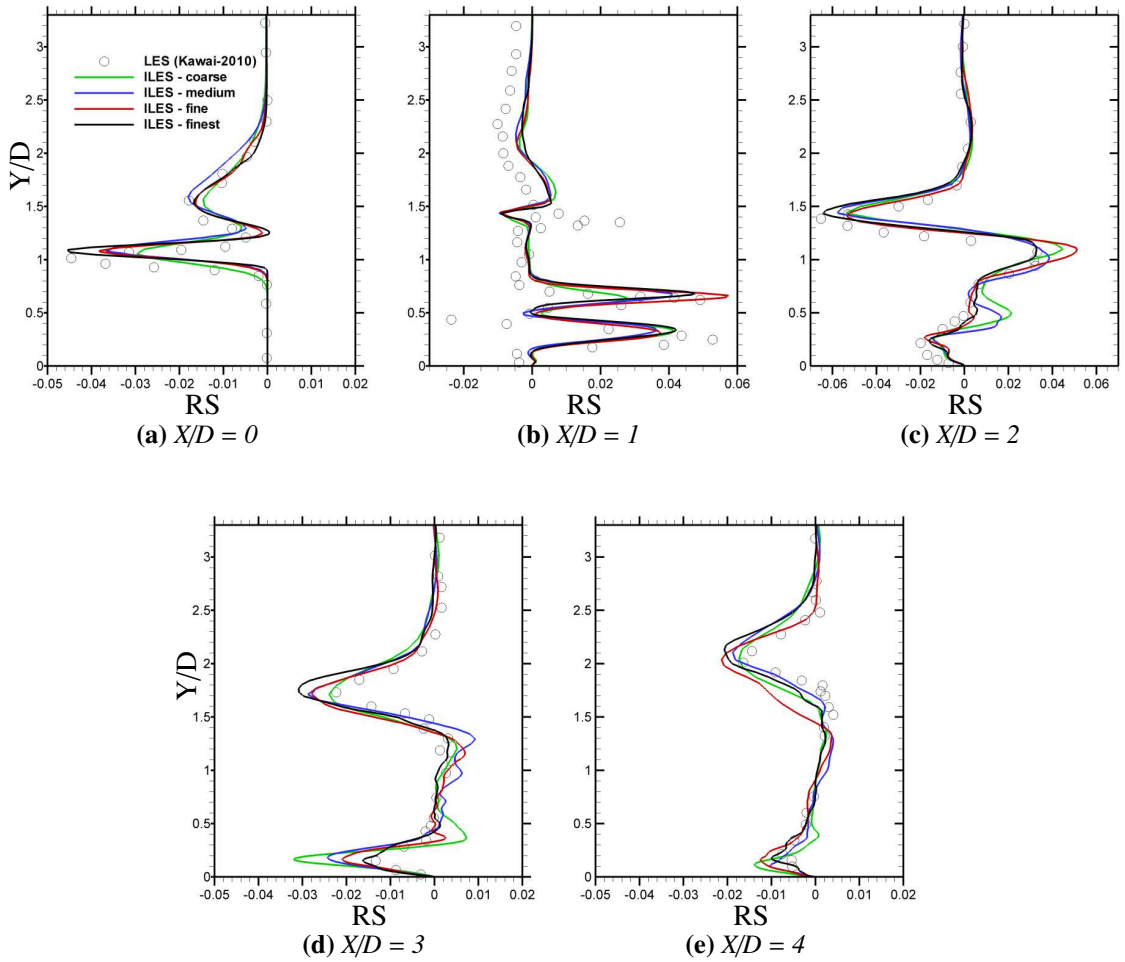

(a) *X/D = 0* **(b)** *X/D = 1* **(c)** *X/D = 2*

(d) *X/D = 3* **(e)** *X/D = 4*

Figure 4.16: *Reynolds shear-stress (RS) profiles are compared with the previous LES results on all grid levels at locations X/D = 0, 1, 2, 3 and 4 on the mid plane (Z/D=0).*

below Y/D = 1.5 which is the region of most of the spanwise activity on the CRVS and TCRVs. The Reynolds shear-stress plots in Figure 4.16 show negative Reynolds shear-stresses at some locations on the mid plane (Z/D = 0) which represents that the barrel shock on the upstream side of the jet plume is very unstable region resulting in a lot of fluctuations and enhanced interactions between fluids. On the Leeward side and further downstream the TKE is not being produced in large quantities and thus more dissipation is observed whereas the Reynolds shear-stresses are positive pointing to the large recirculation zone and area of less activity closer to the walls.

4.4.5 Flow Mixing

Kawai and Lele[89] presented a comparison of passive scalar (PS) of jet fluid for the incoming turbulent flow versus the laminar flow and highlighted the importance of the turbulent flow for the mixing of the two fluids using the quantitative analysis of passive scalar and the RMS of passive scalar. Figure 4.17 shows the contour plots for the RMS of passive scalar for the fine grid at various locations in the flow field. It is clear from Figure 4.17(a) that as soon as the jet is injected in to the supersonic flow, there is a rapid mixing occurring on the windward side of the jet plume and the jet fluid progressively dilutes further downstream. In order to understand the regions of mixing Figures 4.17(a)-(e) must be observed concurrently. It is observed that mixing major mixing areas are the windward side of the jet plume and creating a mixing area that wraps around the jet.

On the leeward side of the jet there is very little mixing activity and this concurs the earlier observation that most of the jet fluid is passing through the windward side of the jet plume (Figure 4.9(a)). This is further understood by analyzing the Figure 4.10(c)-(e) where progressive dilution is clearly seen in the cross view planes (X/D = 1, 2 and 3). Kawai and Lele[89] highlighted that this progressive mixing is a feature of incoming turbulent flow and is not present as clearly in the case of incoming laminar flow and presented a quantitative comparison of these two different incoming flows. In the Figure 4.17(a) some fluid is seen entrained in the upstream recirculation zones. This important observation could imply that in case of a jet of hydrogen in supersonic air (as in the case of scramjet engines) the fuel entrained in the upstream recirculation zone can help early combustion given the right temperatures in the flow field.

Figure 4.18 presents the passive scalar (PS) distributions at various locations along the X/D axis on the mid line plane (Z/D = 0) to compares the results with previous LES with turbulent incoming flow (for the fine and finest grid levels) demonstrating excellent match between the results. Similarly, Figure 4.19 presents the RMS of passive scalar (PS_{rms})at the mid line plane (Z/D =0) and compares the results with previous LES data. This again indicates progressive mixing on the windward side using the STBL in the incoming flow as opposed to laminar inflow case as shown by Kawai and Lele [89]. It must be mentioned here that from the Figures 4.18 and 4.19 it appears that the results from ILES are very slightly under-achieved but the overall profile comparison between both the methods are similar. The mixing mechanism will further be

understood using the instantaneous analysis in the Section 4.5 where flow instabilities will be discussed.

4.4.6 Pressure Distributions

Mean pressure distributions normalized by the freestream pressure (P/P_∞) on the wall has been analyzed, upstream and downstream the jet injection hole, for three levels of grid resolution. The experiment was conducted by Everett *et al.*[50] using Pressure Sensitive Paint (PSP). Figure 4.20(a) represents the pressure distributions on the wall-normal mid line plane (Z/D = 0) showing very high pressure behind the bow shock, comparatively low pressure in the upstream recirculation zones ("R1" and "R2", Figure 4.8(a)) and very low pressure in the recirculation zone behind the jet plume ("R3", Figure 4.8(a)). Figure 4.20(b) shows wall pressure distribution contours (Y/D = 0) indicative of the small rise in the wall pressure just upstream of the jet plume but downstream the wall pressure undergoes a sudden decrease in the recirculation zone "R3". A more quantitative analysis of the wall pressure downstream the jet plume (Figure 4.20(c)) enhances this understanding, where normalized wall-pressure is plotted at various X/D locations. It is shown that the wall pressure along the X/D = 1 line

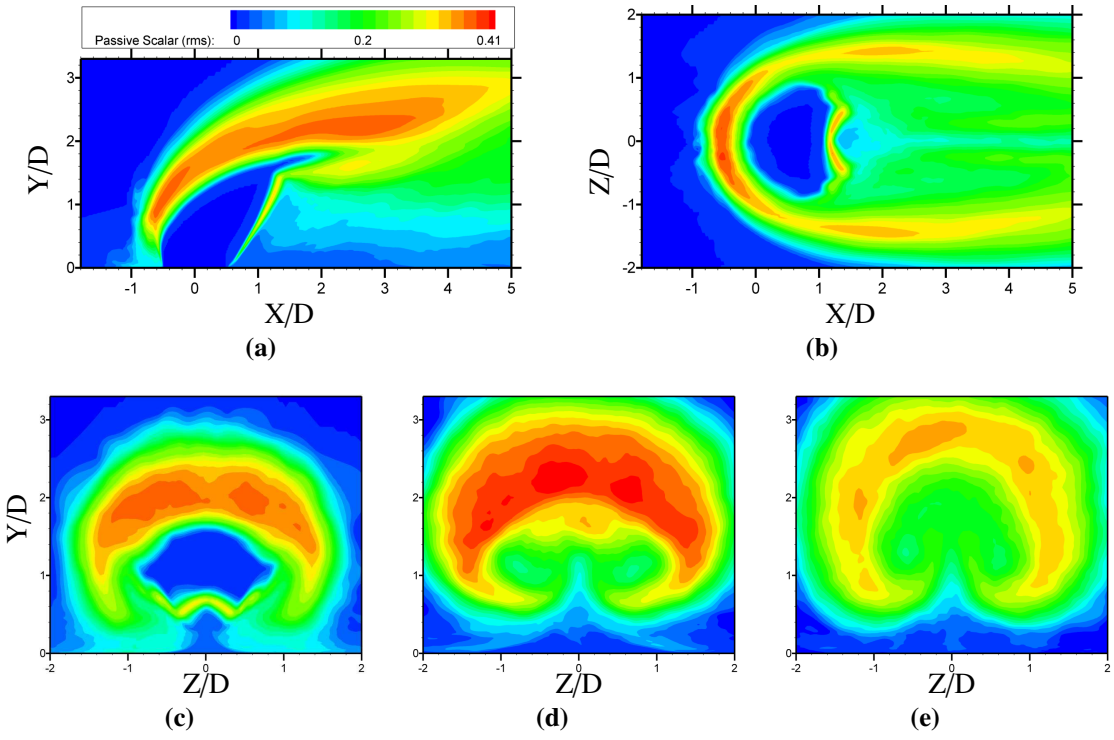

Figure 4.17: *Time averaged contours of root-mean-square (RMS) of jet passive scalar (PS) at various locations in the flow field; (a) wall-normal mid plane (Z/D = 0), (b) wall-parallel plane (Y/D = 1), (c)-(e) wall-normal cross-view planes (X/D = 1, 3 and 5 respectively).*

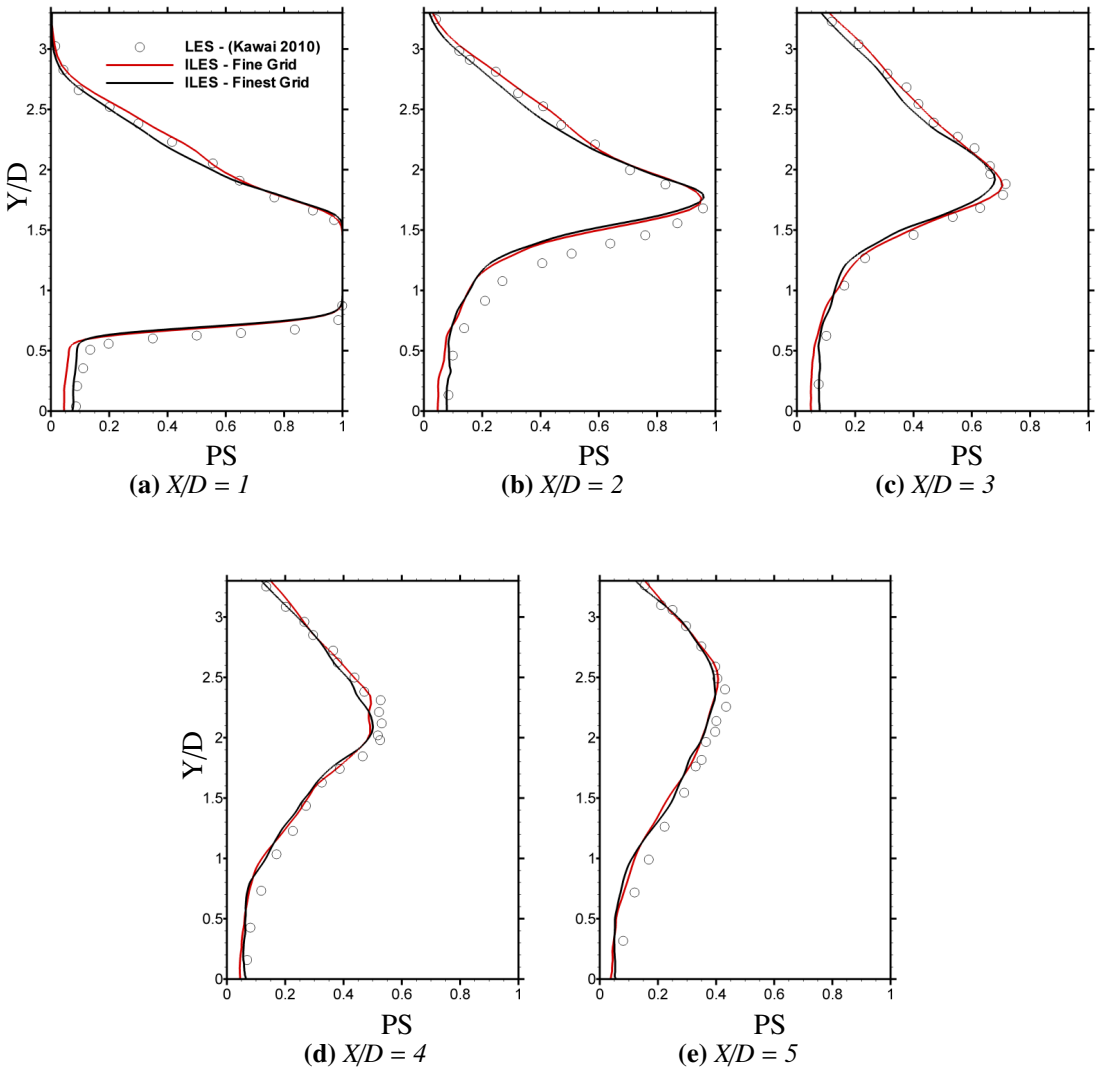

Figure 4.18: *Jet passive scalar (volume fraction) profiles are compared with the previous LES results on all grid levels at locations X/D = 1, 2, 3, 4 and 5 on the mid plane (Z/D=0).*

on the flat-plate is very low just behind the jet plume. Moving further downstream, the wall pressure at the X/D = 2 lines starts to gradually increase. Along the X/D = 3, 4 and 5 lines the wall pressure increases considerably and from the Figure 4.9(d) it is observed that this is the location around where the TCRVs start to emerge which cause an increase in the wall pressure.

In Figure 4.21 the mean wall pressure distributions are compared with the experiment and classical LES at the wall (Y/D = 0) and Z/D = 0, 1 and 2 locations. Figure 4.21(a) shows slight increase in the wall pressure just ahead and decrease in the pressure just after the injection hole. Similar results are found in the Figure 4.21(b) and (c). How-

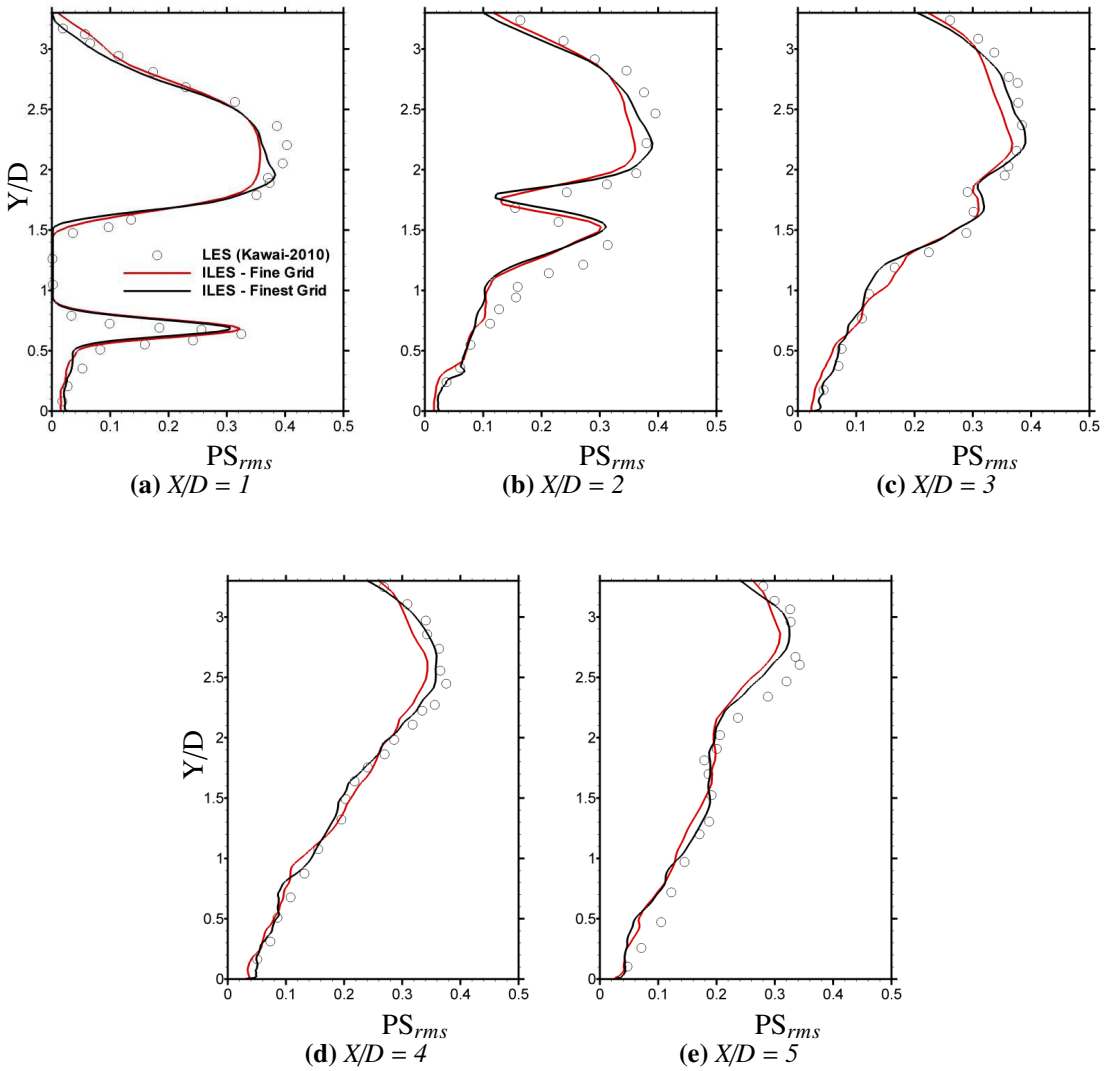

Figure 4.19: *Root-mean-square (RMS) of jet passive scalar (PS_{rms}) profiles are compared with the previous LES results on all grid levels at locations X/D = 1, 2, 3, 4 and 5 on the mid plane (Z/D=0).*

ever, in Figure 4.21(c) small error is found in the results from the current study at location Z/D = 2 which could be due to the coarse grid resolution away from the mid line plane (Z/D = 0) where the bow shock thickness is affected that has results in discrepancy in results at Z/D = 2 location. But overall the results in the Figure 4.21 show that the ILES results concur the experimental and classical LES investigation.

4.4.7 Energy Spectrum

Taylor hypothesis can be acceptable when applied to single large-scale structures that are not undergoing rapid evolution or interaction with neighbouring structures. For interacting large scale structure, Taylor hypothesis has been found to produce large distortions in the spectra of lateral velocity and scalar fluctuations[168], and in the probability density functions of velocity and temperature derivatives[8]. For the above reason, the Taylor hypothesis has not been analysed in this work and Kolomogorov's hypothesis has been used to analyse data. Vincenc Strouhal in 1878 introduced a dimensionless parameter (named after him) as *Strouhal* number (St) that defines the frequency of oscillations in an unsteady flow as,

$$St = \frac{fl}{U} \tag{4.9}$$

where f is the frequency of oscillations, l is the characteristic length which is taken as diameter of the injection hole (D) and U is the flow velocity. Strouhal used this parameter to analyze the vortex shedding in air due to soundwaves. Physically the

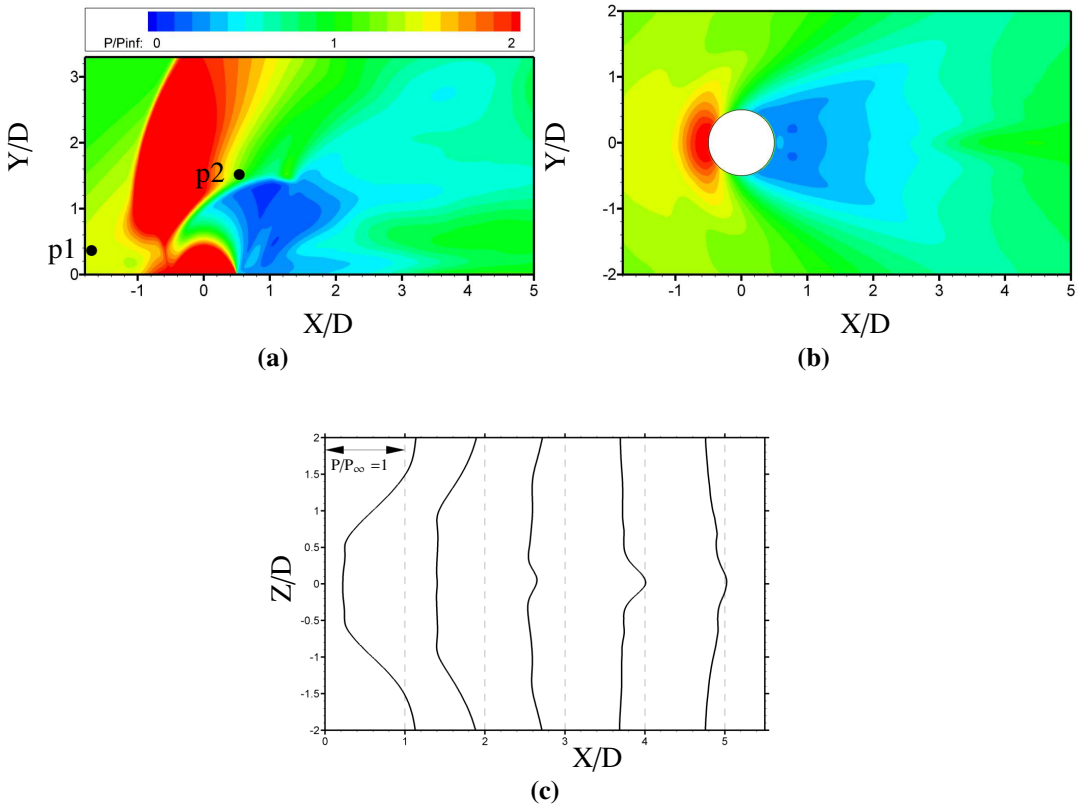

Figure 4.20: *Pressure distributions; (a) mid plane (Z/D = 0), (b) wall-normal (Y/D = 0), (c) Pressure profiles plotted on the flat-plate (Y/D = 0) at various X/D locations. Points p1 and p2 shows approximately the locations for the spectrum plots.*

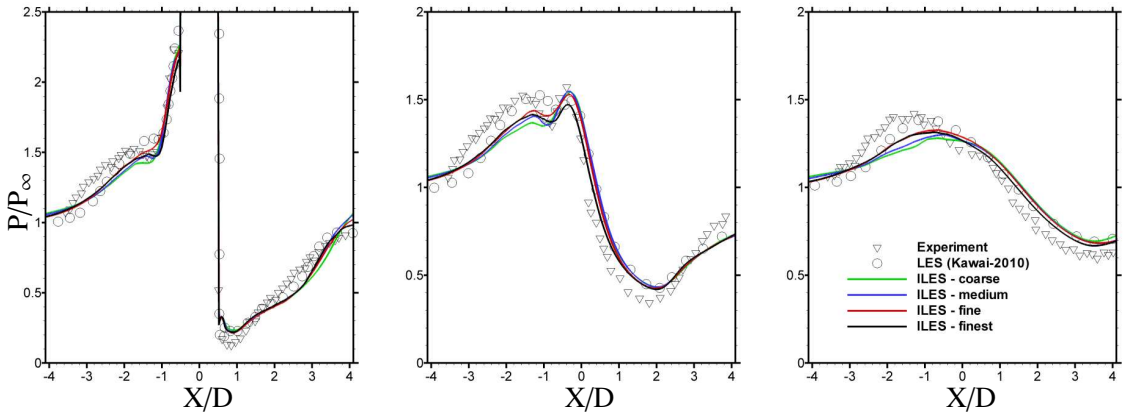

(a) *Z/D = 0* **(b)** *Z/D = 1* **(c)** *Z/D = 2*

Figure 4.21: *Mean pressure profiles on the flat-plate (Y/D = 0)are compared with the experimental and previous LES results on three grid levels at Z/D = 0,1 and 2 positions.*

Strouhal number is considered as "the measure of inertial forces due to the unsteadiness of the flow or local acceleration to the inertial forces due to changes in velocity from one point to another in the flow field" [119]. Strouhal number of the order of 1 in a turbulent flow is considered as large and indicates flow is dominated by viscosity and a small Strouhal number of the order of 10^{-4} indicates rapid development and shedding of vortices representing highly oscillating flow field. The energy spectrum analysis in the JISC flow field has been analyzed using the Strouhal number as shown in the Figures 4.22(a) and (b) for all four grid resolutions.

Figures 2.3 and 2.4 in Chapter 2 present a schematic and experimental data plots for the energy spectrum in turbulent flow fields which can be compared to the energy spectrum plots in the Figure 4.22(a) and (b) where energy spectrum has been plotted against the Strouhal number. The energy spectrum has been plotted at two locations which are carefully selected in the flow field; the first point (p1) in the recirculation zone upstream of the jet (X/D, Y/D, Z/D = -0.75, 0.5, 0) and the second point (p2) on the windward side of the barrel shock of the jet plume (X/D, Y/D, Z/D = 0.5, 1.5, 0). As $k^{-5/3}$ is an asymptotic line, the k^{-2} line is also shown on the plots.

The spectrum plots in the Figure 4.22 show similar trends for all four grid levels indicating clear regions of *production* at high wavenumbers or low Strouhal numbers where large vortices are developed. For high Strouhal numbers (in the range of 1) the plots indicate the energy dissipation regions dominated by the viscous forces. In Figure 4.22(a), the point (p1) is within the recirculation zone closer to the wall, we observe that the energy produced immediately starts to dissipate resulting in a very small region following the $k^{-5/3}$ trend and most of the plot is along the k^{-2} line. The cut-off point for the point (p1) is near 1×10^{-1} and for the point (p2) it is near 3×10^{-1}. With the increase in the grid resolution the cut-off wavenumber is shifted slightly which is due to the fact that any subgrid model does not account subgrid scale perfectly and

an increase in grid resolution results in reducing the effects of numerical method thus shifting the cut-off wavenumber slightly. In the Figure 4.22(a), as the region below the cut-off wavenumber is dominated by the viscous forces most of the plot shows dissipative range and presence of very small inertial subrange of wavenumbers. On the other hand the Figure 4.22(b) shows the spectrum for the point (p2) which lies in the shear-layer presents an excellent match with an ideal energy spectrum showing a clear production region in the highest wavenumber range (or low Strouhal number), a clear inertial subrange for medium wavenumbers and then a prominent dissipation range. In both the Figures 4.22(a) and (b), the region close to the St≈O(1) and above is dominated by the viscous forces.

4.5 Instantaneous Flow Analysis

Time averaged flow analysis above demonstrate various averaged flow properties in the flow field which demonstrate that the flow field is very complex and requires further understanding on the instantaneous flow to establish how the instabilities in the flow help the mixing process. From the previous analysis it appears that the flow field is highly symmetrical whereas the instantaneous snapshots in the Figure 4.23 shows that it is not a symmetrical flow field. Figure 4.23(a) shows the instantaneous view of the jet fluid showing instabilities being generated on the windward sides of the jet plume giving rise to various small and large scale coherent structures that entrain the jet fluid. Figures 4.23(b) and (c) shows the hairpin like turbulent structures using the

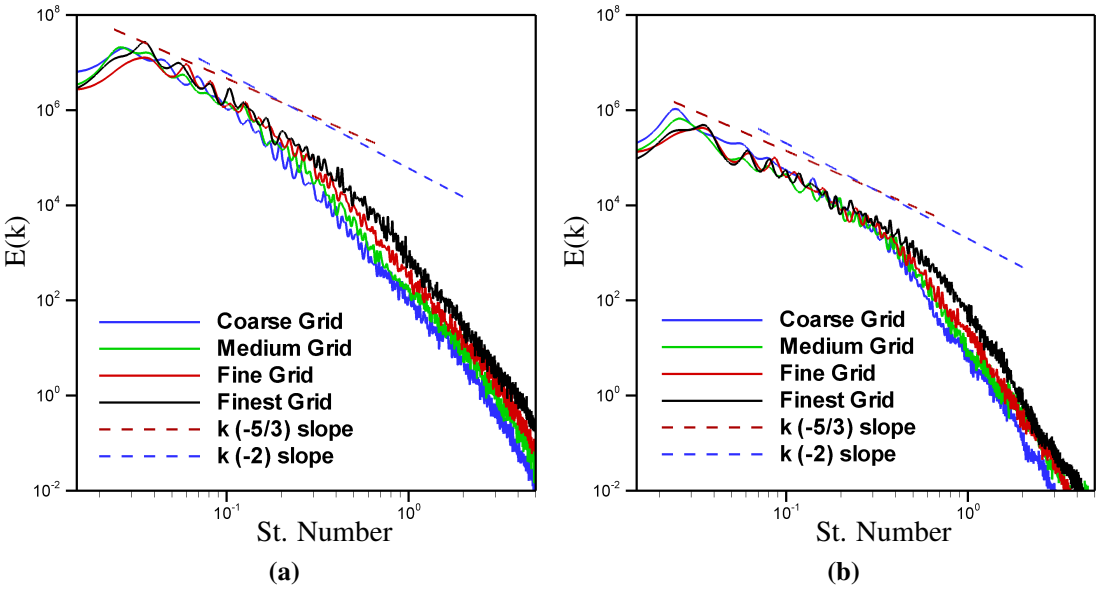

Figure 4.22: *Spectrum analysis; (a) Energy Spectrum at (X/D = -0.75, Y/D = 0.5, Z/D = 0), (b) Energy Spectrum at (X/D = 0.5, Y/D = 1.5, Z/D = 0).*

Q-criterion in the flow field demonstrating a very turbulent flow wrapping around the jet plume which is discussed in this section.

Firstly, an instantaneous view of the flow field is presented in the Figure 4.24 and 4.25 showing the density gradients and jet fluid passive scalar at various locations. The 5^{th} order modifies MUSCL scheme captures the three-dimensional unsteady flow features like the front bow shock, the separation/lambda shock, Mach disc, barrel shock and contact surfaces without spurious oscillations and resolve a wide range of turbulent scales. The turbulent coherent structures in the incoming turbulent boundary layer interact with the bow shock and the jet plume on the windward side as presented in the Figures 4.24(a) and (b). Figures 4.24(c)-(e) shows the density gradient contours on the X/D = 1, 3 and 5 planes demonstrating a very complex three-dimensional highly unsteady and unsymmetrical flow field.

The jet fluid passing through the barrel shock and Mach disc create vortex structures in the windward sides of the jet plume which further develops into finer turbulent eddy structures downstream. The coherent structures play major role in determining the jet fluid mixing with the freestream flow as shown in the Figure 4.25. Because the jet fluid that passes through the barrel shock has larger velocity than the fluid passing through the Mach disc, the vortices generated on the windward side of jet plume roll

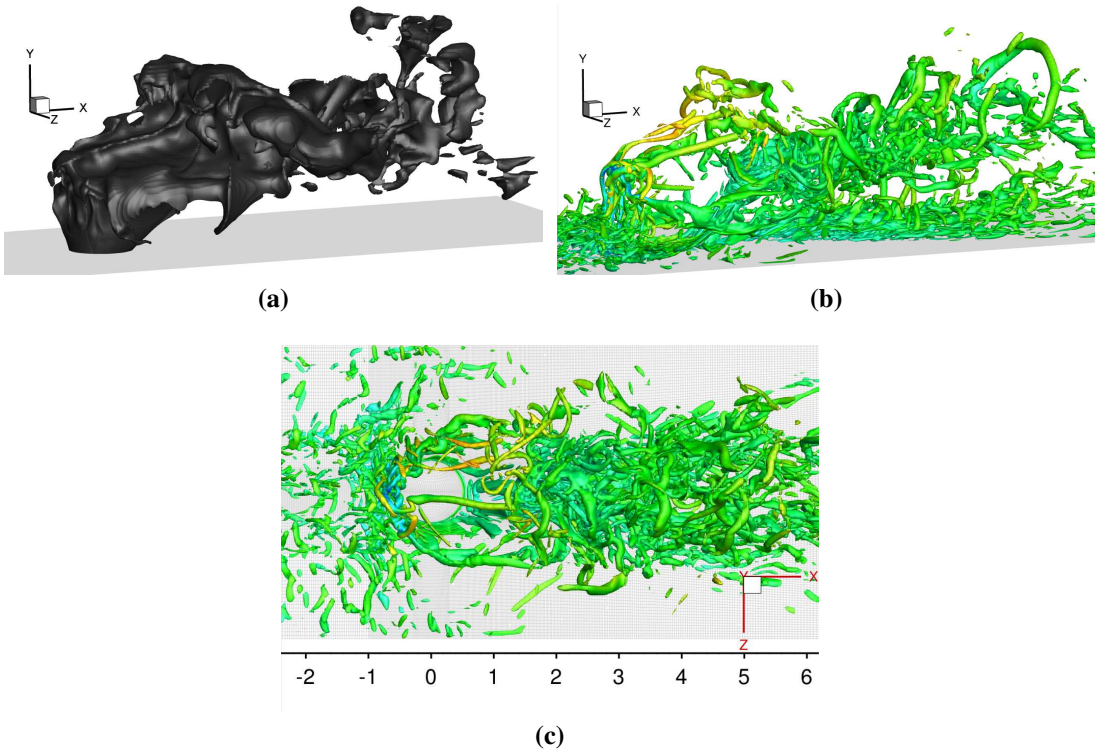

Figure 4.23: *Three dimensional instantaneous view of (a) Jet passive scalar, (b) hair-pin like turbulent streaks using the Q-criterion and (c) two-dimensional top-view of the computation grid showing hairpin like turbulent streaks using the Q-criterion.*

counter-clockwise as shown in the Figure 4.25(a). The rolling action is observed in the spanwise direction as well and it creates a complex three-dimensional Ω shaped intermittent *Circumferential Roller* type vortex structures wrapped around the jet plume creating an area of very active mixing.

As the fluid progresses further downstream, these circumferential roller vortices form the counter rotating vortices (CRVs) which stir-up the spanwise mixing in the fluid. In addition to the large scale CRVs, small scale vortices are also generated on the leeward side near the flat-plate within the turbulent boundary layer along the major CRVs and are termed as Trailing CRVs. These trailing CRVs run along the symmetry plane downstream the jet induced by the suction of the major CRVs. The turbulent structures resulted in these CRVs and trailing CRVs contribute to the high TKE regions as observed on the leeward side of the jet plume. Further downstream the major and the trailing CRVs grow in the spanwise direction and are the major features of the mixing mechanism.

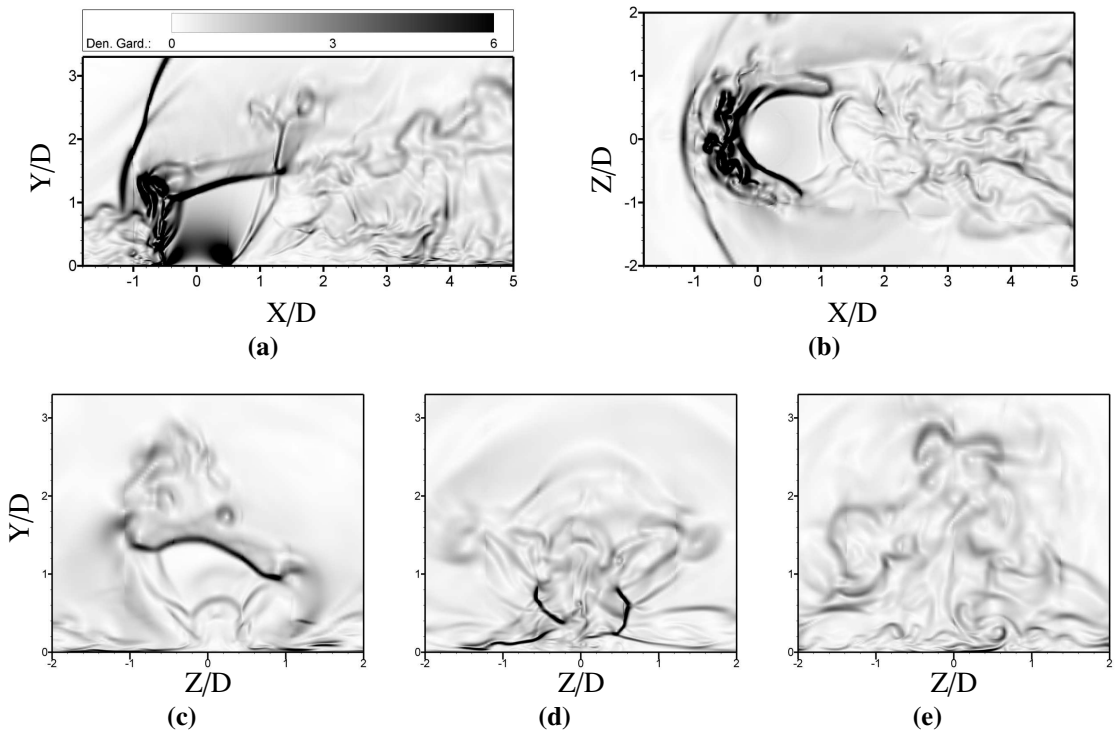

Figure 4.24: *Instantaneous contours of divergence of velocity at various locations in the flow field; (a) wall-normal mid plane (Z/D = 0), (b) wall-parallel plane (Y/D = 1), (c)-(e) wall-normal cross-view planes (X/D = 1, 3 and 5 respectively).*

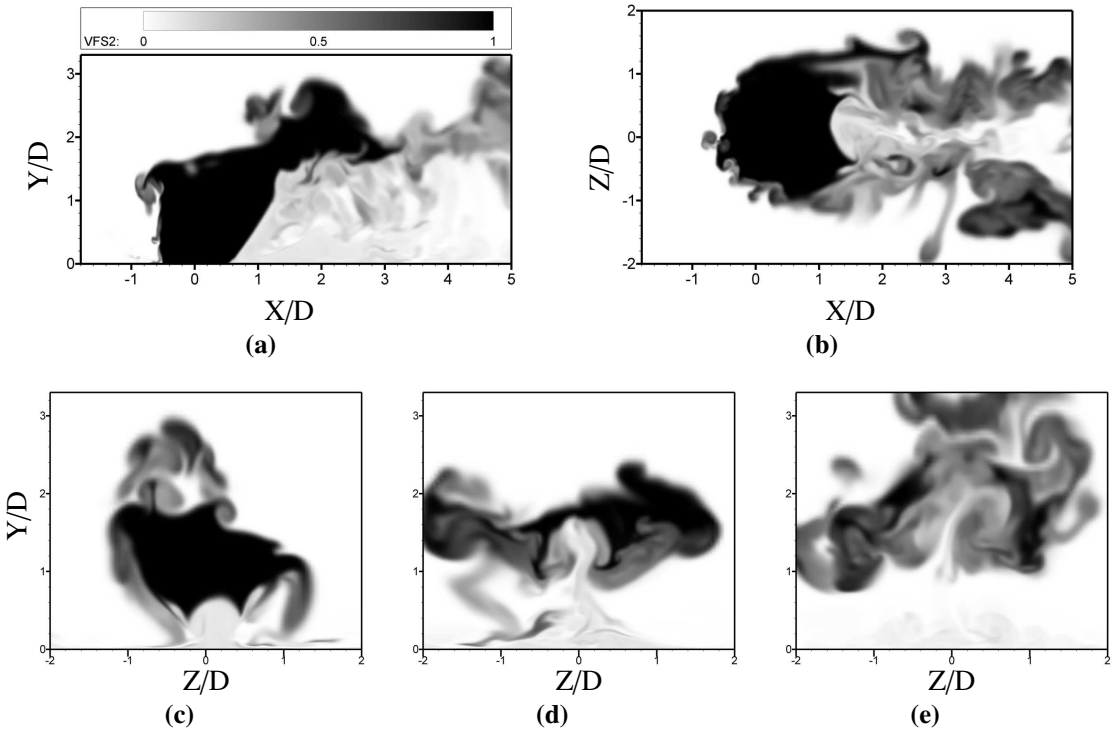

Figure 4.25: *Instantaneous contours of jet passive scalar at various locations in the flow field; (a) wall-normal mid plane (Z/D = 0), (b) wall-parallel plane (Y/D = 1), (c)-(e) wall-normal cross-view planes (X/D = 1, 3 and 5 respectively).*

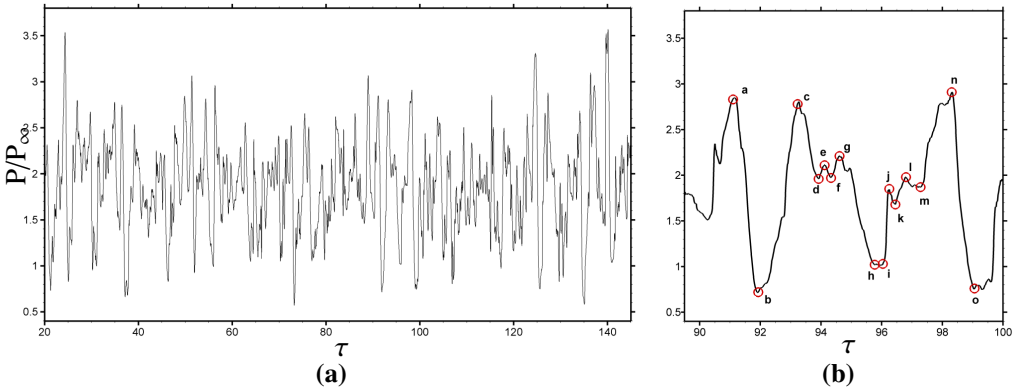

Figure 4.26: *Time history of instantaneous pressure measurement; (a) pressure plot for dimensionless time 20 till 145, (b) focused view of pressure plot against dimensionless time 89.5 till 100 shown various point (a to o) shown on the pressure history plot. These points are described in details in Figure 4.27*

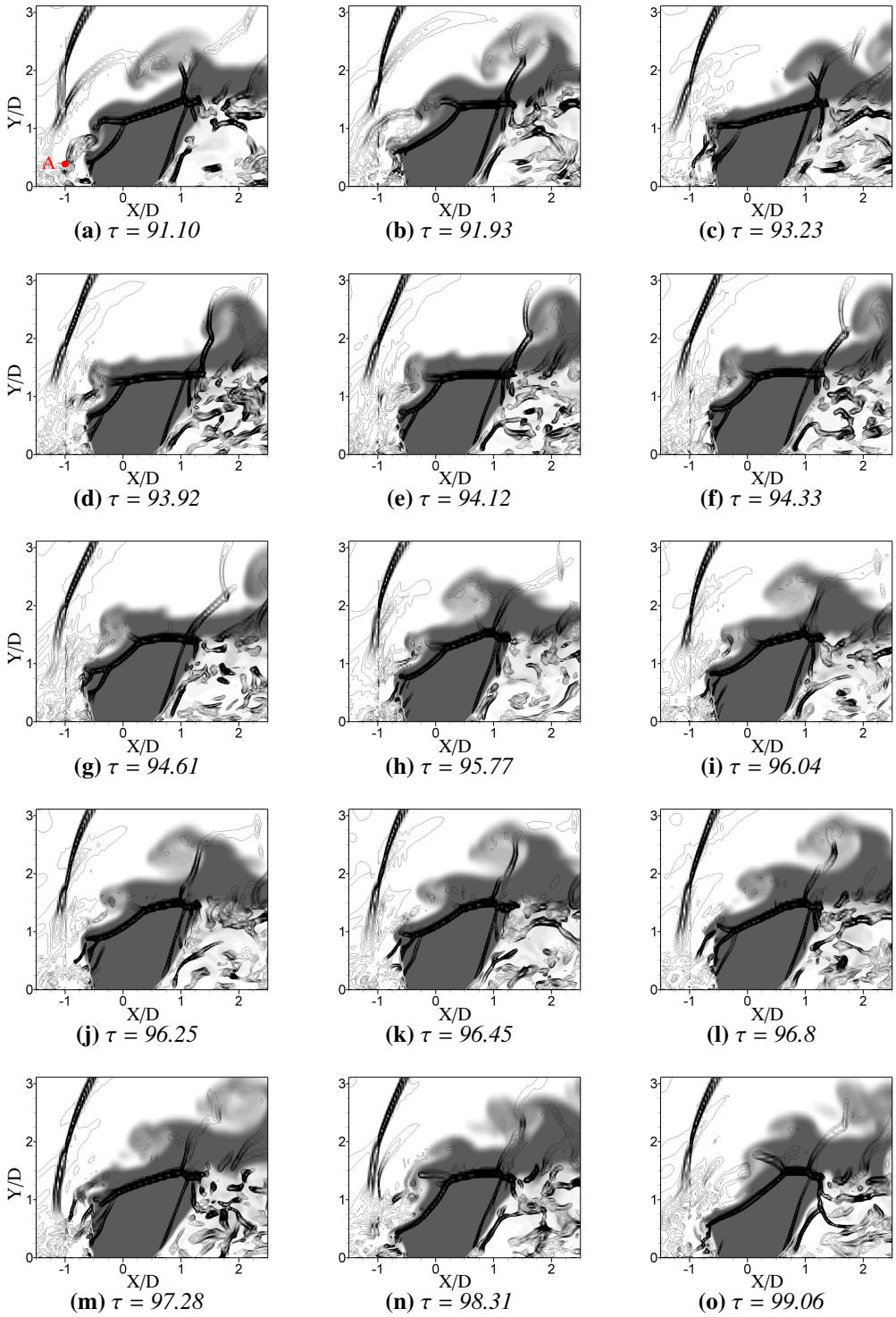

(a) τ = *91.10* **(b)** τ = *91.93* **(c)** τ = *93.23*

(d) τ = *93.92* **(e)** τ = *94.12* **(f)** τ = *94.33*

(g) τ = *94.61* **(h)** τ = *95.77* **(i)** τ = *96.04*

(j) τ = *96.25* **(k)** τ = *96.45* **(l)** τ = *96.8*

(m) τ = *97.28* **(n)** τ = *98.31* **(o)** τ = *99.06*

Figure 4.27: *Instantaneous contours of passive scalar (background) obtained at the mid line plane (Z/D = 0) along with the negative divergence of velocity contours which describe the behaviour of the flow at different time instants as shown by various points in Figure 4.26(b).*

4.5.1 Flow instabilities

In order to further understand what is happening in this region an instantaneous analysis is carried out for the pressure in the region in Figure 4.26. Figure 4.26(a) presents time-history of the non-dimensional pressure data inside the upstream recirculation zone at point X/D = -0.75, Y/D = 0.5 and Z/D = 0 (As shown by the dot "A" in Figure 4.27(a)) for a non-dimensional time (τ) from 20 to 145. Figure 4.26(b) presents a *zoomed-in* version for instantaneous pressure data versus the non-dimensional time (τ) 89.5 to 100 with various locations in time (shown as *a, b,..., o*). Figures 4.27(a)-(o) show the negative instantaneous divergence of the velocity (line contours) along with jet fluid passive scalar (grey contours at the background) at each time instance which correspond to the pressure fluctuation points in Figure 4.26(b).

The instantaneous flow field represents the unsteadiness in the windward side of the jet plume and the process of the start of Kelvin-Helmholtz (KH) instabilities in this region, whereas, the Leeward side of the barrel shock does not show any major instabilities. With the fluctuations in the pressure the jet shear layer on the windward side of the jet plume fluctuates, a local weak shock is developed and a kink is visible in the jet shear layer (Figure 4.27(a)). This local shock is attached to the barrel shock and the pressure difference across the local shock is responsible for the kink in barrel shock. With time advancement this local shock grows in size and entrains the jet fluid. The velocity near the shear layer is higher than the velocity away from it, this difference in velocities result in a KH type instability on the windward side of the barrel shock which also grows as the local shock advances downstream in time. At the junction of barrel shock and Mach disc there is reflected shock as shown in Figure 4.8(a). The local shock grows and merges with the reflected shock at the triple point, but the KH instability is clearly seen as growing in size even after the local shock disappears. The KH instabilities result in large scale vortex structures on the windward and top sides of the jet plume which are rotating counter-clockwise in the Figure 4.27(a - o). The large scale vortices are rotating but also moving in the downstream direction which result in Ω shaped intermittent circumferential rollers on the windward side which run around the jet plume on the jet shear layer (as also described in [11]) creating an area of very active mixing. With the turbulence in the freestream flow this mixing activity is enhanced as compared to laminar freestream flow[89].

On the leeward side of the jet plume, the instantaneous flow analysis shows that there is very less activity, but still there is some mixing occurring in this region. As the local shock develops on the windward side of the barrel shock, it creates a pressure differential due to which there is an inward kink on the upstream side of the local shock. At the same time the downstream side of the local shock the barrel shock kink develops in the outward direction shown clearly in Figure 4.27(e, f and g). As the barrel shock kinks in the outward direction it pulls the whole jet plume with it resulting in a very small deflection of the leeward side of barrel shock. This small disturbance over the time results in fluctuations in the leeward side of the barrel shock. These fluctuations and existing low pressure in this region result in some mixing in

this region shown by light grey contours in the Figure 4.27(a - o). These fluctuations are the cause of high TKE zones on the leeward side of the barrel shock as well as shown in the Figure 4.11(a) and (b). Closer to the flat-plate there is less activity but away from the flat-plate the fluctuations/activity increases and thus gradual increase in the mixing is shown by increased darkness of grey contours in the leeward side of jet plume. Figure 4.28 shows a schematic overview of the JISC flow structures on the mid line wall normal plane as understood from the discussion presented in this chapter.

4.6 Summary

The objectives of this work were three folds. Firstly, to validate the digital filter based turbulent inflow data generator implemented for the generation of STBL in the CNS3D code. Secondly, to accurately simulate a complex high speed flow such as JISC using Godunov type 5^{th} order spatially accurate MUSCL scheme with modified variable extrapolation using high resolution methods within the framework of ILES. Finally, to explore and understanding JISC flow by detailed analysis of the flow features with STBL in order to improve the design optimization process of a scramjet combustion chamber, active flow control in cavities during supersonic flights and thrust control system in rockets. Following are main findings from the work presented in this chap-

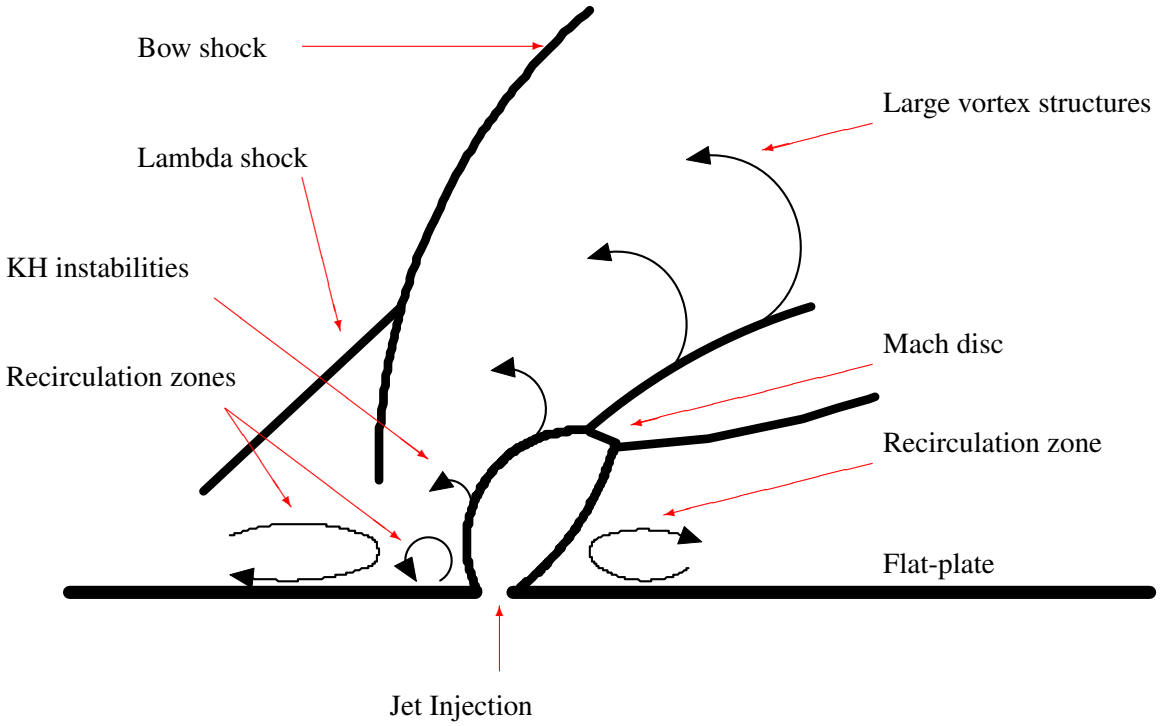

Figure 4.28: *A schematic instantaneous view of sonic jet injection into a supersonic crossflow showing generation of Kelvin-Helmholtz (KH) instabilities in the upper jet shear layer which grows with the time and create large vortex structures downstream of the jet injection.*

ter:

1. The high resolution methods (HRM) provide a fast method for CFD simulations involving discontinuities, using which complicated flows can be captured accurately. JISC is a very complex flow exhibiting various discontinuities and flow structures that involve shock/boundary-layer interactions.

2. Incoming STBL plays an important role in enhancing the mixing of the two fluids as it *"stirs-up"* the fluids after jet injection. The momentum in the STBL also acts to help contain the size of the recirculation zone upstream of the jet injection which entrains the jet fluid in it. This entrained jet fluid in the recirculation zone can be of help in case of fuel injection as if the temperature is high enough can auto-ignite and start the combustion process.

3. Kelvin-Helmholtz (KH) instabilities are generated on the jet shear layer on the windward side of jet plume that produce large scale eddies which results in better mixing of the two fluids and mixing process starts rapidly in the thick shear-layer section of the jet plume.

4. On the leeward side of the jet plume slight fluctuations in the barrel shock result in some mixing in the recirculation zone just downstream of the jet plume which can be helpful in case of fuel (e.g., hydrogen) injection for combustion in the boundary layer.

CHAPTER 5

Reliable Turbulent Data Generation

This chapter presents simulations of the JISC flow with a laminar inflow and five different cases with turbulent inflow. The results from all these methods are compared in order to establish the most accurate and reliable turbulent inflow data generation method among them. The importance of the Exponential correlation used in the digital filter based method is also analyzed. The work presented here serves to justify the suitability and reliability of the digital filter based method.

5.1 Introduction

One of the key issues in the CFD is the turbulence modelling as almost all of the engineering flows are turbulent in nature where the drive is to capture the correct flow physics. Chapter 2 provided an introduction to turbulence where the importance of studying the turbulence has been emphasized and Chapter 3 introduced various CFD techniques to study turbulence i.e. RANS, LES and DNS. Averaged flow analysis using RANS requires turbulence models to be included into the numerical schemes for example $k - \epsilon$ model where the values of k and ϵ has to be specified for any given problem which is most often based upon an educated guess. It is generally considered easier to establish turbulence variables (like turbulence intensity and turbulence length scales) at the start of RANS rather than estimating the turbulence model variables (like turbulent energy and dissipation). Once the turbulence variables are established/calculated, the turbulence model variables can be calculated easily[14, 167, 102, 126, 52, 81]. RANS results although being very good but only provide averaged flow information.

Time-evolving LES or DNS simulations, which can provide instantaneous insight into the flow under investigations, most often require turbulent boundary conditions in order to generate turbulence in the flow field. Although DNS simulations themselves are computationally very expensive (compared to RANS), adding turbulence boundary conditions into the numerical algorithms can affect the computational efficiency drastically, but the cost of ignoring it could be drastic as well. LES, over the time,

has emerged as an alternative to RANS and DNS and is an ideal candidate for studying turbulence where computational cost could be comparatively low yet the accuracy could be high allowing accurate instantaneous flow information. For high speed and high Reynolds number flows the advantages of ILES has been discussed in the Section 3.2 where it has been presented that the latest ILES studies are very successful in the high Reynolds number compressible flows[53, 54, 112, 113, 72, 65, 66, 41, 96, 97]. Time dependent LES or ILES are very sensitive to the inflow conditions and the need is to establish methods to generate turbulent inflow data with high levels of accuracy that could help understand the correct flow physics using this methodology.

Various methods for turbulent boundary conditions have been discussed in the Section 3.2 where the pros and cons of the highly accurate recycling/reintroduction technique and the spatially evolving turbulence technique are presented. Another method which is in use is the random white-noise base turbulence data generation but it has been established that this method fails to properly distribute the energy of the signal according to the wavenumbers resulting in an approximately horizontal spectrum. Section 3.2 also discussed the digital filter based method for the generation of turbulent inflow data for time-evolving simulation based upon [95, 169, 156]. This method have been successfully implemented (as presented in the Section 3.5.1) and utilized in the CNS3D code to study the JISC flow as presented in the Chapter 4. Earlier studies of JISC by Genin and Menon[59] and Kawai and Lele[89] utilized the recycling/reintroduction technique where the computational costs are mentioned by Kawai and Lele to be around 90,000 CPU hours on the (JAXA) Supercomputer System (quad-core CPU with a clock-rate of 2.5 GHz) whereas in the previous chapter it has been demonstrated that equivalent accuracy in the results has been obtained using the digital filter based turbulent boundary condition using only 1,800 CPU hours on the Astral supercomputer (dual-core CPU with a clock-rate of 3 Ghz) at the Cranfield University.

The studies of JISC flow emphasize the importance of the STBL in the flow development, jet penetration and fluid mixing. The Finite Volume modified Godunov[61, 151, 150] type ILES technique (as explained in Chapter c3) is applied to study the JISC flow with four different inflow conditions; laminar inflow, random white-noise based turbulent boundary condition, Reynolds stress based method and the digital filter based synthetic turbulent inflow data generation. Here, the transverse JISC flow has been studied because of two major reasons; firstly this is the flow configuration used in the HyShot-II scramjet combustion chamber and secondly there is a wealth of experimental[139, 50, 161] and CFD[89, 133] data available at both locations (upstream and downstream of the jet injection hole) for comparison of the effect of turbulent boundary conditions. The aim of the chapter is to analyze the STBL upstream of the jet injection with different methods to establish the most accurate and reliable method (among the ones used here) and then analyze the JISC flow itself to understand the effect of the discrepancies in the STBL generated by these methods on the JISC flow. The STBL generated by each technique is compared with established DNS data for the flat-plate case and then the flow properties upstream and downstream of the jet injection are discussed to achieve the said aim.

5.2 Inflow Conditions

In this section the various inflow conditions are explained in detail in the subsections as below:

5.2.1 Laminar inflow. (case-1)

5.2.2 Random white-noise. (cases: 2, 3 and 4)

5.2.3 Digital filter based turbulent inflow boundary condition. (case-6)

5.2.4 Only using the Reynolds stress tensor and ignoring the Exponential correlation in the digital filter based method. For ease of reference it is called a "Reynolds stress method". (case-5)

It should be mentioned here that all the cases are numbered according to the level of accuracy achieved in the results but the description of case-5 comes after the description of case-6 because case-5 requires understanding of case-6.

5.2.1 Laminar Inflow (case-1)

The laminar inflow boundary condition is obtained by simply employing the averaged flow profile obtained from the experiment[139] at the inlet of the computational domain without any fluctuations. The experimental data did not provide any information for the density profile or the density fluctuations therefore it is kept constant. For laminar inflow case (case-1), a supersonic inflow condition has been employed as below:

$$\begin{aligned} \rho_{(x=0)} &= \rho_0 \quad , \\ u_{(x=0)} &= u_0 \quad , \\ v_{(x=0)} &= v_0 \quad , \\ w_{(x=0)} &= 0 \quad , \\ E_{(x=0)} &= \frac{p}{\gamma - 1} + \frac{\rho}{2}\left[u^2 + v^2 + w^2\right] \quad , \end{aligned} \tag{5.1}$$

where ρ is the density, *u, v, w* and E are the three velocity components and total internal energy respectively. u_0 and v_0 are the streamwise and wall-normal velocity profiles at X/D = -5 position from the experiment[139] where $v_0 \ll u_0$ and $v_0 \approx 0$. Finally, p is the pressure and γ is the specific heat ratio.

5.2.2 Random White-Noise (cases: 2-4)

In this section the boundary conditions based on random white-noise are presented as they are used in the current analysis. In random white-noise the power spectral density is a flat profile because the signals are equally distributed within a fixed bandwidth. Adding this random white-noise as fluctuations to an average flow profile can represent the fluctuations in a turbulent flow field.

A normalized density profile (ρ_0) has been obtained for a supersonic turbulent boundary layer as presented by Nothwang[118]. Using this density profile and the averaged velocity profiles from the experiment[139], a random white noise is added to the averaged profiles. The intensity of the perturbations is based upon the information from the experimental data that is the fluctuations are of the order of 1-3% of the averaged streamwise (u_0) and wall-normal (v_0) velocity profiles. Considering r is a set of random numbers and the fluctuations for density, streamwise and wall-normal velocity are represented by ρ', u' and v', then these fluctuations can be calculated as follows:

$$\begin{aligned} \rho' &= (\epsilon\,\rho_0)\; r \quad , \\ u' &= (\epsilon\,u_0)\; r \quad , \\ v' &= (\epsilon\,v_0)\; r \quad , \end{aligned} \tag{5.2}$$

where, ϵ represents the percentage intensity of perturbations. Although the percentage fluctuations are known to be of the order of 1-3% (from experimental data[139]), in this work three different cases are simulated using a different level of perturbations for each case such that for,

- Case-2, $\epsilon = 1\%$ or 0.01
- Case-3, $\epsilon = 5\%$ or 0.05
- Case-4, $\epsilon = 10\%$ or 0.10

Boundary condition for random white-noise cases are implemented as below:

$$\begin{aligned} \rho_{(x=0)} &= \rho_0 + \rho' \quad , \\ u_{(x=0)} &= u_0 + u' \quad , \\ v_{(x=0)} &= v_0 + v' \quad , \\ w_{(x=0)} &= 0 \quad , \\ E_{(x=0)} &= \frac{p}{\gamma - 1} + \frac{\rho}{2}\left[u^2 + v^2 + w^2\right] \quad , \end{aligned} \tag{5.3}$$

For each timestep, a new set of random numbers (r) is generated through the FORTRAN-90 intrinsic function RAND() and thus a new set of perturbations are added to the averaged flow field at each timestep.

5.2.3 Digital Filter Based Turbulent Boundary Condition (case-6)

The digital filter based synthetic turbulent inflow data generation method as implemented in this work for the JISC study has been described in the Section 3.5.1 and Section 4.2. Here the boundary condition implementation is briefly presented for completion only, as in Equation (5.4):

$$\begin{aligned} \rho_{(x=0)} &= \rho_0 + \rho'' \quad , \\ u_{(x=0)} &= u_0 + u'' \quad , \\ v_{(x=0)} &= v_0 + v'' \quad , \\ w_{(x=0)} &= 0 \quad , \\ E_{(x=0)} &= \frac{p}{\gamma - 1} + \frac{\rho}{2}\left[u^2 + v^2 + w^2\right] \quad , \end{aligned} \tag{5.4}$$

where, the fluctuations in density and velocity components (ρ'', u'' and v'') are obtained from the Equations (4.4) and (4.5) in Chapter 4.

5.2.4 Reynolds Stress Method (case-5)

In this method, the random number sets are generated in the same manner as for the digital filter based method (as explained in the Section 3.5.1), but instead of filtering the random numbers through the Exponential correlation function (Equation (3.64)), the un-filtered random number sets are used in the Equation (3.71). The purpose of this method is to analyze the importance of the Exponential correlation function in the original digital filter based method (case-6). Assuming r_{k1} and r_{k2} are two sets of random numbers then velocity fluctuations are obtained as below:

$$\begin{bmatrix} u''' \\ v''' \\ w''' \end{bmatrix} = \begin{bmatrix} \sqrt{R_{11}} & 0 & 0 \\ R_{21}/\sqrt{R_{11}} & \sqrt{R_{22} - \left(R_{21}/\sqrt{R_{11}}\right)^2} & 0 \\ 0 & 0 & 0 \end{bmatrix} \begin{bmatrix} r_{k1} \\ r_{k2} \\ 0 \end{bmatrix} \tag{5.5}$$

where $()'''$ are the fluctuations from the Reynolds stress method, and the density fluctuations are obtained as below:

$$\rho''' = \rho\,(0, y, z) \cdot \frac{\sqrt{R_{11}}}{U_\infty} \cdot r_{k1} \tag{5.6}$$

The inflow conditions are implemented using the fluctuations from the Equations (5.5) and (5.6) as below:

$$
\begin{aligned}
\rho_{(x=0)} &= \rho_0 + \rho''' \quad , \\
u_{(x=0)} &= u_0 + u''' \quad , \\
v_{(x=0)} &= v_0 + v''' \quad , \\
w_{(x=0)} &= 0 \quad , \\
E_{(x=0)} &= \frac{p}{\gamma - 1} + \frac{\rho}{2}\left[u^2 + v^2 + w^2\right] \quad ,
\end{aligned}
\tag{5.7}
$$

For the next timestep, new sets of random numbers are generated and the fluctuations are calculated using the Equations (5.5) and (5.6). Thus the fluctuations generated are not filtered and correlated as specified in the original digital filter based method and are only scaled using the Reynolds stresses obtained from the experiment[139].

5.3 Computational Grid and Initialization

The physical domain of the JISC experiments[139, 161, 50] is a flat-plate with a circular injection hole allowing transverse air injection into a supersonic (Mach 1.6) free-stream air as shown in the schematic diagram in Figure 4.2. The physical space has been converted into a computational domain using a structured grid technique (Figure 4.3). Four grid level were used in the JISC analysis in the Chapter 4 but in the current analysis we only require one grid level. For this purpose the "fine" grid from the previous JISC analysis has been selected; Table 5.1 below presents the computational grid characteristics for all the six simulation cases. Table 5.2 presents the initial conditions from the JISC experiment for the main crossflow (c) and the jet flow (j).

Table 5.1: *Computational grids used in the current study to analyze various inflow boundary conditions.*

Case	Inflow Method	N_x [(a)]	N_y	N_z	Total(M)
Case-1	Laminar	522 (242+280)	116	151	9.2 (4.3 + 4.9)
Case-2	Turb - RWN (1%)[(b)]	522 (242+280)	116	151	9.2 (4.3 + 4.9)
Case-3	Turb - RWN (5%)	522 (242+280)	116	151	9.2 (4.3 + 4.9)
Case-4	Turb - RWN (10%)	522 (242+280)	116	151	9.2 (4.3 + 4.9)
Case-5	Turb - RSM[(c)]	522 (242+280)	116	151	9.2 (4.3 + 4.9)
Case-6	Turb - DF-TBC[(d)]	522 (242+280)	116	151	9.2 (4.3 + 4.9)

(a) Numbers in the parentheses refer to STBL domains and JISC domains, respectively.

(b) Random white-noise used as fluctuations in the flow field and the percentage is the intensity of the white noise.

(c) Reynolds stress method.

(d) Digital filter based turbulent boundary condition.

Table 5.2: *The averaged stagnation inflow conditions from experiment are used to initialize the flow. The subscripts c and j refer to cross-flow and jet properties respectively.*

Property	Value	Units	Property	Value	Units
Mach Number(c)	1.6		Mach Number(j)	1.0	
Stag. Pressure(c)	241	kPa	Stag. Pressure(j)	476	kPa
Stag. Temperature(c)	295	K	Stag. Temperature(j)	295	K
Average Velocity(c)	446.1	m/s	Reynolds Number	2.4E+04	

5.4 Incoming STBL Analysis

The convergence of all six simulation cases is presented in Figure 5.1. Table 5.3 presents the non-dimensional wall distance (y^+), the non-dimensional time ($\tau = tU_\infty/D$) and computational (CPU) time for each simulation case along with the integral length scales prescribed for digital filter based turbulent inflow data generator. As noticed in Table 5.3, all cases were simulated for nearly 150 non-dimensional time (τ) and the computational time required for each of them is almost identical. Figure 5.1 presents the averaged pressure (non-dimensionalised by the freestream pressure P_∞) at a point within the recirculation region just upstream of the jet injection. This point is within a very turbulent region on the mid plane (X/D = -1, Y/D = 0.5, Z/D = 0). It can be noticed here that all the mean flow properties have reached a point which approximates

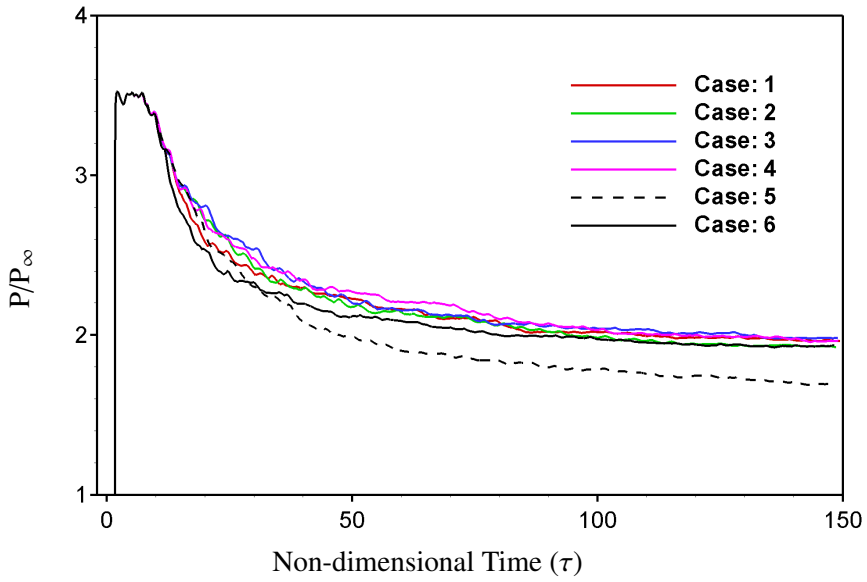

Figure 5.1: *Convergence plots for the six cases analyzed in this chapter showing similar levels of convergence achieved for all the cases over a period of approximately 150 non-dimensional time (τ).*

Table 5.3: *Attributes of the digital filter based turbulent inflow data generator and computational time for each simulation case.*

Case	L_y	L_z	y^+	Total Sims Time(τ)[(a)]	CPU Time[(b)]
Case-1	-	-	14	149.426	1852
Case-2	-	-	14	148.614	1867
Case-3	-	-	14	148.982	1868
Case-4	-	-	14	149.082	1859
Case-5	-	-	14	148.729	1857
Case-6	0.5	0.2	14	148.308	1862

(a) Non-dimensional time for simulations.
(b) CPU Time in hours; Simulation performed on Astral Supercomputer at Cranfield University, U.K.

convergence. The results presented in this study are time-averaged which are obtained by averaging nearly 2000 solutions, between a non-dimensional time $\tau \approx 50$ to $\tau \approx 150$, with equal Δt.

A comparison of the accuracy of the two turbulent boundary conditions has been very briefly discussed by Klein *et al.* (in the Figure 1 of [95]) where they showed that the digital filter based turbulent boundary condition they used provided an accurate turbulent flow field, whereas, the conventional random fluctuations dissipated very quickly resulting in no turbulence in the flow field. Six different boundary conditions are utilized in this work to analyze the effect of each on the generation of supersonic turbulent boundary layer in the flow field. Figure 5.2 below presents the instantaneous schlieren view of the STBL generated by six methods at a non-dimensional time (τ = 102.93). From the visual analysis it can be noticed in the Figure 5.2 that for the cases: 1-4 (i.e., the laminar and three random white-noise cases) the incoming flow field is very similar. For the laminar inflow (case-1) the thickness of the boundary introduced at the inflow plane (X/D = -8) is maintained in the flow field up to the jet injection hole.

On the other hand for the random white-noise inflow (cases: 2-4) although the boundary layer thickness is visible but the random noise added to the STBL velocity profile has dampened immediately in the flow field. The result is that the turbulent coherent structures are not visible anywhere in the flow visualization of the cases: 2-4 which could mean that the flow is re-laminarizing. The result in all four cases (cases: 1-4) is that the laminar or re-laminarizing inflow when reached the jet injection hole, it came across a blockage in the flow in the form of the jet plume, and the recirculation zone created at the upstream side of the jet plume is enlarged such that it can be traced back to locations (X/D = -6). It has been established[139, 89, 133] for this JISC flow that the lambda shock is at Mach 1.5 which interacts with the STBL near X/D = -3 location and there are two small recirculation zones upstream of the jet plume confined between

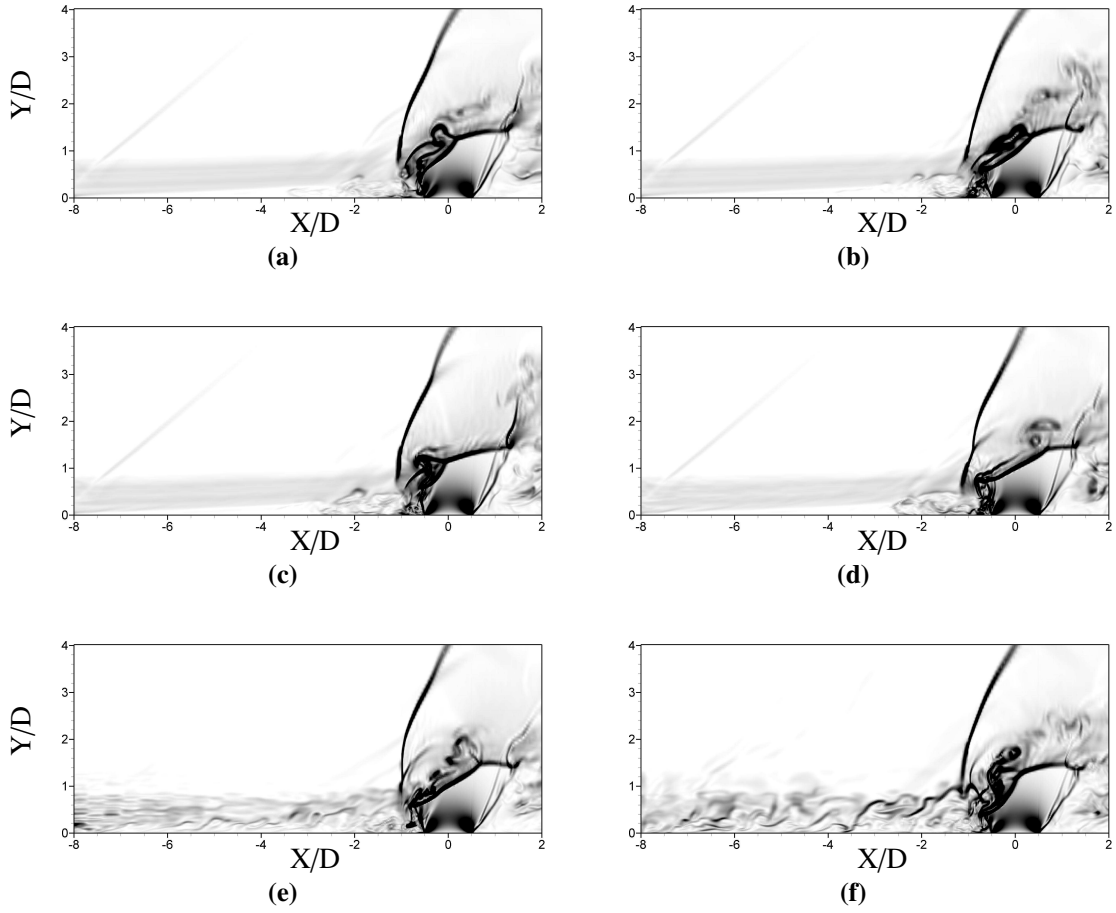

Figure 5.2: *For all six cases; the instantaneous schlieren views of the supersonic turbulent boundary layer at the wall-normal mid plane (Z/D = 0) at the same physical time to understand the development of the STBL (a) case-1; (b) case-2; (c) case-3; (d) case-4; (e) case-5; (f) case-6.*

the jet plume and the lambda shock.

For the Reynolds stress based inflow (case-5 in Figure 5.2(e)) few turbulent coherent structures are visible in the instantaneous flow which indicates that the perturbations introduced are not dampened immediately. The strength of the coherent structures in the boundary layer is, however, slightly less compared to those in the boundary layer in Figure 5.2(f) which is the instantaneous view from digital filter based simulations (case-6). This indicates that for case-5 the turbulence in the boundary is not immediately dampened but losing intensity gradually. As the length of the upstream domain is short the actual effect is not very clear and a detailed analysis of the boundary layer is necessary as it is anticipated that the flow in case-5 would eventually re-laminarize. But for case-6 the fluctuations and coherent structures in the boundary layer are strong to produce the physically correct recirculation zones and the lambda shock which interacts with the STBL near the X/D = -3 location as indicated in the experiment and

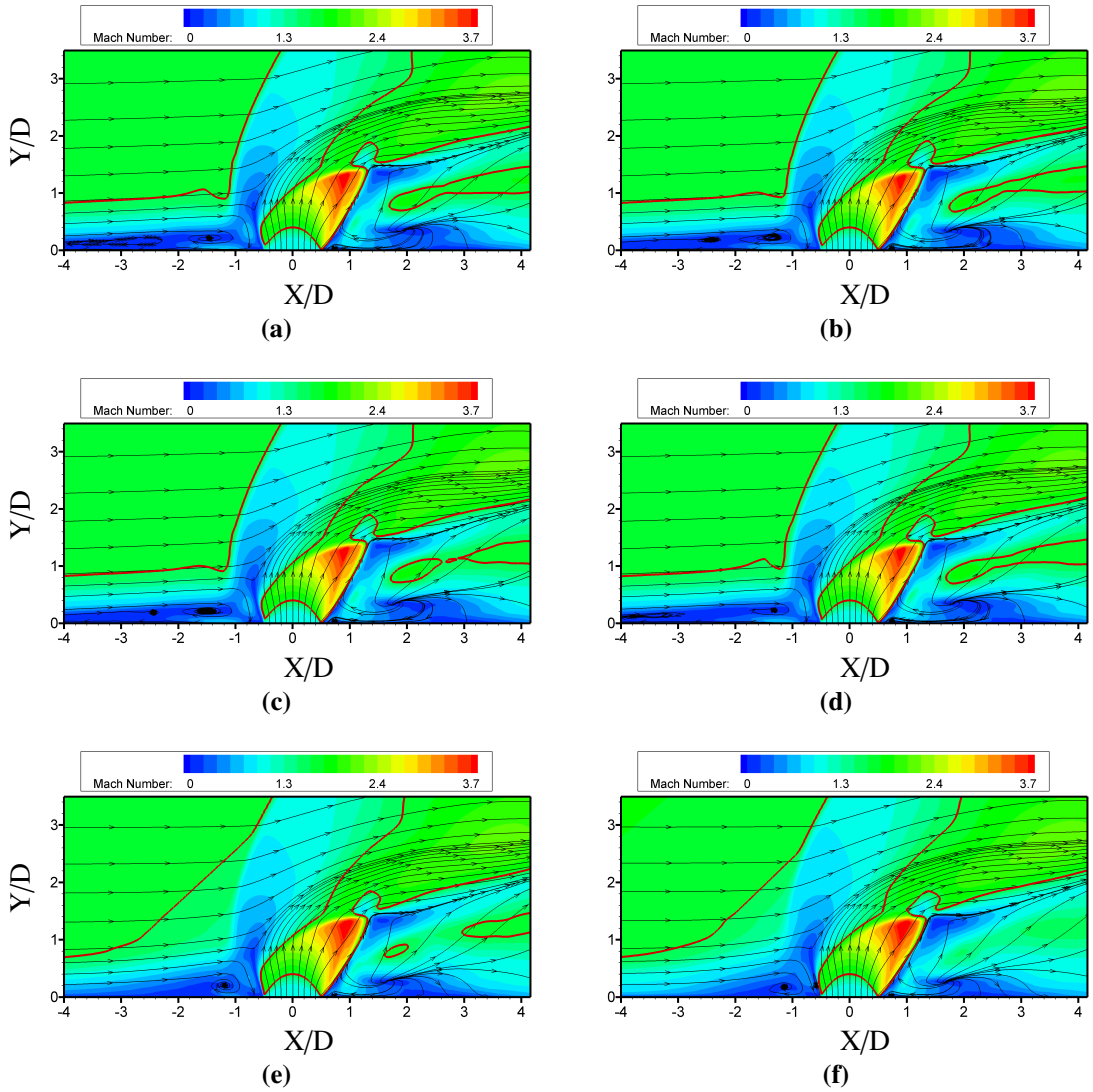

Figure 5.3: *For all six cases; the time-averaged Mach number contours at the wall-normal mid plane (Z/D = 0) showing the flow structure upstream of jet injection hole and the impact of incoming STBL, (a) case-1; (b) case-2; (c) case-3; (d) case-4; (e) case-5; (f) case-6. The red line shows Mach 1.5 location for the lambda shock upstream of the jet plume.*

previous CFD studies.

To understand the overall result of these instantaneous effects Figure 5.3 presents the time-averaged Mach number contours on the wall-normal mid plane (Z/D = 0) for all cases. The red line is the Mach number 1.5 line which for all the cases should show a clearly developed lambda shock except for the case-1 where the inflow was laminar. For the random white-noise cases: 2-4 the lambda shock is not visible in the time-averaged flow. It appears that for cases: 2-4 the incoming boundary layer has dissipated all of the fluctuations introduced at the inflow plane. The immediate result is

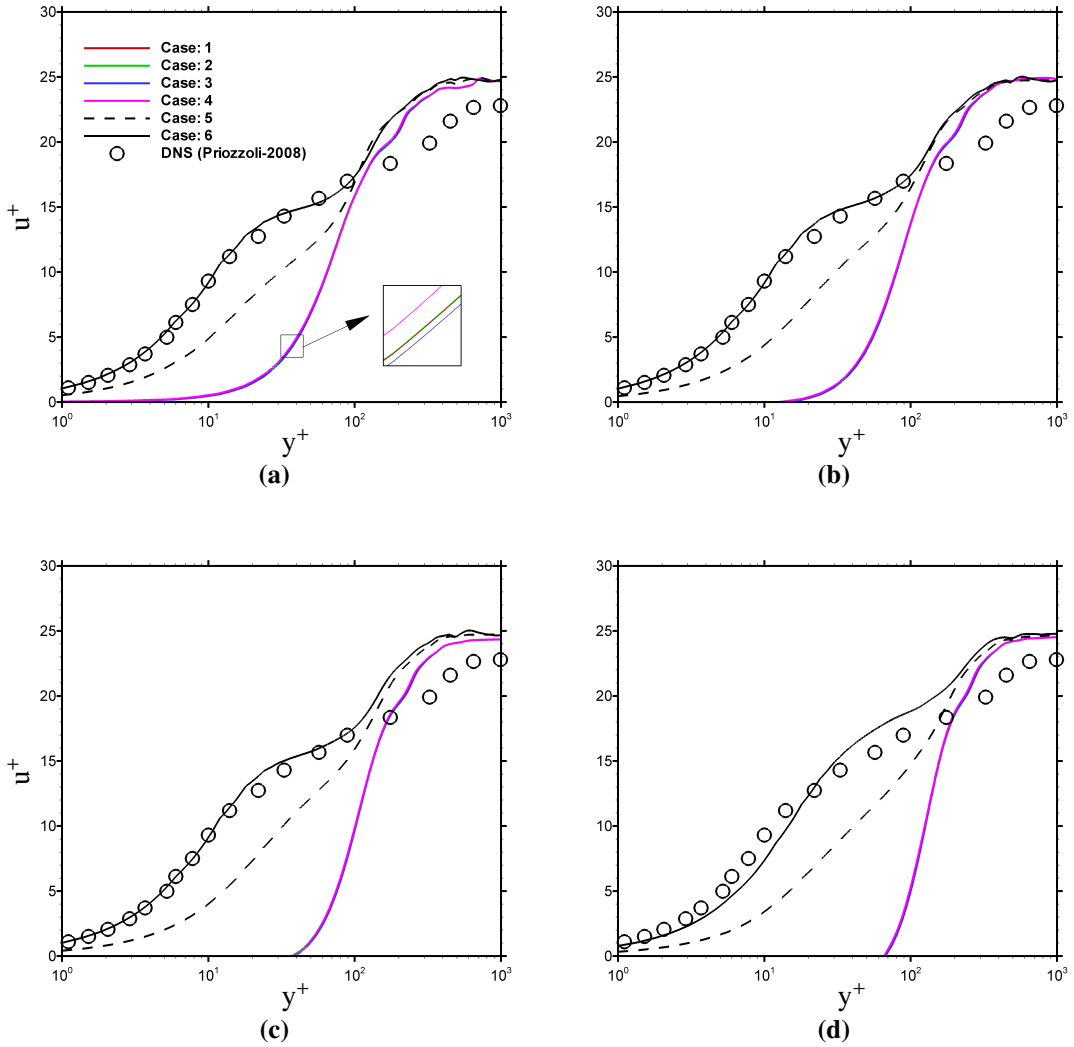

Figure 5.4: *For all six cases; the supersonic turbulent boundary layer is analyzed by plotting the mean streamwise velocity (u^+) against non-dimensional wall-normal distance (y^+) on a semi-logarithmic scale at various locations to understand the development of the STBL (a) X/D = -6.5; (b) X/D = -6; (c) X/D = -5; (d) X/D = -4.*

the longitudinal growth of the recirculation region upstream of the jet injection similar to the recirculation zone for laminar case in Figure 5.3(a). On the other hand, for case-5 the lambda shock is visible but only one recirculation zone is visible contrary to the established knowledge of the flow field from experiments and CFD analysis. In the digital filter based turbulent boundary condition (case-6), however, the stream lines in the Figure 5.3(f) indicate two small recirculation zones in accordance with established knowledge. Although the downstream analysis is presented in the next section, here is important to mention that this discrepancy results in an incorrect capture of flow physics upstream and downstream of jet injection even in the case-5 where the lambda

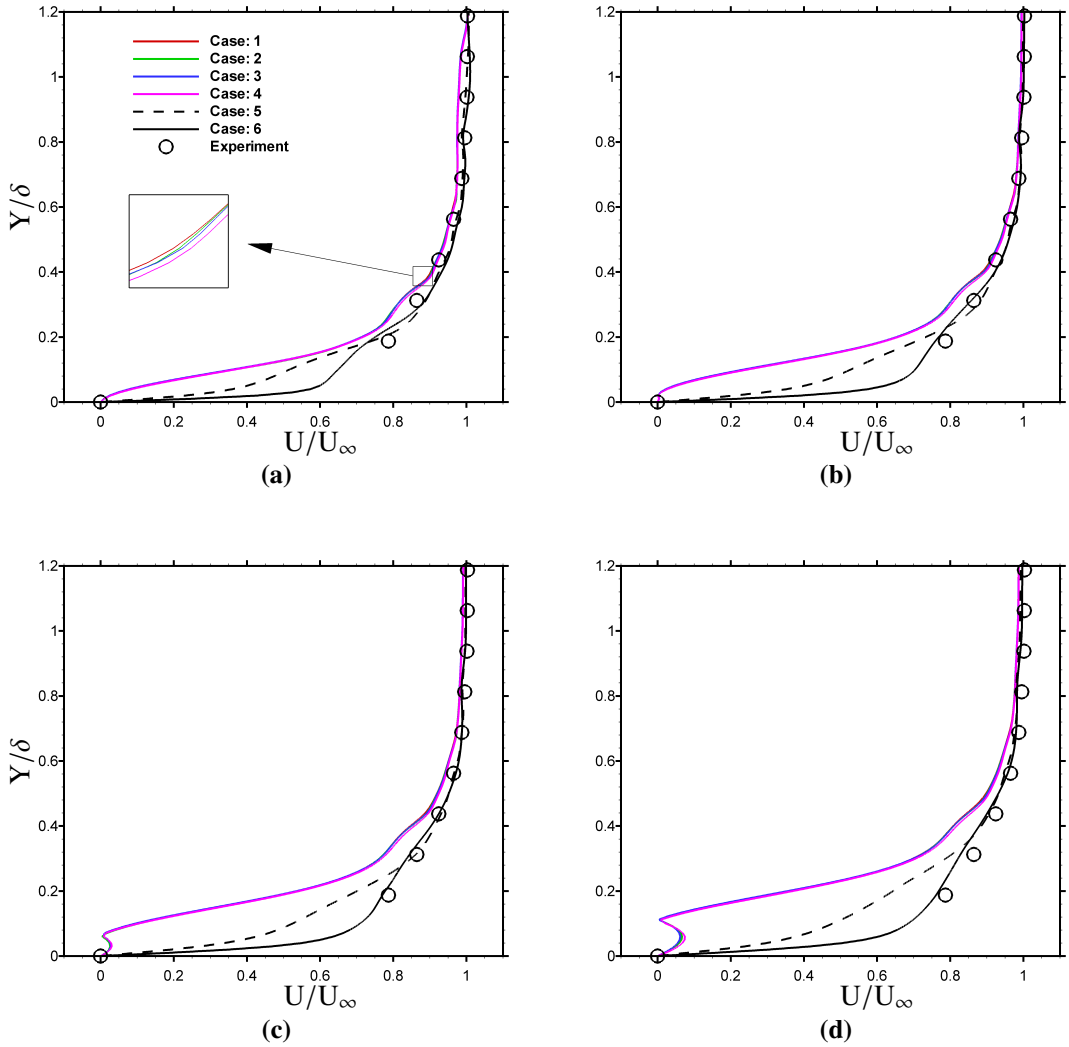

Figure 5.5: *For all six cases; the mean streamwise velocity (U/U_∞) against wall-normal distance non-dimensionalised by the thickness of boundary layer (y/δ) at various locations to understand the development of the STBL (a) X/D = -6.5; (b) X/D = -6; (c) X/D = -5; (d) X/D = -4, and the results are compared with the average velocity profile from the experiment[139].*

shock is developed.

Figure 5.4 presents the mean streamwise velocity profile plotted using the Van Driest transformation[126] against the non-dimensional wall distance on a semi-logarithmic scale for all six cases and the results are compared with the DNS of Pirozzoli[123]. In order to systematically analyze the incoming boundary layers in each case, the plots are provided for the upstream locations X/D = -6.5, -6, -5 and -4. A turbulent boundary layer plot should clearly show a log-layer (fully turbulent region), a buffer zone and viscous sublayer. In the case of the digital filter based inflow boundary condition

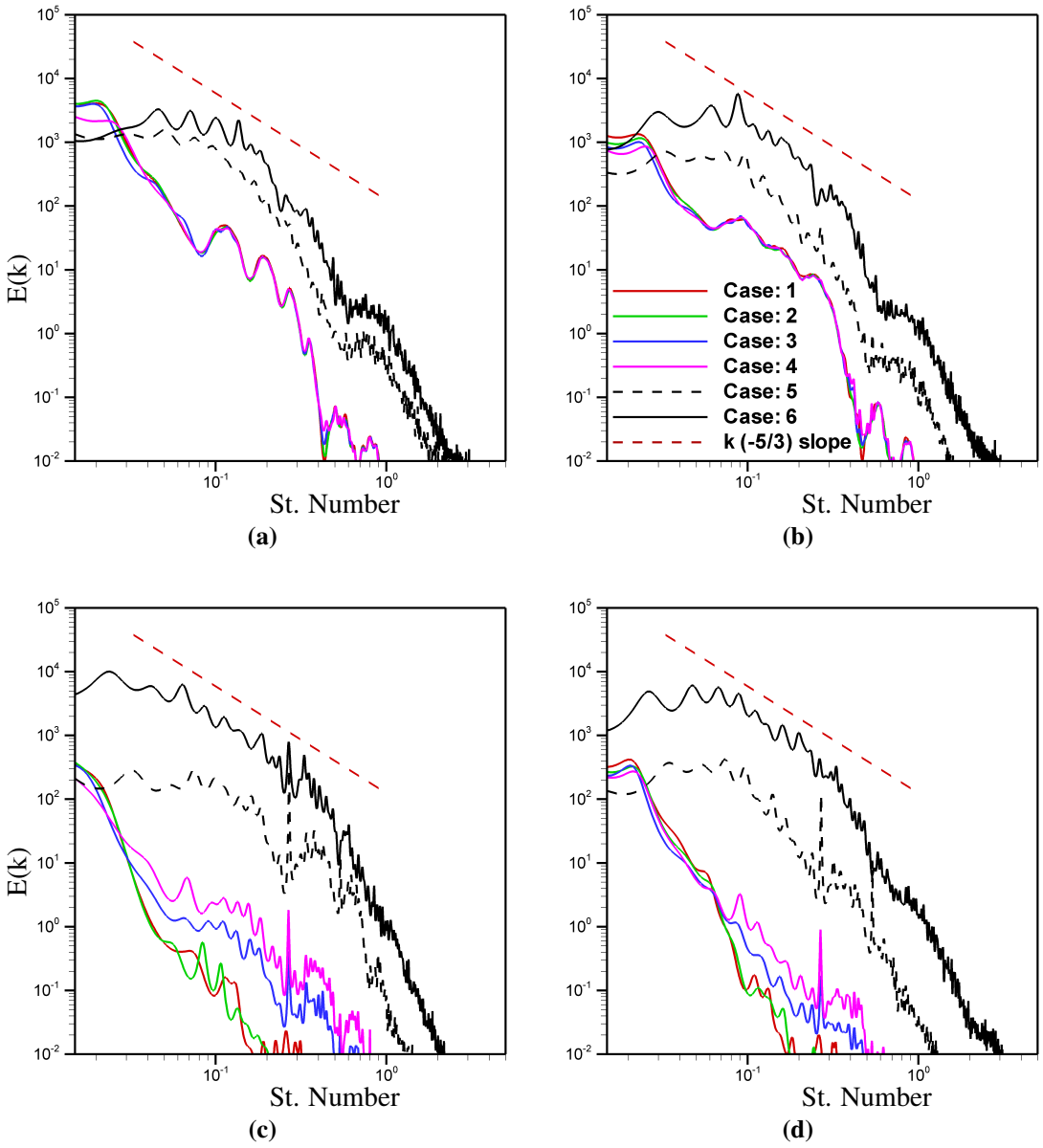

Figure 5.6: *For all six cases; Spectrum analysis of the incoming turbulent boundary layer at various locations on the wall-normal mid plane (Z/D =0) at (X/D, Y/D), (a) at (-6.5, 0.35); (b) at (-6, 0.35); (c) at (-5, 0.35); (d) at (-4, 0.35)*

(case-6) one can easily compare the velocity profile with a fully developed turbulent boundary layer velocity profile showing all the above mentioned regions clearly at all the upstream locations exhibiting a nice match with the DNS data. Although, the plot of the viscous sublayer region lacks confidence as the y^+ was set at 14, as the linearly interpolated data in this region is in agreement with the DNS data. It should be mentioned here that as the location X/D = -4 is very close to the lambda shock and the recirculation region (which can affect the boundary layer profile) hence a slight

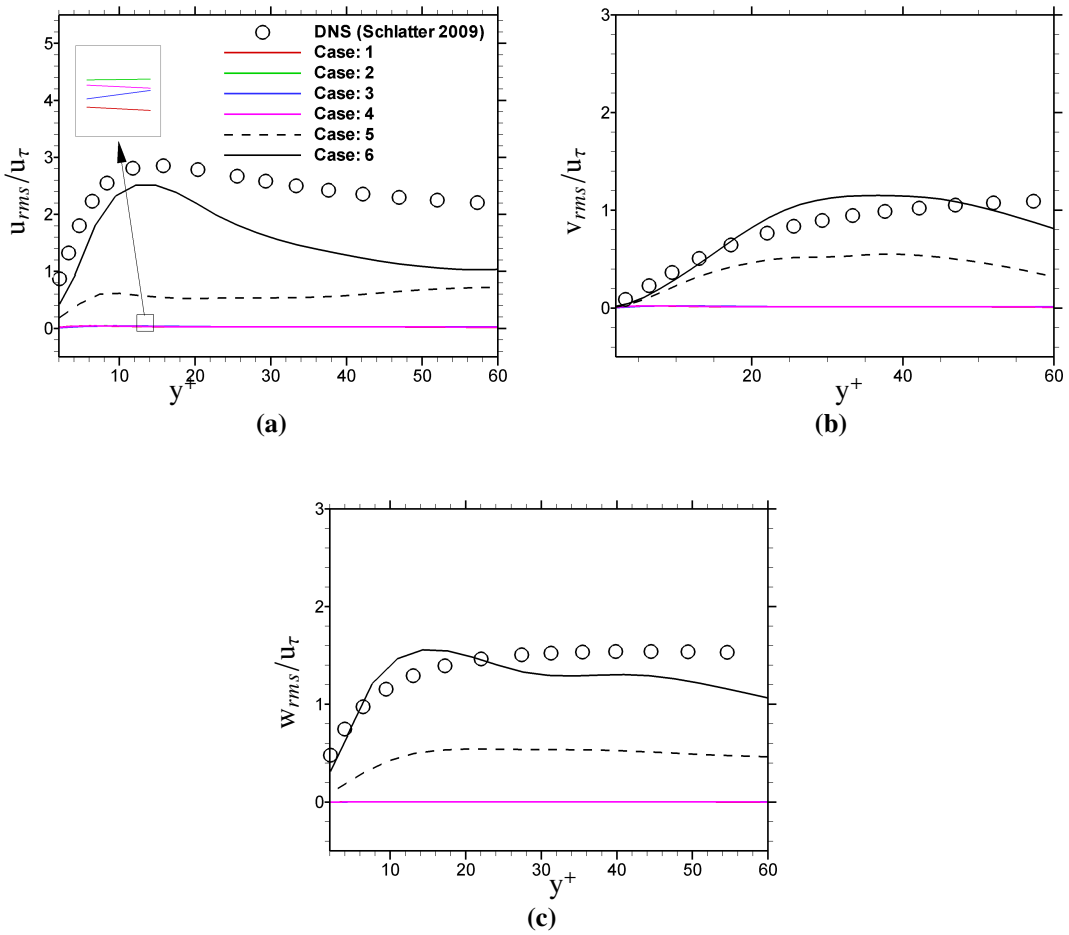

Figure 5.7: *For all six cases; the RMS of velocity fluctuations are plotted against the non-dimensional wall-normal distance at the X/D = -5 location on the wall-normal mid plane (Z/D = 0), (a) u_{rms}/u_τ plot ; (b) v_{rms}/u_τ plot; (c) w_{rms}/u_τ plot.*

discrepancy in the case-6 results can be observed at location X/D = -4. For the case-5, however, a clear log-layer region is not visible and furthermore, the profile obtained at location X/D = -6.5 has flattened at location X/D = -4 showing no log-layer. This indicates that for case-5 although we see some turbulence in the upstream boundary layer but it is being dissipated gradually. On the other hand for the cases: 2-4 the typical log-layer in a turbulent boundary layer is not visible even at the location X/D = -6.5 and the same profile continues up to the location X/D = -4; the profiles indicate a re-laminarized flow similar to the laminar inflow case-1.

The major difference in a turbulent and laminar velocity profile is that a turbulent velocity profile is much fuller than the laminar velocity profile and steep gradients in velocity are found closer to the wall. Figure 5.5 presents the velocity profiles for the six cases at various locations on the wall-normal mid plane (Z/D = 0) and compares the results with the experimental data which have been extracted at location X/D = -5.

These plots exhibit the development of the velocity profiles in each case and present (if any) the effects of the upstream recirculation regions on the velocity profiles. For the laminar inflow (case-1) the velocity profile shows the recirculation zone reaching up to X/D = -6.5 and closer to the jet plume the effect of the recirculation region on the velocity profile is becoming more visible at location X/D = -5 and -4. For the random white-noise (cases: 2-4) the velocity profiles match that from the laminar inflow case (case-1), as also shown in the Figure 5.2(a-d) and Figure 5.3(a-d) because of the immediate dampening of the fluctuations in the flow field. Closer to the wall all these four cases (cases: 1-4) show the presence of a recirculation zone upstream of the jet injection. The velocity profile for case-5, although, does not show the longitudinally enlarged recirculation zone but the velocity profiles for case-5 are closer to a laminar velocity profile with moderate velocity gradients closer to the wall. For case-6 the velocity profiles remain "fuller" as expected for a developed turbulent boundary layer and steep gradients in the velocity profiles can also be seen for the case-6. Although from the experiment the values close to the wall are not available but the velocity profile for case-6 is a close match to the experimental data.

Figure 5.6 presents the energy spectrum on the wall-normal mid plane (Z/D = 0) for all six cases against the Strouhal number (St). The location for the energy spectrum points is within the boundary layer at Y/D = 0.35 and X/D = -6.5, -6, -5 and -4. The energy spectra show a possible inertial range following Kolmogorov's $k^{-5/3}$ trend for the cases 5 and 6 towards the start of the computational domain. For the case-5 the turbulence is dissipating gradually having, firstly, smaller levels of energy compared to the case-6 in all the ranges, and secondly, the spectra dissipation is greater case-6. For cases: 1-4, the energy levels for all the ranges is much lower than the cases: 5 and 6 and no energy containing range is visible in the spectra. At locations X/D = -6.5 and -6 the spectra for cases: 1-4 follow the same trends, however, at locations X/D = -5 and -4 are slightly different. Despite this, similar trends are shown indicating almost no inertial range and hence a laminar flow.

Finally, Figure 5.7 shows the variance of fluctuations (u_{rms}, v_{rms}, w_{rms}) for all six cases on the wall-normal mid plane (Z/D = 0) at X/D = -5 location where recently performed DNS data from Schlatter *et al.*[142] is utilized for comparison. These plots exhibit the trends observed in the discussion above that for cases: 2-4 there are nearly zero fluctuations present in the flow field resembling a laminar inflow (case-1). For the Reynolds stress method (case-5) some fluctuations are visible but smaller in scale than case-6. Whereas, for case-6 the plots show a reasonable match between the ILES and DNS data with the digital filter based method. From the above discussion, it can be established now that although fluctuations were introduced at the inflow boundary for cases: 2-4, dissipation is rapid and the resultant inflow is laminar. For case-5 where only the Reynolds stress tensor was used and the exponential correlation was eliminated for obtaining the turbulent inflow data the results are slightly better than cases: 2-4 but still the fluctuations in the flow field are gradually dissipating and there is a phases difference between the case-5 and case-6 results. On the other hand, in case-6, where the digital filter based turbulent inflow boundary condition was used, the flow

field upstream of jet injection remains fully turbulent resulting in a fully developed STBL from the start of computational domain till the jet injection. In the next sections, the effects of incoming laminar and turbulent flows are discussed for the JISC case.

5.5 Effects of Inflow on JISC Flow

5.5.1 Velocity Field Analysis

To understand the effects that the incoming boundary layer can have on the flow at and downstream the jet injection, an analysis of the velocity field is presented in this section. Figure 5.3 presented Mach number contours at the mid plane (Z/D = 0) for six cases of simulations where the red line indicated the Mach 1.5 line for the lambda shock. It appears that for case-5 and case-6 the lambda shock is captured correctly, but a comparison of these two cases is presented in Figure 5.8. This comparison demonstrates that although there is a similar lambda shock for case-5, but it is not captured correctly and is offset to lambda shock for case-6. There are, also, additional Mach 1.5 lines which are not visible in the experimental data[139] or the ILES data in case-6. This discrepancy in the lambda shock will have effect on the upstream pressure distributions closer to the jet plume (discussed later).

It can be noticed in Figures 5.3 that for the case-6 the height of the recirculation zone upstream of jet plume is larger than all other cases. Due to this height of the recirculation zone in case-6, the bow shock is positioned away from the flat-plate and the net result is a generation of thick (in height) horseshoe vortex around the jet injection position. This horseshoe vortex is present in the earlier five cases as well but it is smaller in height than in case-6. It is, also, noted from Figure 5.3 that the Mach disc is captured in cases: 5 and 6 whereas in first four cases the Mach disc is not captured correctly. Figure 5.9 shows the Mach number contours at the wall-parallel plane (Y/D = 1) along

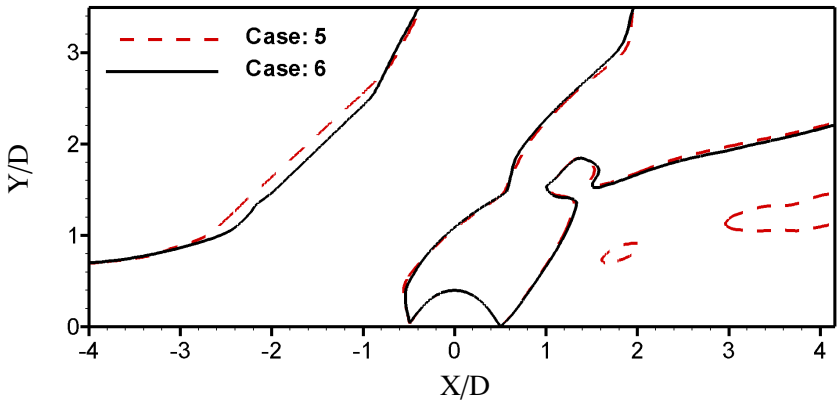

Figure 5.8: *Mach 1.5 lines are shown for the case-5 and the case-6 showing the incorrect capturing of the location of the lambda shock with case-5.*

with the streamlines where this effect can be visualized better. Here in the Figure 5.9(a) two areas are highlighted by circles “A” and “B”. Analysis of Figures 5.9(a-f) in these areas shows that the cases: 1-4 exhibit similar Mach number contours i.e., same behaviour of flow physics and for case-5 the contours are slightly improved, but the contour plot for case-6 is very much different especially in the areas “A”. Similar trends in contours can be seen in area “B” in the Figures 5.9(a-f).

Figure 5.10-5.12 show the Mach number contours on the wall-normal cross-view planes (X/D = 1, 3 and 5) along with the streamlines. The contour plots for the first four cases (cases: 1-4) are very similar, therefore for the purpose of brevity Figures 5.11 and 5.12

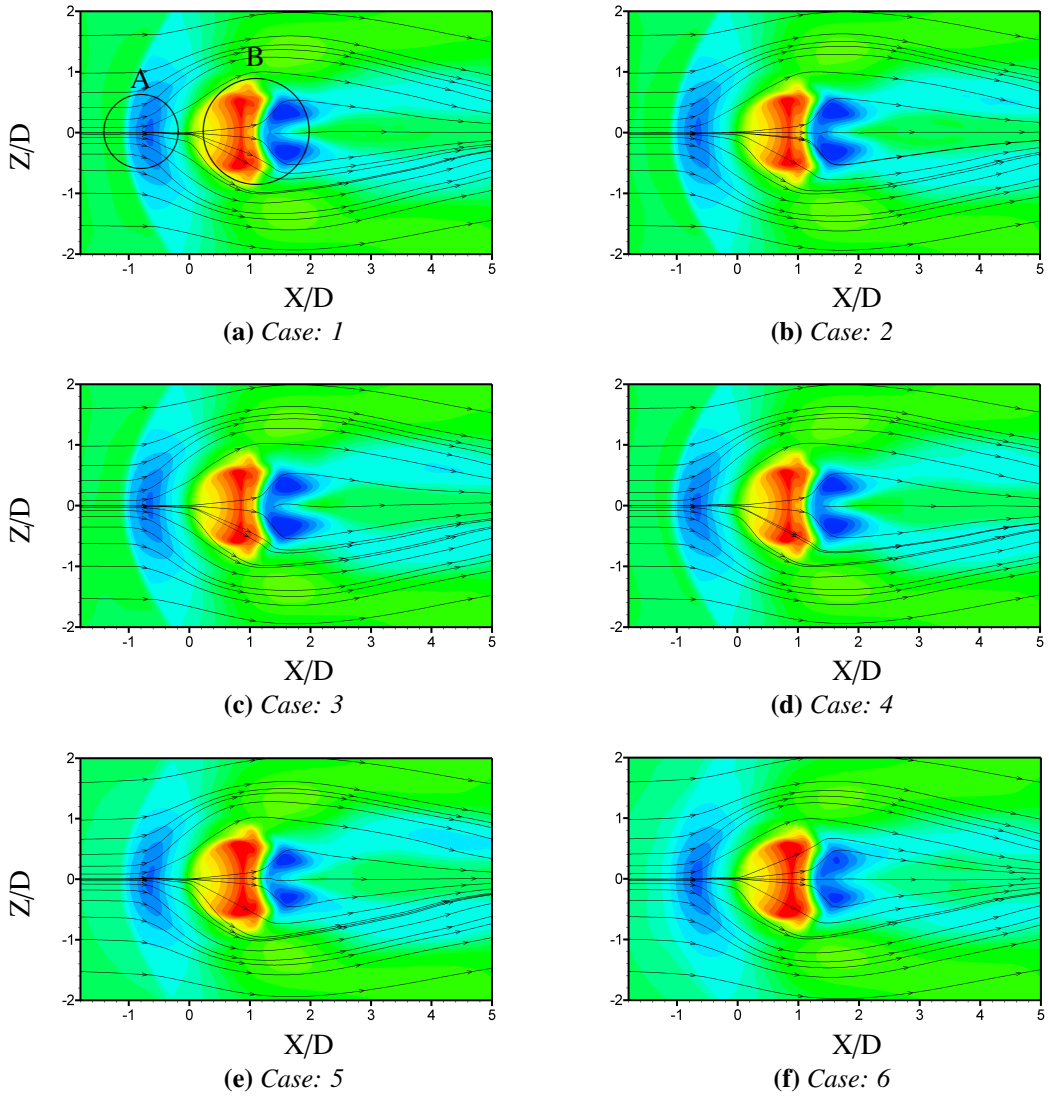

(a) *Case: 1* **(b)** *Case: 2*

(c) *Case: 3* **(d)** *Case: 4*

(e) *Case: 5* **(f)** *Case: 6*

Figure 5.9: *For all six cases: Mach number contour plots on wall-parallel plane (Y/D = 1) showing various flow features captured for each case showing similar contours for cases: 1-4, where as for cases: 5 and 6 the contour plots are slightly different. (contours legend same as in Figure 5.3).*

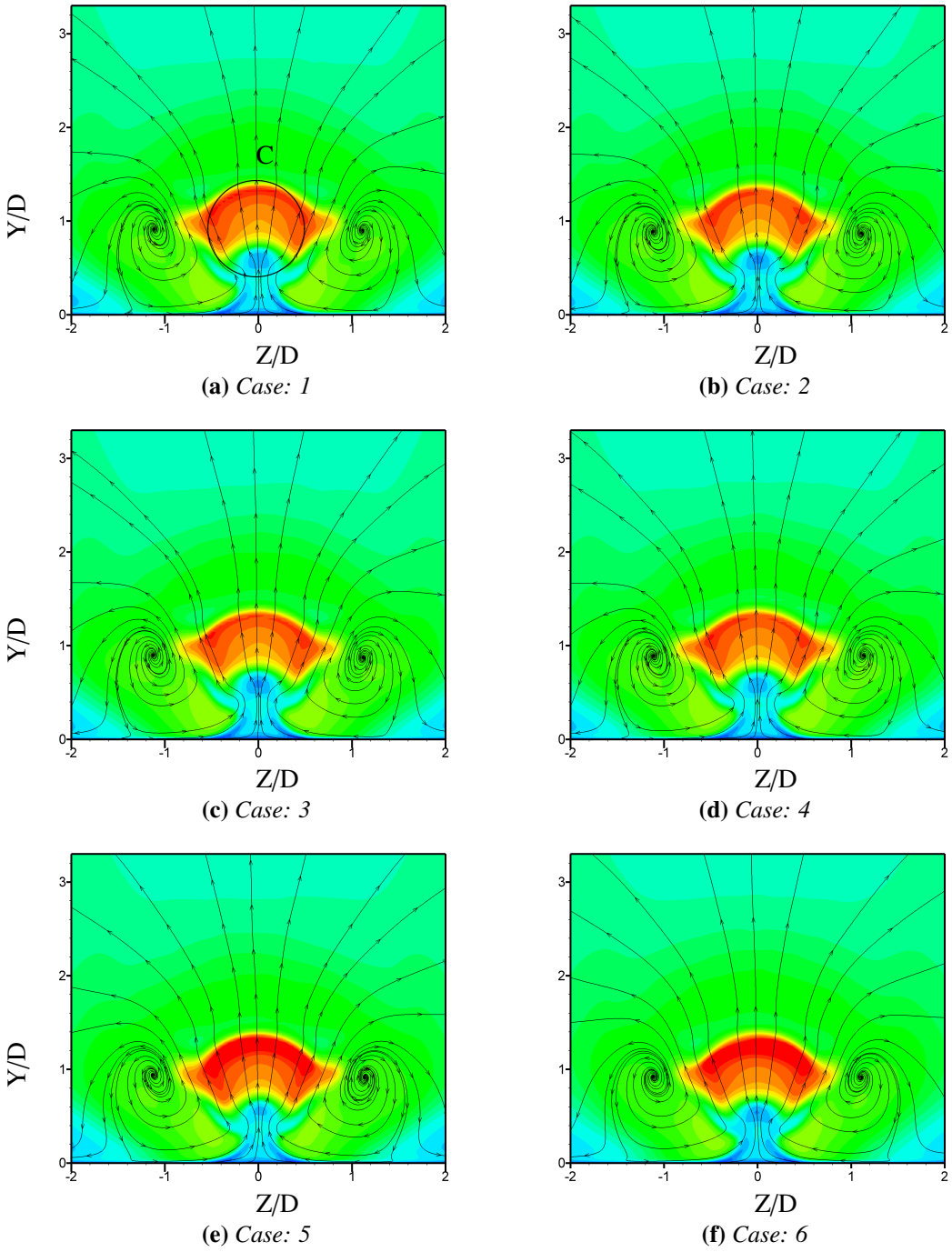

(a) *Case: 1* **(b)** *Case: 2*

(c) *Case: 3* **(d)** *Case: 4*

(e) *Case: 5* **(f)** *Case: 6*

Figure 5.10: *For all six cases: Mach number contour plots on wall-normal cross-view plane (X/D = 1) showing various flow features captured for each case showing similar contours for cases: 1-4, where as for cases: 5 and 6 the contour plots are slightly different. (contours legend same as in Figure 5.3).*

only show one of three cases i.e., only contour plots for case-1 and 4 are shown from now on as the representative of all three cases of random white-noise based cases (2-4). In Figure 5.10, the generation of kidney-shaped counter-rotating vortices (CRVs) is clear at the X/D = 1 plane. The CRVs are more spread out in the cases: 5 and 6 than in the earlier cases: 1-4. Figure 5.11 and 5.12 also show the similar trends that for cases: 1-4 the streamlines showing the CRVs are closely packed, whereas, in case-5 the streamlines are spread out. The emergence of another small CRVs close to the flat-plate is visible which are commonly termed as Transient CRVs (TCRVs).

The CRVs and TCRVs are major features of JISC flow where the CRVs act to enhance the mixing process in the downstream direction of jet injection and in the shear layer. A detailed analysis of how these CRVs and TCRVs act together is presented in the Chapter 4. Generally, the CRVs and TCRVs rotate counter to each other and create a

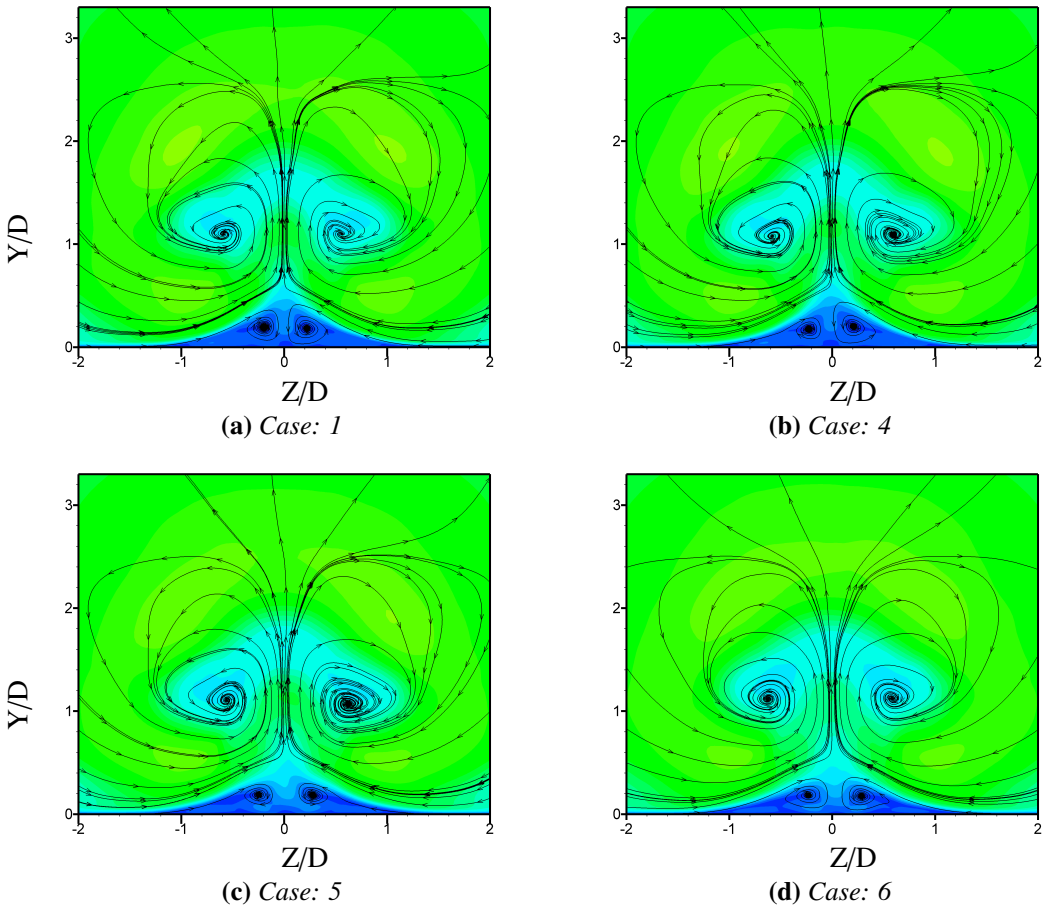

(a) *Case: 1* **(b)** *Case: 4*

(c) *Case: 5* **(d)** *Case: 6*

Figure 5.11: *Mach number contour plots on wall-normal cross-view plane (X/D = 3) showing various flow features captured for each case showing similar contours for cases: 1-4, where as for cases: 5 and 6 the contour plots are slightly different. (contours legend same as in Figure 5.3)(Only case-4 contour plot is shown as representative of the cases: 2-4).*

very active mixing zone downstream of the jet injection and in the spanwise direction. If the spread of the CRVs is not captured correctly, for example due to the lack of an incoming STBL, it can affect the prediction of the flow properties. In Figures 5.10-5.12, close analysis of the area shown as a circle "C" (in Figure 5.10(a)) indicates incorrect capture of Mach number for the cases: 1-4 but for the cases: 5 and 6 the contour maps are similar. To conclude the above, the Mach number contour plots indicate similar plots for the first four cases (case-1-4) and similar plots for the later two cases (cases: 5-6). A quantitative analysis of the velocity can reveal more about how closely the six cases match at the downstream location of the jet plume.

Figure 5.13 and 5.14 presents the streamwise and wall-normal velocity profiles normalized by the mean flow velocity (U_{avg}) on the mid wall-normal plane (Z/D = 0) at various location along the x-axis. In order to understand the effect of incoming

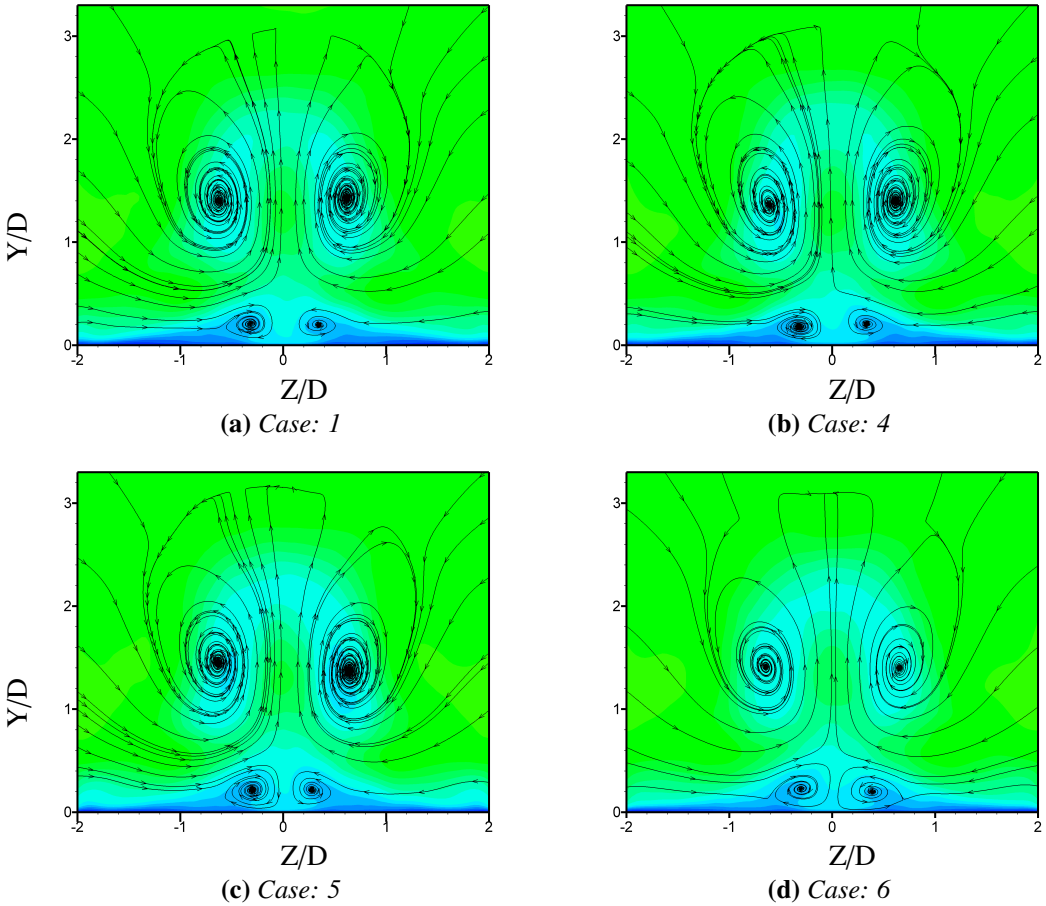

(a) *Case: 1* **(b)** *Case: 4*

(c) *Case: 5* **(d)** *Case: 6*

Figure 5.12: *Mach number contour plots on wall-normal cross-view plane (X/D = 5) showing various flow features captured for each case showing similar contours for cases: 1-4, where as for cases: 5 and 6 the contour plots are slightly different. (contours legend same as in Figure 5.3)(Only case-4 contour plot is shown as representative of the cases: 2-4).*

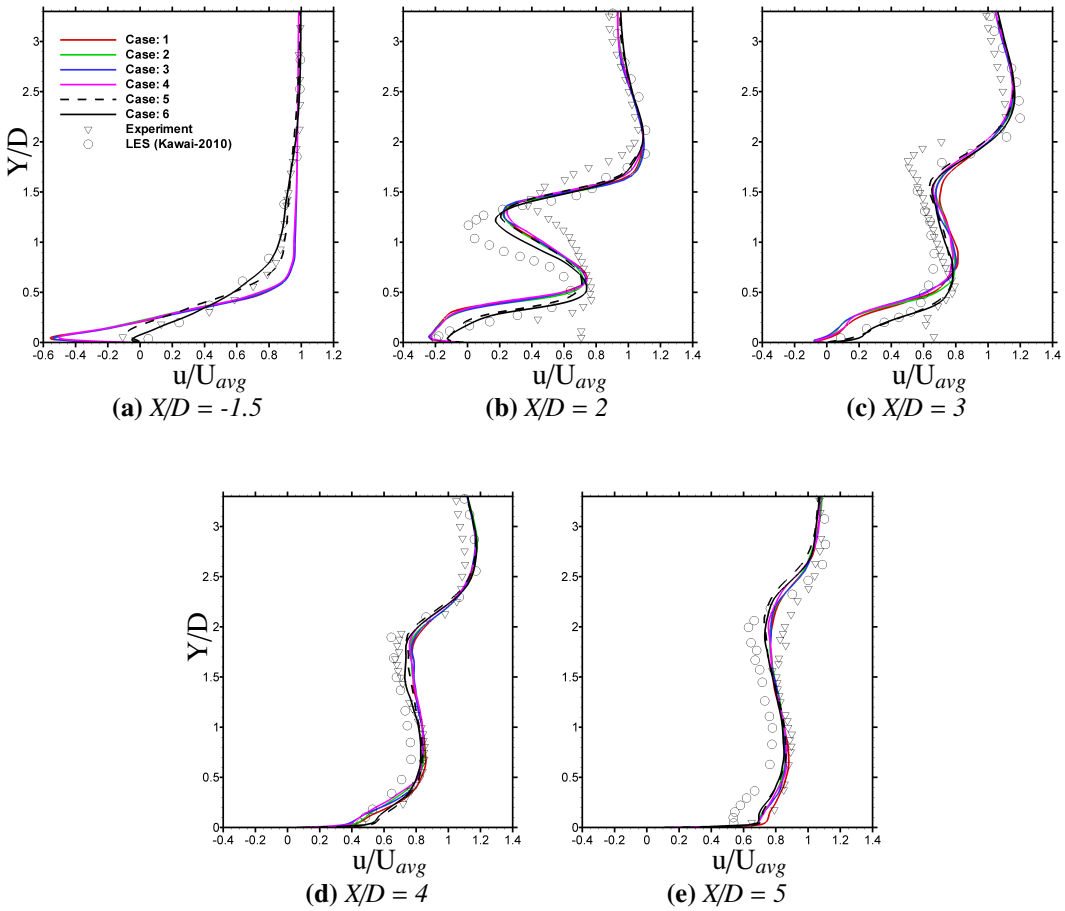

Figure 5.13: *Stream-wise velocity profiles at various locations on the wall-normal mid plane (Z/D = 0) for all six cases and are compared to the experiment and previous LES results shown difference of velocity profiles for turbulent and laminar incoming boundary layers.*

turbulent boundary layer, the velocity plots are compared at the X/D = -1.5 location which is just upstream of the jet injection and is within the very active upstream re-circulation zone. Figure 5.13(a) is the normalized streamwise velocity profile at X/D = -1.5 location. The experimental data has indicated a kink in the velocity profile at approximately Y/D = 2 which is due to the lambda shock and indicates that lambda shock is a weak shock. The velocity profile for cases 1-4 do not exhibit as there is no lambda shock and a large recirculation zone near the wall. On the other hand, the velocity profile for case-5 do show the kink in the profile at Y/D = 2 location but we have learnt from Figure 5.8 the position of lambda shock is incorrect. For the case-6 the streamwise velocity profile clearly shows small jump in the velocity profile and is a nice match to the experimental and classical CFD data including closer to the wall. In the downstream direction at locations X/D = 2 and 3 the velocity profiles for cases: 1-4 are offset from the experimental, classical LES and case-6 data below the Y/D =

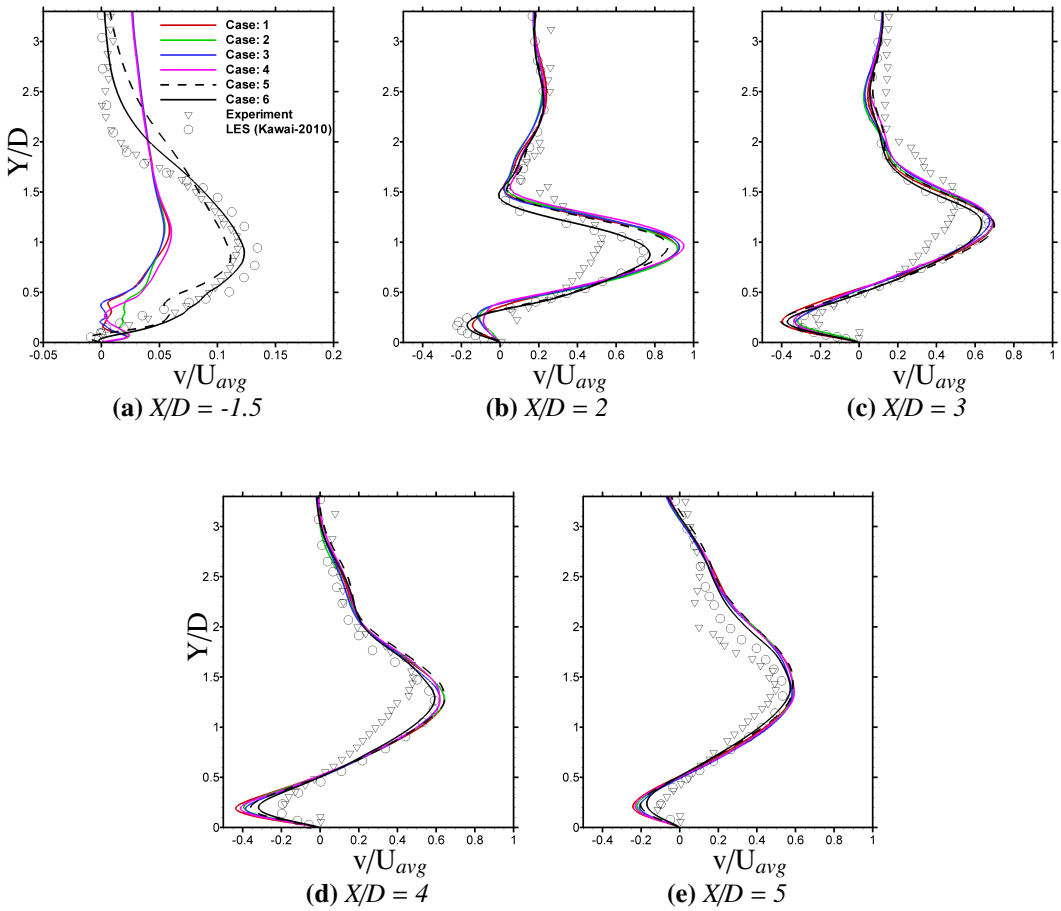

(a) *X/D = -1.5* **(b)** *X/D = 2* **(c)** *X/D = 3*

(d) *X/D = 4* **(e)** *X/D = 5*

Figure 5.14: *Wall-normal velocity profiles at various locations on the wall-normal mid plane (Z/D = 0) for all six cases and are compared to the experiment and previous LES results showing the effect of incoming turbulent and laminar boundary layers.*

2, whereas, above this point all the profiles are in agreement. The case-5 data however shows intermittent behaviour in comparison with the case-6 indicating that although close match to the case-6 but still some discrepancy in the data is exhibited. This difference is more pronounced closer to the jet injection but away from the jet injection at location X/D = 5 all the velocity profiles are very similar.

Wall-normal velocity profiles are shown in Figure 5.14. The profiles for cases: 2-4 at location X/D = -1.5 are all very similar, exhibiting a laminar profile as it matches the profile of the case-1, whereas, for case-6 the profile is in nice agreement with the experimental and classical LES data. Again, case-5 data is tending to follow the case-6 but is slightly offset. Downstream the jet injection a similar trend is seen as for the streamwise velocity profile. In essence, the cases: 1-4 exhibit a laminar profile and case-6 provides a velocity profile with STBL in agreement with the experimental and numerical data. It is observed that major area of concern for JISC flow is closer to the jet injection (upstream and downstream) where the incoming flow would play a major

role. An analysis of turbulent kinetic energy in section 5.5.3 will address the question as to why the velocity profiles for all the cases match at X/D = 5 location.

5.5.2 Pressure Distributions

In this section, an analysis is presented for the pressure distributions on the flat-plate to assess the influence of the incoming STBL using different methods (cases: 1-6). It has been established now that for cases: 2-4, the incoming boundary layer has dissipated the fluctuations and is laminar exhibiting results similar to case-1, whereas, for case-6 the velocity profiles are matching the experiment and classical LES data. Figure 5.15 presents the pressure distributions on the flat-plate in the longitudinal directions at locations Z/D = 0, 1 and 2 in comparison with experimental and classical LES data. For cases: 1-4 the effects of the incoming boundary layer are clear for the pressure distribution as well, where the pressure distributions upstream of the jet injection are well away from the experimental data. The small recirculation region confined between the lambda shock and the jet injection hole increases the pressure distribution on the flat-plate in Figure 5.15(a). A similar pattern is seen in Figure 5.15(b and c) away from the mid plane of the computational grid. For the case-5 it can be noticed that the pressure distribution is somewhere between the laminar/re-laminarized inflow cases (case-1-4) and fully developed STBL (case-6) conforming to our finding in the velocity field analysis. This has been attributed to the slow decay fluctuations in the flow.

In Figure 5.15(b), apart from the difference of the pressure distribution upstream of the jet injection, the pressure peaks are located offset to that as in case-6 or the experimental data. The reason for this is the bow shock and horseshoe vortex discussed earlier. For the cases: 2-4 due to re-laminarization of the incoming flow, the bow shock and

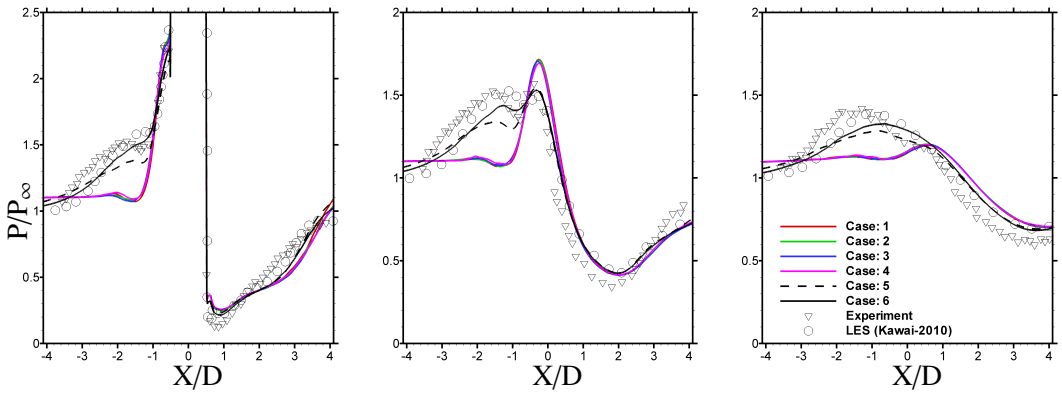

(a) *Z/D = 0* **(b)** *Z/D = 1* **(c)** *Z/D = 2*

Figure 5.15: *Pressure distributions at various longitudinal locations on the flat-plate and are compared to the experiment and previous LES results showing the effects of incoming turbulent and laminar boundary layers.*

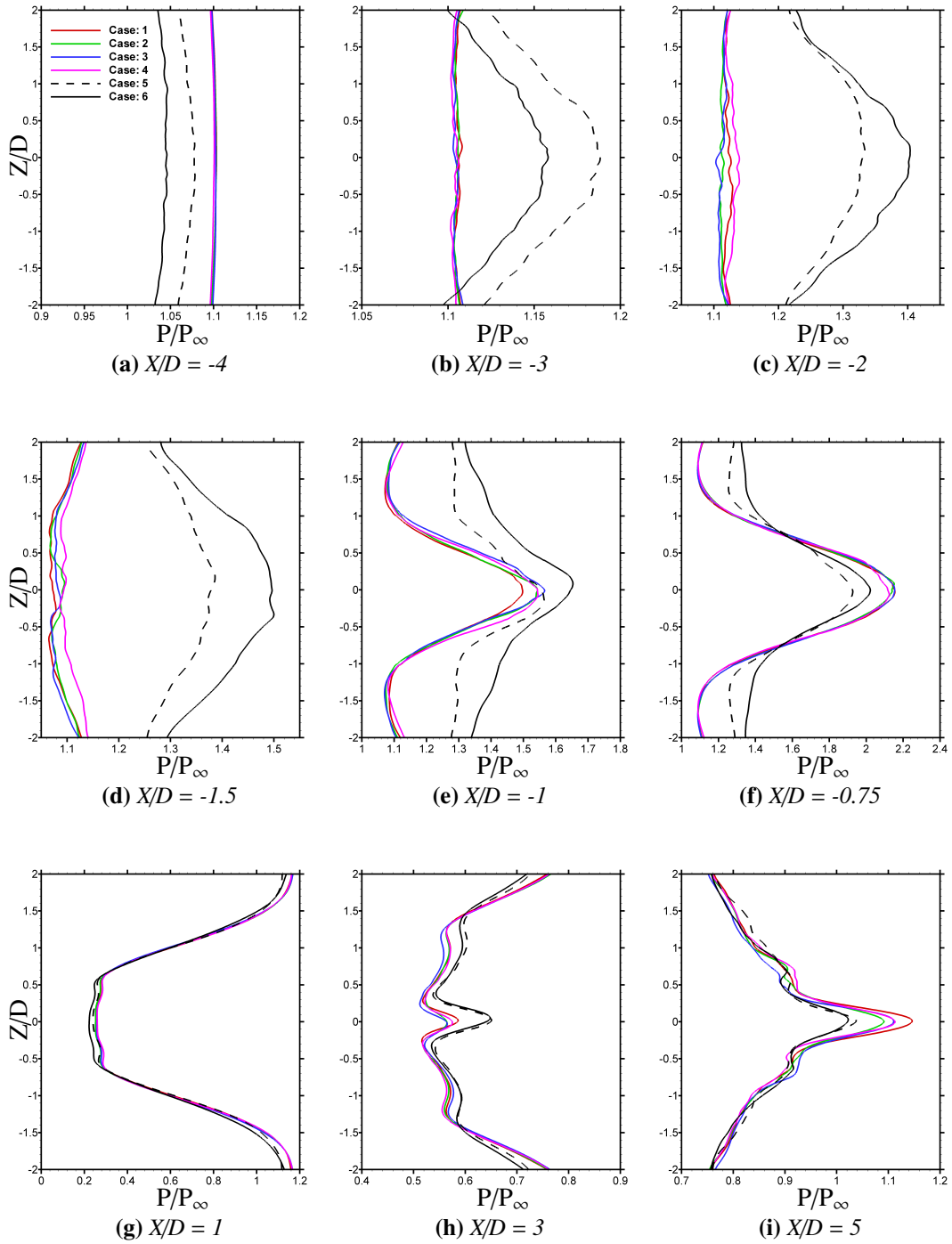

(a) *X/D = -4* **(b)** *X/D = -3* **(c)** *X/D = -2*

(d) *X/D = -1.5* **(e)** *X/D = -1* **(f)** *X/D = -0.75*

(g) *X/D = 1* **(h)** *X/D = 3* **(i)** *X/D = 5*

Figure 5.16: *Pressure distributions at various spanwise locations on the flat-plate showing the effects of incoming turbulent and laminar boundary layers.*

the horseshoe vortex are not located at the correct position and are offset. This effect has become prominent further away at (Z/D = 2) location where it appears that the bow shock is weakened to extent that pressure jump is very small compared to case-6. Although the pressure distribution is similar in all six cases tending towards the experimental data, there is still a small offset between the profiles of cases 1-5 and case-6 values downstream of the jet injection.

This analysis has been extended to study the span-wise pressure distributions on the flat-plate at various locations along the x-axis in the Figure 5.16 where span-wise pressure is plotted at location X/D = -4, -3, -2, -1.5, -1, -0.75, 1, 3 and 5. More upstream locations have been chosen here to emphasize the importance of incoming STBL. At location X/D = -4 we observe lower pressure for case-6 than for cases 1-4 due to the fact that for the earlier cases the upstream recirculation zone has extended "unrealistically". In case-5, the pressure distribution is between case-6 and cases: 1-4 due to the fact that the lambda shock in case-5 is not located at the correct position. The outcome is a slightly larger recirculation zone which resulted in the pressure measurements higher for the case-5 at the locations X/D = -4 and -3. At location X/D = -3, the effects of thickened recirculation zone for case-6 and lambda shock are clearly visible. As the lambda shock is a circular arc around the bow shock with maximum strength on the mid plane, there is maximum pressure in the mid plane at this location.

Closer to the jet injection, the pressure for the case-6 is higher than all other cases, which do not capture the second recirculation zone present in this area very close to the jet plume. At location X/D = -1, a sudden increase in the pressure is observed but cases: 1-4 do not match the case-6 whereas for X/D = -0.75 the pressure overshoots the case-6 profile. Downstream of jet injection we observe the same offset in the pressure distributions but the difference here is small compared to the upstream pressure distribution. One important feature to notice here is that away from the mid plane and near the Z/D = ±2 locations there is large offset in pressure measurements which is due to the incorrect location of bow shock and horseshoe vortex in cases 1-5. From all these figures we observe that for laminar (case-1), random white-noise (cases: 2-4) and the case-5, an unrealistic pressure distribution is obtained that can mislead the engineering analysis.

5.5.3 Turbulent Kinetic Energy (TKE)

In this section turbulent kinetic energy (TKE) is presented for the flow field comparing the six cases (cases: 1-6) with the classical LES data of [89] where no experimental data is available for comparison. TKE for the flow field has been calculated as below:

$$TKE = \left(\langle u'u' \rangle + \langle v'v' \rangle + \langle w'w' \rangle\right) / 2U_{\infty}^{2} \tag{5.8}$$

Figure 5.17 shows contours of TKE on the mid wall-normal plane (Z/D = 0) for cases: 1, 4, 5 and 6. First of all, notice that the position of the bow shock is close to the flat-

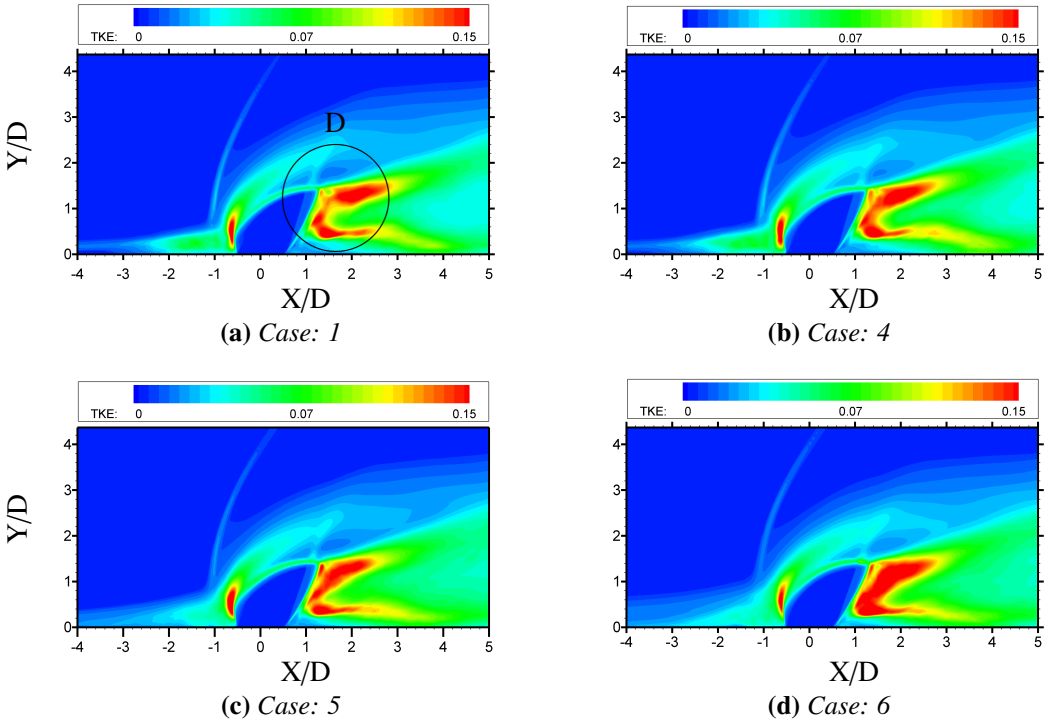

Figure 5.17: *Turbulent kinetic energy (TKE) contour plots on the mid wall-normal plane (Z/D = 0) showing areas of maximum and minimum TKE.*

plate for case: 1, 4 and 5 as compared to the case-6 where in Figure 5.17(d) the STBL has thickened and thus the bow shock is away from the flat-plate. For this reason the angle of the bow shock has changed slightly as well. Focusing on the area referred to as circle "D", although the areas of high TKE concentration are similar in all cases, in case-6 it can be noticed that the downstream high TKE region is showing slightly higher contour regions compared to the other cases.

Figure 5.18 presents the TKE contours on the wall-parallel plane (Y/D = 1) for cases: 1, 4, 5 and 6. The effect of the thickened upstream recirculation zone is much clearer in this contour plot comparing the area indicated by the circle "E" in the Figure 5.18 where we can see the bow shock at the Y/D = 1 plane but for the case-6 the bow shock is not visible on this plane. Comparatively higher TKE is present in the jet shear layer in case-6 compared to the other cases in the area "F". Figure 5.18(d) also represents a more spread-out TKE region as compared to confined TKE region in Figure 5.18(a-c).

The jet shear-layer is a major activity zone generating Kelvin-Helmholtz instabilities (KHI). In the first five cases the incoming boundary layer does not remain very turbulent, whereas in case-6, the incoming STBL enhances the activity in this area and hence effects the results in the jet shear layer[133]. This answers the question raised earlier as to why the velocity and pressure distributions are different nearer to the jet plume yet away from the jet (at X/D $\approx$ 5) look similar. This is because maximum TKE is present in the region closer to the jet plume enhanced by the incoming STBL, but

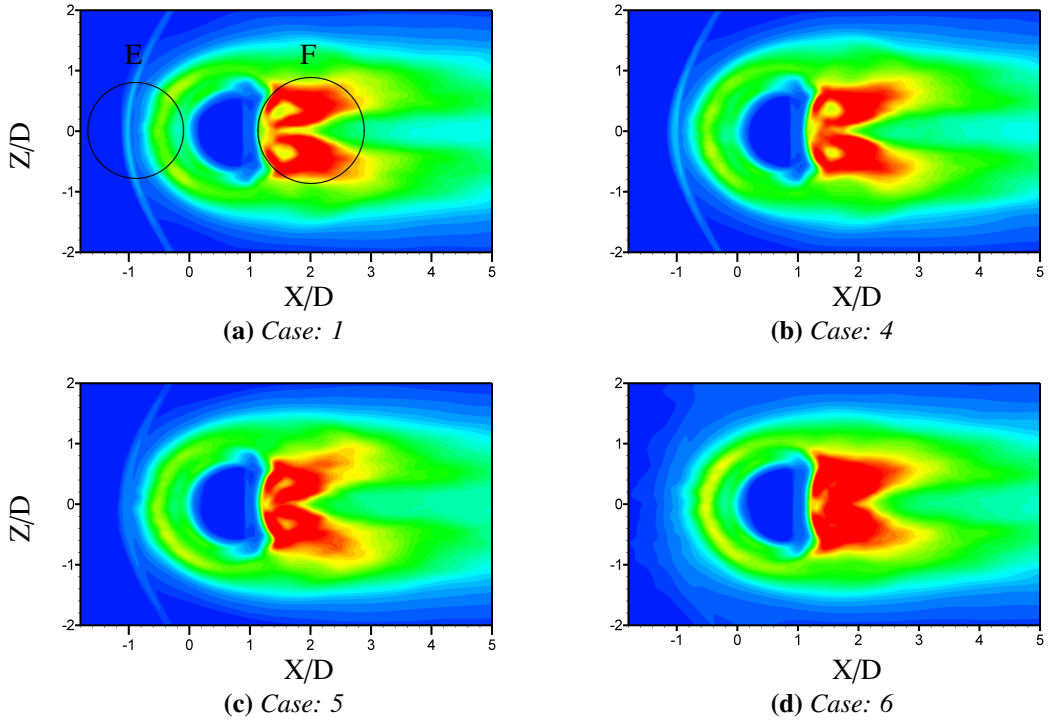

(a) *Case: 1* **(b)** *Case: 4*

(c) *Case: 5* **(d)** *Case: 6*

Figure 5.18: *Turbulent kinetic energy (TKE) contour plots on the wall-parallel plane (Y/D = 1) showing areas of maximum and minimum TKE.*

further downstream the jet plume where TKE has dissipated the flow exhibits nearly same features for all six cases.

Figure 5.19 shows the plots of TKE on the mid wall-normal plane (Z/D = 0) in comparison with the classical LES data[89]. At the X/D = 0 location some discrepancy is visible between the cases: 1-5 and case-6 in the shear-layer region. This discrepancy is further exaggerated at locations X/D = 1, 2 and 3. At location X/D = 4 all the TKE values are similar which indicates that in case-6 the TKE has also dissipated and eventually all the cases exhibit the same results far from the jet plume. The jet shear-layer is the major mixing zone and due to the fact that TKE in this region is enhanced in case-6, mixing can be captured better by using the STBL simulated with adequate accuracy. Figure 5.20 presents a comparison of RMS of the jet fluid passive scalar fluctuations at various locations on the mid plane (Z/D = 0) where, again, a slight discrepancy can be observed between the cases: 1-5 and the case-6.

5.6 Summary

The objective of this chapter was to compare different inflow boundary conditions with the digital filter based turbulent inflow data generator to find the most accurate and computationally efficient method for turbulent unsteady simulations. To achieve this

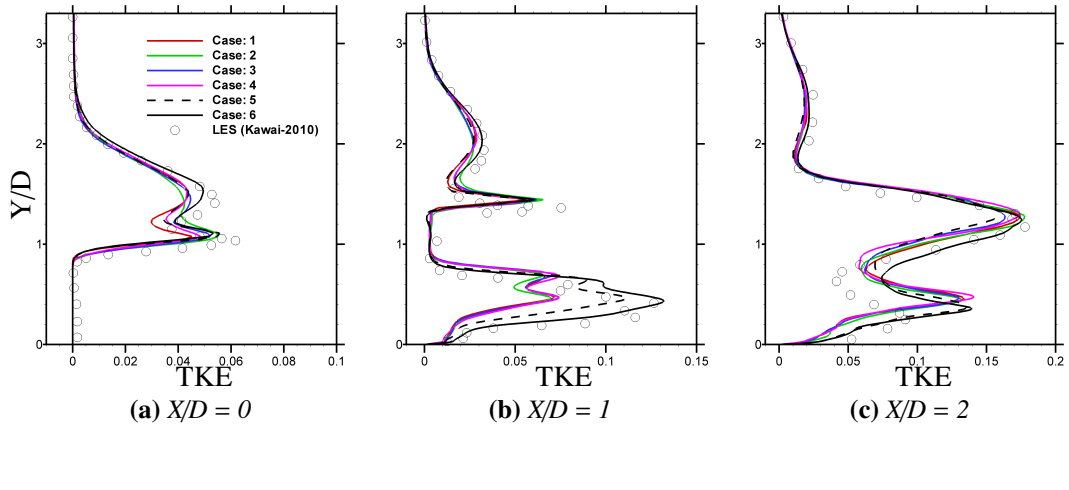

(a) *X/D = 0* **(b)** *X/D = 1* **(c)** *X/D = 2*

(d) *X/D = 3* **(e)** *X/D = 4*

Figure 5.19: *Turbulent kinetic energy (TKE) profiles on the mid wall-normal plane (Z/D = 0) showing effects of turbulent and laminar incoming boundary layers in comparison with previous LES results.*

objective a complex multi-species flow, sonic jet injection into a supersonic crossflow (JISC) was considered as the test case. Six unsteady simulations have been performed where the first case enforced laminar inflow conditions, the 2^{nd}, 3^{rd} and 4^{th} cases used the random white-noise with different intensities, the 5^{th} case used the Reynolds stress tensor along with a set of random numbers to generate fluctuations and finally the 6^{th} case utilized the digital filter based turbulent inflow data generator as the inflow boundary condition. A comparison has been presented for the incoming STBL for all six cases against the available experimental and CFD data to show that:

- For the random white-noise based cases (case:2-4), the fluctuations in the velocity data dissipation rate is very high. The incoming STBL immediately dissipates its fluctuating kinetic energy regardless of the initial intensities and relaminarizes, resulting in the boundary layer velocity profiles very similar to the laminar inflow case (case-1).

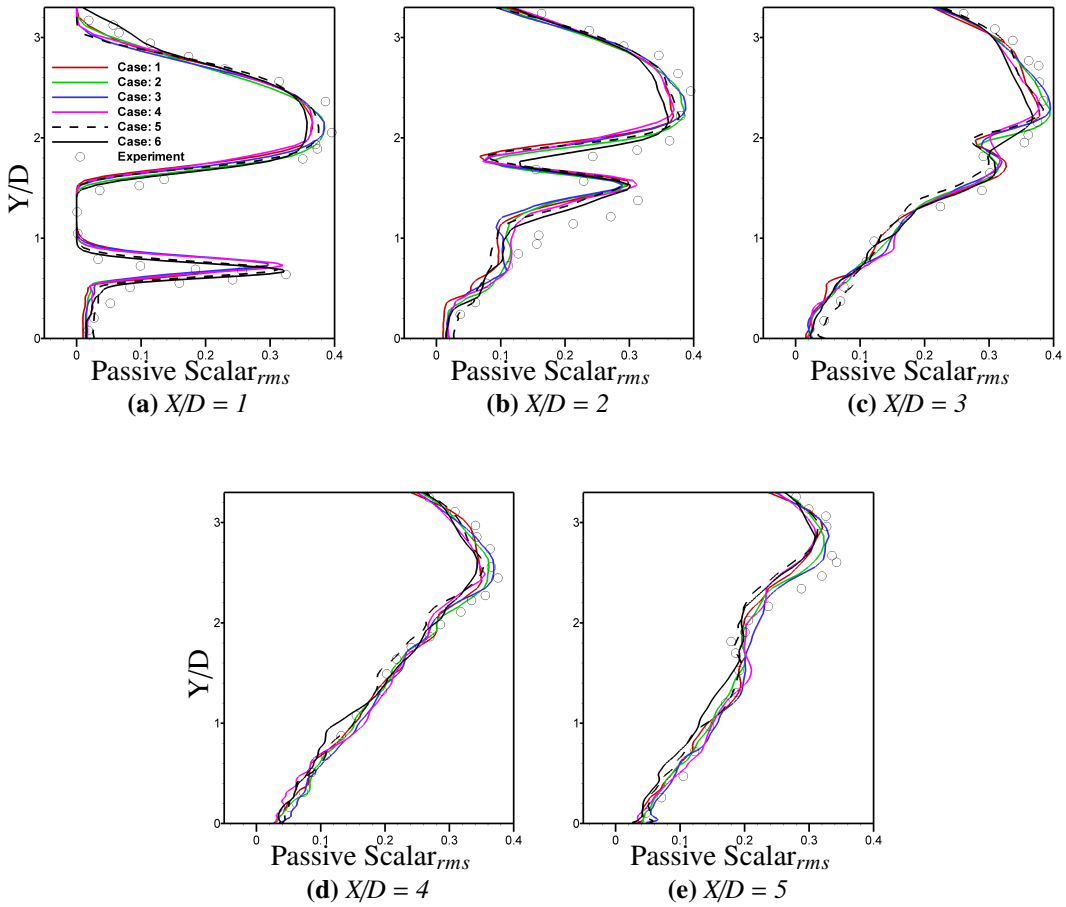

Figure 5.20: *Root-mean-square fluctuations of jet fluid (passive scalar) profiles on the mid wall-normal plane (Z/D = 0) showing effects of turbulent and laminar incoming boundary layers in comparison with previous LES results.*

- The use of only the Reynolds stress tensor (eliminating the Exponential correlation from the digital filter technique) has a slightly improved result than the cases: 2-4 but still the STBL generated dissipates gradually in the flow field resulting in physically incorrect results.

- The digital filter based method (case-6) offers a great advantage in terms of accuracy and reliability in generating turbulent inflow data in the flow field. The method of implementing the digital filter based turbulent inflow data generator presented here has proved its reliability, accuracy and computational efficiency.

- The study emphasized the importance of the Exponential correlation in the digital filter based technique. This method (case-6) generated fluctuations which transformed into a stable STBL with minimal energy losses. This is because the digital filter based method incorporates length and time scales, thus can preserve energy in the low frequency wavenumber range in the STBL.

- The turbulent boundary layer has a vital role in physically correct time-dependant simulations of a complex multi-species flow such as JISC where flow properties are affected by the incoming STBL.
- Flow properties are mainly affected in the region closer to the jet plume, but further downstream from jet plume at about X/D $\approx$ 5 where the turbulent kinetic energy has dissipated, the flow features are not greatly influenced. To predict mixing with adequate accuracy it is vital to study JISC with proper and accurate turbulence in the flow field.

CHAPTER 6

HyShot-II Scramjet Analysis

This chapter presents the analysis of the full geometry of the HyShot-II scramjet to obtain the combustion chamber inflow conditions in two dimensions, where the air is treated as a thermally perfect gas. Using these conditions, the digital filter based turbulent inflow boundary condition is applied to the three-dimensional combustion chamber for generating the supersonic turbulent boundary layer in the incoming flow. The sonic circular jet of hydrogen is injected to study the dynamics of the flow inside the combustion chamber.

6.1 Introduction

Hypersonic Air-breathing Propulsion (HAP) devices, such as scramjet engines, are required for efficient hypersonic propulsion. The scramjets employ supersonic combustion, typically above Mach 2, in order to generate thrust for propulsion. HAP systems eliminate the requirement to carry oxygen on-board the flight as the device would scoop oxygen from the atmosphere as it goes along and that is a huge savings in terms of weight and possibly size. But this is not as simple as it sounds. HAP systems such as scramjets have no thrust at all while standing still. Research has continued in this area with a view to develop a Single-Stage-To-Orbit (SSTO) propulsion system that can operate from zero runway speed to hypersonic cruise (above Mach 5), and at hypersonic velocities the scramjet would start producing the necessary thrust.

A detailed review of the research in this area has been presented in the Chapter 1. In 2001, Escher [49] proposed seven operating modes of a supercharged ejector scramjet engine (SESJ) combined cycle engine. In this study Escher examined both SSTO and Two-Stage-To-Orbit (TSTO) applications for this engine. Hiraiwa et al [77] presented their study of a scramjet and rocket-ramjet combined cycle engine which included both wind tunnel experiments and CFD evaluation of the combined cycle engine. The experiments were carried out at HIEST (High Enthalpy Shock Tunnel) and RJTF (Ramjet engine Test Facility) at the Kakuda space center, Japan. Mach 6 conditions were tested using a subscale model of the engine. The engine was designed to operate at ejector-jet

mode at low speed (start from zero velocity), then Ramjet mode activated at supersonic speeds. To achieve hypersonic speeds the scramjet and rocket modes were activated. The work presented achieved a net thrust in lower Mach numbers and tests are underway for higher Mach numbers.

Several configurations have been considered for the fuel injection inside a scramjet including inclined[51] and transverse which is applied in the HyShot-II configuration. The success of a scramjet engine largely depends upon the mixing of fuel, entering into the combustion chamber, with the air stream at supersonic velocities. The residence time of air inside the combustion chamber is very short (in the range of 2-4 ms), therefore, it is extremely important to design the combustion chamber for efficient mixing of fuel and air. Because of the short residence time and extreme conditions inside the combustion chamber, it is very difficult to visualize the flow. Computational Fluid Dynamics is playing a vital role in the development of hypersonic flow understanding and technology development for HAP devices, especially flow visualization, flow physics at such extreme conditions and extrapolation to flight conditions.

HyShot is a major scramjet research project that was started by the University of Queensland in Australia to obtain pressure measurements in supersonic combustion chamber. Currently it has developed into a multi-national project with sponsorships from various organizations from Australia, UK, USA, Japan, South Korea and Germany including several defence organizations. The main objective is to develop an understanding of supersonic combustion and its application for passenger aircraft, for the projects such as LAPCAT. The HyShot-II scramjet was flight tested in 2002 and it successfully achieved supersonic combustion at Mach 7.8 at an altitude between 23 km and 35 km. The fuel used for this flight test was hydrogen and flight test data was collected for fuel-off and fuel on conditions inside two separate combustion chambers.

Apart from actual test flights of the HyShot-II scramjet engine wind tunnel studies were carried out using the T4 Shock Tunnel at the University of Queensland in Australia [122, 148]. This work was further developed using the High Enthalpy Shock Tunnel Gottingen, HEG, of the German Aerospace Center, DLR [57]. The High Enthalpy Shock Tunnel Gottingen (HEG) is capable of testing a complete scramjet with internal combustion and external aerodynamics. It can generate a pulse of gas to a nozzle at stagnation pressure of up to 200 MPa and stagnation Enthalpy of up to 24 MJ/kg[58]. After the successful test flight of the HyShot-II scramjet, ground based testing was carried out to analyze the data from flight test. For this purpose two test conditions were developed for nominal flight altitudes of 32.5 km and 27.1 km which is the range of altitude where the flight test (HyShot-II) achieved supersonic combustion and data was collected. The idea behind is to develop a methodology for ground based testing of scramjet engines for further developments [57, 74, 48, 58]. A most recent study of the scramjet wind tunnel test was presented by Schramm [143]. In this ground based test of the HyShot-II model at the DLR, the HEG tunnel was used and the actual flight test conditions were duplicated for the ground test for measurement of surface pressure, heat transfer and high speed flow visualization inside the HyShot-II

combustion Chamber.

CFD analysis is also being carried out on the HyShot-II at various institutions and the results are compared with flight test and wind tunnel test data[85, 86, 94, 129, 128, 131]. All these efforts have highlighted the extreme difficulty associated with capturing even just the turbulent non-reacting flow inside the combustor where two jet streams meet. Most of these studies have been performed either without fuel injection or with fuel injection for combustion which requires huge computational resources. The aim of this chapter is to study and understand the dynamics and physics of hydrogen injection into the supersonic air flow inside the HyShot-II combustion chamber without the combustion, thus the analysis can be performed quickly and accurately to provide flow prediction for the scramjet combustion chamber.

For transverse fuel injection, as in the HyShot-II scramjet, the flow is generally termed as JISC (as studied in the Chapter 4). Understanding the physics of mixing in a JISC flow is very important in order to get improvements in air-fuel mixing and successful combustion to achieve useful thrust from a scramjet engine. Gruber *et al*[67], in 1995, carried out an experimental study of transverse jet mixing. The freestream conditions used in his experiment were Mach 2 and the jet entered into the free-stream at sonic velocity. He presented a structure of bow shock and horseshoe vortex being generated as the jet entered the free-stream. Ben-Yakar *et al*[11] also carried out a similar experimental study of the same phenomenon and presented his results in 2006 at a freestream Mach number of 3.3 and sonic jet. He compared two different fuels entering the freestream, namely hydrogen and ethylene, to observe large variations in injection velocities due to the difference in molecular weights of two fuels. These differences led to "*substantial variation in the jet shear layer growth rate and the mixing properties[11]*". Later on Kawai and Lele[89] presented a CFD study of this phenomenon using classical LES approach.

Chapter 4 presented the CFD study of the JISC experiment by Santiago and Dutton[139] using a digital filter based turbulent inflow boundary condition to generate the STBL in the incoming flow, and provided instantaneous analysis for the instabilities around the jet plume and how these help promote the mixing. The computational efficiency of the methods employed was also demonstrated. In this chapter same technique is used to study the hydrogen injection (cold case) inside the HyShot-II scramjet engine. The complete HyShot-II scramjet analysis is divided into two parts. Firstly, the full HyShot-II geometry in two dimensions is analyzed using the high temperature gas formulation (as presented in the Chapter 2 Section 3.4.3) with variable ratio of specific heats (γ) to obtain the correct shock structures in and around the scramjet and inside the combustion chamber. Using this analysis, the properties of the flow entering the combustion chamber are obtained. These are then applied to the three-dimensional analysis of full combustion chamber analysis where velocity, pressure distributions, turbulent kinetic energy (TKE), Reynolds shear-stresses (RS) along with jet penetration and flow mixing are analyzed.

6.2 Computational Domain and Initialization

6.2.1 Full Geometry

The Knudsen number (Kn) for the HyShot-II full geometry can be astimated by using the relation:

$$Kn = \frac{M}{Re}\sqrt{\frac{\gamma\pi}{2}} \sim 10^{-6} \tag{6.1}$$

where M and Re are the Mach number and the Reynolds number respectively. This Knudsen number allows the use of continuum approach for the analysis of HyShot-II scramjet. A schematic drawing of the HyShot-II scramjet is shown in the Chapter 1 Figure 1.5, which has been presented here for ease of referencing. On the HyShot-II flight test two of these configurations were used; one for no-fuel pressure measurements on the inlet ramp and inside the combustion chamber, and second with fuel measurements. Each scramjet has three major parts; the inlet ramp, combustion chamber (combustor) and exhaust. The inlet ramp is 18° half angle wedge with a span of 100 mm. The combustion chamber is 9.8 mm in height and 75 mm in span with an overall length of around 300 mm. Between the inlet ramp and the combustor is a floor and two side bleeds. The purpose of the bleeds is to spill the boundary and entropy layers as well as to disgorge the shock generated by front edge of the cowl. The aim is to make the flow inside the combustion chamber as smooth and free of discontinuities as possible. The cowl of the HyShot-II has an angle of 18° on the top side. The bottom wall also has an angle of 16.5° at the bottom face as shown in the Figure 6.1. The wall thickness of the inlet ramp, the cowl and the bottom wall is 20 mm, 20 mm and 17 mm respectively. Finally, the exhaust nozzle is a simple divergent type nozzle.

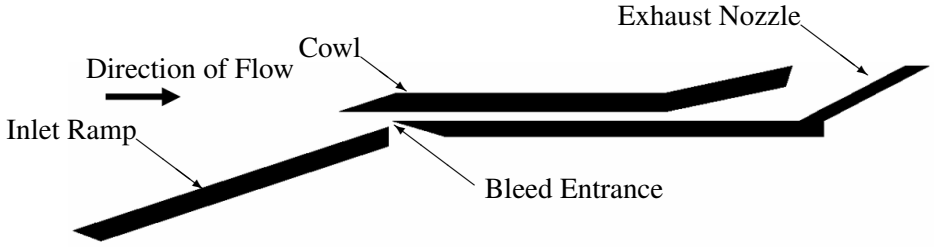

Figure 6.1: *Schematic diagram of HyShot-II scramjet (source: Gardner and Hannemann [57]).*

The full geometry of HyShot-II has been represented as a computational domain as shown in the Figure 6.2, along with the boundary conditions selected for the two-dimensional analysis of the HyShot-II geometry and the domain is bounded between symmetry boundary conditions. In the real scramjet case the bleed hole is a physical outlet drawing the boundary layer and the cowl shock out of the system. However in the case of numerical solution this arrangment requires special considerations and is

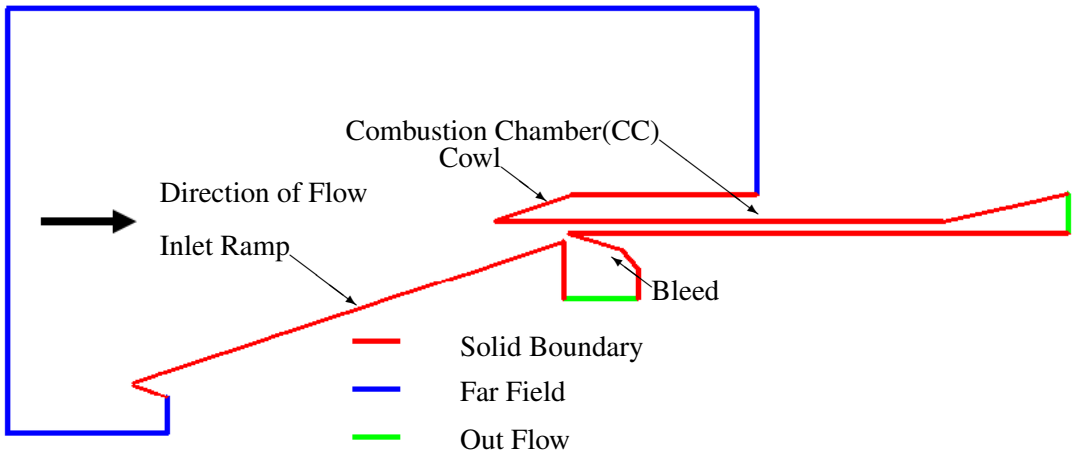

Figure 6.2: *Computation Flow Field and Boundary Conditions for HyShot-II Simulation.*

a very complex problem numerically. This is because the large back pressure from the bleed hole can stall the numerical flow and simulations can crash. In order to simplify this task an approach is used whereby the solution is "created" to obtain the combustion chamber inlet profiles by matching them with the existing CFD and experimental results, although this by no means guarantees the uniqueness. A structured grid technique is utilized in this work and two levels of grids are used to study the full geometry which is shown in the Table 6.1. As explained earlier, the objective to study the two-dimensional full geometry is to obtain the combustion chamber inlet conditions, therefore, the non-dimensional wall distance (z^+) is not very critical to this part of the study and is kept at 50 for both the grids. Table 6.2 presents the initial conditions utilized for the two-dimensional analysis[86]. Although the components of air are presented in the table but in simulation air is considered as one species.

6.2.2 Combustion Chamber

For the combustion chamber the Knudsen number is estimated using the Equation (6.1) and is $\sim 10^{-5}$ and allows the use of continuum approach. The combustion chamber plan view is shown in the Figure 6.3. Four, equidistant, injection holes are located at 58 mm from the front edge of the bottom wall of combustor. These are holes of 2

Table 6.1: *Two grid resolutions used to study the two-dimensional HyShot-II geometry.*

Grid	Resolution
Coarse	0.13×10^6
Fine	0.53×10^6

mm diameter to allow for the fuel (hydrogen) to be injected into the combustor. From the two-dimensional HyShot-II analysis, the combustor inlet conditions are obtained at the x = 355 m position as shown in the Figure 6.3. Then the combustor is studied in three-dimensions and the domain selected for analysis is shown in green in Figure 6.3. It consists of one fuel injection hole which is in the center of the domain. This arrangement is similar to those presented in the experimental studies of the sonic jet mixing with a supersonic flow stream[11, 67, 161, 89, 133] making comparison process simple. Similar to the JISC case in Chapter 4, the Reynolds number used for the computations is 50,000 based upon the freestream Mach number and the diameter (D) of the injection port such that:

$$Re_D = \frac{\rho_\infty U_\infty D}{\mu_\infty} = 5.0 \times 10^4 \tag{6.2}$$

which is six times smaller compared to the experiment to allow for a reasonable resolution of the computational domain for ILES.

The computational domain for the combustion chamber simulations is shown in Figure 6.4 with the boundary conditions utilized, where the dimensions are normalized by

Table 6.2: *Averaged Inflow Condition for 2D Intake for Flow Field Analysis [86].*

Property	Value	Units
Angle of Attack	3.56	Degrees
Mach Number	7.40013	
Static Pressure	1812.53	Pa
Temperature	242.44	K
Density	0.025962	kg/m^3
Reynolds Number	3.8E6	m^{-1}
N_2 Mass Fraction	7.48784E-1	
N Mass Fraction	3.85178E-10	
NO Mass Fraction	2.40283E-2	
O_2 Mass Fraction	2.27054E-1	
O Mass Fraction	1.34457E-4	

Table 6.3: *Computational meshes used for the simulation of the HyShot-II combustor; using ILES and digital filters based turbulent inflow data generator.*

Grid	N_x	N_y	N_z	Total ($\times 10^6$)	L_y	L_z	z^+
Coarse	509	101	101	5.2	0.5	0.2	10
Medium	765	121	111	10.2	0.5	0.2	10
Fine	1176	141	121	20.1	0.5	0.2	10

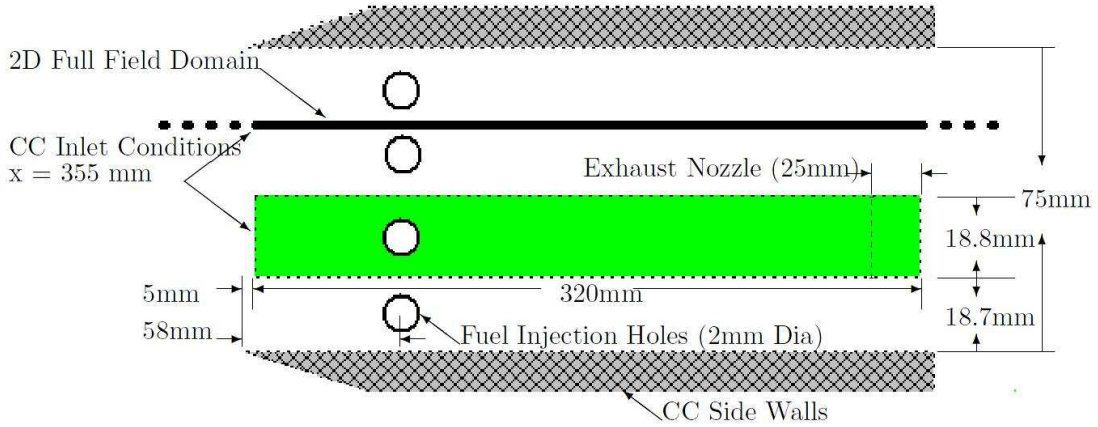

Figure 6.3: *Plan view of the combustion chamber; 3D domain is shown in green to cover the complete combustion chamber and includes 25 mm of the exhaust nozzle.*

the height of the combustor (i.e., 9.8 mm). This conversion makes the x = 355 mm position equal to X/D = -26.5 and brings the X/D = 0 at the center of the injection holes making the analysis process simpler. Three grid resolutions are employed for the combustor analysis and Table 6.3 presents the details for these. Due to the lack of data available for comparison, the validity of the results is based upon previous simulations cases presented in the Chapter 4 using the same algorithms and methodology where the results demonstrated excellent agreement with the experiment and classical LES results. The grids for the combustion chamber simulations utilized the similar non-dimensional lengths as used in the previous study[133]. The fine grid simulations were carried out using nearly 7500 CPU hours on Cranfield University HPC cluster "Astral" (dual-core CPU with a clock-rate of 3 Ghz).

6.3 Full Geometry Analysis

Two dimensional computations of the full geometry are performed using the initial conditions presented in the Table 6.1 and the high temperature gas formulation (Section 3.4.3) which allows for variable ratio of specific heats (γ) for thermally perfect gas. The aim of this two dimensional work is to understand the shock structures inside the combustor and to obtain the initial conditions for the three dimensional combustor simulations (at x = 355 mm or X/D = -26.5 location). Figure 6.5(a) shows the full geometry domain flow field along with the shock generated at the leading tip of the inlet ramp and Figure 6.5(b) represents a close-up view of the combustion chamber inlet position showing another shock generated at the cowl which is disgorged through the bleed hole along with the boundary layer generated at the inlet ramp. Another weak shock develops at the bottom wall of the combustion chamber which enters the chamber and creates a shock train inside by reflecting from top and bottom walls of the combustion chamber. Figure 6.5(d) shows a shock train travelling inside the com-

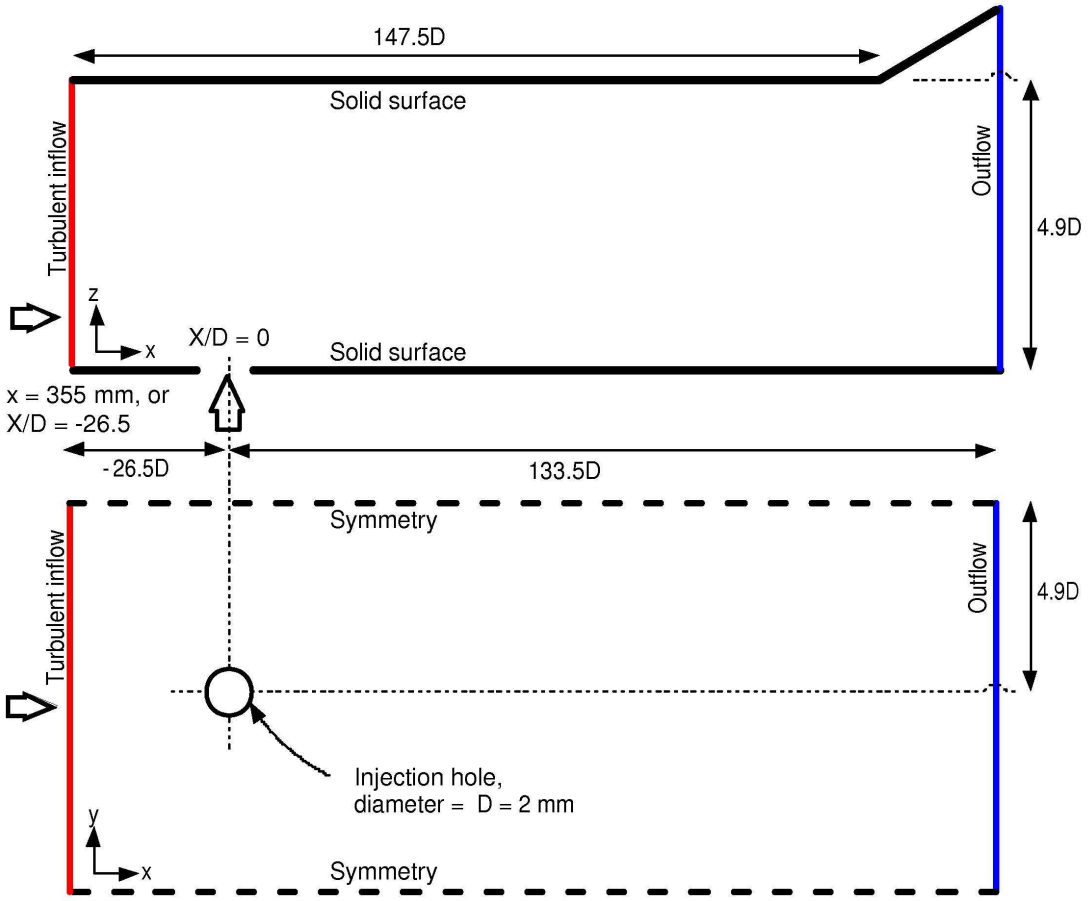

Figure 6.4: *Computational domain for combustion chamber (CC) simulations.*

bustion chamber but as the shock is very weak it slightly changes the flow properties inside the chamber.

Figure 6.6 presents the pressure distribution on the inlet ramp and inside the combustion chamber of HyShot-II scramjet without any fuel injection. For both the grid levels are in good accordance with the experimental data but are slightly offset from the CFD data on the inlet ramp in Figure 6.6(a). Pressure distributions inside the combustion chamber are compared with previous CFD and experimental data[86] in Figure 6.6(b and c) on the top and bottom walls of the combustion chamber. On both the locations the ILES data is in excellent agreement with the experimental and CFD data towards the start and mid of the combustion chamber but some discrepancy can be observed in the data towards the end of the combustion chamber, still it captures same number of shockwaves travelling inside it shown by the peaks in the pressure distributions.

The combustion chamber flow properties are captured at the X=355 mm (or X/D = -26.5) as shown in the Figure 6.7 which are used as initial conditions for three dimensional combustion chamber simulations along with hydrogen fuel injection. Both the grid level data are presented for the velocity profiles, Temperature and pressure distributions at the X = 355 mm or X/D = -26.5D location. Slight discrepancy in the data

can be observed for the coarse grid level but the fine grid level is a nice match to the previous CFD data obtained at DLR (Germany). The shock-train travelling inside the combustion chamber can be observed by the jump in the three profiles. This data is used along with these discontinuities in the profiles in order to simulate the combustion chamber with the shock train, as it is anticipated that this shock train helps trigger the mixing process when the fuel is injected in the combustion chamber.

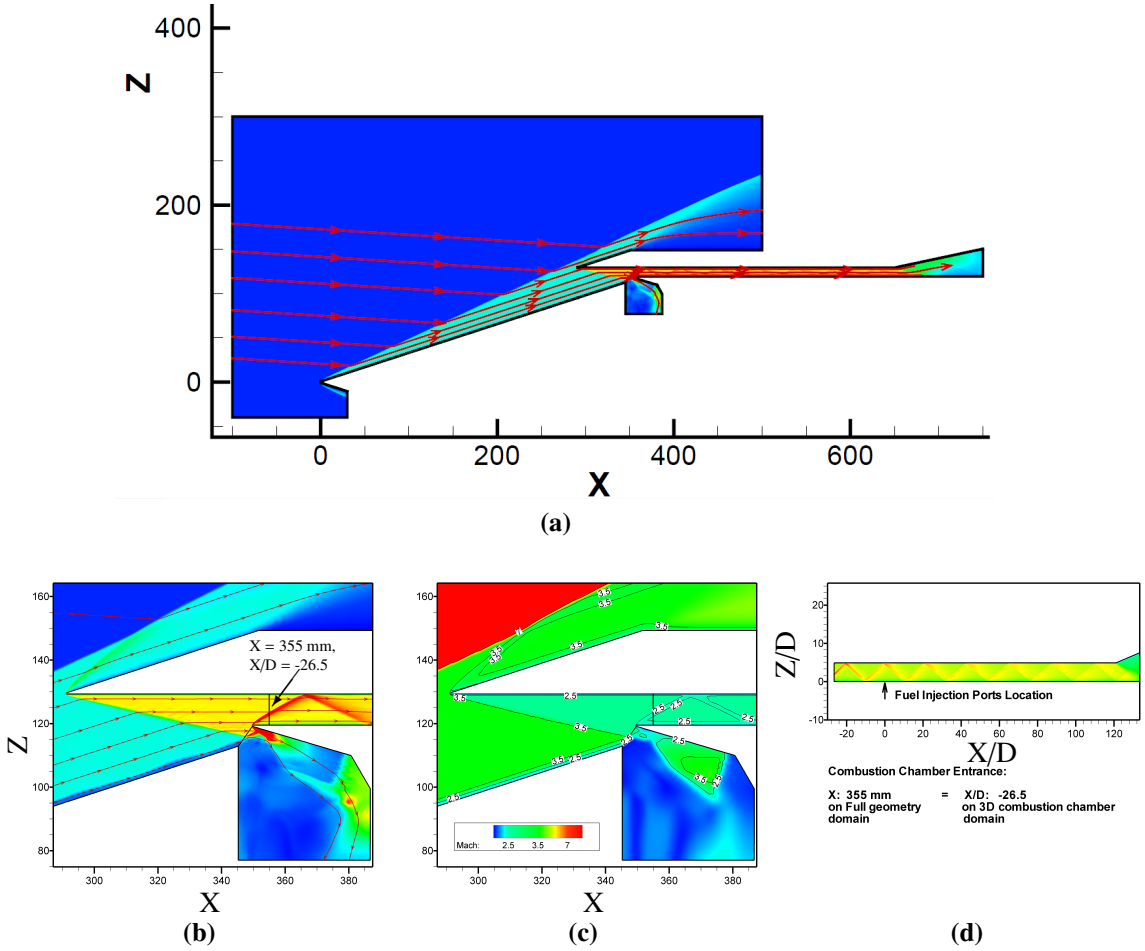

Figure 6.5: *Internal and external shock formations around the HyShot-II scramjet engine; (a) Two dimensional full geometry analysis; (b) Close-up view of shock formations at the bleed section and the combustion chamber entrance showing a shock generated by the bottom wall and entering into the combustion chamber; (c) Mach number contours at the combustion chamber entrance; (d) Shock train travelling inside the combustion chamber.*

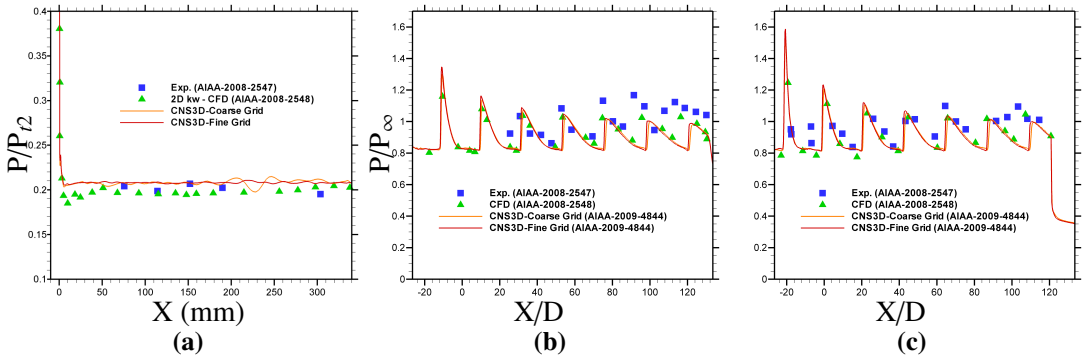

Figure 6.6: *Normalized pressure distributions, a) at the inlet ramp, and inside the combustion chamber without the fuel injection, (b) Lower wall; (c) Upper wall, of the combustion chamber.*

6.4 Combustion Chamber Analysis

The flow of hydrogen inside the combustion chamber is a sonic circular jet transverse to the freestream turbulent supersonic air flow. Such a flow is generally termed as jet injection into a supersonic crossflow (JISC). Typical features of JISC are lambda, bow and barrel shocks, Mach disc, horseshoe vortices and counter-rotating vortices (CRVs). The results and discussion in the Chapter 5 demonstrated that without the supersonic turbulent boundary layer (STBL) in the incoming flow upstream the jet injection the lambda shock in front of the bow shock cannot be captured correctly. Therefore, the STBL in the incoming flow has been simulated using a digital filter based synthetic turbulence inflow data generator[95, 169, 156] which has been validated in the Chapter 4 for a similar JISC case at Mach 1.6 where the results has been compared with the

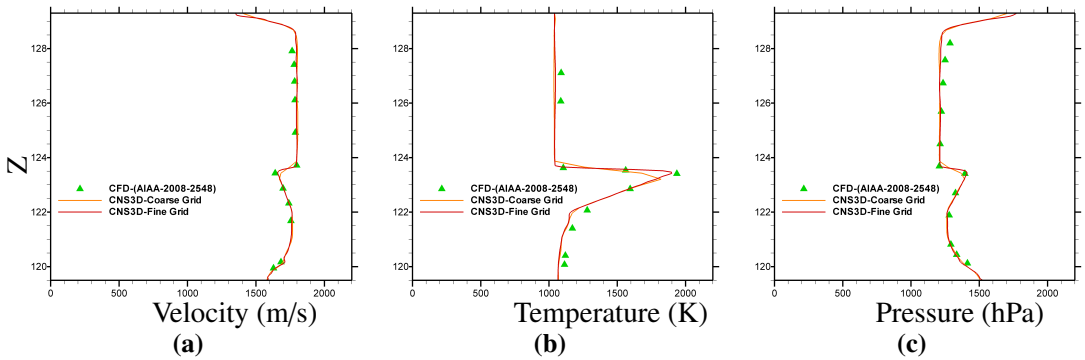

Figure 6.7: *Combustion chamber inlet profiles for various flow features obtained at the X = 355 mm position (or, X/D = -26.5) as shown in the Fig. 6.5(a and c)). These profiles are used as inflow conditions for the three dimensional combustion chamber simulations, (a) Velocity profile; (b) Pressure profile; (c) Temperature profile.*

previous LES[89] and experimental data[139, 50, 161]. As no experimental or CFD data is available in order to compare the results of hydrogen injection into the HyShot-II combustion chamber without combustion, the results presented in this chapter base their validity upon the validation cases presented in the Chapter 4 and 5 and published earlier[127, 130, 133, 132].

Figure 6.8 presents a time-averaged three-dimensional flow structures of hydrogen injection in the HyShot-II combustion chamber using the Q-criterion. When the circular jet of fuel is injected, it generates a horseshoe vortex upstream of the jet injection port and a pair of counter rotating vortices (CRVs) which runs downstream the jet plume. Figure 6.8 shows that these CRVs have distorted after the X/D = 15 ~ 20 which is an interesting finding and will be discussed later. Also shown is the bow shock being reflected from the top wall of the combustion chamber and creating a train of bow shocks in the downstream direction. From around X/D ~ 20 the flow does not show any clear structures and is a very complex mix of various flow features which are interacting with each other and enhancing the flow mixing. It can also be observed that the shockwaves are reflecting from the symmetry walls. The flow development in the combustion chamber is discussed below. Figure 6.9 shows the time-averaged three-dimensional Mach contours at various locations showing averaged flow development as the hydrogen jet is injected inside the combustion chamber.

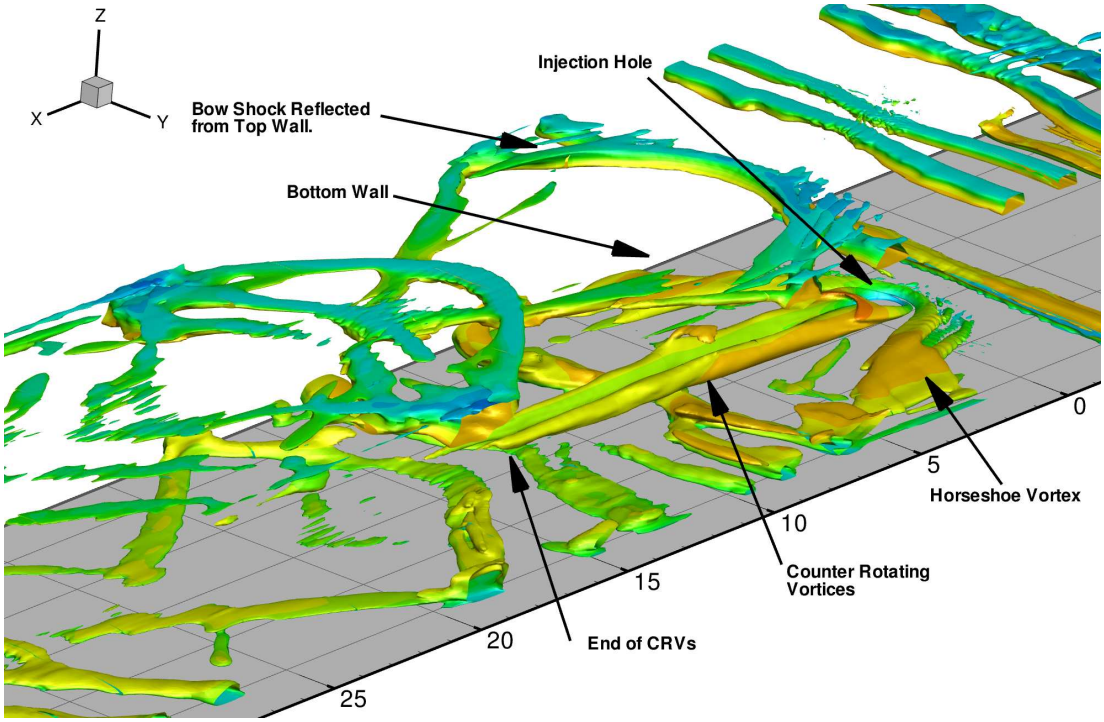

Figure 6.8: *Time averaged three dimensional flow structure using the Q-criterion showing various JISC flow structures inside the HyShot-II combustion chamber.*

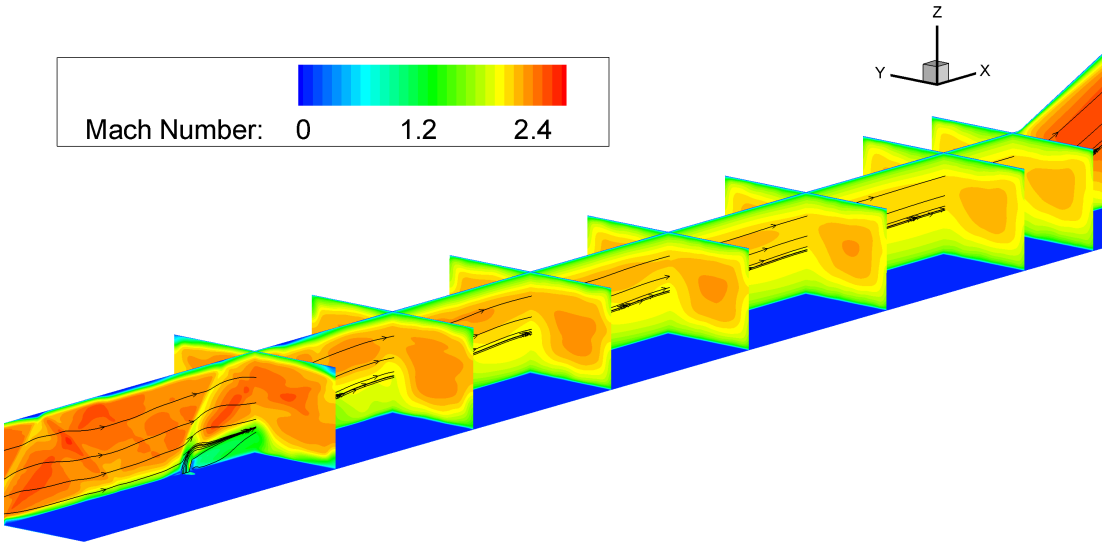

Figure 6.9: *Three dimensional Mach contours showing flow development as the hydrogen jet is injected inside the HyShot-II combustion chamber.*

6.4.1 Instantaneous Flow

Before discussing various time-averaged flow features and flow mixing, in this section, instantaneous flow has been analyzed to understand the flow development inside the combustion chamber. Figure 6.10 shows the instantaneous pressure signature at a point within the upstream recirculation zone (X/D, Y/D, Z/D) = (-0.8,0,0.25) for a non-dimensional time (τ) between 120 and 150 for all three grid levels. This is the point where the instantaneous flow features such as KH instabilities originate as the supersonic inflow hits the jet plume. As discussed in the Chapter 4 Figure 4.26 and 4.27, the fluctuations in the pressure signature occurs with the KH instabilities. For all grid levels similar levels of pressure peaks are observed in the Figure 6.10. Figure 6.11 presents instantaneous snapshots of the jet fluid volume fraction on the mid plane (Y/D = 0) for the three grid levels where the grid improvement effects are clearly visible by the capture of small scale coherent structures at the "fine" grid level.

Figure 6.12 presents the instantaneous flow development at another non-dimensional time τ = 148.57 at various locations on the "fine" grid level. On the wall-normal mid plane (Y/D = 0) the flow mixing occurs instantaneously as soon as the jet of hydrogen is injected in the mainstream flow. Traces of hydrogen can be visualized entrained in the upstream recirculation zone which can be helpful in early combustion of hydrogen. On the spanwise wall-normal planes at various locations (X/D = 1, 3, 5, 15 and 90) the flow mixing is developing gradually. Initially maximum fuel concentration is in the path of the jet plume, where the CRVs can be seen originating. Gradually as the flow develops the hydrogen volume fraction is filling in the space around the CRVs as the CRVs trigger the spanwise fluid mixing. It has been established earlier [86] that

the inflow for full geometry of HyShot-II and the combustion chamber is highly two-dimensional, but as soon as the hydrogen jet is injected and the mixing process starts, the flow becomes highly three-dimensional as shown in the Figure 6.12(b-f).

Energy spectra at various upstream and downstream locations are presented in Figure 6.13 against the Strouhal number (St) for the three grid levels. Two points (p1 and p2) are selected in the incoming STBL on the upstream of the jet plume, two points (p3

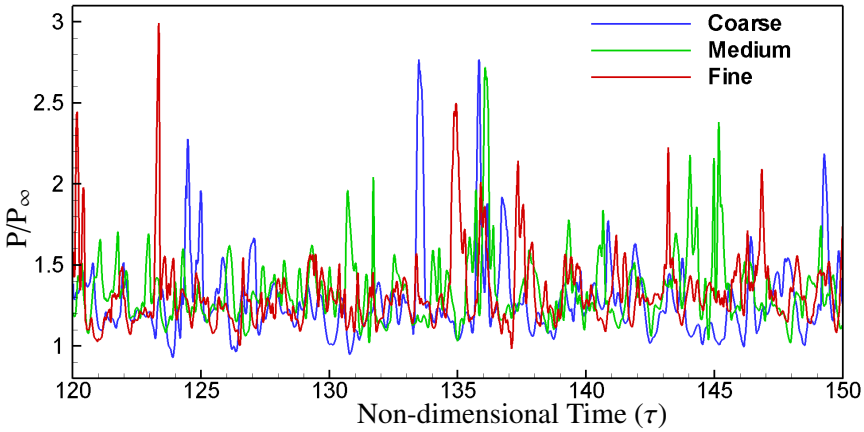

Figure 6.10: *Time history of instantaneous pressure signature within upstream recirculation region for non-dimensional time between 120 and 150.*

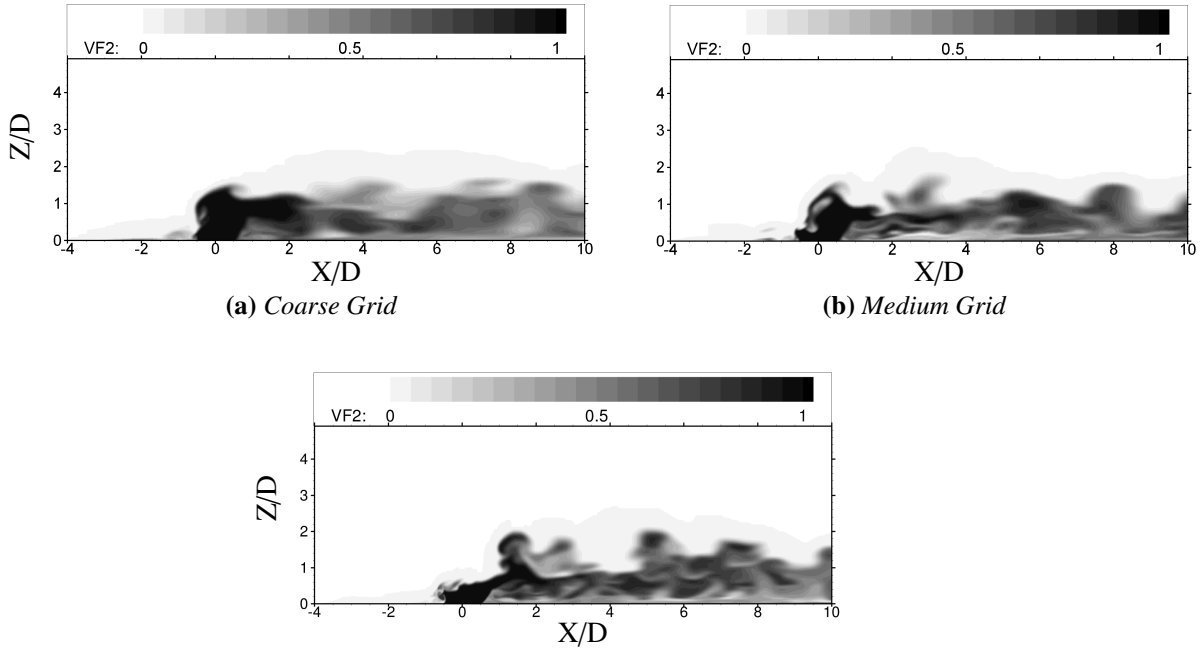

(a) *Coarse Grid*

(b) *Medium Grid*

(c) *Fine Grid*

Figure 6.11: *Instantaneous snapshots of the jet fluid volume fraction at τ = 120.21 on the mid plane (Y/D = 0) for three grid levels.*

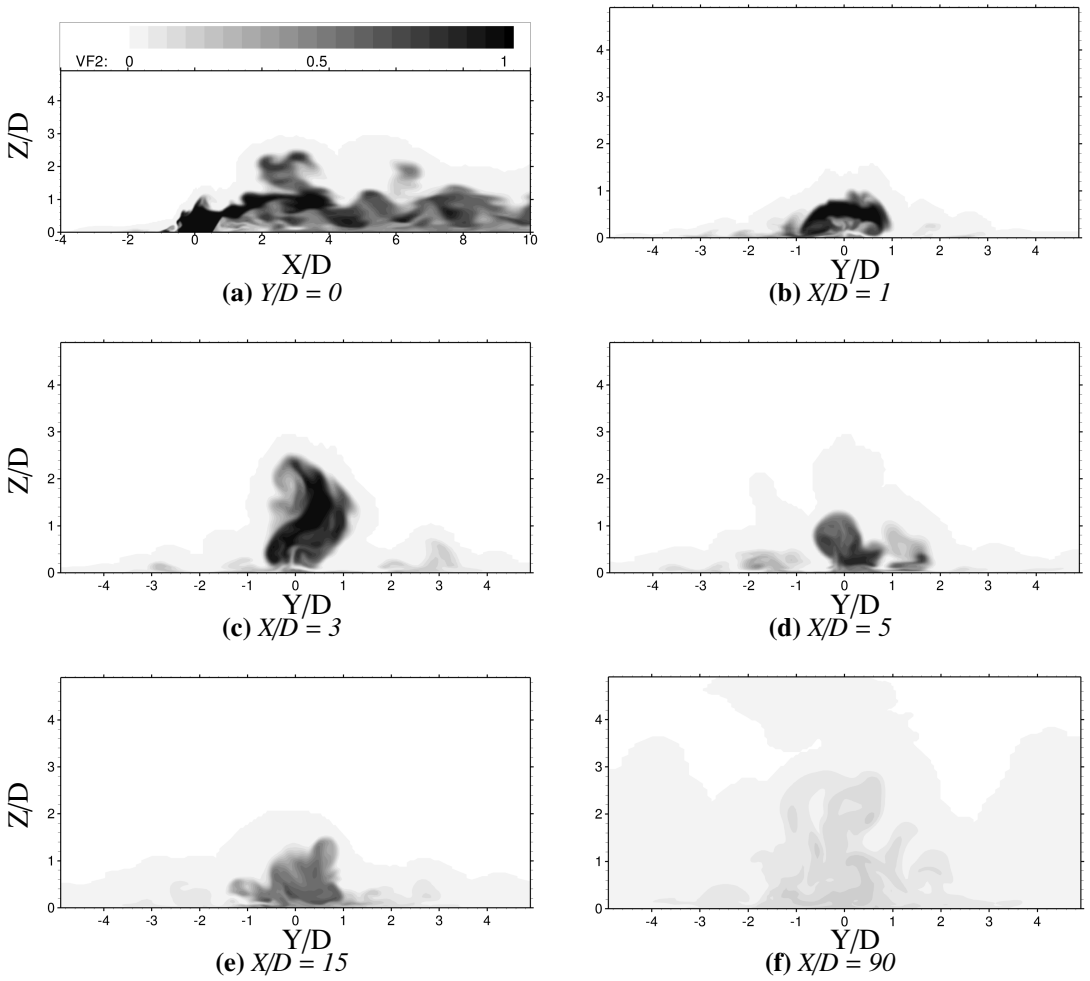

(a) *Y/D = 0* **(b)** *X/D = 1*

(c) *X/D = 3* **(d)** *X/D = 5*

(e) *X/D = 15* **(f)** *X/D = 90*

Figure 6.12: *Instantaneous views of the jet fluid volume fraction presenting the flow development inside the HyShot-II combustion chamber at τ = 148.57 on the mid plane (Y/D = 0) and wall-normal planes (X/D = 1, 3, 5 15 and 90) for "fine' grid.*

and p4) are around the jet plume where the KH instabilities are being generated, point (p5) is the in the downstream location close to the jet plume and finally the point (p6) is downstream away from the jet plume, all on the mid plane (Y/D = 0) for all grid levels. The spectra at the points p1 and p2 reasonable generation of energy with the STBL but as the flow is dominated by the viscous forces close to the wall excessive dissipation can be observed as well. The points p3 and p4 are within the shear layer flow areas and demonstrate reasonable match to an ideal energy spectra. Overall, the energy spectra at all the points demonstrate the trends in accordance with the Kolmogorov's $k^{-5/3}$ trend showing clear production regions in the highest wavenumber range (or low Strouhal number), clear inertial subrange for medium wavenumbers and prominent dissipation range.

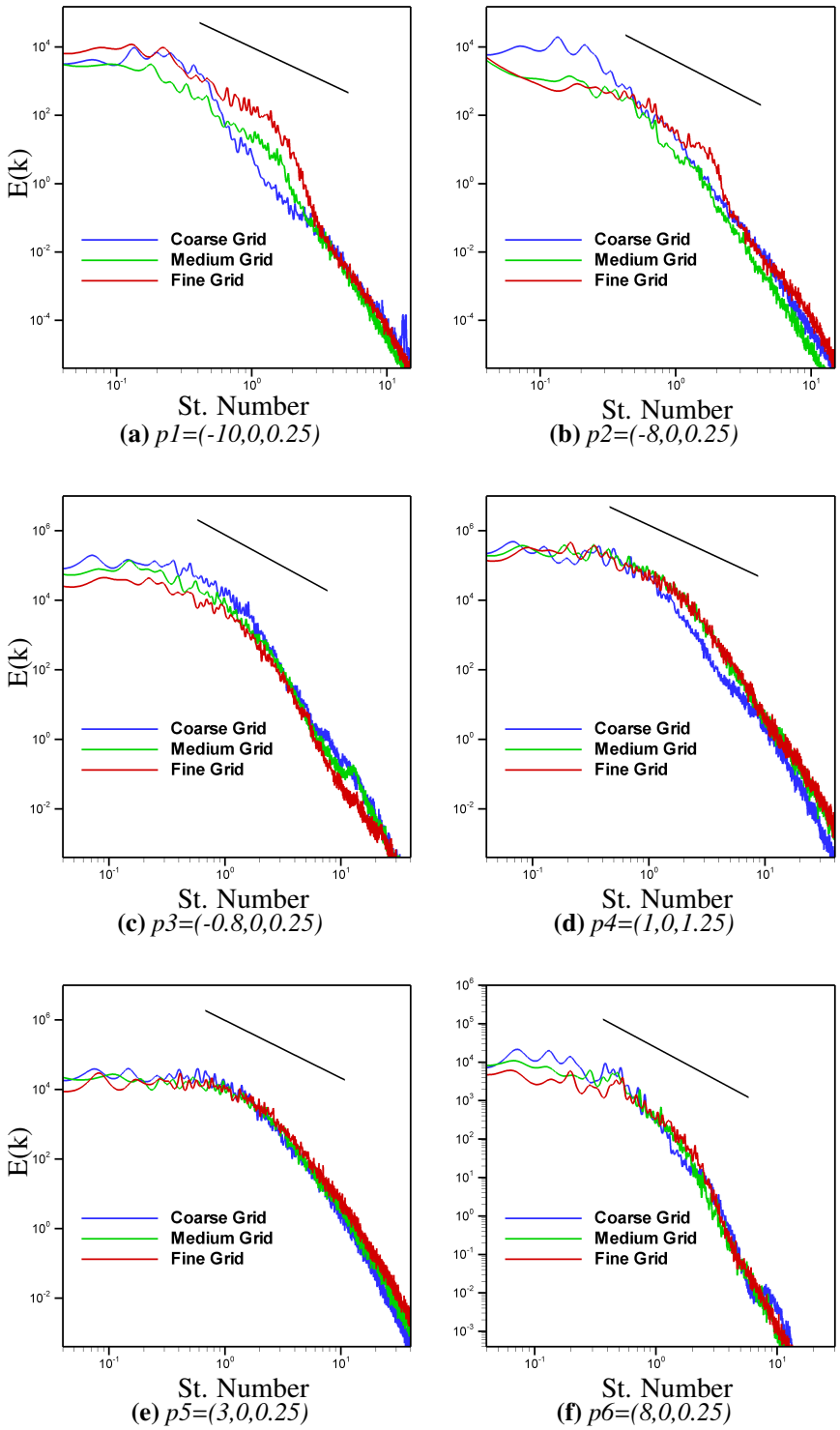

(a) *p1=(-10,0,0.25)* **(b)** *p2=(-8,0,0.25)*

(c) *p3=(-0.8,0,0.25)* **(d)** *p4=(1,0,1.25)*

(e) *p5=(3,0,0.25)* **(f)** *p6=(8,0,0.25)*

Figure 6.13: *Energy spectra are presented at various locations upstream and downstream of the jet plume. The "p" represents the point locations as (X/D,Y/D,Z/D) for each point.*

6.4.2 Jet Penetration

In this, and the following, sections the time-averaged flow inside the combustion chamber is analyzed. The time-averaged data presented here has been obtained for a non-dimensional time ($\tau \sim 160$) by averaging 2000 instantaneous equi-timestep files. The trajectory of maximum jet concentration has been obtain by using a correlation (Equation 6.3) proposed by Abramovich[2], which has also been used by Orth and Funk[120] in their experiments to study the jet penetration in supersonic flow where they demonstrated that the Equation (6.3) agrees *"reasonably well with the experimental values"* for X/D $\leq$ 8.

$$Z/D = \left(P_j/P_c\right)^{0.434} (X/D)^{0.333} \tag{6.3}$$

where, P represents the dynamic pressure and the subscripts j *and* c represent the jet and cross-flow respectively. Figure 6.14 presents the jet trajectory as calculated using Equation 6.3 on the wall-normal mid plane (Z/D = 0). It can be noticed that the trajectory is nice curve from the jet orifice till the Mach disc and after the Mach disc it is running in almost a straight path parallel to the bottom wall of the combustion chamber. The straight path in the trajectory can be because of low jet-to-crossflow momentum flux ratio[141] ($J \approx 0.3$) in this case. This forces the jet plume to bend in the direction of flow and does not allow much penetration of the jet plume which results in the jet trajectory being almost horizontal and closer to the bottom plate of the combustor than in the previous JISC case (Chapter 4, where the inflow was at Mach 1.6 and $J \approx 1.7$).

6.4.3 Velocity Field

Figures 6.15-6.16 shows time-averaged Mach number and hydrogen volume fraction (passive scalar) contours inside the combustion chamber at different locations along

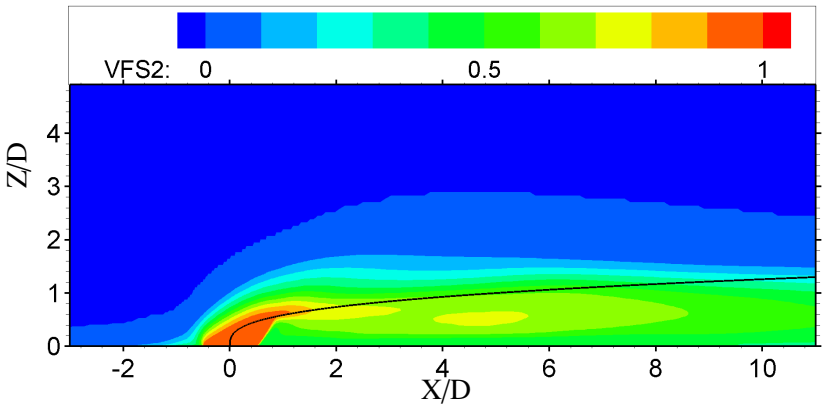

Figure 6.14: *Jet penetration shown as a curve for the trajectory of maximum hydrogen concentration on the wall-normal mid plane (Y/D=0).*

with the streamlines to understand the flow. Figure 6.15(a and b) are the contour plots on the wall normal mid plane (Y/D = 0). As the fuel is injected it acts as a barrier to the free-stream flow and resulting major flow features can be identified like the lambda, bow and barrel shocks on the mid plane. The lambda shock interacts with the incoming STBL at around X/D ~ -4 location. The fuel jet immediately turns in to the freestream flow direction. There is a large recirculation zone in front of the fuel port which entrains some fuel inside it. Provided the temperature is high enough and appropriate ignition time of hydrogen, this entrained fuel in the recirculation zone could lead to early combustion which is important as the residence time of fuel inside the combustion chamber is of the order of 2-4 ms.

Downstream of the jet injection two regions can be clearly seen for the fuel and air separately in the Figure 6.15(b) which emphasize the point that the jet expansion is restricted in this area and two fluids mix only in the lower half of the combustion chamber. This is the region where a pair of CRVs is developing and resulting in enhanced longitudinal and spanwise mixing of the two fluids. The feature of these CRVs that enhances the fluid mixing is the counter-rotation which *"stirs"* the two fluid together and creates a larger area of mixing on the top and sides of CRVs. Figure 6.16 shows the contours plots on the wall-normal cross-view planes (X/D = 1, 3, 5, 15 and 90) demonstrating the development of the CRVs. Initially, the time-averaged flow is highly symmetrical and the two CRVs start immediately after the hydrogen jet injection as shown in the Figure 6.16(a) at X/D=1 location.

Figure 6.16(c-e) are showing the growth of the CRVs further downstream locations. At these locations the reflected shocks from the top and bottom walls of the combustion chamber interacts with the CRVs to disrupt and weakens them. This also causes the CRVs to distort considerably as shown in the Figure 6.16(g) at location X/D = 15. A pair of trailing CRVs (TCRVs) also emerges at location X/D = 5, below the major CRVs, which has grown in size at location X/D = 15. All these CRVs act to enhance the mixing mechanism closer to jet injection which is demonstrated by the jet passive scalar contours at the respective locations. Further downstream the combustion

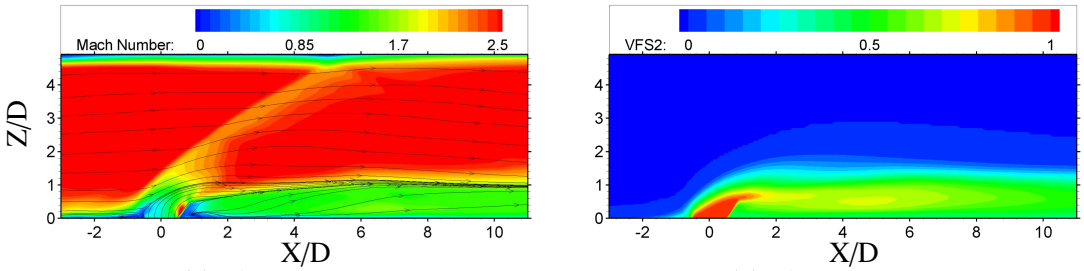

(a) *Plane: Y/D = 0* **(b)** *Plane: Y/D = 0*

Figure 6.15: *Time averaged Mach number and hydrogen volume fraction (passive scalar) inside the combustion chamber at the wall-normal mid plane (Y/D = 0) along with the streamlines.*

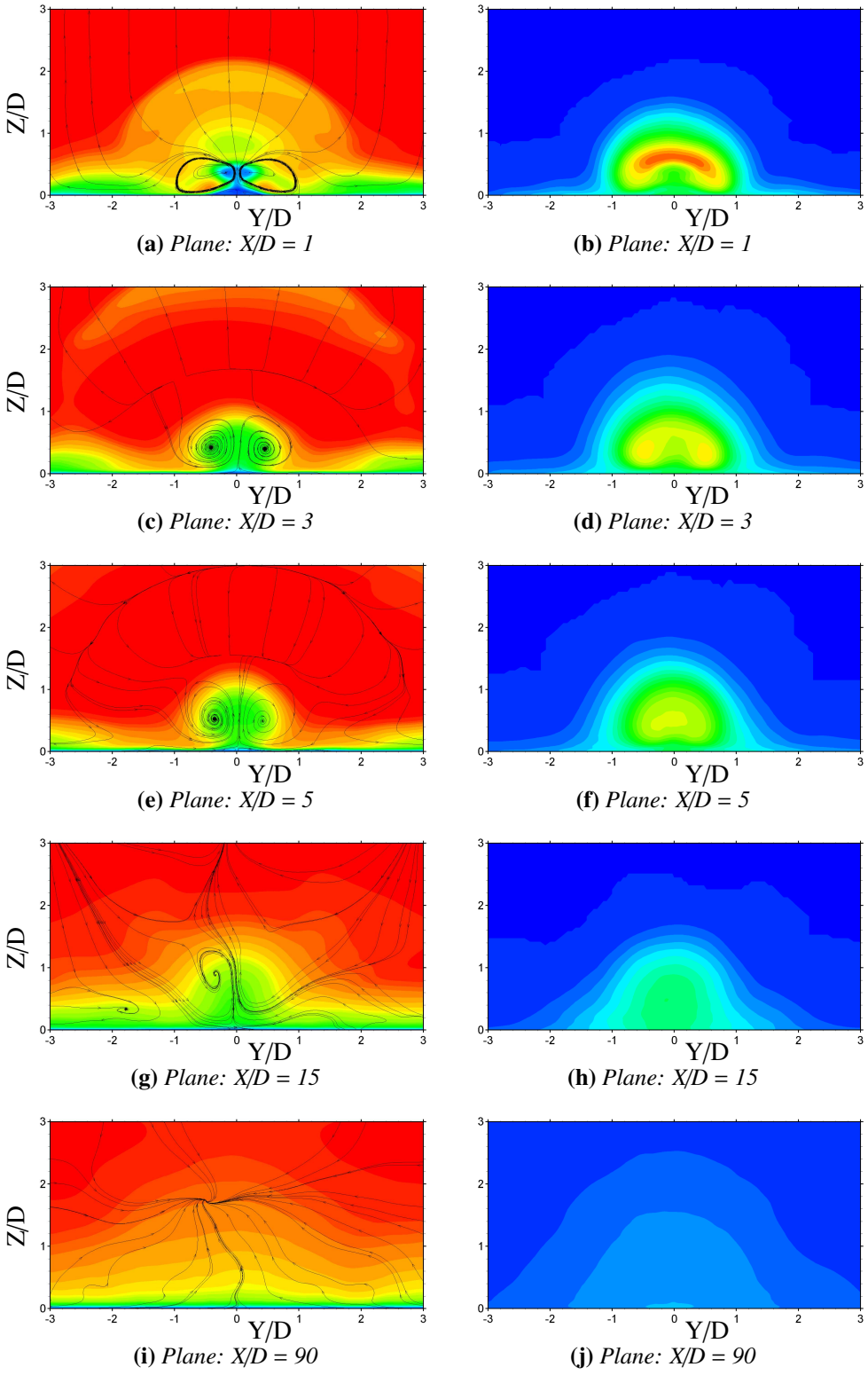

(a) *Plane: X/D = 1*
(b) *Plane: X/D = 1*
(c) *Plane: X/D = 3*
(d) *Plane: X/D = 3*
(e) *Plane: X/D = 5*
(f) *Plane: X/D = 5*
(g) *Plane: X/D = 15*
(h) *Plane: X/D = 15*
(i) *Plane: X/D = 90*
(j) *Plane: X/D = 90*

Figure 6.16: *Time averaged Mach number and hydrogen volume fraction (passive scalar) inside the combustion chamber at the cross-flow plane (X/D = 1, 3, 5, 15 and 90) along with the streamlines (contour legend same as shown in the Figure 6.15)*

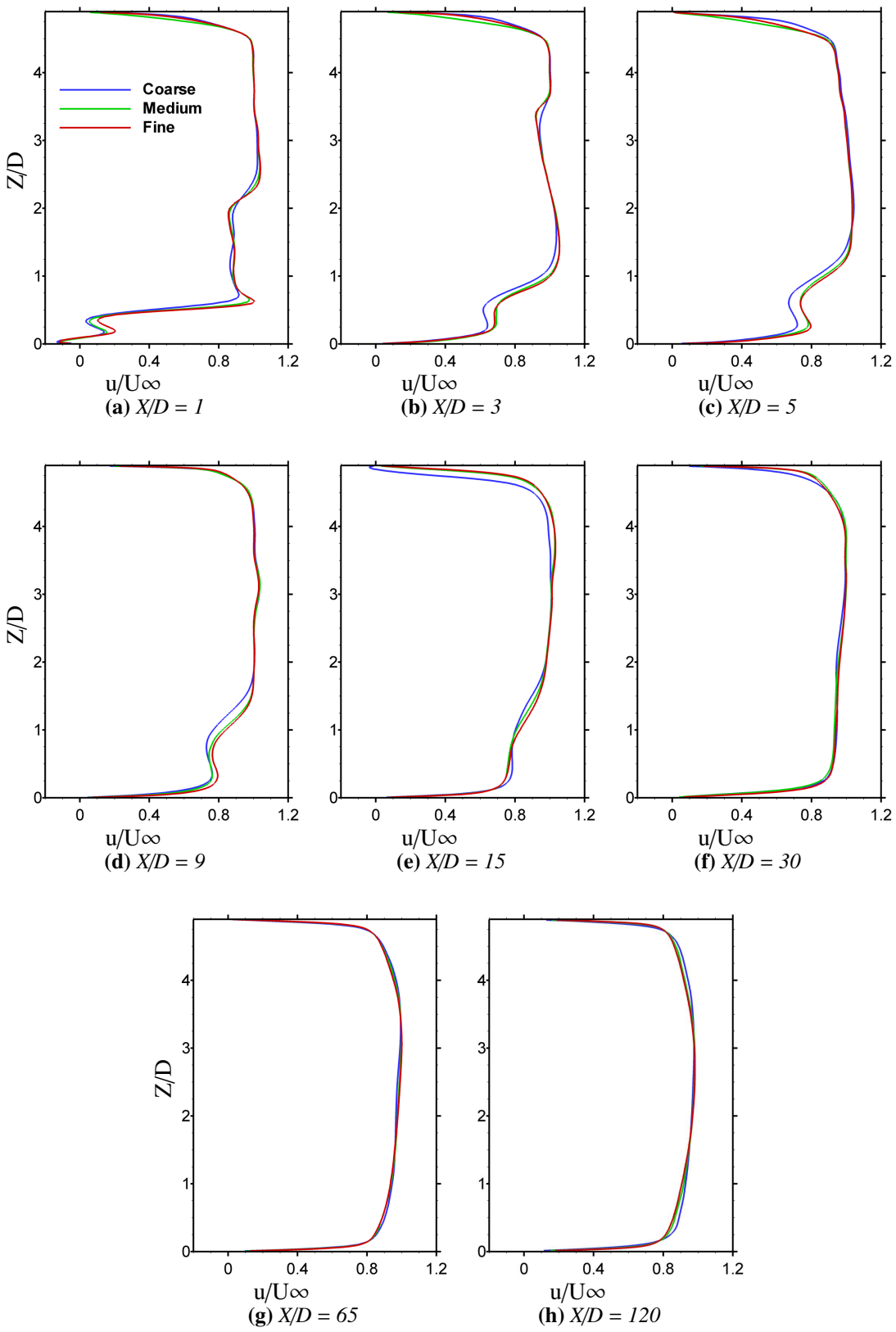

Figure 6.17: *Normalized stream-wise velocity profiles at various locations on the wall-normal mid plane (Y/D = 0).*

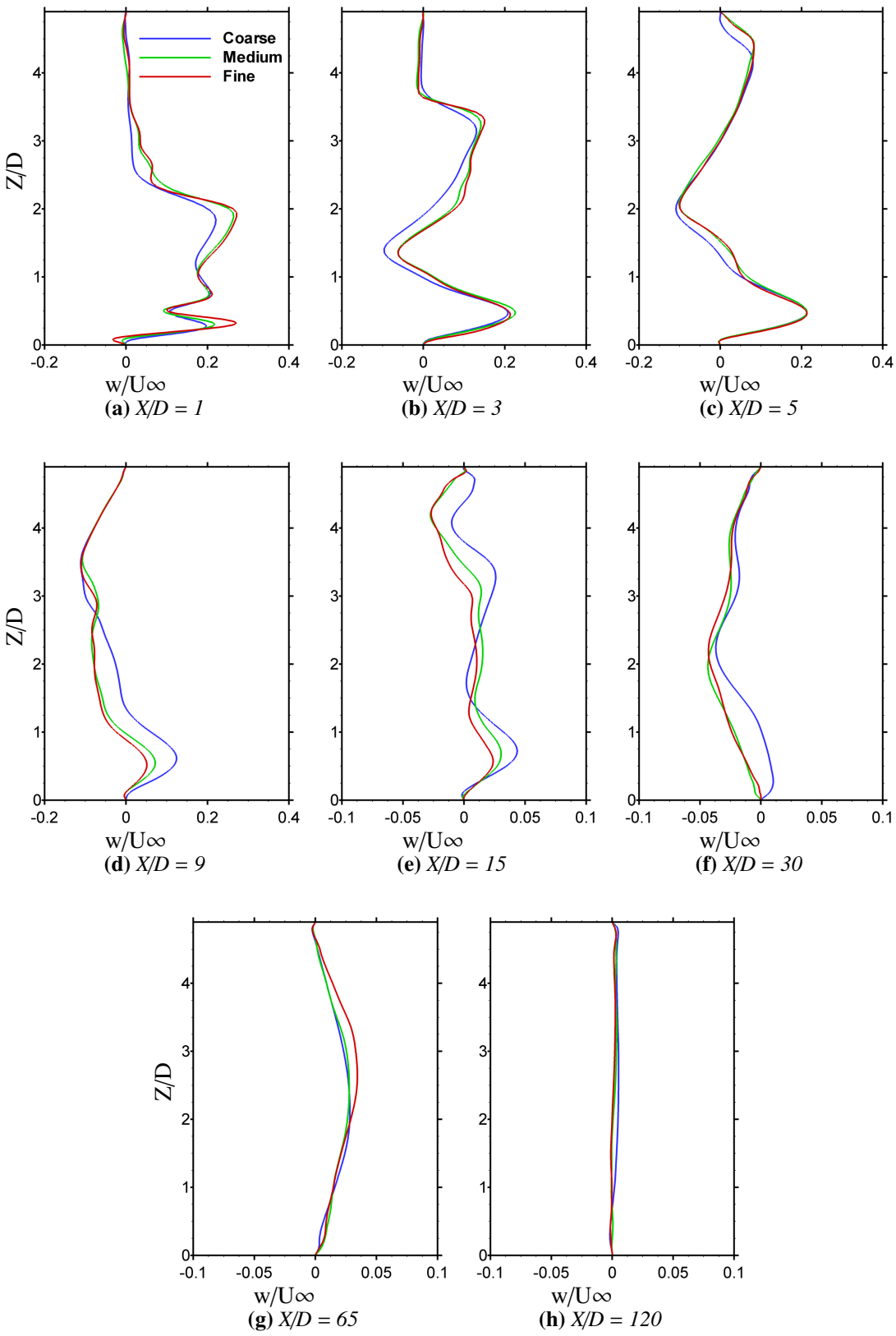

Figure 6.18: *Normalized wall-normal velocity profiles at various locations on the wall-normal mid plane (Y/D = 0).*

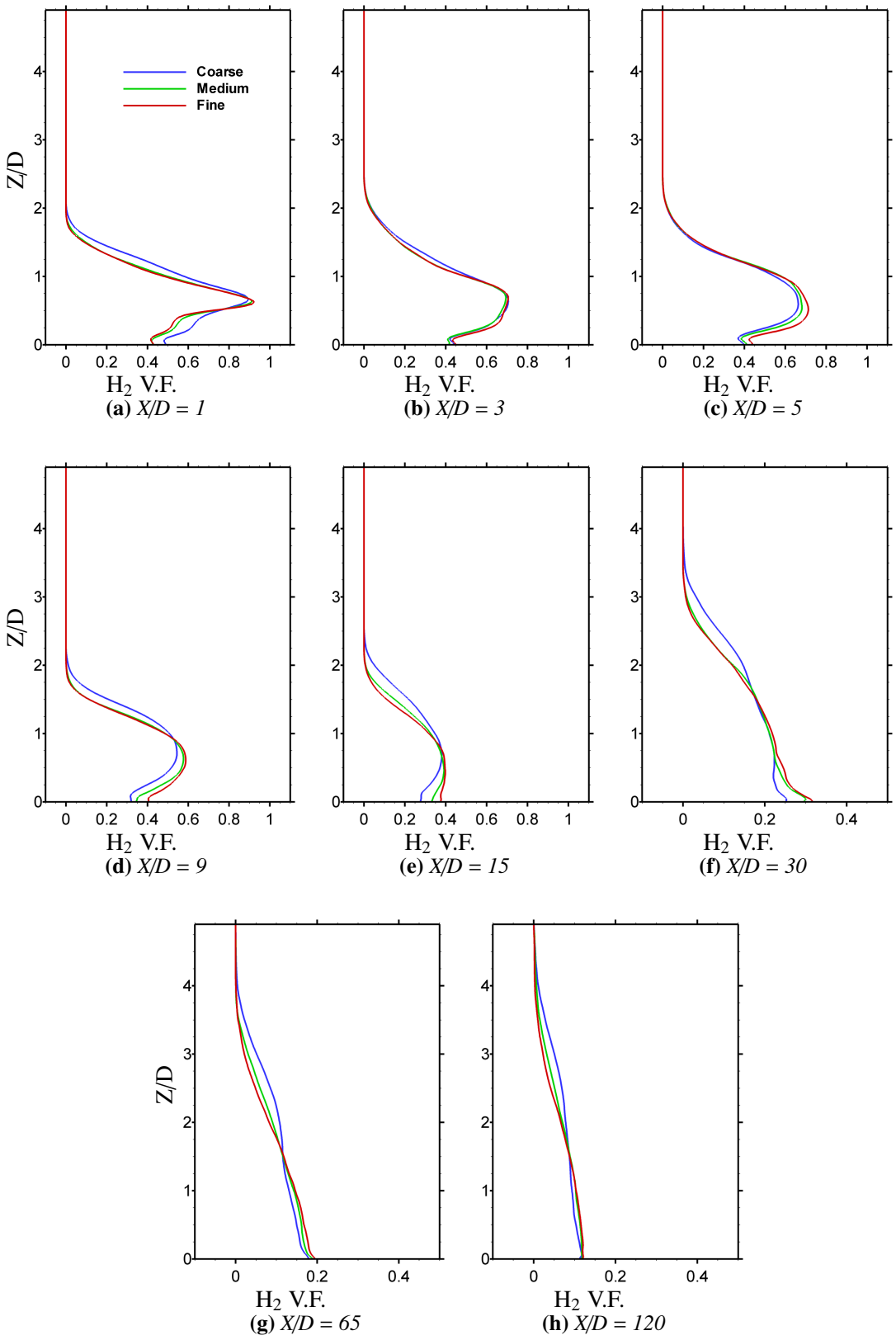

Figure 6.19: *Hydrogen volume fraction (H_2 V.F.) profiles at various locations on the wall-normal mid plane (Y/D = 0).*

chamber at location X/D = 90, we do not see clear CRVs or trailing CRVs.

Figures 6.17 and 6.18 show the streamwise and wall-normal velocities on the wall-normal mid plane (Y/D = 0) at various locations throughout the combustion chamber downstream of the hydrogen jet injection. From the Mach number contour in Figure 6.15(a) we understand that there is a recirculation zone downstream of the jet injection. This has been validated by the streamwise velocity profile at location X/D = 1 in Figure 6.17(a) as well. At location X/D = 3 the recirculation zone is not visible but there are kinks in the streamwise velocity profiles due to the CRVs. Similarly, the Figure 6.18 shows changes in the wall-normal velocity profiles at the corresponding locations. It is observed from these profiles that the CRVs are stronger closer to the jet injection port, further downstream they are increasing in size and also gaining height with the jet trajectory, but are losing wall-normal velocities. The streamwise velocity profiles are becoming more symmetric to a channel type flow. The CRVs are mainly acting in the region between x/D = 1 to X/D $\sim$ 15, after which they disappear and the flow becomes highly symmetrical especially from X/D = 20 and onwards.

Figure 6.19 shows the hydrogen volume fraction at various locations on the wall-normal mid plane (Y/D = 0). It can be seen that the hydrogen concentration is maximum closer to the injection port but it occupies less area whereas it decreases away from injection point but occupies more area. The auto-ignition temperature of hydrogen in air is nearly 800 K and it forms a flammable mixture when the concentration of hydrogen gas is 4-74% in air. It is clearly seen that the hydrogen concentration on the wall-normal mid plane (Y/D = 0) is well within the limits of a flammable mixture and as the temperature inside the HyShot-II combustion chamber is above 1000 K, this mixture would begin to burn depending upon the auto-ignition time to hydrogen in this particular case. The contour plots of hydrogen concentration in Figure 6.16(b, d, f, h and j) indicate similar phenomenon that spreads throughout the combustion chamber further downstream.

6.4.4 Pressure Distributions

Time-averaged pressure distributions have been plotted in the Figure 6.20 and 6.21 inside the combustion chamber on the bottom and top walls, respectively. Comparing this figure to the pressure distributions plot (without fuel injection) in Figure 6.6 it is noted that the pressure on the top and bottom walls inside the combustion chamber has increased, but at the same time the intensity of the shock waves travelling inside the combustion chamber is decreased especially towards the end of the combustion chamber. This is due to the reason that the shocks interact with the pair of CRVs in the region between X/D = 0 to X/D = 20 which weakens the shocks and breakup the CRVs as well. It is also noticed that close to the injection port, the pressure distribution is smooth on the bottom wall but it is fluctuating on the top wall on the mid line plane (Y/D = 0), which is due to the bow shock hitting the top wall of the combustion chamber. Away from the mid plane at location Y/D = 3, close to the injection port the pressure distribution fluctuates on the bottom wall due to the horseshoe vortex covering

a wide area but it is smooth on the top wall as it is not affected by the bow shock far away from the mid line plane.

6.4.5 Turbulent Kinetic Energy and Reynolds Stresses

The contours of time-averaged turbulent kinetic energy (TKE) are calculated as:

$$TKE = \langle u'u' \rangle + \langle v'v' \rangle + \langle w'w' \rangle \; / \; \left(2U_{\infty}^{2}\right) \tag{6.4}$$

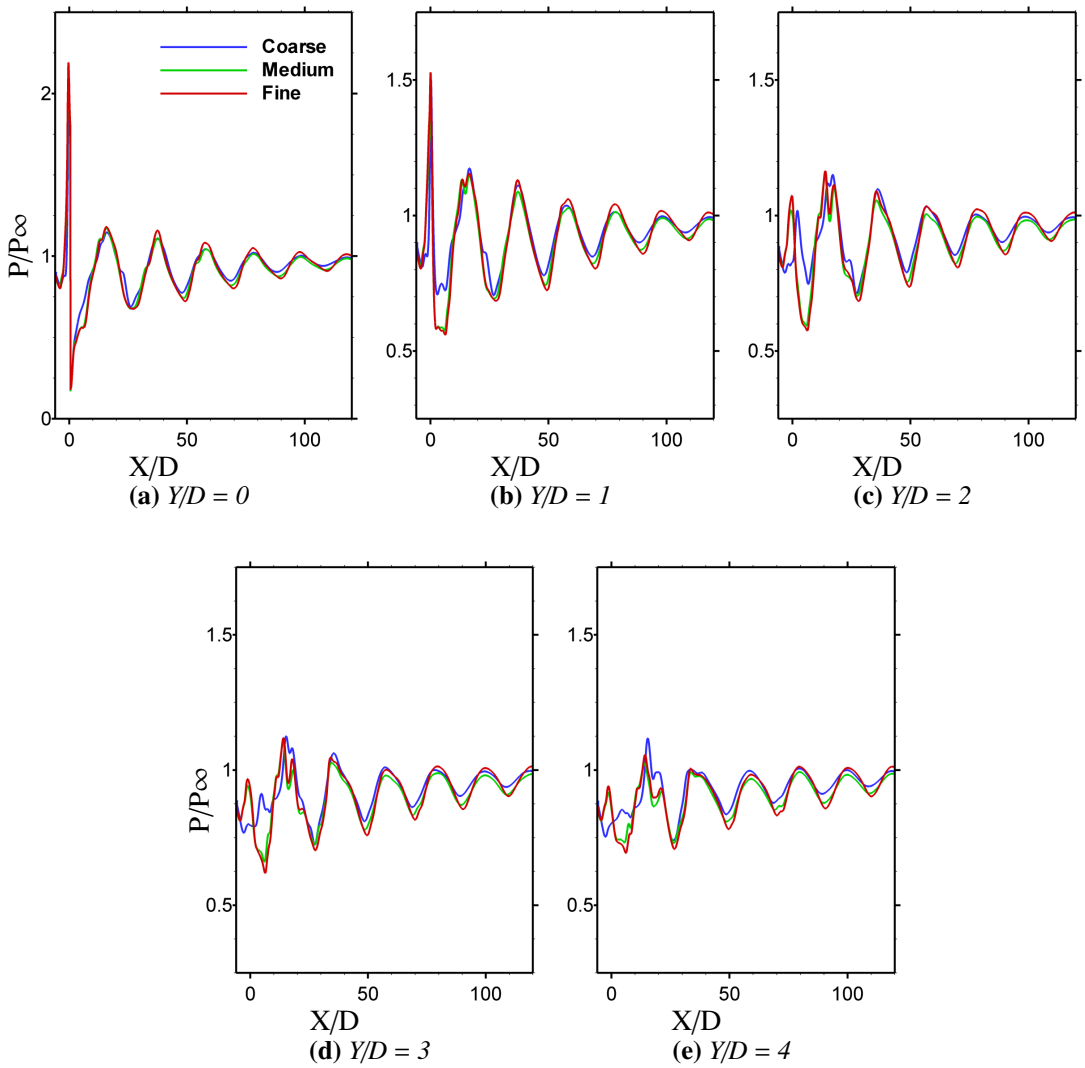

Figure 6.20: *Normalized longitudinal pressure profiles on the bottom wall of the combustion chamber after the hydrogen injection at various locations on the wall (Y/D = 0, 1, 2, 3 and 4).*

and the Reynolds shear-stress as:

$$RS = \langle u'v' \rangle \ / \ U_\infty^2 \tag{6.5}$$

where both (TKE and RS) are non-dimensionalised by the freestream velocity, are presented in Figure 6.22 and 6.23 at various locations in the flow field. Figure 6.22 presents TKE and RS at the wall-normal mid plane (Y/D = 0). There are three high TKE zones clearly visible; one is in the upstream region in the recirculation zone and the others downstream of the jet injection port. The higher TKE region upstream of the

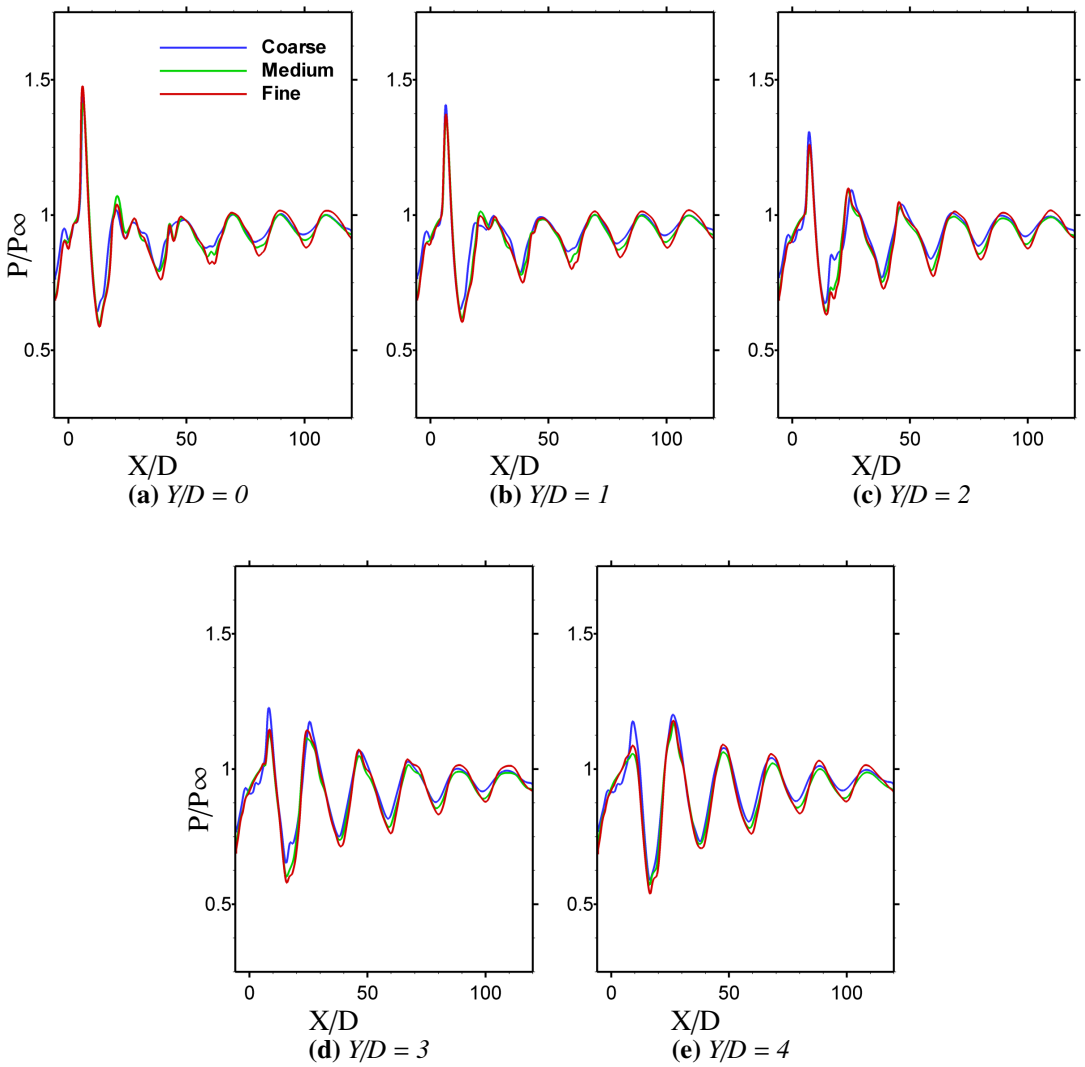

Figure 6.21: *Normalized longitudinal pressure profiles on the top wall of the combustion chamber after the hydrogen injection at various locations on the wall (Y/D = 0, 1, 2, 3 and 4).*

jet plume corresponds to the recirculation region upstream and generation of the KH instabilities in this region. The high TKE region downstream of the jet plume is related to the fluctuations in the leeward side of the jet plume as described in the Chapter 4. It can also be noted that TKE dissipation increases very rapidly after X/D = 5 position.

At the same time, there are two high RS regions, one upstream and the other downstream of the jet injection port but both of them are in opposite directions. The negative RS region upstream of the jet injection port corresponds to high activity in the jet shear layer region where the mixing starts. The results and discussion in the Chapter 4 demonstrated that this is due to the Kelvin Helmholtz type instabilities generating in the jet shear layer region which are shown earlier in the Section 6.4.1. Figure 6.23 shows TKE and RS at the wall-normal cross-view planes (X/D = 1, 3, 5, 15 and 90) where very strong RS are visible in the region of CRVs indicating strong vortex generation and away from jet plume RS decreases. The TKE contours plots indicate that maximum TKE region is close to the jet injection port and away from it TKE dissipates very quickly; at location X/D = 5 there is much less TKE visible and at location X/D = 90 some TKE is present only in the turbulent boundary layer region.

The RS plots in Figure 6.23 shows that strong RS (but in opposite directions) are present in the pair of CRVs region which dissipates gradually at locations X/D = 15. This is because in this chapter the RS is presented for the streamwise and the spanwise velocity components as opposed to the streamwise and wall-normal velocity components in the Chapter 4. Similar to the TKE, there is very less RS present at far away location downstream of the jet injection at X/D = 90. This analysis indicates that maximum mixing takes place in the jet shear layer and just downstream of the jet injection ports, and the flow is fully developed at around X/D ≈ 20 after which mostly the chemical reaction would take place throughout the rest of the combustion chamber length. Long combustion chamber and small auto-ignition time of hydrogen can help combustion process but it would depend upon the residence time of the flow inside the combustion chamber mainly.

Figure 6.24 and 6.25 shows quantitative plots for the TKE and RS at the Y/D = 0 plane

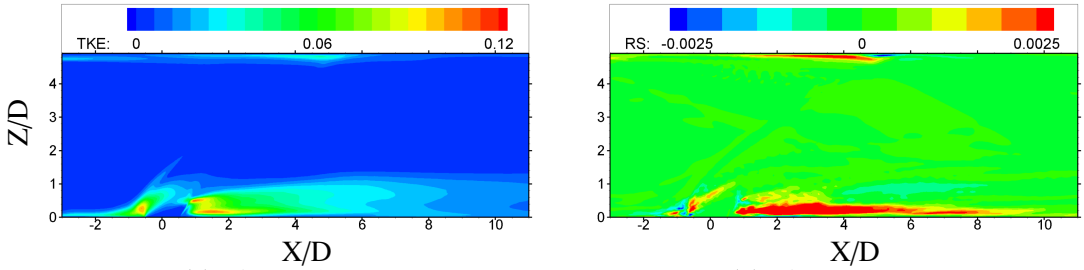

(a) *Plane: Y/D = 0* **(b)** *Plane: Y/D = 0*

Figure 6.22: *Time averaged turbulent kinetic energy and Reynolds shear-stress contours inside the combustion chamber at the wall-normal mid plane (Y/D = 0) along with the streamlines.*

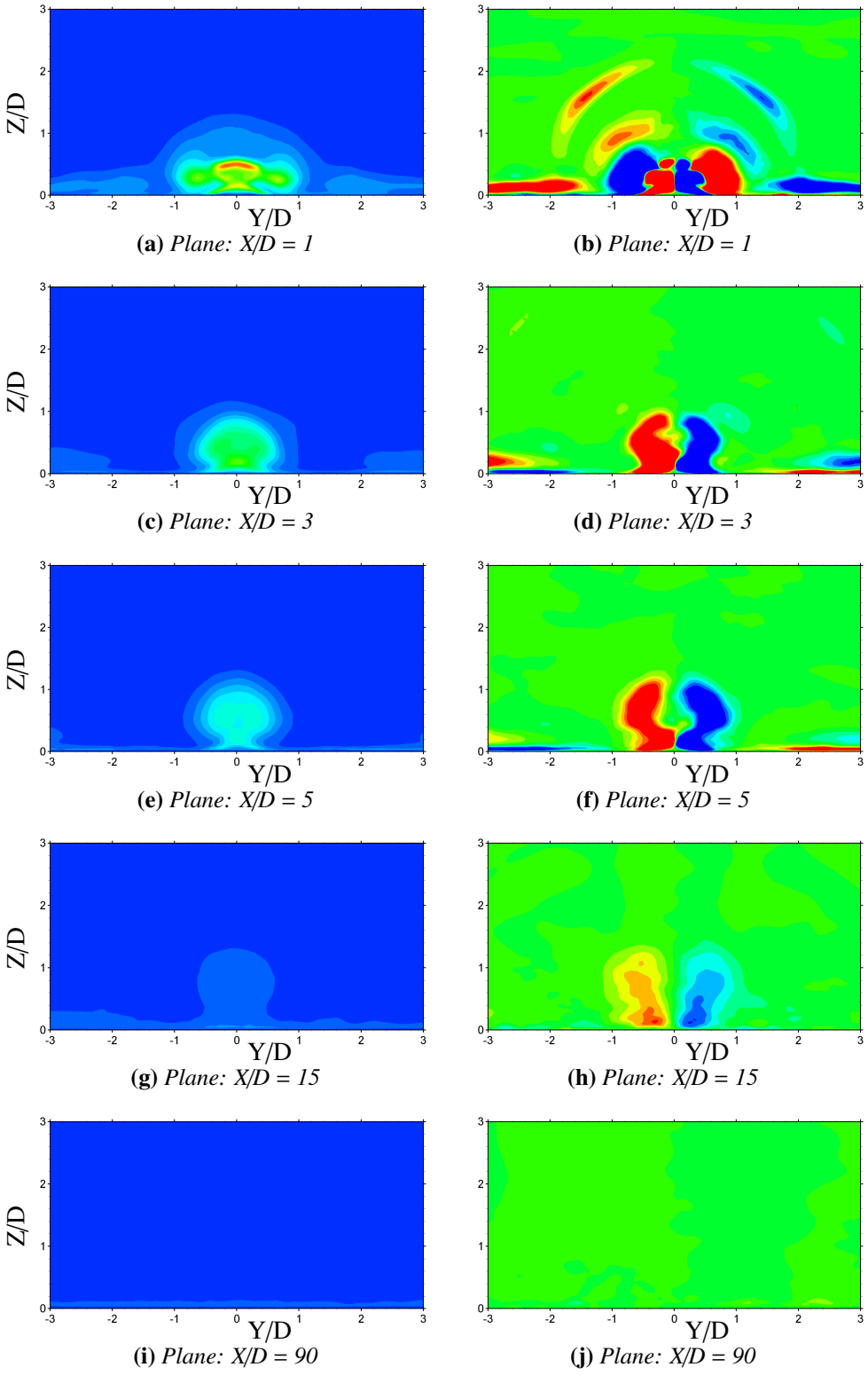

(a) *Plane: X/D = 1*
(b) *Plane: X/D = 1*
(c) *Plane: X/D = 3*
(d) *Plane: X/D = 3*
(e) *Plane: X/D = 5*
(f) *Plane: X/D = 5*
(g) *Plane: X/D = 15*
(h) *Plane: X/D = 15*
(i) *Plane: X/D = 90*
(j) *Plane: X/D = 90*

Figure 6.23: *Time averaged turbulent kinetic energy and Reynolds shear-stress contours inside the combustion chamber at the cross-flow plane (X/D = 1, 3, 5, 15 and 90) along with the streamlines (contour legend same as shown in the Figure 6.22)*

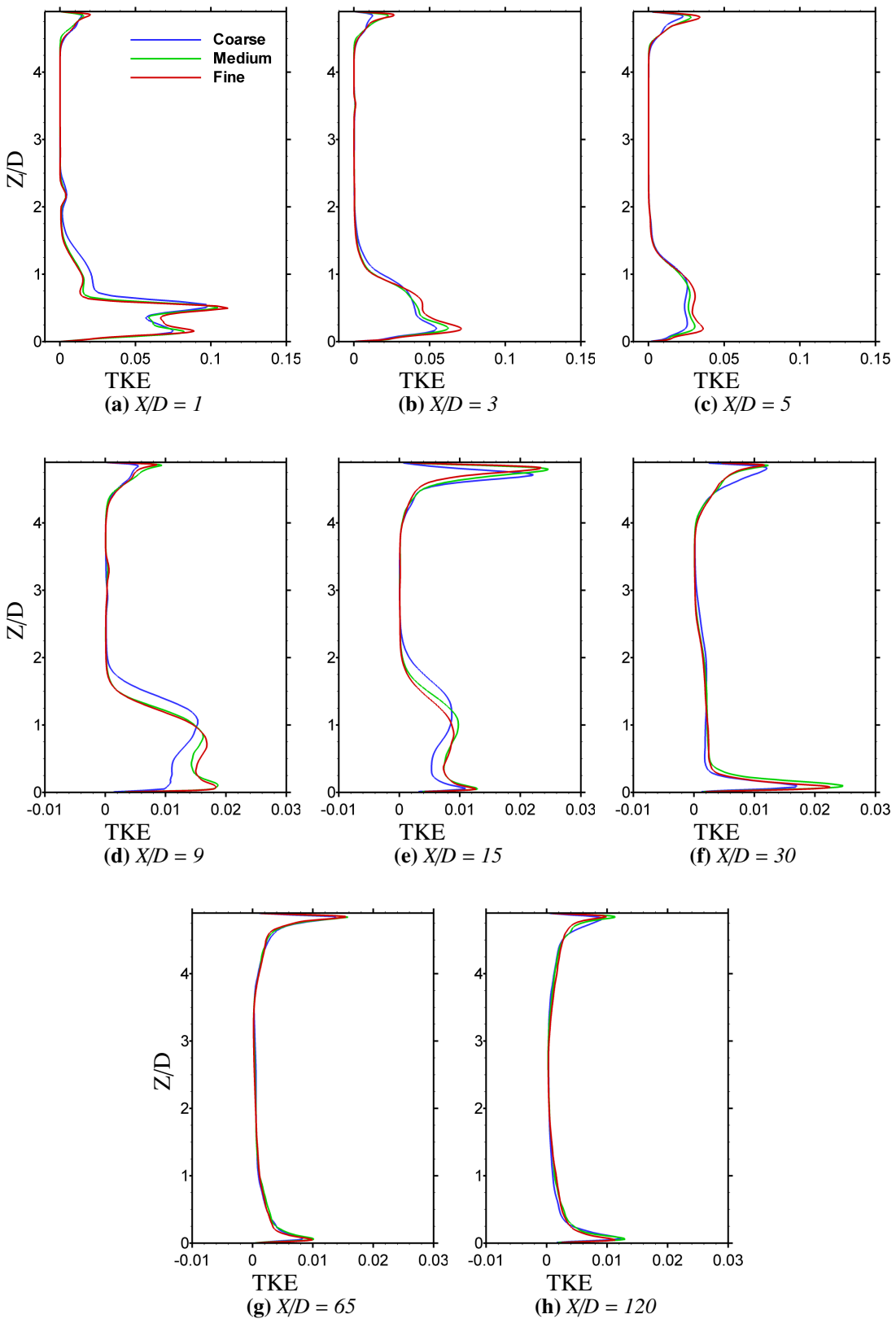

Figure 6.24: *Turbulent kinetic energy (TKE) profiles at various locations on the wall-normal mid plane (Y/D = 0).*

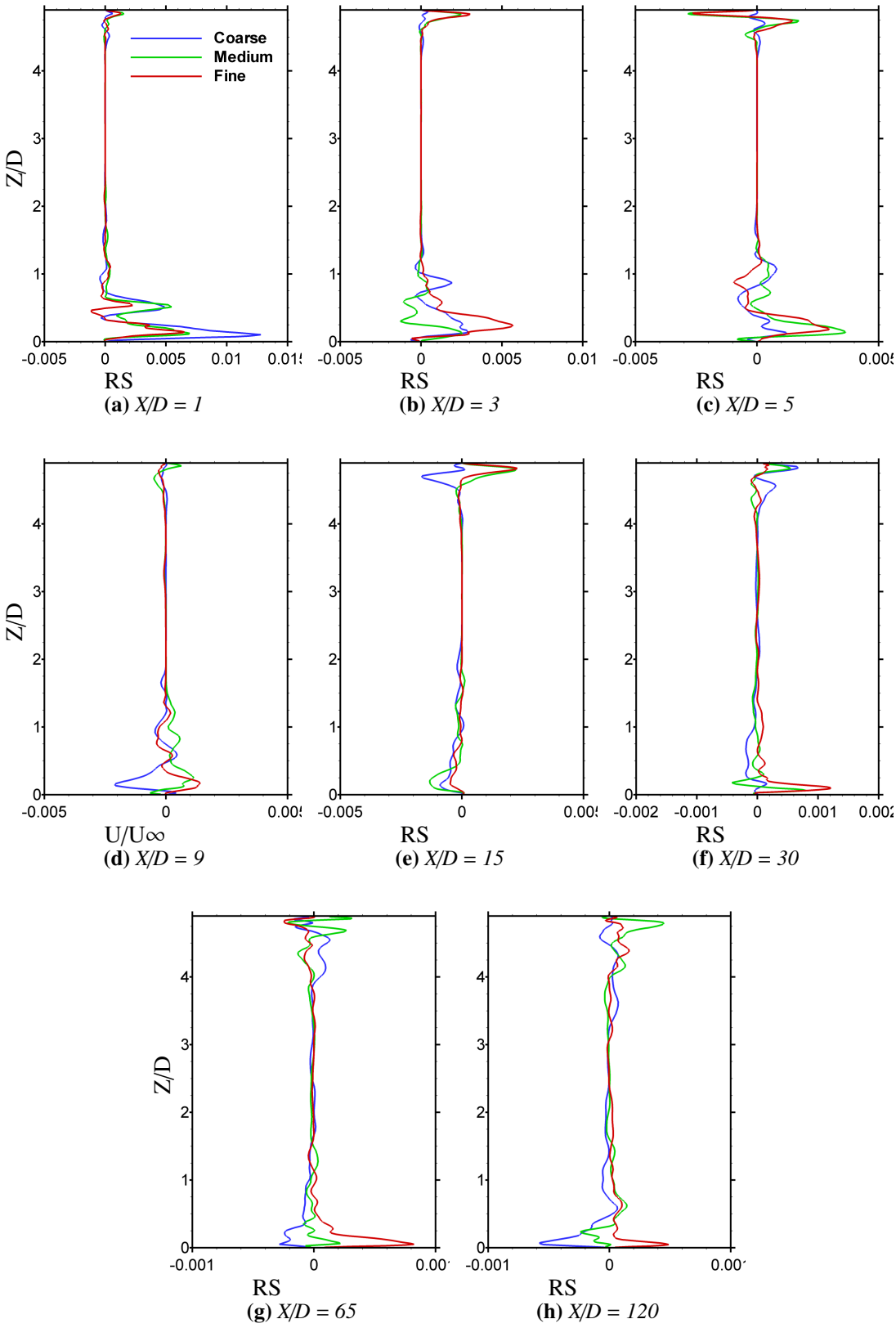

Figure 6.25: *Reynolds shear-stress (RS) profiles at various locations on the wall-normal mid plane (Y/D = 0).*

at various X/D locations, verifying the finding discussed above. Note that the TKE and RS plots at location X/D = 5 are very different from those at location X/D = 90. Based upon this discussion the whole length of the HyShot-II combustion chamber can be divided into three separate regions. First region from the injection port up to X/D =5 location where maximum mixing is taking place. The second region is up to location X/D ~ 20 where the flow has released most of its TKE and finally the rest of the length of the combustion chamber where full combustion would take place.

6.4.6 Temperature Profiles and Flow Mixing

Figures 6.26 and 6.27 represents the contour plots of the temperature and the root mean square (RMS) of fluctuations in the hydrogen volume fraction at various locations in the flow field. These contour plots illustrate the major mixing zones inside the combustion chamber and indicative temperatures in these areas. Again, it is noted from the Figure 6.26(b) and Figure 6.27(b) that the majority of the mixing is occurring in the windward side of the hydrogen jet plume. Temperature contours at these locations indicate that this region is well within the auto-ignition temperature range and thus combustion process would start immediately in these areas. It can also be observed from Figure 6.26(a and b) that there is some hydrogen and air mixing in the upstream recirculation zone. This is the boundary layer region where the temperature is very high as indicated by the temperature contours. Therefore, it is understood that early combustion would start in the upstream recirculation zone, which is very helpful considering short residence time of air-fuel mixture inside the combustor.

Figure 6.28 and 6.29 presents quantitative results of the RMS of the fluctuations in the hydrogen volume fraction and the temperature profiles on the wall normal mid plane (Y/D =0) at various locations. Downstream from the jet plume, the mixing area is increasing gradually and the temperature remains well above the auto-ignition temperature of the hydrogen-air mixture (~ 800 K). It can be noted that the jet shear layer is an area of maximum activity. This is the area where the KH instabilities are generating

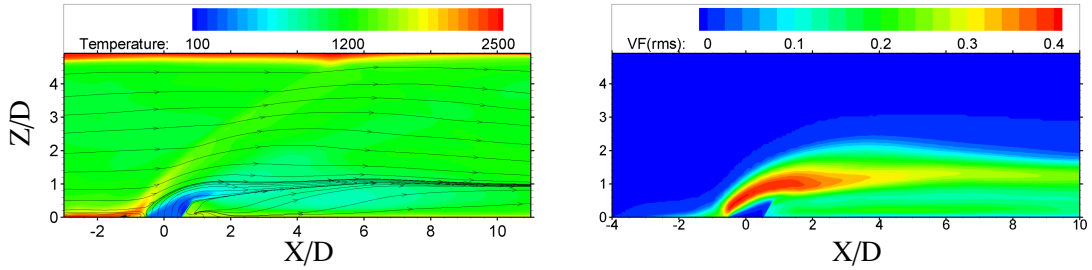

(a) *Plane: Y/D = 0* **(b)** *Plane: Y/D = 0*

Figure 6.26: *Time averaged temperature and RMS contours of the fluctuations in the hydrogen volume fraction (passive scalar) inside the combustion chamber at the wall-normal mid plane (Y/D = 0) along with the streamlines.*

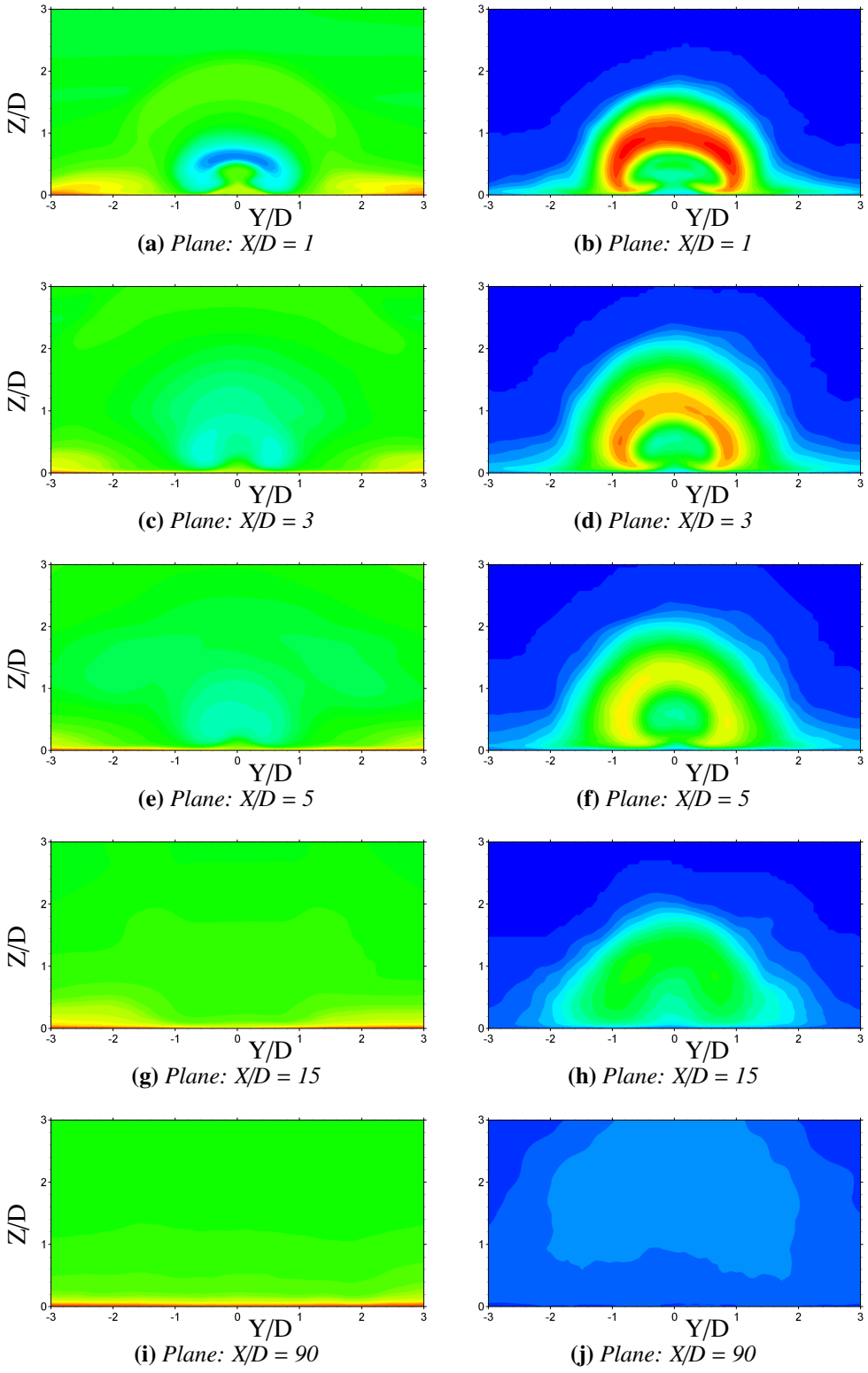

(a) *Plane: X/D = 1*
(b) *Plane: X/D = 1*
(c) *Plane: X/D = 3*
(d) *Plane: X/D = 3*
(e) *Plane: X/D = 5*
(f) *Plane: X/D = 5*
(g) *Plane: X/D = 15*
(h) *Plane: X/D = 15*
(i) *Plane: X/D = 90*
(j) *Plane: X/D = 90*

Figure 6.27: *Time averaged temperature and RMS contours of the fluctuations in th hydrogen volume fraction (passive scalar) inside the combustion chamber at the cross-flow plane (X/D = 1, 3, 5, 15 and 90) along with the streamlines (contour legend same as shown in the Figure 6.26)*

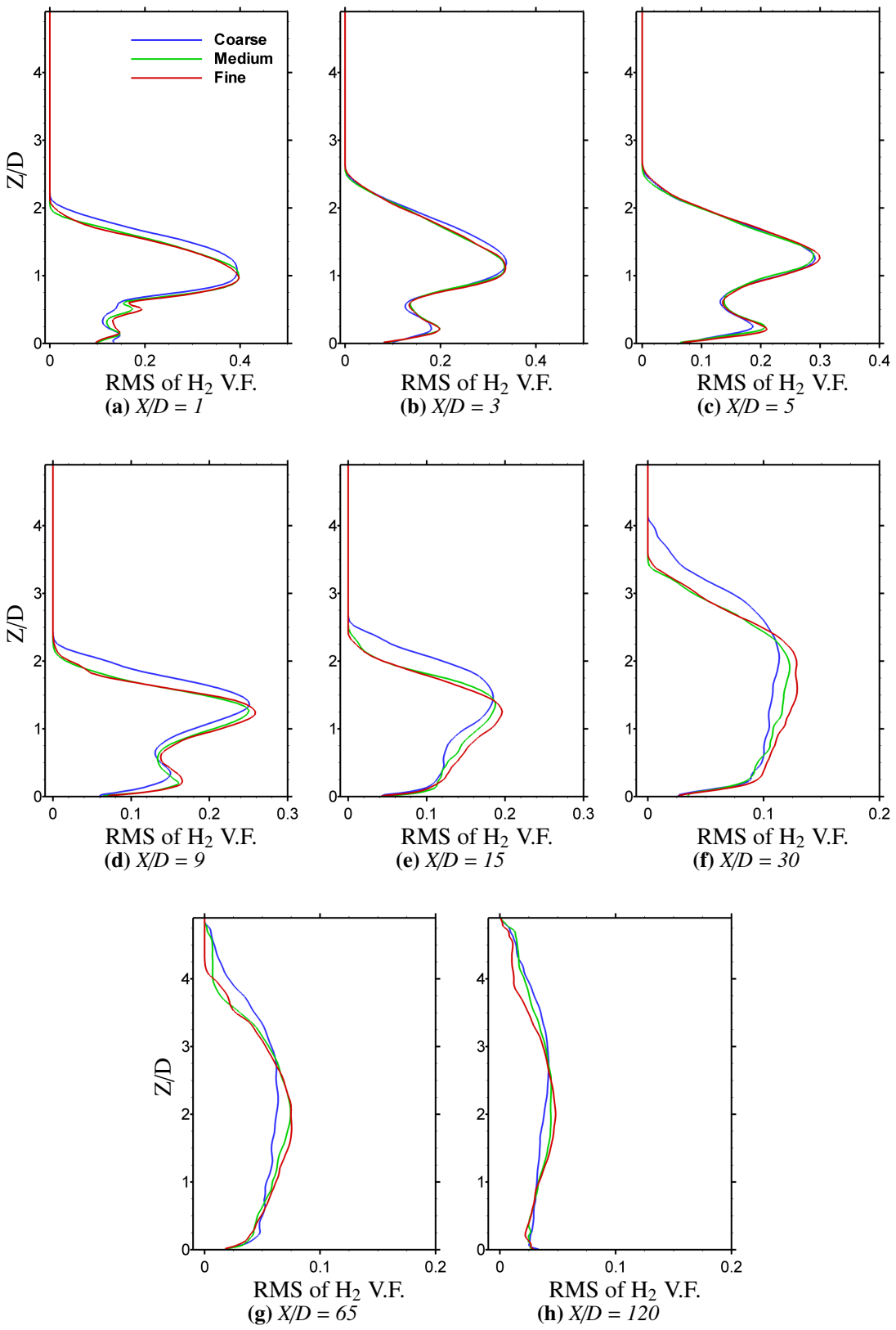

Figure 6.28: *RMS of fluctuations in hydrogen volume fraction (passive scalar) profiles at various locations on the wall-normal mid plane (Y/D = 0).*

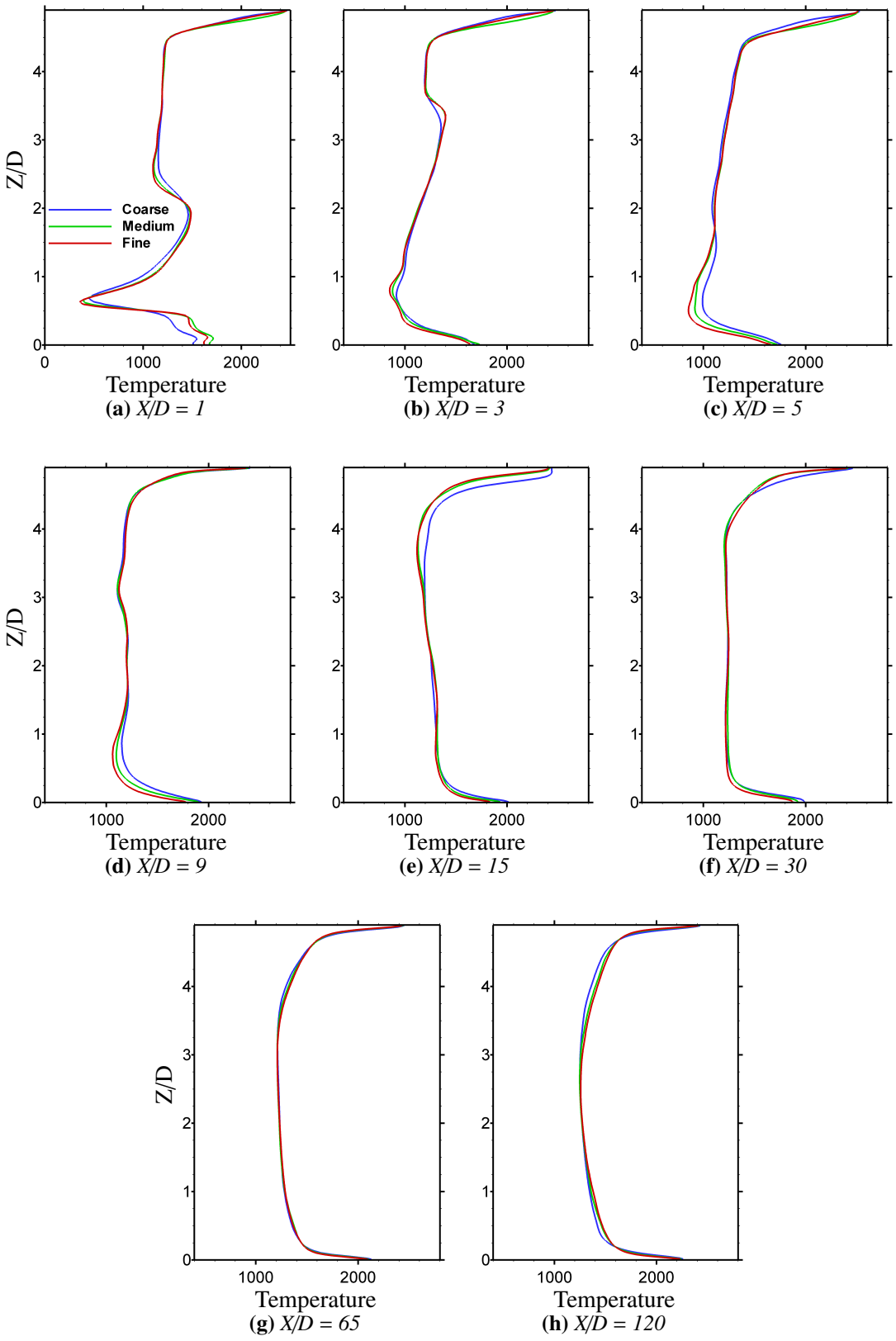

Figure 6.29: *Temperature profiles at various locations on the wall-normal mid plane (Y/D = 0).*

as discussed earlier. Some mixing is also occurring in the boundary layer area just downstream of the jet injection port which is the leeward side of the jet plume. A detailed analysis in this area has been presented in the Chapter 4 where slight fluctuation in the leeward side of barrel shock results in some mixing in this area. Considering that the temperature is high enough in the this area and the boundary layer region, combustion all around the jet plume is expected as soon as the hydrogen is injected inside the combustion.

Far downstream the jet plume, the mixing area expands in size covering almost the entire slice in Figure 6.27(d, f, h and j) which is also demonstrated by the RMS plots in Figure 6.28 showing reducing RMS but an increase of the area it is occupies. As not much activity (TKE, RS etc.,) has been identified in this area, this will be the area where full combustion/chemical reactions should be taking place for the entire length of the combustion chamber. It can be deduced from the analysis that for the HyShot-II scramjet, the length of the combustion chamber and the spanwise distance between the injection ports allows for proper mixing of hydrogen and air inside the combustion chamber. Figure 6.30 shows the percentage of air-fuel mixture within the flammability range on the wall-normal mid plane (Y/D = 0). It can be seen in the Figure 6.30 that the hydrogen entrained in the upstream recirculation zone is with the flammability range and would help start early ignition. The extent to how complete the combustion process would be depends upon the residence time of the air-fuel mixture inside the combustion chamber and requires chemical analysis in details. Based upon the Figure 6.30 and the

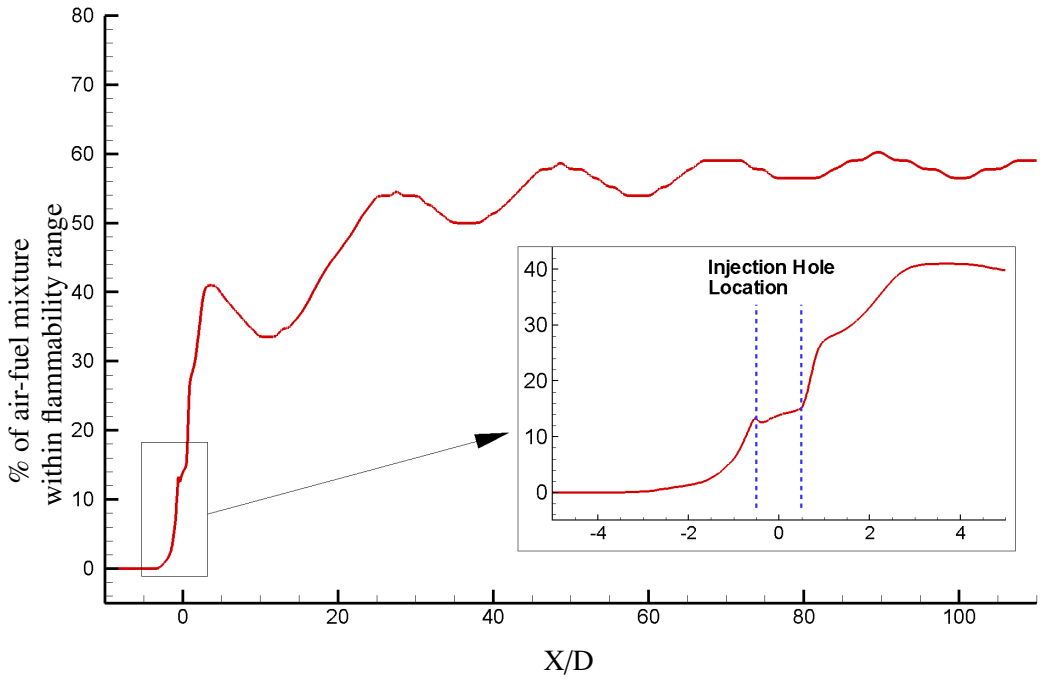

Figure 6.30: *Percentage of hydrogen-air mixture within the flammability range on the wall-normal mid plane (Y/D = 0). In the close-up view the dashed blue line shows the location of the injection hole.*

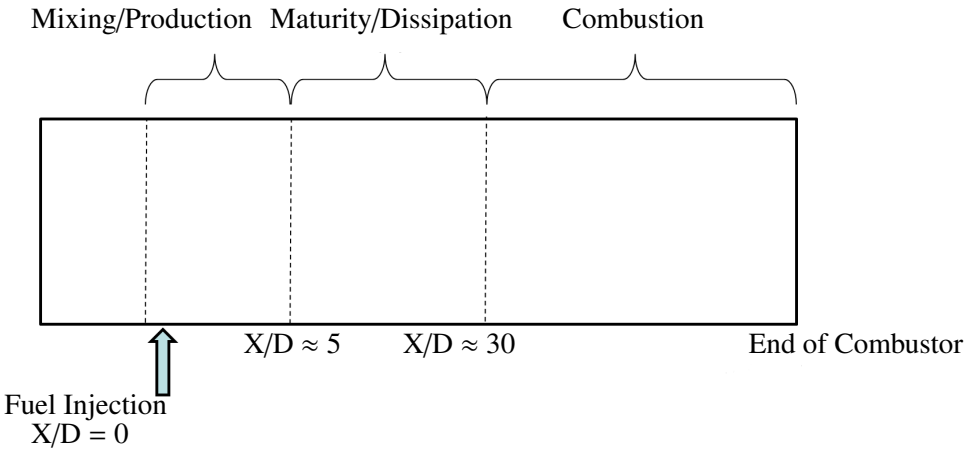

Figure 6.31: *Schematic diagram of HyShot-II combustion chamber showing percentage area of combustible air-fuel mixture.*

analysis of the HyShot-II combustion chamber, the chamber can be divided into three sections as in the Figure 6.31. Part one from upstream recirculation zone to X/D $\sim$ 5 where most of the mixing is occurring and high TKE and RS regions are found which is also the region where CRVs and the shocks act to enhance the mixing mechanism. Second part can be up to X/D $\sim$ 30 where the major flow features dissipate away and lastly the third part can be the rest of the combustion chamber where full mixing has achieved and full and thorough combustion should be observed. This methodology of analyzing cold fuel flow inside a combustion chamber can be implemented at the design stage of a scramjet combustion chamber.

6.5 Summary

In this chapter a complex multi-species flow outside and inside the HyShot-II scramjet engine has been analyzed. The supersonic turbulent boundary layer has been generated using a digital filter based turbulent inflow data generation method which has been validated for a similar case previously. The emphasis of this study was the fuel injection, penetration and mixing inside the HyShot-II combustion chamber without any chemical reactions in order to understand the flow features and properties. As no experimental or CFD result were available to compare the data, the validity of the results for the combustion chamber are based upon the results presented in the Chapter 4 where same methodology has been implemented and the results were compared with the experimental and previous LES data. Important finding of the analysis are itemized below:

1. The internal and external flow around the HyShot-II scramjet consists of very complex shock structures and under thermal and chemical equilibrium assumptions as discussed in the Chapter 3 the air can be described as a thermally perfect

gas. The bleed region just ahead of the combustor helps disgorge the boundary layer and shocks and clean the combustor inflow, but there is a weak shock train running inside the combustor which is generated at the front edge of the bottom wall of combustor.

2. The jet penetration greatly depends upon the jet-to-crossflow momentum flux ratio. As for the sonic hydrogen injection case, this is very low and the jet plume is distorted by the high momentum of the incoming supersonic turbulent boundary layer giving a jet trajectory close to horizontal.

3. Hydrogen is entrained in the recirculation region upstream the jet plume and because the temperature in this region is well above the auto-ignition temperature of hydrogen-air mixture, combustion would start in the upstream region of jet plume.

4. A pair of counter rotating vortices is generated just after the jet injection, but due to the interaction with the shock train inside the combustor the CRVs are distorted and after X/D $\sim$ 20 it is not clear if coherent counter rotating vortices are present in the flow.

5. Around the jet plume the areas of maximum mixing is the leading edge of the jet shear layer. The interaction of counter rotating vortices with the shocks enhances the mixing process for hydrogen and air in the downstream of jet plume.

6. Maximum turbulent kinetic energy and Reynolds shear-stresses are present in the region closer to the jet plume (upstream and downstream). Downstream the jet at approximately X/D = 5 the TKE and RS start to dissipate very quickly.

CHAPTER 7

Conclusion

This chapter presents the main findings and lessons learnt during the study of jet injection into a supersonic crossflow and the HyShot-II scramjet combustion chamber analysis. Furthermore, some suggestions are presented in order to gain a deeper insight into this complex topic in future, which can aid the quest for high-fidelity simulations at a reasonable computational cost.

7.1 Conclusion

The simulations of the high-speed compressible turbulent multi-species flows, where the high temperatures of the gas can also affect the flow physics, require capturing of correct flow dynamics and the discontinuities present in the flow. The work in this thesis covered a range of issues pertinent to the numerical prediction of complex flow of transverse circular sonic jet injection into a supersonic crossflow (JISC). The numerical technique, used to study the JISC flow, employed high-resolution methods in the context of Implicit Large-Eddy Simulations where no explicit subgrid scale was used in order to model the wavenumbers in the dissipation range. The behavior of a fifth-order MUSCL scheme with modified variable extrapolation was assessed, in combination with a three-stage second-order strong-stability-preserving Runge-Kutta scheme for temporal advancement.

The TVD based Finite Volume discretization methods allow strong shock waves to be resolved with adequate accuracy and without any spurious oscillations and are considered suitable for compressible flows with discontinuous solutions. The emphasis was on the application of the said MUSCL scheme which has already shown very good results for homogeneous decaying turbulence at low speeds using modified variable extrapolation[154] where the velocity jumps were scaled by the Mach number allowing for a constant dissipation rate in low Mach regions. Combining the above mentioned two characteristics, the numerical scheme was a very worthy candidate to investigate complex super/hyper-sonic flows with discontinuities and subsonic recirculation/separation zones, such as the JISC flow. For multi-species flows, correct and fast

species tracking was vital, therefore, in this thesis a volume fraction model by Allaire *et al.*[4] has been utilized.

The JISC case study is a typical fuel injection strategy for a scramjet engine and can also be used as part of a missile thrust vector control system and noise control in cavities during flight. In this thesis the emphasis was on the numerical study of a JISC experiment at Mach $\sim$ 1.6 crossflow over a flat-plate and hydrogen injection into a Mach $\sim$ 2.5 crossflow inside the HyShot-II scramjet engine. The aim of the research was to investigate JISC flow characteristics such as the supersonic turbulent boundary layer (STBL) in the incoming flow, jet penetration, separation regions, several three-dimensional features that enhance the fluid mixing, pressure distributions inside the combustion chamber, turbulent kinetic energy and the Kelvin-Helmholtz (KH) instabilities in the flow field as the sonic jet is injected. The JISC although is related to high Mach number flows but it, in fact, contains subsonic flow regions such as separation and recirculation regions near the wall which play vital role in the defining the overall flow features and profiles.

For the generation of turbulent inflow data, a method based upon digital filters has been implemented as the turbulent boundary condition with a proposed simpler method of implementation on the structured grids. The STBL in the incoming supersonic flow for the JISC was generated using the digital filter based turbulent inflow boundary condition and four levels of increase grid resolution cases were presented. The ILES results for all the grid resolutions were compared with the experimental and classical LES data on the upstream and downstream of the jet injection hole. Time-averaged flow features (two and three dimensional) were presented to understand the flow structure as the jet was injected into the supersonic crossflow. The jet penetration study was conducted for the jet-to-crossflow momentum flux ratio as in the Santiago and Dutton[139] experiment. Furthermore, the turbulent/fluctuating kinetic energy and Reynolds shear stress profiles were compared with the classical LES. Instantaneous flow field analysis demonstrated that maximum fluid mixing occurs on the jet shear layer but at the same time some mixing was demonstrated on the leeward side of the jet plume, which was due to the fluctuations in the leeward barrel shock. Entrainment of the jet fluid in the upstream recirculation zone was also demonstrated by the presence of jet volume fraction in this region.

The digital filters based turbulent inflow data generation method as implemented in the current work is a computationally efficient and accurate method. In order to support this thesis a series of simulations were carried out for the JISC flow with different inflow conditions (such as laminar inflow, random white-noise based inflow and Reynolds stress based method) and the results were compared to the digital filter based method. The one dimensional kinetic energy spectrum was examined in the incoming STBL and around the jet plume to demonstrate the effects of grid resolutions and other methods of turbulent inflow data generation on the energy dissipation rate. An ideal $k^{-5/3}$ decay of energy was presented in a certain range which improved with the grid resolution for the digital filters based technique, whereas, for other techniques almost no inertial range was visible. This investigation used the Reynolds stress based method

for the generation of turbulent inflow data, which was effectively obtained by eliminating the exponential correlations from the digital filter based technique. The purpose of this investigation was to demonstrate that by eliminating the Exponential correlation from the digital filter based technique the accuracy and effectiveness of the method is seriously diminished. Hence, the ability of digital filter based technique to produce statistical results in good agreement with the various DNS results was demonstrated in the Chapters 4 and 5. This comparison demonstrated that the digital filter based technique provided a consistent, accurate and computationally efficient turbulent inflow data, whereas, the other methods showed immediate or gradual dissipation of the fluctuations. The effects of various incoming boundary layers on the actual JISC flow were also presented in order to demonstrate the reliability and accuracy of the digital filter based technique.

The HyShot-II is a hypersonic air-breathing propulsion (HAP) device which operates at hypersonic velocities (above Mach $\sim$ 5) where high temperatures can affect the behavior of the air and it can act as a thermally perfect gas. The aim was to investigate the combustion chamber of HyShot-II scramjet; in order to obtain the combustion chamber inflow condition, firstly, the full geometry of HyShot-II scramjet was analyzed using the thermally perfect gas formulation which allowed variable γ (specific heat ratio) at higher temperatures. The inflow conditions thus obtained were applied to the three dimensional combustion chamber simulations with hydrogen injection to study the flow dynamics (without chemical reactions). A validation study for the thermally perfect gas formulation was presented in comparison to the NACA-1135[147] report and the NASA's Thermally Perfect Gas (TPG) code, in the Chapter 3. The full geometry HyShot-II analysis demonstrated a very complex flow field developing at the start of the combustion chamber full of shocks and thick boundary layer. It has been presented that the geometry of the HyShot-II allowed for these two to be disgorged from the system through the bleeds on the either side of the geometry. Still the flow inside the combustion chamber contained a strong shock train traveling inside it which was generated at the bottom wall of the combustion chamber.

The pressure distributions at the inlet ramp and inside the combustion chamber (without fuel injection) were compared to the experimental and RANS data from DLR to demonstrate excellent agreement. The inflow conditions were obtained at the X = 355 mm or X/D = -26.5 location towards the start of the combustion chamber and are again compared to the CFD data from DLR. The grid sizes used for the full geometry analysis is $1/3^{rd}$ of the grid used in RANS but still produced similar levels of accuracy in data. The combustion chamber analysis was carried out on a three dimensional grid with three levels of grid resolutions. The JISC of hydrogen injection (without fuel injection) demonstrated that the jet plume is very distorted in the flow field because of the high Mach number (and thus high momentum flux ratio) of the inflow. As no experimental of CFD data was available to compare, the validity of the results presented for the HyShot-II combustion chamber are based upon the test cases investigated in the earlier parts of the thesis. The analysis demonstrated that although the jet penetration is very low, the fluid mixing started immediately and hydrogen was entrained in the

recirculation zone upstream of the jet plume. Flow visualization at various locations showed that the length of the combustion chamber allowed for good mixing of the two fluids. The temperature analysis indicated that the temperatures were high enough throughout the length of the combustion chamber to allow for combustion, although, full combustion would depend upon several other critical factors that were beyond the aim of the current study. Based upon the analysis presented, it was proposed that a typical combustion chamber can be divided into three sections.

Major contributions to knowledge during this research are identified as below:

- A digital filter based turbulent inflow data generation method has been implemented in a very simple manner within the framework of ILES. The method has been validated and verified using the extensive analysis of the JISC test case at different grid levels. It was also demonstrated to be accurate, reliable and computationally efficient compared to other simpler techniques.
- It has been established in much greater detail that the random white-noise based turbulent inflow data generation method dissipates fluctuations very quickly in the flow field and do not provide any turbulence in the flow field.
- The importance of the Exponential correlation in the digital filter based technique has been studied which is now established to be a key feature in the digital filter based technique.
- The variable ratio of specific heats formulation has been implemented which has been demonstrated to be an accurate method when compared to the NASA TPG code and provides a simpler formulation to simulate thermally perfect gas flows.
- Using these methods within the ILES framework, the JISC experiment[139] was studied computationally which has been demonstrated as a substantially faster method than the classical LES, with the similar or better level of accuracy compared to the classical LES data.
- A much clearer two and three dimensional flow features identification has been carried out inside the JISC flow field.
- The generation of KH-instabilities have been demonstrated to be the key mixing mechanism on the jet shear layer.
- It has been identified that the fluctuations on the leeward side of the barrel shock are also responsible for some mixing in the downstream of jet injection hole.
- The fifth-order MUSCL scheme with modified variable extrapolation within the framework of ILES has been validated on a hypersonic external flow on the HyShot-II scramjet geometry and high-speed multi-species turbulent compressible flows. Based upon its accuracy and efficiency it offers great potential for future research into combustion using this tool.

7.2 Suggestions for Future Research

It has been learnt that in the field of scientific research there is not *only one way* to explore any idea. Similarly, the work presented in this thesis is one way and considering the vastness and complications of the subject the author recognizes that need is to explore other methods as well. Firstly, it is recommended to explore other methods for implementing the thermally perfect gas formulation in the code such as curve fitting method. This would mean that the method is not dependant upon the "characteristic temperature (Θ)" and would allow to include more mono- and poly-atomic gases and fuels at even higher temperatures than can be simulated using the NACA-1135 thermally perfect gas formulation.

A very thorough analysis of the JISC cases has been presented in this thesis and the CNS3D code have proved to be an excellent tool for computational efficiency and accuracy of the results. The digital filter based turbulent inflow data generator has also demonstrated its strengths compared to other methods and is also currently been used for a channel flow case in another PhD research. The suggestion would be to use the same spatial and temporal accuracy because of its benefits detailed above and research should be continued in the area of scramjet combustion chamber. The need is it to develop the code for the non-premixed combustion of hydrogen or hydrocarbons as the latest scramjet NASA's X-51 uses hydrocarbons. Considering the confidentialities involved in the scramjet research, but if possible more geometries, especially X-51, should be explored. Its is also recommended that the O-grid topologies should be investigated for the fuel injection ports and the fuel pipes should be simulated in order to reduce the errors further down. It is also suggested that the digital filter based method implemented in this research should be investigated further as the author believes that it can offer huge benefits in computations of complex flow field. Investigations of this method combined with ILES can result in further contributions to both numerical methods and physics of flows.

Bibliography

[1] "Global Hypersonic News for a High Mach World". *AIAA HyTASP Program Committee Inaugural Newsletter*, Vol.1,Iss.1, 2008.

[2] G.N. Abramovich. *The Theory of Turbulent Jets*. Massachusetts Institute of Technology Press, Cambridge, Mass., English ed., 1963, Chap. 12, Sec. 4.

[3] T. Admason and J. Nicholls. "On the Structure of Jets from Highly Underexpanded Nozzles into Still Air,". *Journal of th Aerosspace Sciences*, Vol.26:pp. 16–24, 1959.

[4] G. Allaire, S. Clerc, and S. Kokh. "A Five-equation Model for the Simulation of Interfaces between Compressible Fluids.". *Journal of Computational Physics*, Vol. 181(2):pp:577–616, 2002.

[5] J.D. Anderson. *Computational Fluid Dynamics: The Basics with Applications*. McGraw-Hill Inc., 1995.

[6] J.D. Anderson. *Hypersonic and High-Temperature Gas Dynamics*. AIAA Education Series, 2006.

[7] J.D. Anderson. *Modern compressible flow with historical perspective*. McGraw-Hill Inc., 3rd ed, 2003.

[8] R ANTONIA, A.J. CRAMBERS, and N. PHAN-THIEN. "On the Behaviour of Upwind Schemes in the Low Mach Number Limit.". *J . Fluid Mech.*, Vol. 100:pp:193, 1980.

[9] G. Aswin and D. Chakraborty. "Numerical Simulation of Transverse Side Jet Interaction with Supersonic Free Stream,". *Aerospace Science and Technology.*, Vol.14,:pp:295–301, 2010.

[10] A. Bagabir and D. Drikakis. "Numerical Experiments using High-Resolution Schemes for Unsteady, Inviscid, Compressible Flows,". *Computer Methods in Applied Mechanics and Engineering*, Vol.193:pp. 4675–4705, 2004.

[11] A. Ben-Yakar, G. Mungal, and R. Hanson. "Time Evolution and Mixing Characteristics of Hydrogen and Ethylene Transverse Jets in Supersonic Crossflows,". *Physics of Fluids*, Vol.18:pp. 315–323, February 2006.

[12] D. Benson. "Computational Methods in Lagrangian and Eulerian Hydrocodes.". *Comput. Meth. Appl. Mech. Eng.*, pages pp:235–394, 1992.

[13] F. Billig, R. Orth, and M. Lasky. "A Unified Analysis of Gaseous Jet Penetration,". *AIAA Journal.*, Vol. 9:pp. 1048–1058, 1971.

[14] J. Blazek. *Computational Fluid Dynamics: Principles and Apllications*. Elsevier, London, U.K., 2001.

[15] J.P. Boris, F.F. Grinstein, E.S. Oran, and R.J. Kolbe. "New Insights into Large Eddy Simulation.". *Fluid Dynamics Research*, Vol. 10,:pp: 199., 1992.

[16] R.R. Boyce, S. Gerard, and A. Paull. "The Hyshot Scramjet Flight Experiment Flight Data and CFD Calculations Compared". *12th AIAA International Space Planes and Hypersonic Systems and Technologies, Virginia, AIAA-7029*, 2003.

[17] R.R. Boyce and A. Paull. "Scramjet Intake and Exhaust CFD Studies for the Hyshot Scramjet Flight Experiment". *10th AIAA International Space Planes and Hypersonic Systems and Technologies Conference, Japan, AIAA-1891*, 2001.

[18] L. Cattafesta, D. Williams, C. Rowley, and F. Alvi. "Review of Active Control of Flow Induced Cavity Resonance". *AIAA paper: 2003-3567*, 2003.

[19] N. Chauvet, S. Deck, and L. Jacquin. "Shock Patterns in a Slightly Underexpanded Sonic Jet Controlled by Radial Injections,". *Physics of Fluids.*, Vol.19, Iss. 4.:Article Number: 048104, DOI: 10.1063/1.2720836, 2007.

[20] L. Cohen, L. Coulter, and W. Egan. "Penetration and Mixing of Multiple Gas Jets subjected to a Ccrossflow,". *AIAA Journal.*, Vol. 9:pp. 718–724, April 1971.

[21] R. Courant, K. Friedrichs, and H. Lewy. "On the Partial Difference Equations of Mathematical Physics". *IBM Journal of Research and Development*, vol. 11, Iss. 2:pp.215–234, 1967.

[22] Library of Congress. Daniels, John T. (photographer) "First Flight December 17 1903". American Treasures of the Library of Congress exhibition.

[23] D. Davidenko, I. Gokalp, E. Dufour, and P. Magre. "Numerical Simulation of Hydrogen Supersonic Combustion and Validation of Computational Approach". *12th AIAA International Space Planes and Hypersonic Systems and Technologies, Virginia, AIAA-7033*, 2003.

[24] Web Reference: Image downloaded on 1st April 2011 from:. `http://media.web.britannica.com/eb-media/91/145291-004-011EE181.jpg`.

[25] Web Reference: Image downloaded on 1st April 2011 from:. `http://www.cora.nwra.com/~werne/eos/images/volcano.gif`.

[26] Web Reference: Image downloaded on 1st April 2011 from:. http://ecomodder.com/forum/showthread.php/aerodynamics-rockets-vs-cars-1862.html.

[27] Web Reference: Image downloaded on 1st April 2011 from:. http://fdrc.iit.edu/research/images/TurbulentBoundaryLayer.jpg.

[28] Web Reference: Image downloaded on 1st April 2011 from:. http://www.cortana.com/Drag_Description.htm.

[29] Web Reference: Image downloaded on 1st April 2011 from:. http://www.brockmann-consult.de/CloudStructures/images/kelvin-helmholtz-instab/k-w-system.gif.

[30] Web Reference: Image downloaded on 1st April 2011 from:. http://www.cora.nwra.com/dave/movies/KH/KHRi=0.05threebillow.jpg.

[31] Web Reference: Image downloaded on 1st April 2011 from:. http://www.grc.nasa.gov.

[32] Web Reference: Image downloaded on 1st April from:. http://www.nytimes.com/2007/06/12/business/12turbulence.html?_r=1.

[33] Web Reference: Image downloaded on 30th March 2011 from:. http://en.wikipedia.org/wiki/File:Ohain_USAF_He_178_page61.jpg.

[34] Web Reference: Image downloaded on 30th March 2011 from:. http://walesairnetwork.files.wordpress.com/2010/05/air_france_concorde.jpg.

[35] Web Reference: Image downloaded on 30th March 2011 from:. http://apod.nasa.gov/apod/image/0403/x43a2_nasa_big.jpg.

[36] Web Reference: Image downloaded on 30th March 2011 from:. http://en.wikipedia.org/wiki/File:Turbo_ram_scramjet_comparative_diagram.svg.

[37] Web Reference: Image downloaded on 30th March 2011 from:. http://www.boeing.com/defense-space/military/waverider/index.html.

[38] Web Reference: Image downloaded on 30th March 2011 from:. http://www.reactionengines.co.uk.

[39] Web Reference: Image downloaded on 30th March 2011 from:. http://www.uq.edu.au/hypersonics/index.html?page=19501.

[40] P.G. Drazin and W.H. Reid. *Hydrodynamic Stability.* Cambridge University Press, 2004.

[41] D. Drikakis. "Very Large Eddy Simulation". *Special Issue of Internat. Journal of Numerical Methods in Fluids*, Vol. 39:pp. 763864, 2002.

[42] D. Drikakis. "Advances in Turbulent Flow Computations using High-Resolution Methods,". *Progress in Aerospace Science*, Vol.39:pp. 405–424, 2003.

[43] D. Drikakis, M. Hahn, A. Mosedale, and B. Thornber. "Large Eddy Simulation using High-Resolution and High-Order Methods,". *Phil. Trans. R. Soc. A*, Vol.367:pp. 2985–2997, 2009.

[44] D. Drikakis and W. Rider. *High-Resolution Methods for Incompressible and Low-Speed Flows*. Springer-Verlag Berlin Heildelberg, 2005.

[45] D. Drikakis and S. Tsangaris. "On the Accuracy and Efficiency of CFD Methods in Real Gas Hypersonics,". *International Journal for Numerical Methods in Fluids*, Vol.16:pp. 759–775, 1993.

[46] D. Drikakis and S. Tsangaris. "Real Gas Effects for Compressible Nozzle Flow,". *ASME Journal of Fluid Engineering*, Vol.115:pp. 115–120, 1993.

[47] P. Druault, E. Lamballais, J. Delville, and J.P. Bonnet. "Development of Experiment/Simulation Interfaces for Hybrid Turbulent Results Analysis via the use of DNS.". *in: TSFP2, 2nd International Symposium on Turbulence and Shear Flow Phenomena, vol. II, Stockholm.*, pages pp: 5–14, 2001.

[48] G. Eitelberg. "First Results of the Calibration and use of the HEG". *18th AIAA Aerospace Ground Testing Conference, Colorado Springs, AIAA-2525*, 1994.

[49] W.J.D Escher. "The Seven Operating Modes of the Supercharged Ejector Scramjet (SESJ) Combined-cycle Engine". *AIAA-3240*, pages pp–340, 2001.

[50] D. Everett, M. Woodmansee, J. Dutton, and M. Morris. "Wall Pressure Measurements for a Sonic Jet Injected Transversely into a Supersonic Crossflow,". *Journal of Propl. and Power.*, Vol.14:pp. 861–868, 1998.

[51] A. Ferrante, G. Matheou, and P.E. Dimotakis. "LES of an Inclined Sonic Jet into a Turbulent Crossflow at Mach 3.6.". *Journal of Turbulence*, Vol. 12, Art. No. N 2:DOI: 10.1080/14685248.2010.522580., 2011.

[52] U. Frisch. *Turbulence*. Cambridge University Press, Cambridge, UK., 1998.

[53] C. Fureby and F.F. Grinstein. "Large Eddy Simulation of High-Reynolds-Number Free and Wall-Bounded Flows.". *Journal of Comp. Phys.*, Vol. 181:pp: 68–97., 2002.

[54] C. Fureby, D. Knight, and M. Kupianinen. *"Compressible Turbulent Shear Flows", in Implicit Large Eddy Simulation: Computing Turbulent Fluid Dynamics*. Chap:11, Cambridge University Press, Cambridge, UK., 2007,.

[55] C. Fureby, F. Tabor, H.G. Weller, and A.D. Gosman. "A Comparative Study of Subgrid Scale Models in Homogeneous Isotropic Turbulence.". *Phys. Fluids.*, Vol. 9(5):pp: 14161429., 1997.

[56] M. Furudate, B. Lee, and I. Jeung. "Computation of Hyshot Scramjet Flows in the T4 Experiments". *AIAA/CIRA 13th International Space Planes and Hypersonics Systems and Technologies, AIAA-3353*, 2005.

[57] A.D. Gardner and K. Hannemann. "Evaluation of Full-Engine Scramjet Technology". Technical report, The German Aerospace Center, DLR, DLR-IB 224-2004-A-11, 2004.

[58] A.D. Gardner, K. Hannemann, J. Steelant, and A. Paull. "Ground Testing of the Hyshot Supersonic Combustion Flight Experiment in HEG and Comparison with Flight data". *40th AIAA/ASME/SAE/ASEE Joint Propulsion Conference and Exhibit, Florida, AIAA-3345*, 2004.

[59] F. Genin and S. Menon. "Dynamics of Sonic Jet Injection into Supersonic Crossflow,". *Journal of Turbulence.*, Vol.11, No.4,:pp:1–30, DOI: 10.1080/14685240903217813, 2010.

[60] B.J. Geurts. *Elements of Direct and Large-Eddy Simulation*. R.T. Edwards, 2003.

[61] S.K Godunov. "A Finite-Difference Method for the Computation of Discontinuous Solutions of the Equations of Fluid Dynamics.". *Mat. Sb.,*, Vol.47:pp.271–295, 1959.

[62] L. Graf and L. Kleiser. "Large-Eddy Simulation of Double-row Compound-angle Film Cooling: Setup and Validation.". *Computers and Fluids*, Vol. 43:pp: 58–67, 2011.

[63] F. Grinstein, L. Margolin, and W. Rider. *Implicit Large Eddy Simulation: Computing Turbulent Fluid Dynamics*. Cambridge University Press, USA., 2007.

[64] F.F. Grinstein and C.R. DeVore. "Coherent Structure Dynamics in Spatially Developing Square Jets.". *AIAA-1992-3441*, 1992.

[65] F.F. Grinstein and C.R. DeVore. "Dynamics of Coherent Structure and Transition to Turbulence in Free Shear Jets.". *Physics of Fluids*, Vol. 8:pp: 1237–1251, 1996.

[66] F.F. Grinstein and G.E. Karniadakis. "Alternative LES and Hybrid RANS/LES.". *ASME Journal of Fluids Engineering*, Vol. 124:pp: 821–942, 2002.

[67] M. Gruber, A. Nejad, T. Chen, and J. Dutton. "Mixing and Penetration Studies of Sonic Jets in a Mach 2 Freestream,". *Journal of Propulsion and Power*, Vol.11:pp. 315–323, 1995.

[68] H. Guillard. "Recent Developments in the Computation of Compressible Low Mach Number Flows.". *Flow Turbul. Combust.*, Vol. 76:pp:363–369, 2006.

[69] H. Guillard and A. Murrone. "On the Behaviour of Upwind Schemes in the Low Mach number limit: Ii. Godunov type Schemes,". *Comput. Fluids.*, Vol.33:pp. 655–675, 2004.

[70] H. Guillard and C. Viozat. "On the Behaviour of Upwind Schemes in the Low Mach Number Limit.". *Comput. Fluids.*, Vol. 28:pp:63–86, 1999.

[71] M. Hahn. *Implicit Large-Eddy Simulation of Low-Speed Separated Flows Using High-Resolution Methods*. PhD thesis, School of Engineering, Cranfield University, Cranfield, U.K., 2008.

[72] M. Hahn and D. Drikakis. "Large Eddy Simulation of Compressible Turbulence using High-Resolution Methods.". *International Journal of Numerical Methods in Fluids*, Vol. 47:pp: 971–977, 2004.

[73] A.N. Hakim, S. Aso, and Y. Tani. "Experimental Study on Effects of Shock Wave Impingement on Supersonic Combustion". *Memoirs of the Faculty of Engineering, Kyushu University, Japan*, Vol.68, Iss.1, 2008.

[74] K. Hannemann. "High Enthalpy Flows in the HEG Shock Tunnel: Experiment and Numerical Rebuilding". *41st AIAA Aerospace Sciences Meeting and Exhibit, Reno, AIAA-0978*, 2003.

[75] A. Harten. "High Resolution Schemes for Hyperbolic Conservation,". *J. Comput. Phys.*, Vol.49:pp.375–393., 1983.

[76] W.H. Heiser and D.T. Pratt. *Hypersonic Airbreathing Propulsion*. AIAA Education Series, Ohio., 1994.

[77] T. Hiraiwa, K. Ito, S. Sato, S. Ueda, K. Tani, S. Tomioka, and T. Kanda. "Recent Progress in Scramjet/Combined Cycle Engines at JAXA, Kakuda Space Center". *Acta Astronautica*, Vol.63:565–574, 2008.

[78] E.H. Hirschel. *Basics of Aerothermodynamics*. Springer-Verlag, Berlin Heidelberg, 2005.

[79] C.W. Hirt. "Computer Studies of Time-dependent Turbulent Flows.". *Physics of Fluids*, Vol. 2:pp: 219–227, 1969.

[80] K.A. Hoffmann and S.T. Chiang. *Computational Fluid Dynamics: Volume I*. Engineering Education Systems, Kansas, USA, 4th ed., August 2000.

[81] K.A. Hoffmann and S.T. Chiang. *Computational Fluid Dynamics: Volume II*. Engineering Education Systems, Kansas, USA, 4th ed., August 2000.

[82] K.A. Hoffmann and S.T. Chiang. *Computational Fluid Dynamics: Volume III*. Engineering Education Systems, Kansas, USA, 4th ed., August 2000.

[83] R.W. Humble, G.N. Henry, and W.J. Larson. *Space Propulsion Analysis and Design.* McGraw-Hill Companies Inc., USA., 2nd ed., 1995.

[84] T.A. Jackson. "Power for a Space Plane". *Scientific American*, pages 56–63, August, 2006.

[85] I. Jeung and J. Choi. "Numerical Simulation of Supersonic Combustion for Hypersonic Propulsion". *5th Asia-Pacific Conference on Combustion, Australia*, 2005.

[86] S. Karl, K. Hannemann, A. Mack, and J. Steelant. "CFD Analysis of the Hyshot-II Scramjet Experiments in the HEG Shock Tunnel". *15th AIAA International Space Planes and Hypersonic Systems and Technologies Conference, Ohio, AIAA-2548*, 2008.

[87] L.G. Kaufman II. "Hypersonic Flow past Transverse Jets ,". *Journal of Spacecraft and Rockets.*, Vol.4:pp: 1230–1235, 1967.

[88] S. Kawai and S. Lele. "Large-Eddy Simulation of Jet Mixing in a Supersonic Turbulent Crossflow,". *19th AIAA Computational Fluid Dynamics, San Antonio, Texas, (AIAA-2009-3795)*, June 2009.

[89] S. Kawai and S. Lele. "Large-Eddy Simulation of Jet Mixing in Supersonic Turbulent Crossflows,". *AIAA Journal.*, Vol. 48, September 2010.

[90] R.M. Kelvin. "Hydrokinetic Solutions and Observations.". *Phil. Mag.*, Vol. 42:pp:362–377, 1871.

[91] K. Kemenov and S. Menon. "Explicit Small-Scale Velocity Simulation for High Reynolds Number Turbulent Flows". *Journal of Comp. Phys.*, Vol. 220:pp: 290–311., 2006.

[92] A. Kempf, M. Klein, and J. Janicka. "Efficient Generation of Initial- and Inflow-Conditions for Transient Turbulent Flows in Arbitrary Geometries.". *Flow Turbulence Combust.*, Vol. 74:pp: 67–84, 2005.

[93] K.H. Kim and C. Kim. "Accurate, Efficient and Monotonic Numerical Methods for Multidimensional Compressible Flows. Part II. Multi-dimensional Limiting Process". *J. Comput. Phys.*, Vol. 208:pp:570–615, 2005.

[94] M. Kindler, M. Lempke, T. Blacha, P. Peter Gerlinger, and M. Aigner. "Numerical Investigation of the Hyshot Supersonic Combustion Configuration". *44th AIAA/ASME/SAE/ASEE Joint Propulsion Conference & Exhibit, CT, AIAA-5165*, 2008.

[95] M. Klein, A. Sadiki, and J. Janicka. "A Digital Filter Based Generation of Inflow Data for Spatially Developing Direct Numerical or Large Eddy Simulations,". *Journal of Computational Physics*, Vol.186:pp.652–665., 2003.

[96] D. Knight. *Elements of Numerical Methods for Compressible Flows*. Chap:11, Cambridge University Press, Newyork., 2006,.

[97] D. Knight, H. Yan, A. Panaras, and A. Zheltovodov. "Advances in CFD Prediction of Shock Wave Turbulent Boundary Layer Interactions". *Progress in Aerospace Sciences*, Vol.39:pp: 121–184, 2003.

[98] H. Ko and W.S. Yoon. "Performance Analysis of Secondary Gas Injection into a Conical Rocket Nozzle". *Journal of Prop., and Power*, Vol.18, Iss.3:pp:585–591, 2002.

[99] I.W. Kokkinakis. *Investigation of High-Resolution Methods in Large Eddy Simulation of Subsonic and Supersonic Wall Turbulent Flows*. PhD thesis, School of Engineering, Cranfield University, Cranfield, U.K., 2009.

[100] A.N. Kolomogorov. "The Local Structure of Turbulence in an Incompressible Fluid at Very High Reynolds numbers,". *Dokl. Akad. Nauk. SSSR*, Vol.30,299, 1941.

[101] A.K. Kuczaj and B.J. Geurts. "Mixing in Manipulated Turbulence.". *Journal of Turbulence*, Vol. 7, No. 15,:DOI: 10.1080/14685240500331595., 2006.

[102] M. T. Landahl and E. Mollo-Christensen. *Turbulence And Random Processes in Fluid Mechanics*. Cambridge University Press, Cambridge, UK., Second ed., 1992.

[103] C.B. Laney. *Computational Gasdynamics*. Cambridge University Press, 1998.

[104] L. Larcheveque, P. Sagaut, I. Mary, and O. Labbe. "Large-Eddy Simulation of a Compressible Flow past a Deep Cavity.". *Phys. Fluids*, Vol. 15:pp:193–209.

[105] S. Lardeau, E. Lamballais, and J.P. Bonnet. "Direct Numerical Simulation of a Jet Controlled by Fluid Injection.". *Journal of Turbulence*, Vol. 3:pp. 1–25, 2002.

[106] S. Lee, S. Lele, and P. Moin. "Simulation of Spatially Evolving Compressible Turbulence and the Application of Taylors Hypothesis.". *Physics of Fluids.*, Vol. 4, Iss. 8,:pp: 1521–1530, 1992.

[107] M. Lesieur and O. Metais. "New Trends in Large-Eddy Simulations of Turbulence.". *Annu. Rev. Fluid Mech.*, Vol. 28:pp: 4582., 1996.

[108] E. Love and C. Grigsby. "Some Studies of a Symmetric Free Jets Exhausting from Sonic and Supersonic Nozzles into Still Air and into Supersonic Streams,". *NACA Report RM-L54L31.*, 1955.

[109] T.S. Lund, X. Wu, and K.D. Squires. "Generation of Turbulent Inflow Data for Spatially-Developing Boundary Layer Simulations,". *J. Comput. Phys.*, Vol.140:pp.233–258., 1998.

[110] A. Mack and J. Steelant. "Mixing Enhancement by Shock Impingement in a Generic Scramjet Combustion Chamber". *European Conference on Computational Fluid Dynamics, Netherlands*, 2006.

[111] A. Mack, J. Steelant, J.M. Schramm, and K. Hannemann. "Sensitivity Analysis for the Hyshot Generic Supersonic Combustion Configuration using CFD". *ISABE-2007-1310*, 2007.

[112] L.G. Margolin and W.J. Rider. "A Rationale for Implicit Turbulence Modeling.". *International Journal of Numerical Methods in Fluids*, Vol. 39:pp: 821–841, 2002.

[113] L.G. Margolin and W.J. Rider. "The Design and Construction of Implicit LES Models.". *International Journal of Numerical Methods in Fluids*, Vol. 47:pp: 1173–1179, 2005.

[114] J. McGuire, R. Boyce, and N. Mudford. "Comparison of Computational and Experimental Studies on Shock Induced Ignition in Scramjets". *AIAA/CIRA 13th International Space Planes and Hypersonics Systems and Technologies, AIAA-3394*, 2005.

[115] D.J. McNabb. *INVESTIGATION OF ATMOSPHERIC REENTRY FOR THE SPACE MANEUVER VEHICLE.* PhD thesis, Thesis, Air Force Institute of Technology, Wright-Patterson Air Force Base, Ohio., 2004.

[116] T.H. New and W.L. Tay. "Effects of Cross-stream Radial Injections on a Round Jet.". *Journal of Turbulence*, Vol. 7:DOI: 10.1080/14685240600847466., 2006.

[117] W. Noh. "Errors for Calculations of Strong Shocks using and Artificial Viscosity and an Artificial Heat Flux.". *J. Comput. Phys.*, Vol. 72:pp:78–120, 1987.

[118] G.J. Nothwang. "An Evaluation of Four Experimental Methods for Measuring Mean Properties of a Supersonic Turbulent Boundary Layer.". *NACA Report-1320*, pages pp: 939–949, January 1957.

[119] Web Reference: on 1st April 2011 from:. `http://www.engineeringtoolbox.com/strouhal-number-d_582.html`.

[120] R.C. Orth and J.A. Funk. "An Experimental and Comparative Study of Jet Penetration in Supersonic Flow,". *Journal of Spacecraft and Rockets.*, Vol. 4,:pp. 1236–1242, 1967.

[121] R. L. Panton. *Incompressible Flow*. John Wiley and Sons, 1984.

[122] A. Paull, M. Frost, and H. Alesi. "Hyshot-T4 Supersonic Combustion Experiments". Technical report, The University of Queensland, Australia, NAG-1-2113.

[123] S. Pirozzoli, M. Bernardini, and F. Grasso. "Characterization of Coherent Vortical Structures in a Supersonic Turbulent Boundary Layer". *J. of Fluid Mechanics*, Vol.613:pp. 205231, DOI:10.1017/S0022112008003005, 2008.

[124] S. Pirozzoli and F. Grasso. "Direct Numerical Simulation of Impinging Shock Wave/Turbulent Boundary Layer Interaction at M = 2.25". *Phys. Fluids.*, Vol. 18(6), 2006.

[125] S. Pirozzoli, F. Grasso, and T.B. Gatski. "Direct Numerical Simulation and Analysis of a Spatially Evolving Supersonic Turbulent Boundary Layer at M2.25". *Physics of Fluids*, Vol.16, No.3:pp. 530545, DOI: 10.1063/1.1637604, 2004.

[126] S.B. Pope. *Turbulence*. Cambridge University Press, Cambridge, UK., 2000, ISBN: 0521591252.

[127] Z.A. Rana and D. Drikakis. "Investigation of Sonic Jet Mixing in a Stream of Supersonic Cross-flow using Large Eddy Simulations,". *Proceedings of 27th Congress of the International Council of the Aeronautical Sciences (ICAS-2010), Nice, France. (ISBN: 9780956533302)*, 2010.

[128] Z.A. Rana, B. Thornber, and D. Drikakis. "CFD Analysis of a Scramjet Model using High-Resolution Methods,". *Proceedings of European Air & Space Conference, Manchester, UK. (CEAS-2009)(ISBN: 1857682084)*, 2009.

[129] Z.A. Rana, B. Thornber, and D. Drikakis. "Large Eddy Simulation of a Scramjet Model (Hyshot-II) using High-Resolution Methods,". *45th AIAA/ASME/SAE/ASEE Joint Propulsion Conference & Exhibit, Denver, Colorado, USA.*, 2009.

[130] Z.A. Rana, B. Thornber, and D. Drikakis. "An ILES Analysis of Transverse Jet Injection in to Supersonic Cross-flow with Synthetic Turbulent Boundary Layer,". *49th AIAA Aerospace Sciences Meeting & Exhibit, 4-7 January 2011, Orlando, FL, USA. (AIAA-2011-231)*, 2011.

[131] Z.A. Rana, B. Thornber, and D. Drikakis. "Analysis of Hydrogen Injection into the Combustor of HyShot-II Scramjet Engine using ILES,". *49th AIAA Aerospace Sciences Meeting & Exhibit, 4-7 January 2011, Orlando, FL, USA. (AIAA-2011-506)*, 2011.

[132] Z.A. Rana, B. Thornber, and D. Drikakis. "On the Importance of Generating Accurate Turbulent Boundary Condition for Unsteady Simulations". *submitted to Jour. Turb.*, Vol. 12, No. 35:DOI: 10.1080/14685248.2011.613836, 2011.

[133] Z.A. Rana, B. Thornber, and D. Drikakis. "Transverse Jet Injection into a Supersonic Turbulent Cross-Flow.". *Phys. Fluids*, Vol: 23, Iss: 4,:(DOI:10.1063/1.3570692), April, 2011.

[134] P.J. Roache. *Fundamentals of Computational Fluid Dynamics.* Hermosa Publishers, Albuquerque, New Mexico., 1998.

[135] P.J. Roache. *Verification and Validation in Computational Science and Engineering.* Hermosa Publishers, Albuquerque, New Mexico., 1998.

[136] P.J. Roache, K. Ghia, and F. White. "Editorial Policy Statement on the Control of Numerical Accuracy.". *ASME Journal of Fluids Engineering*, Vol. 108(1):pp: 2., 1986.

[137] C. W. Rowley and D. R. Williams. "Dynamics and Control of High Reynolds number Flow over Open Cavities". *Annual Review of Fluid Mechanics*, vol. 38:pp. 251–276, 2006.

[138] N.D. Sandham, Y.F. Yao, and A.A Lawal. "Large-Eddy Simulation of Transonic Turbulent Flow Over a Bump". *Int. J. Heat Fluid Flow*, Vol.24:pp: 584–595, 2003.

[139] J. Santiago and J. Dutton. "Velocity Measurements of a Jet Injected into a Supersonic Flow,". *Journal of Propulsion and Power.*, Vol.13:pp. 264–273, March-April 1997.

[140] R.L. Sarno and M.E. Franke. "Suppression of Flow-Induced Pressure Oscillations in Cavities". *Journal of Aircraft*, Vol.31, Iss.1:90–96, 1994.

[141] J. Schetz and F. Billig. "Penetration of Gaseous Jets Jnjected into a Supersonic Stream,". *Journal of Spacecraft and Rockets.*, Vol. 3:pp. 1658–1665, November 1966.

[142] P. Schlatter, R. Orlu, Q. Li, G. Brethouwer, J.H.M. Fransson, A.V. Johansson, P.H. Alfredsson, and D.S. Henningson. "Turbulent Boundary Layers up to Re=2500 studied through Simulation and Experiment.". *Physics of Fluids*, Vol. 21:DOI: 10.1063/1.3139294, 2009.

[143] J.M. Schramm, S. Karl, K. Hannemann, and J. Steelant. "Ground Testing of the Hyshot-ii Scramjet Configuration in HEG". *15th AIAA Space Planes and Hypersonic Systems Conference, Dayton, AIAA-2547*, 2008.

[144] P.R. Spalart. "Direct Simulation of a Turbulent Boundary Layer up to Re = 1410". *J. of Fluid Mechanics*, Vol.187:pp. 6198, 1988.

[145] P.R. Spalart and A. A. Leonard. "Direct Numerical Simulation of Equilibrium Turbulent Boundary Layers.". *in Proc. 5th Symp. on Turbulent Shear Flows, Ithaca, NY, USA.*, 1985.

[146] R.J. Spiteri and S.J. Ruuth. "A New Class of Optimal High-Order Strong-Stability-Preserving Time Discretization Method,". *SIAM Jour. Numer. Anal.*, Vol.40; Iss.2:pp. 469–491, 2002.

[147] AMES Research Staff. "Equations, Tables and Charts for Compressible Flows". Technical report, National Advisory Committee for Aeronautics (NACA), 1135, 1953.

[148] R.J. Stalker, A. Paull, D.J. Mee, R.G. Morgan, and P.A. Jacobs. "Scramjets and Shock tunnels the Queensland Experience". *Progress in Aerospace Sciences*, Vol.41:471–513, 2005.

[149] B. Thornber and D. Drikakis. "Large Eddy Simulation of a Deep Cavity using High-Resolution Methods". *46th AIAA Aerospace Sciences Meeting and Exhibit, AIAA-0730*, vol. 46, No. 10:pp. 2634–2645, 2008.

[150] B. Thornber, D. Drikakis, R.J.R. Williams, A. Mosedale, and D. Youngs. "An Improved Reconstruction Method for Compressible Flows with Low Mach Number Features,". *J. Comput. Phys.*, Vol.227;Iss.10:pp.4873–4894., 2008.

[151] B. Thornber, D. Drikakis, R.J.R. Williams, and D. Youngs. "On Entropy Generation and Dissipation of Kinetic Energy in High-resolution Shock-capturing Schemes,". *J. Comput. Phys.*, Vol.227;Iss.10:pp.4853–4872., 2008.

[152] B. Thornber, D. Drikakis, D. Youngs, and R.J.R. Williams. "The Influence of Initial Conditions on Turbulent Mixing due to Richtmyer-Meshkov Instability,". *J. Fluid. Mech.*, Vol.654:pp.99–139., 2010.

[153] B. Thornber, M. Starr, and D. Drikakis. "Implicit Large Eddy Simulation of Ship Airwakes,". *Aeronaut. J.*, Vol.114:pp.99–139., 2010.

[154] B.J. Thornber. *Implicit Large Eddy Simulation for Unsteady Multi-Component Compressible Turbulent Flows*. PhD thesis, School of Engineering, Cranfield University, Cranfield, U.K., 2007.

[155] E.F. Toro. *Riemann Solvers and Numerical Methods for Fluid Dynamics: A Practical Introduction*. Springer-Verlag Berlin Heidelberg, 3rd ed, 2009.

[156] E. Touber and N. Sandham. "Large-Eddy Simulation of Low-Frequency Unsteadiness in a Turbulent Shock-Induced Separation Bubble,". *Theor. Comput. Fluid Dynamics*, Vol.23:pp. 79–107, 2009.

[157] L. S. Ukeiley, M. K. Ponton, J. M. Seiner, and B. Jansen. "Suppression of Pressure Loads in Cavity Flows". *AIAA Journal*, Vol.42, Iss.1:70–79, 2004.

[158] A. D. Vakili and C. Gauthier. "Control of Cavity Flow by Upstream Mass-Injection". *Journal of Aircraft*, Vol.31, Iss.1:169–174, 1994.

[159] B. Van-Leer. "Towards the Ultimate Conservative Difference Scheme-IV. A New Approach to Numerical Convection,". *Journal of Compu. Phys.*, Vol.23:pp. 276–299, 1977.

[160] M. Vanierschot, T. Persoons, and E. Van den Bulck. "A new Method for Annular Jet Control based on Cross-Flow Injection,". *Physics of Fluids.*, Vol.21, Iss. 2.:Article Number: 025103, DOI: 10.1063/1.3037343, 2009.

[161] W. VanLerberghe, J. Santiago, J. Dutton, and R. Lucht. "Mixing of a Sonic Transverse Jet Injected into a Supersonic Flow,". *AIAA Journal.*, Vol.38, March 2000.

[162] I. Veloudis, Z. Yang, J.J. McGuirK, G.J. Page, and A. Spencer. "Novel Implementation and Assessment of a Digtial Filter Based Approach for the Generation of LES Inlet Conditions.". *Flow Turbulence Combust.*, Vol. 79(1):pp: 1–24, 2007.

[163] H.K. Versteeg and W. Malalasekera. *An Introduction to Computational Fluid Dynamics; The FV Method*. Longman Scientific & Technical, England., 1995.

[164] V. Viti, R. Neel, and J.A. Schetz. "Detailed Flow Physics of the Supersonic Jet Interaction Flow Field,". *Physics of Fluids.*, Vol.21, 2009.

[165] G. Volpe. "Performance of Compressible Flow Codes at Low Mach Number.". *AIAA J.*, Vol. 31:pp:49–56, 1993.

[166] T. von Kármán. "Mechanische Ähnlichkeit und Turbulenz". *Nachrichten von der Gesellschaft der Wissenschaften zu Gttingen, Fachgruppe 1 (Mathematik), (also as: Mechanical Similitude and Turbulence, Tech. Mem. NACA, no. 611, 1931)*, vol. 5:pp: 58–76, 1930.

[167] F. M. White. *Viscous Flow Field*. McGraw-Hill Book Company, 1974.

[168] C. WYNGAARD and S.F. CLIFFORD. "Recent Developments in the Computation of Compressible Low Mach Number Flows.". *Atrnos. Sci.*, Vol. 34:pp:922, 1977.

[169] Z.T. Xie and I.P. Castro. "Efficient Generation of Inflow Conditions for Large Eddy Simulation of Street-Scale Flows,". *Flow Turbulence Combust.*, Vol.81:pp.449–470., 2008.

[170] D.L. Youngs. "Three-Dimensional Numerical Simulation of Turbulent Mixing by Rayleigh-Taylor Instability.". *Phys. Fluids.*, Vol. 3(5):pp: 13121320., 1991.

[171] V. Zakkay, W. Calarese, and L. Sakell. "An Experimental Investigation of the Interaction between a Transverse Sonic Jet and a Hypersonic Stream,". *AIAA Journal.*, Vol.9:pp: 674–681, 1971.

[172] J. Zoltak and D. Drikakis. "Hybrid Upwind Methods for the Simulation of Unsteady Shock-Wave Diffraction Over a Cylinder,". *Computer Methods in Applied Mechanics and Engineering*, Vol.162:pp. 165–185, 1998.

[173] N. Zong, H. Meng, S.Y. Hsieh, and V. Yang. "A Numerical study of Cryogenic Fluid Injection and Mixing under Supercritical Conditions,". *Physics of Fluids.*, Vol.16, Iss. 12:pp. 4248–4261, DOI: 10.1063/1.1795011, 2004.

[174] E.E. Zukoski and F.W. Spaid. "Secondary Injection of Gases into a Supersonic Flow,". *AIAA Journal.*, Vol.2:pp: 1689–1696, 1964.